Lipid Fingerprinting by Mass Spectrometry and Laser Light

Inaugural-Dissertation
to obtain the academic degree
Doctor rerum naturalium (Dr. rer. nat.)

submitted to the Department of Biology, Chemistry, Pharmacy
of Freie Universität Berlin

by

Carla Kirschbaum

2023

This work was performed at the Freie Universität Berlin and the Fritz-Haber-Institut der Max-Planck-Gesellschaft in Berlin from October 2019 to December 2022 under the supervision of Prof. Dr. Kevin Pagel.

First Reviewer: Prof. Dr. Kevin Pagel, Freie Universität Berlin

Second Reviewer: Prof. Dr. Rainer Haag, Freie Universität Berlin

Date of Defense: March 7, 2023

Statutory Declaration

I hereby declare that I have prepared my thesis independently and have not used any sources or aids other than those indicated. All quotations and citations have been duly acknowledged.

Berlin, January 3, 2023

Carla Kirschbaum

«Ce travail est parfois lent, rendu un peu plus lent encore par notre désir — qui, en cherchant à l’accélérer, l’entrave — [...] et n’aboutit que quand nous avons cessé de désirer»

Marcel Proust, A la recherche du temps perdu, 1918.

Abstract

Lipids have accompanied the emergence of life on Earth. Their tendency to form spherical assemblies in water afforded the separation of organisms from their environment while still allowing controlled exchange of substances between the inside and outside. Lipids enable cellular compartmentalization, modulate membrane proteins, and are involved in intra- and intercellular signaling. The multitude of biological functions is reflected in a tremendous structural diversity, which involves the frequent occurrence of isomers with very specific biological roles. Although highly relevant from a biological perspective, many lipid isomers cannot be distinguished by state-of-the-art mass spectrometry-based analytical techniques.

This work explores the potential of coupling mass spectrometry with infrared spectroscopy to analyze lipid isomers and study lipid fragmentation mechanisms. Infrared spectroscopy adds a structural dimension to the mass spectrometric analysis and previously yielded promising results for other biomolecules. We recorded the first high-resolution infrared spectra of ionized lipids and glycolipids using helium nanodroplets as a cryogenic spectroscopic matrix. Isomeric glycolipids were found to be unambiguously distinguishable based on their diagnostic spectroscopic fingerprints. The high resolution and sensitivity of the technique enabled the relative quantification of low-abundant glycolipid isomers in biological samples by spectral deconvolution. A similar approach was used to analyze double bond isomers in lipids extracted from cancer cells, which revealed significant differences between cancer types. The position and geometry of C=C bonds in sphingolipids and fatty acids were rendered visible by amines, which interact with the C=C bond and induce diagnostic vibrations. Furthermore, infrared spectroscopy was employed in combination with computational chemistry to gain fundamental understanding of lipid fragmentation in tandem mass spectrometry. A key fragmentation mechanism used for the structural analysis of glycerolipids was thus unveiled and found to occur with high regioselectivity. In addition, unknown fragmentation pathways of vitamin E derivatives were identified by spectroscopy-based assignment of fragment structures. Overall, the coupling of mass spectrometry and infrared spectroscopy has proven to be a powerful approach to study lipid fragmentation mechanisms and to identify biologically relevant lipid isomers from minute sample amounts. The technique is expected to drive important advances in lipid analysis in the near future.

Zusammenfassung

Seit seiner Entstehung ist das Leben auf der Erde untrennbar mit Lipiden verbunden. Lipidmembranen ermöglichen die räumliche Abtrennung von Organellen innerhalb von Zellen, von Zellen innerhalb von Organismen und von Organismen in ihrer unbelebten Umgebung. Lipide beeinflussen zudem die Funktion von Membranproteinen und sind als Botenstoffe am intra- und interzellulären Informationsaustausch beteiligt. Die Vielzahl ihrer biologischen Funktionen spiegelt sich in der strukturellen Vielfalt der Lipide und dem häufigen Auftreten von Isomeren wider. Viele dieser Isomere, die oft sehr spezifische biologische Funktionen erfüllen, können mit modernen massenspektrometrischen Analysemethoden nicht unterschieden werden.

Durch die Kopplung von Massenspektrometrie mit Infrarotspektroskopie werden neben der Masse von Molekülen auch strukturelle Informationen erhalten. Die Technik wurde bereits erfolgreich für andere Biomoleküle angewendet und wird in dieser Arbeit erstmals für die Analyse von isomeren Lipiden und die Untersuchung von Lipidfragmentierung eingesetzt. Für die Aufnahme von hochaufgelösten Infrarotspektren ionisierter Lipide und Glykolipide wurden Heliumtröpfchen als kryogene spektroskopische Matrix verwendet. Isomere Glykolipide konnten mit dieser Technik eindeutig voneinander unterschieden und in biologischen Proben durch Dekonvolution der Infrarotspektren quantifiziert werden. Eine ähnliche Methode wurde zur relativen Quantifizierung von Doppelbindungsisomeren in Lipidextrakten aus Krebszellen angewendet. Die Analyse zeigte eindeutige Unterschiede in der Isomerenverteilung zwischen verschiedenen Krebstypen. Die Position und Geometrie der C=C Bindungen wurden mit Hilfe von Aminen bestimmt, die als Doppelbindungssensoren spezifische Wechselwirkungen mit der C=C Bindung eingehen. Darüber hinaus wurde mittels Infrarotspektroskopie und quantenchemischen Methoden der regioselektive Mechanismus einer der wichtigsten Fragmentierungsreaktionen in der Analytik von Glycerolipiden aufgeklärt. Außerdem wurden Fragmentstrukturen von Vitamin E Derivaten spektroskopisch identifiziert und plausible Fragmentierungswege berechnet. Die Ergebnisse dieser Arbeit zeigen, dass mittels kryogener Infrarotspektroskopie ein grundlegendes Verständnis von Fragmentierungsmechanismen in der Lipidanalytik gewonnen werden kann. Zusätzlich können mit der Technik biologisch relevante Lipidisomere mit minimalem Probenverbrauch unterschieden werden. Die Kopplung von Massenspektrometrie mit Infrarotspektroskopie hat daher großes Potential, die nächsten Entwicklungen in der Lipidanalytik wesentlich voranzutreiben.

Abbreviations

ATD	Arrival time distribution
CCS	Collision cross section
Cer	Ceramide
CID	Collision-induced dissociation
CoA	Coenzyme A
DAG	Diacylglycerol
DC	Direct current
DEA	Dissociative electron attachment
DFT	Density functional theory
DT	Drift tube
EID	Electron-induced dissociation
ESI	Electrospray ionization
FA	Fatty acid
FEL	Free-electron laser
FWHM	Full width at half maximum
GAA	α-Glucosidase
Gal	Galactose
Gb3	Globotriose
GLA	α-Galactosidase
Glc	Glucose
HCD	Higher-energy collisional dissociation
HPLC	High-performance liquid chromatography
iGb3	iso-Globotriose
IM-MS	Ion mobility-mass spectrometry
IMS	Ion mobility spectrometry
IR	Infrared
IRMPD	Infrared multiple photon dissociation
LC	Liquid chromatography
LINAC	Linear accelerator
MS	Mass spectrometry
MS/MS	Tandem mass spectrometry
m/z	Mass-to-charge
NMF	Non-negative matrix factorization
NMR	Nuclear magnetic resonance
NKT cell	Natural killer T cell
OPA	Optical parametric amplifier
OPO	Optical parametric oscillator
OzESI	Ozone electrospray ionization
OzID	Ozone-induced dissociation
PA	Phosphatidic acid
PC	Phosphatidylcholine
PE	Phosphatidylethanolamine
PES	Potential energy surface
PG	Phosphatidylglycerol
PI	Phosphatidylinositol
PS	Phytosphingosine or Phosphatidylserine
RDD	Radical-directed dissociation
RF	Radio frequency
SA	Sphinganine
SLIM	Structures for lossless ion manipulation
SM	Sphingomyelin
s/n	Signal-to-noise
sn	Stereospecific numbering
SNFG	Symbol nomenclature for glycans
SO	Sphingosine
TAG	Triacylglycerol
TM	Trajectory method
UPLC	Ultra-high performance liquid chromatography
UV	Ultraviolet
UVPD	Ultraviolet photodissociation

Contents

1 Introduction

In the last few decades, mass spectrometry has revolutionized lipid analysis and boosted the comparably young field of lipidomics. State-of-the-art workflows allow to identify and quantify lipids from picomolar quantities within short times and map their distribution in tissue. Why is it then still worth exploring new and innovative techniques for lipid analysis? This chapter aims to provide answers to this question. Several common types of lipid isomers will be presented, whose differentiation remains a particular challenge and requires novel analytical approaches. Subsequently, the prospects of solving some of the current challenges in lipidomics by coupling mass spectrometry with infrared spectroscopy will be outlined. The motivation is followed by a concise overview of this work.

1.1 Motivation

Among the four big classes of biomolecules—nucleotides, proteins, carbohydrates, and lipids—the latter certainly constitutes the most heterogeneous group. The structural diversity of lipids is tremendous and notably reflected in the multitude of their biological functions. Lipids are involved, for example, in energy storage, signaling, cell compartmentalization, modulation of membrane proteins, and protection against free radicals.[1] Because structure defines function, individual lipid isomers can fulfill specific roles in the metabolism, and their relative abundance varies between different tissues and in the pathogenesis and course of diseases.[2–6] For example, cancer cells were found to produce elevated amounts of lipid isomers with unusual double bond positions, which could be used as diagnostic biomarkers.[7,8] In the light of this and other recent findings, modern lipid analysis increasingly strives for complete structural elucidation of individual lipid species, including all possible isomers.[9–16] Only then can their distinct functions in metabolism and pathogenesis, and their distribution in biological tissues be properly investigated.

Lipidomics is a relatively young field, which is concerned with the structural and functional characterization of all lipids within a biological system.[17] After having lagged behind genomics and proteomics, lipidomics has gained momentum since the early 2000s, mainly owing to developments in the field of mass spectrometry.[18,19] The gold-standard technique for lipid analysis combines soft ionization with tandem mass spectrometry employing collisional activation to dissociate lipids into smaller fragments. Lipid fragmentation provides essential structural information; however, certain structural features do not yield diagnostic fragments upon collisional activation (Figure 1.1).[12] These features include the position and configuration (*cis* (*Z*) or *trans* (*E*)) of C=C bonds within aliphatic chains. Similarly, the location and stereochemistry of chain modifications such as hydroxyl- and other oxygen-containing functional groups are difficult to determine. Another source of isomerism is glycerol, which is one of the most common lipid backbones and features three different linkage positions numbered from *sn*-1 to *sn*-3 (*sn* = stereospecific numbering). In phospholipids, the *sn*-3 position bears a phosphate-containing headgroup. The remaining two positions are occupied by fatty acids, which results in *sn*-positional isomers. The linkage type by which the lipid chains are attached to the glycerol backbone (ester, ether, vinyl ether) gives rise to further isomers. In the case of glycolipids, the carbohydrate attached to the *sn*-3 position adds a whole new dimension of structural complexity.[20]

The past years have witnessed the emergence of numerous advanced mass spectrometry-based approaches that were specifically developed for the analysis of lipid isomers.[11,12] Those techniques are often restricted to one particular kind of isomerism, require specific sample treatment or instrumentation, and are therefore not yet integrated into routine analytical workflows. Infrared spectroscopy, on the other hand, is in principle not restricted to a specific structural

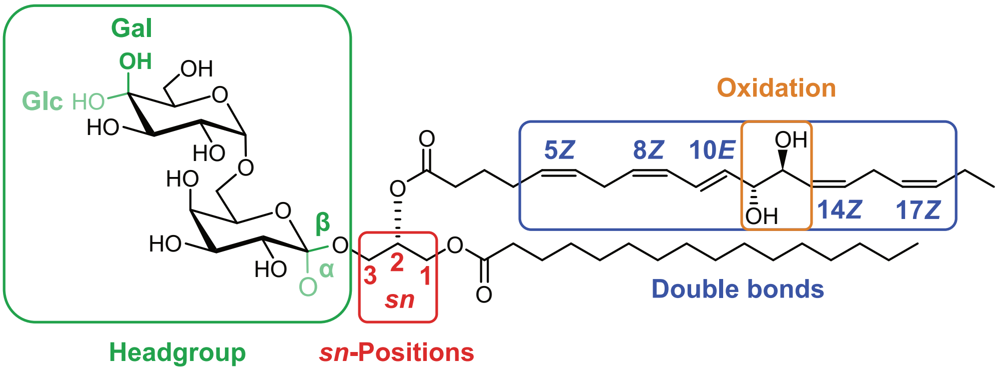

Figure 1.1: Illustration of structural features that give rise to lipid isomers: headgroup, *sn*-positions of fatty acids, position and configuration of double bonds, and oxidation. The depicted molecule is a natural glycoglycerolipid isolated from a marine alga.[21] Glc = glucose, Gal = galactose.

feature. It probes the global structure of a molecule, which is affected by functional groups and their intramolecular interactions. Coupling infrared spectroscopy with mass spectrometry in an approach called *infrared action spectroscopy* provides structural information about possible isomers underlying each peak in the mass spectrum. The technique has shown enormous potential in the analysis of various biomolecules, but had not been used to study lipids prior to this work.[22–25] The aim of this thesis is to investigate the potential of infrared action spectroscopy to fill critical gaps in modern lipid analysis.

1.2 | Outline of this Thesis

In this thesis, the potential of infrared action spectroscopy in the structural analysis of lipids is discussed. Several kinds of isomers that are particularly challenging to distinguish by established analytical techniques are studied throughout a range of representative lipid classes. The fundamentals of lipids, lipid analysis, and infrared spectroscopy are introduced in **Chapter 2**, followed by a description of the utilized experimental techniques in **Chapter 3**. Each of the ensuing chapters addresses one or more of the structural features shown in Figure 1.1. In **Chapter 4**, synthetic and biological glycolipids are investigated with a focus on isomeric glycan headgroups. Double bond regio- and stereoisomers in sphingolipids and fatty acids are studied in **Chapter 5** by taking advantage of amines that act as chemical double bond sensors and also allow differentiation of hydroxylation positions in sphingolipids. In the final **Chapter 6**, infrared action spectroscopy is employed in combination with computational chemistry to investigate the *sn*-specific fragmentation mechanisms of glycerolipids and to reveal unknown fragmentation pathways of chromane-derived antioxidants. The thesis is concluded by **Chapter 7**, which provides an outlook on the future role of infrared action spectroscopy in the lipidomics toolbox.

2 Fundamentals

This chapter provides fundamental knowledge related to the key terms of this work: *lipids* and *infrared action spectroscopy*. The first section is devised to bring order into the complex world of lipids and to yield a brief glance into their manifold structures, functions, and the role of isomers. The overview is followed by a presentation of mass spectrometry-based techniques for lipid analysis and the main challenges they face vis-à-vis the vast structural diversity of lipids. The second part of the chapter is dedicated to infrared spectroscopy. After a general description of the technique, the concept of action spectroscopy in studying ions in the gas phase is introduced. Subsequently, the properties of superfluid helium as a cryogenic spectroscopic matrix are outlined. The chapter concludes with a description of infrared spectroscopy in superfluid helium nanodroplets and its application for the structural analysis of biomolecules.

2.1 | Structural and Functional Diversity of Lipids

Lipids are colloquially known as *fats* in the context of nutrition and health. According to popular opinion, fats are either “good” if they contain, for example, essential omega-3 fatty acids, or “bad” in case of saturated or *trans* fats that are often generated during industrial food processing.[26] In any form, fats deliver more than twice as much energy as the same mass of carbohydrates or proteins, and serve as energy providers for fasting periods.[27] What is commonly known as fats, however, is not to be equated with lipids. Strictly spoken, the term *fats* only embraces triacylglycerols, which represent a lipid subclass among many other lipid (sub-)classes. Those different classes comprise very diverse molecular structures, which fulfill a multitude of biological functions far beyond energy delivery and storage.[28] Lipids are hormones and fat-soluble vitamins, act as second messengers in cellular signaling cascades, and constitute the main components of cell membranes, which enable cellular compartmentalization while supporting dynamic exchange of substances.[1] In their entirety, lipids constitute one of the four big classes of biomolecules besides nucleic acids, proteins, and carbohydrates. However, whereas the other biomolecules are assembled from well-defined building blocks—nucleotides, amino acids, and monosaccharides—lipids lack a universal core structure. Historically, they were merely defined by their hydrophobicity and solubility in non-polar solvents.[29] In an effort to support the emerging field of lipidomics in the early 2000s, the International Lipid Classification and Nomenclature Committee elaborated a more concrete definition of lipids and specified them as *“hydrophobic or amphipathic small molecules that may originate entirely or in part by carbanion-based condensations of thioesters and/or by carbocation-based condensations of isoprene units.”*[30] The two alternative biosynthetic pathways included in this definition generate ketoacyl or isoprene motifs, respectively, and provide the basis for the current LIPID MAPS classification system.[30–32] The classification of lipids into different categories, their respective characteristics, and the relevance of lipid isomers will be detailed in the following.

2.1.1 | Lipid Classification

The large number and structural heterogeneity of lipid species identified to date require a general classification system to enable international communication and seamless integration of newly discovered lipids. For this purpose, the comprehensive LIPID MAPS classification system was established in 2005.[30–32] The system divides lipids into eight categories containing subordinate classes and subclasses, which form the framework of the LIPID MAPS structure database.[33] The eight lipid categories are: fatty acyls, glycerolipids, glycerophospholipids, sphingolipids, saccharolipids, polyketides, prenol lipids, and sterol lipids (Figure 2.1). With the exception of sterol and prenol lipids, the *de novo* lipid biosynthesis relies on the carbanion-based condensation of acetyl-CoA and malonyl-CoA (CoA = coenzyme A), which yields aliphatic chains

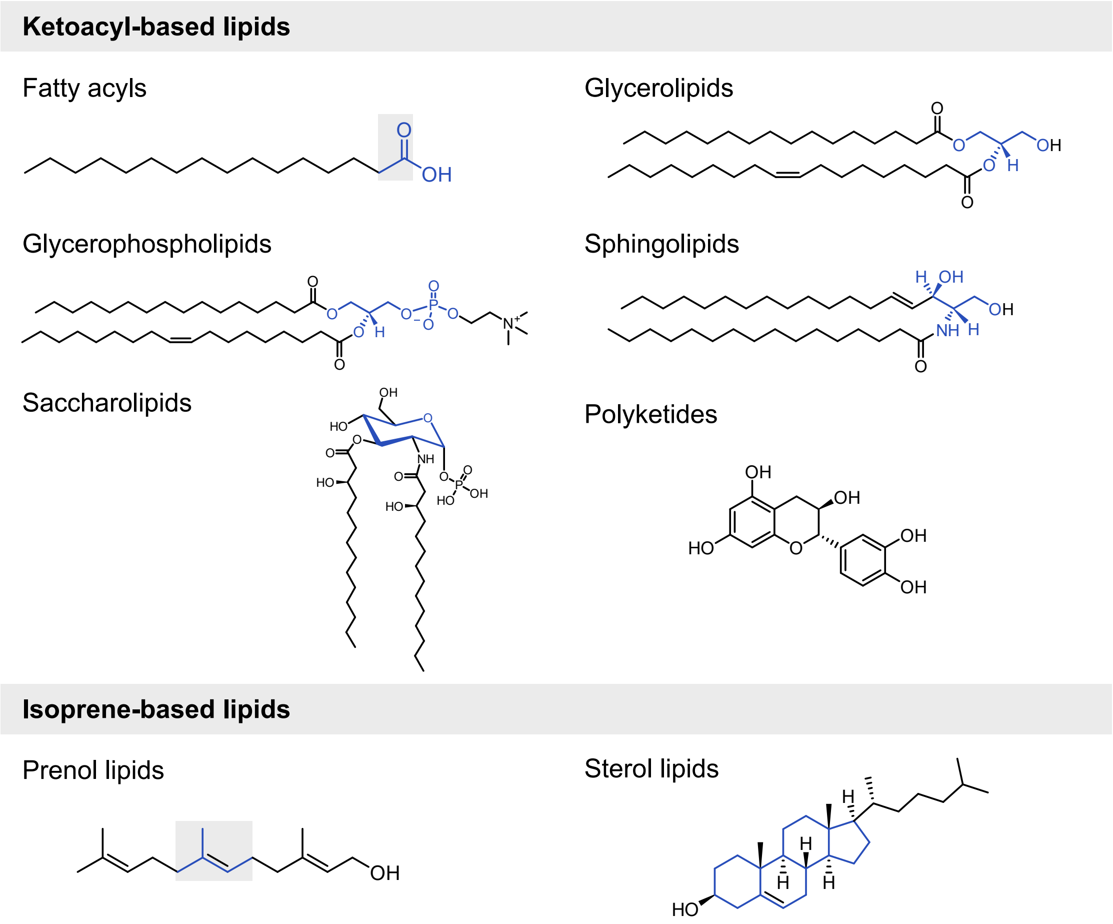

Figure 2.1: Lipid classification into eight categories according to the LIPID MAPS classification system.[30] For each category, one representative example is shown. The characteristic structural features of each category are traced in blue, except for the structurally highly diverse polyketides. The acetyl and isoprene motifs are exemplarily highlighted in the fatty acyl and prenol lipid category, respectively.

with ketoacyl motifs.[34] On the other hand, the characteristic isoprene motifs in sterol and prenol lipids derive from the carbocation-based condensation of dimethylallyl pyrophosphate and isopentenyl pyrophosphate, which are isomeric five-carbon building blocks.[30] Despite those well-defined biosynthetic pathways, variable post-synthetic modifications such as elongation, desaturation, oxidation, or cyclisation can render the basic structural motifs unrecognizable and lead to a large structural diversity.

Fatty acids are the simplest ketoacyl-based lipids and the most abundant representatives of the fatty acyl category. They are usually even-numbered aliphatic carboxylic acids, which can be saturated, mono-, or polyunsaturated. Double bonds are predominantly in the *cis* (*Z*) configuration and separated by methylene groups in polyunsaturated fatty acids. However, *trans* (*E*) double bonds can be formed during industrial processes such as fat hardening or frying, and occur naturally in increased amounts in dairy products and meat of ruminants.[35] The widely accepted shorthand nomenclature for fatty acids (FAs) is composed of two numbers: the number of carbon atoms and the number of C=C bonds, which are separated by a colon.[32,36] The position and stereochemistry (*E*, *Z*, or Δ if unknown) of the C=C bonds are indicated in brackets behind the number of unsaturations. In the recommended Δ-nomenclature, which will be used throughout this work, the double bond position is counted starting from the carboxyl group. The alternatively employed omega (ω-) or *n*-nomenclature indicates the distance of the C=C bond from the opposite methyl end. The ω- or *n*-nomenclature is useful to describe polyunsaturated fatty acids, whose physiological properties are strongly influenced by the distance of the first C=C bond from the methyl end.[37]

Fatty acids are mostly taken up with the diet, but can also be synthesized *de novo* in the cytosol.[34] The precursors for fatty acid synthesis are derived from excess carbohydrates, which are metabolized into acetyl-CoA and further transformed into malonyl-CoA. The successive elongation of an acetyl-CoA primer with malonyl-CoA units yields mainly palmitic acid (FA 16:0) and low amounts of myristic acid (FA 14:0) and stearic acid (FA 18:0).[34] In the endoplasmic reticulum, the fatty acids can subsequently be modified by elongation and desaturation.[38] Certain fatty acids cannot be produced by mammals because none of the mammalian desaturases inserts C=C bonds further than nine carbon atoms away from the carboxylic end.[38] In typical fatty acids with 16 or more carbon atoms, this corresponds to the absence of double bonds from position ω-1 to ω-6. Fatty acids with unsaturations in this region, such as linoleic acid (FA 18:2, ω-6) and α-linolenic acid (FA 18:3, ω-3), are hence essential fatty acids and must be taken up with the diet.[37] Linoleic acid is required for the biosynthesis of arachidonic acid (FA 20:4, ω-6), which is the major precursor of an entire class of oxygenated polyunsaturated fatty acyls with regulatory functions, known as eicosanoids.[39] The biosynthesis of eicosanoids requires the initial mobilization of arachidonic acid from membrane glycerophospholipids because the concentration of free fatty acids in the cytosol is very low.[34,39] Instead, fatty acids are usually incorporated in more complex lipids such as glycerophospholipids and triacylglycerols.[34]

Glycerolipids and glycerophospholipids are formed by the esterification of glycerol-3-phosphate with CoA-activated fatty acids.[40] The successive addition of two fatty acids to glycerol-3-phosphate yields phosphatidic acid (PA), the common precursor of glycerolipids and glycerophospholipids. Glycerol-based lipids can be interconverted into one another by various biochemical pathways.[41] Their structures are usually reported using the stereospecific numbering (*sn*-) nomenclature, which specifies the substituents at the three carbon atoms of the glycerol backbone (Fig. 2.2).[36] It is important to note that non-symmetrically substituted glycerolipids are chiral, and hence their *sn*-1 and -3 positions are non-identical. In triacylglycerols (TAG), all three hydroxyl groups of glycerol are esterified with fatty acids, whereas diacylglycerols (DAG) bear only two fatty acids and a free hydroxyl group. In glycerophospholipids, the *sn*-3

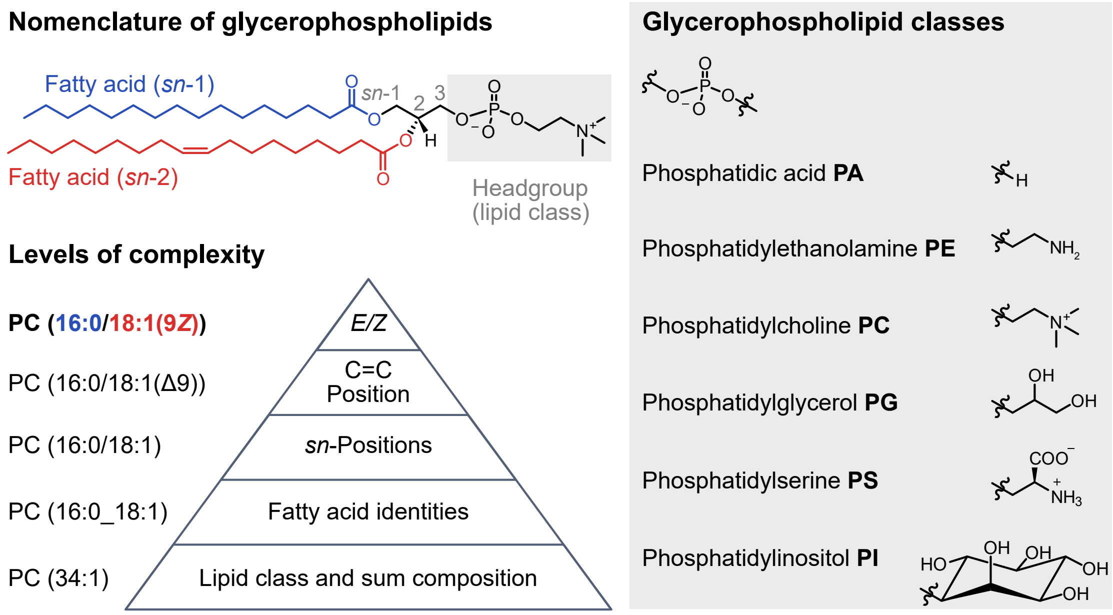

Figure 2.2: Structure and nomenclature of glycerophospholipids. Glycerophospholipids can be analyzed on different levels of complexity, as illustrated for the phosphatidylcholine PC (16:0/18:1(9*Z*)). The analytical challenge increases from the bottom to the top of the pyramid. The glycerophospholipid class is determined by the structure of the phosphate headgroup. Six prominent classes are shown.

hydroxyl group is esterified with a phosphate-containing headgroup that determines the lipid class. The most common glycerophospholipid classes besides PA are phosphatidylethanolamine (PE), phosphatidylcholine (PC), phosphatidylglycerol (PG), phosphatidylserine (PS), and phosphatidylinositol (PI). The terms *glycerophospholipid* and *phospholipid* are used interchangeably. Glycerophospholipid structures can be analyzed on different levels of complexity. Therefore, a universal nomenclature was established to unambiguously convey which structural features have been identified in the analysis.[32,36] At the lowest level, the glycerophospholipid class (headgroup) and sum composition of the fatty acids are reported. At the higher levels, the individual sum composition of the fatty acids, their connectivity on the glycerol backbone, and C=C bond position and configuration are determined. If the position of the fatty acids on the glycerol backbone is unknown, an underscore is employed in the shorthand notation. Otherwise, the fatty acid attached to the *sn*-1 position is written before the fatty acid at the *sn*-2 position, separated by a slash. The same convention is applied to report structures of DAGs, TAGs, and other glycerolipids.

Glycerolipids and glycerophospholipids are involved in a plethora of biological processes. DAGs are tightly regulated lipid second messengers,[42] whereas TAGs constitute a long-term storage for fatty acids and hence an essential source of energy.[43] Because of their hydrophobicity and limited solubility in the cytosol, TAGs are deposited into lipid droplets, which are particularly abundant in adipose tissue.[34] Fatty acids can be released from lipid droplets by lipolysis and subsequently catabolized in the mitochondria to gain energy.[34] Contrary to hydrophobic TAGs, glycerophospholipids are amphiphilic molecules, which constitute the scaffold of cell membranes and confine lipid droplets. Cell membranes are complex matrices whose macroscopic properties, such as membrane fluidity, stability, thickness, and permeability, are determined by the entirety of membrane lipids.[40] Glycerophospholipids influence membrane properties both by the nature of their hydrophilic headgroup and the structure of the hydrophobic lipid chains, including length, degree of unsaturation, and even the position of double bonds.[40,44,45] They also influence the structure and function of membrane proteins by specific and non-specific interactions.[46–48] Furthermore, proteins can be covalently linked to glycosylphosphatidylinositol, which anchors them in the outer leaflet of cell membranes.[49,50] Anchored proteins, sphingolipids, and cholesterol are enriched in microdomains termed *lipid rafts*, which are involved in signal transduction and membrane trafficking.[51,52]

Sphingolipids are fatty acid-derived lipids, which make up around 30 % of cell membrane lipids.[53] They owe their name to the mythical sphinx because their complex molecular structure appeared enigmatic to their discoverer J. Thudichum, and was not elucidated until more than half a century later.[54] The biosynthesis of sphingolipids is initiated by the condensation of palmitoyl-CoA with L-serine, yielding the C18 molecule 3-ketosphinganine.[55] Reduction of 3-ketosphinganine yields the amino alcohol sphinganine (d18:0), which is the precursor of more complex sphingolipids. In the nomenclature employed for sphinganine and other sphingoid bases, the letter indicates the number of hydroxyl groups (m = mono, d = di, t = tri).[36] The following digit specifies the length of the aliphatic chain, followed by a colon and the number of C=C bonds, consistent with the nomenclature for fatty acids. The most common sphingoid base in mammalian sphingolipids is sphingosine (d18:1), whereas phytosphingosine (t18:0) is more abundant in plants.[56] Phosphorylation of sphingosine yields sphingosine-1-phosphate, which is known as an important signaling molecule involved in cell growth and suppression of apoptosis.[53] Besides sphinganine, sphingosine, and phytosphingosine, a tremendous variety of sphingoid bases have been identified in nature.[54]

Complex sphingolipids are modularly assembled by *N*-acetylation of the sphingoid base with a fatty acid and attachment of a hydrophilic headgroup (Fig. 2.3).[55,57] The initial *N*-acetylation yields ceramides (Cer), which are subsequently often phosphorylated or glycosylated. The most abundant phosphosphingolipids in mammalian cells are sphingomyelins (SM), which bear a phosphocholine headgroup.[57] In glycosphingolipids, a glycan is glycosidically linked to the terminal hydroxyl group of the sphingoid base. Mammalian glycosphingolipids carry either β-glucose (Glc) or β-galactose (Gal) as the first monosaccharide.[20,55] β-Glucosylceramides are further elongated into lactosylceramides, followed by the stepwise attachment of further monosaccharides in a variety of diverging biosynthetic routes.[55,58] The attachment of *N*-acetylneuraminic

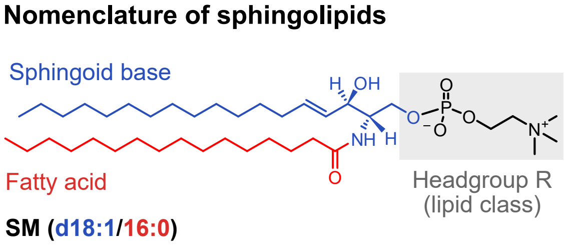

Sphingolipid classes

Ceramide **Cer**	R = OH
Phosphosphingolipid	R = PO_4-X
- Sphingomyelin **SM**	R = Phosphocholine
Glycosphingolipid	R = Glycan
- Glucosylceramide **GlcCer**	R = Glucose

Figure 2.3: Structure and nomenclature of sphingolipids. Sphingolipids are modular assemblies composed of a sphingoid base (here sphingosine; d18:1), a fatty acid, and a headgroup, based on which they are classified. The most common sphingolipid classes are ceramides, phosphosphingolipids including sphingomyelins, and glycosphingolipids.

acid yields gangliosides, which are highly abundant in the brain.[59] Importantly, glycolipids must not be confused with saccharolipids, which form an entirely separate lipid category.[30] Although saccharolipids are equally composed of a glycan and a lipid part, the lipid chains are not glycosidically linked, but attached to the hydroxyl groups of the glycan backbone. The most prominent example is lipid A, which occurs in the membranes of gram-negative bacteria as part of lipopolysaccharides.[60] The lipid chains are immersed in the outer bacterial membrane and thereby expose the hydrophilic glycan to the outside, where it can trigger severe immune reactions of infected hosts.

Sterol and prenol lipids are characterized by their carbon scaffold composed of five-membered building blocks. Contrary to ketoacyl-based lipids, the synthesis of sterol and prenol lipids is initiated by the condensation of isopentenyl pyrophosphate and dimethylallyl pyrophosphate.[61] Sterol lipids are readily recognizable by their sterane scaffold composed of four fused hydrocarbon rings. The most abundant sterol lipid in eukaryotes is cholesterol, which modulates membrane fluidity and is the precursor of bile acids, oxysterols, and steroid hormones, such as estrogen, testosterone, and cortisol.[61] The cholesterol precursor dehydrocholesterol is required for the ultraviolet (UV) light-induced formation of vitamin D in the skin.

Prenol lipids form a diverse category of natural products. They are often used as color, flavor, or fragrance agents, such as carotenoids, menthol, or limonene.[62] Furthermore, they include the fat-soluble vitamins A, E, and K, which are required for vision, oxidative protection, and blood coagulation, respectively.[30] The antioxidant effect of vitamin E protects membrane lipids and is based on its ability to stabilize free radicals *via* its aromatic chromane scaffold.

This brief walkthrough of the kingdom of lipids was focused on the lipid classes studied in this work and therefore only provides an incomplete picture of the manifold lipid structures and functions. The lipids investigated in this thesis include fatty acids, (glyco-)glycerolipids, glycerophospholipids, (glyco-)sphingolipids, and vitamin E derivatives.

2.1.2 | Isomerism in Lipids

The structural diversity of lipids in nature is reflected in an enormous number of isomers. Even simple fatty acids can form an unexpected variety of isomers by changing the location and stereochemistry of C=C bonds and other chain modifications such as hydroxylation, cyclopropanation, and methyl branching.[14] In the case of more complex lipids containing fatty acids and additional building blocks such as glycerol or a sphingoid base, the number of possible isomers greatly increases. Their structural diversity arises not only from isomeric building blocks, but also from their combinatorial assembly and the regio- and stereochemistry of the connections between them. For example, isomeric glycolipids emerge from the structural variety in the lipid chains and the glycan headgroup, the countless possibilities to combine different lipid chains and glycan headgroups, and the stereochemistry of the glycosidic bond connecting the glycan to the lipid part.[55] In the following, the individual sources of isomerism in complex lipids and their biological significance are broken down according to Figure 1.1.

Isomeric glycans are of fundamental importance in biology, and substantially complicate the structural analysis of glycolipids.[58,63] Although mammalian glycans are mainly composed of ten different monosaccharides, their structures are highly complex.[64] Each monosaccharide contains several hydroxyl groups of defined stereochemistry, which are potential connection points to attach the next monosaccharide. Isomerism in complex glycans emerges from four sources (Figure 2.4).[65] First of all, glycans consist of monosaccharides, many of which have the same atomic composition but differ in one stereocenter, such as Glc and Gal. Secondly, monosaccharides are connected *via* glycosidic bonds of defined regiochemistry between the anomeric carbon of the first monosaccharide and any free hydroxyl group of the next monosaccharide. Furthermore, the monosaccharides can be assembled in different orders, such as Glc-Gal *vs.* Gal-Glc. The third source of isomerism is the configuration of glycosidic bonds, which can be α or β. Lastly, glycans are not strictly linear like nucleic acids and proteins, but often form branched structures by the attachment of further monosaccharides to free hydroxyl groups. As the number of monosaccharides increases, the number of possible isomers rises dramatically. From just three different monosaccharides, each with four free hydroxyl groups in addition to the anomeric hydroxyl group, a total of 3! (sequence) x 4^2 (regiochemistry) x 2^2 (stereochemistry) = 384 hypothetical isomeric trisaccharides can be generated by connecting the anomeric carbons with one of the four non-anomeric hydroxyl groups of the next mononosaccharide.[66] This calculation does not even consider branched structures and different ring sizes. To depict complex glycan structures in a simplified, yet accurate way, the symbol nomenclature for glycans (SNFG) was developed.[67,68] Monosaccharides are represented by symbols that are connected at defined angles to represent the regiochemistry of the glycosidic bonds. Their stereochemistry is encoded in dashed (α) or solid (β) lines.

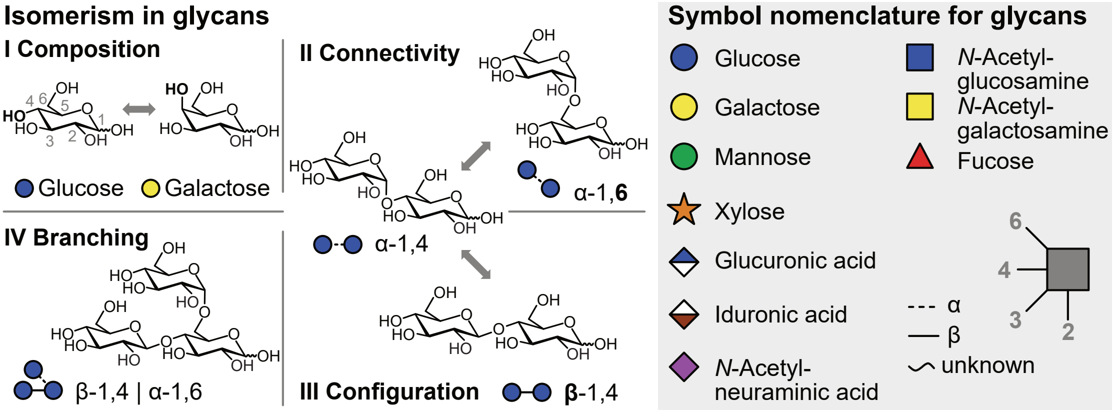

Figure 2.4: Illustration of the structural diversity in glycans. Isomeric glycans emerge from isomeric monosaccharides connected *via* glycosidic bonds of defined regio- and stereochemistry. The symbol nomenclature for glycans (SNFG) is used for simplified but unambiguous representation of glycan structures. Figure adapted from Grabarics *et al.*[69]

Glycans are involved in highly specific molecular interactions such as antigen-antibody reactions that rely on a particular regio- and stereochemistry.[70] Accordingly, any structural change in the glycan structure, however small, can completely alter the biological function of a glycolipid. For example, α-glycosylceramides, which are found in the cell walls of bacteria and are thus a signal for microbial infection, trigger a T-cell subset called natural killer T cells.[71,72] In contrast, β-glycosylceramides, which are common in mammalian cells, have no antigenic activity. Another drastic example of how small structural changes determine the biology of glycolipids are the human blood groups, which are defined by the glycan structure of glycolipids on red blood cells. The A and B antigens differ only in the presence or absence of an *N*-acetyl group at the terminal galactose, but this seemingly minor difference prohibits blood transfusion between blood groups A and B.[73]

Double bond isomers occur throughout all lipid classes. The C=C bond position(s) and geometry in aliphatic chains can have a minor or a decisive influence on the biological function of the lipid.[74] Double bonds with *cis* geometry lead to a kink in unsaturated fatty acids, which increases the membrane fluidity and disorder, especially if the C=C bond is located in the middle of the chain.[44] On the contrary, *trans* fatty acids are straight and can therefore be packed more tightly in ordered membrane domains, similar to saturated fatty acids.[45] The distribution of double bond isomers was found to vary between tissues and between healthy and cancerous cells.[3–6] Cancer cells produce fatty acids with C=C bonds at unusual positions that are not found in healthy tissue and may be used as biomarkers.[7] In extreme cases, isomeric fatty acids with different C=C bond position and configuration can have opposite biological effects.[2]

***sn*-Isomers** arise from permutation of fatty acids along the glycerol backbone in glycerolipids and glycerophospholipids. They are often found in varying relative concentrations in different tissues, suggesting cell-specific lipid metabolism.[75] Several subtypes of human breast cancer cells were discriminated only based on the distribution of *sn*-isomers, although the accuracy was significantly increased by the simultaneous identification of C=C bond isomers.[6] Individual *sn*-isomers can have specific biological activities, for example, if a specific arrangement of the fatty acids is necessary for protein binding.[76] This is often the case for signaling molecules such as DAGs. Because isomer-specific DAG-protein binding is required for protein activation, only the *sn*-1,2 DAG isomer has signaling properties.[77] DAG-metabolizing enzymes precisely distinguish between the *sn*-1,2, -2,3, and -1,3 DAG isoforms.[42]

Chain modifications including hydroxylation, methyl branching, and cyclopropanation are particularly abundant in bacterial lipids.[78] Like C=C bonds, they can be found at different positions and have a defined stereochemistry. Hydroxylation of lipids plays an important role in the formation of second messengers such as eicosanoids, which are oxidation products of arachidonic acid.[39] Hydroxy fatty acids are omnipresent in nature and differ in number, position, and stereochemistry of hydroxyl groups.[79,80] Their bioactivity strongly depends on the hydroxylation position.[81] Apart from enzymatic pathways, less selective free radical reactions of unsaturated fatty acids with oxygen produce hydroxylated lipids, which are a sign for oxidative stress.[82] Methyl-branched fatty acids are the major constituent of membrane lipids in many bacteria.[83] In general, methylation of fatty acids has a disruptive effect on lipid packing and increases the membrane fluidity.[84] The extent of this effect varies with the position and distance of methyl groups in polymethylated chains.[85] Cyclopropanation renders bacterial phospholipids more tolerant towards adverse conditions and occurs in response to stress by the addition of a methylene group to a C=C bond under retention of the original stereochemistry of the double bond.[84] Molecular dynamics simulations suggest that *cis* and *trans* cyclopropane fatty acids have markedly different effects on the fluidity and order of membranes.[86]

Other isomers result from variations in the bond types connecting lipid chains to the glycerol backbone in glycerophospholipids.[36] Apart from the classical ester linkage between glycerol and fatty acids, alkyl chains can be attached *via* ether or vinyl ether linkages to the *sn*-1 position, which are difficult to analyze and distinguish.[87,88] In phosphate-containing lipids such as phosphorylated PI and lipid A, phosphate groups can be attached at different positions, which affects the signaling activity and virulence of the resulting regioisomers.[40,89] While there are many more, less common types of isomerism, not all are discussed in this work.

2.2 | Mass Spectrometry-based Lipidomics

The entirety of lipids in a given biological system is termed the *lipidome.* Accordingly, *lipidomics* is the discipline in charge of identifying and quantifying all lipids in the lipidome and to determine their individual roles within the biological system.[19] The tasks of lipidomics were defined in an early editorial as the following: (I) development of analytical approaches to identify lipids on a molecular level, (II) investigation of lipid-protein interactions, especially in the context of biomembranes, and (III) identification of lipid networks in the metabolism.[17] The overall aim is to integrate lipidomics with genomics, proteomics, and glycomics to understand the interplay between genes, primary (proteins), and secondary (glycans and lipids) gene products. However, before the biological roles of lipids in cellular networks can be investigated, a key requirement must be fulfilled: the ability to reliably identify individual lipids on a molecular level.[9] Lipidomics is confronted with a large structural diversity and a wide range of concentrations spanning up to five orders of magnitude.[90] Since the early 2000s, the discipline has been fueled by developments in the field of mass spectrometry (MS).[10,12–15,19,91,92]

2.2.1 | General Approaches

Modern mass spectrometers enable fast, large-scale lipid profiling with a very high sensitivity and mass resolution.[93] For MS, neutral lipids must be ionized and transferred into the gas phase, which prevented mass spectrometric analysis of complex lipids until the advent of soft ionization techniques in the late 1980s.[94,95] The main ionization technique for lipid analysis today is electrospray ionization (ESI), which transfers large, non-volatile molecules into the gas phase with little or no fragmentation and has made MS universally applicable to different lipid classes.[96] In ESI, the dissolved analytes are sprayed under ambient conditions from a capillary in the presence of a high electric field, leading to the formation of protonated or metal-adducted lipids in positive ion mode and deprotonated or anion-adducted lipids in negative ion mode.[97,98] Matrix-assisted laser desorption/ionization is another common ionization technique, which is mainly used to ionize lipids directly from tissue and map their spatial distribution by MS imaging.[99]

ESI-MS-based approaches for lipidomics are divided into two strategies: direct infusion (shotgun) analysis and high-performance liquid chromatography (HPLC)-MS analysis.[100] Direct infusion of crude mixtures into the mass spectrometer enables comprehensive lipid profiling of the entire sample.[19] However, this approach suffers from spectral congestion and ion suppression of low-abundance and/or less ionizable lipids.[101] HPLC and other separation techniques can significantly reduce spectral complexity and promote the detection of minor lipid species.[19] Different lipid classes are efficiently separated by normal-phase liquid chromatography (LC), whereas reversed-phase LC separates lipids based on different chain lengths and number of

C=C bonds.[102] Another separation technique that is often used for lipid analysis is ion mobility spectrometry (IMS).[103,104] This gas-phase electrophoretic technique separates ions based on their mobility, which is related to their mass, charge, size, and shape. While the ions traverse a gas-filled cell under the influence of an electric field, they undergo collisions with the buffer gas, which separates large, extended ions from more compact ions that collide less often with the gas particles. Ion mobility-mass spectrometry (IM-MS) can differentiate lipid classes, subclasses, and isomers.[103,105,106] In particular, ultra-high resolution IMS technologies such as cyclic IMS and structures for lossless ion manipulation (SLIM) IMS enable the separation of lipid and glycolipid isomers with only minor structural differences.[107–110] Furthermore, the ion mobility can be converted into a collision cross section (CCS), which is an instrument-independent parameter that can be stored in databases and calculated by computational methods.[111] Hyphenated LC-IM-MS workflows thus provide three structural parameters, namely retention time, CCS, and mass-to-charge (*m/z*), which significantly improves the confidence in lipid identification.[112]

To obtain further structural information, collision-induced dissociation (CID) is routinely used to fragment lipids in tandem MS (MS/MS).[12] After *m/z*-selection, the precursor ion is accelerated by an electric field and collides with buffer gas atoms or molecules, which eventually leads to the formation of lipid class-specific fragments.[98,113,114] Structural analysis of lipids can be performed on different levels of complexity, of which there are at least five for glycerol-based lipids: lipid class, fatty acid identities, *sn*-positions, C=C bond location(s), and geometry (*cf.* Fig. 2.2).[6] The lipid class and fatty acid identities can be readily determined by CID, which generates headgroup-specific fragments in positive ion mode and fatty acid carboxylate anions in negative ion mode.[98] The connectivity of the fatty acids on the glycerol backbone is less straightforward to identify by CID. Depending on the instrument and ion type, fatty acid cleavage from one of the two positions is preferred over the other, which enables the distinction of *sn*-regioisomers.[113] However, the approach requires careful calibration with authentic standards to analyze isomeric mixtures because it relies on relative fragment intensities rather than exclusive fragments.[115,116] The position and stereochemistry of C=C bonds and other chain modifications cannot be determined by CID because carbon-carbon bonds within the aliphatic chains are not dissociated.[14] Similarly, the analysis of glycan headgroups in glycolipids requires alternative analytical strategies,[69] as CID leads to neutral loss of the glycan headgroup and thus to a complete loss of information about the glycan structure.[98] Overall, ESI-CID-MS/MS is a robust technique to rapidly detect and identify a range of different lipids from complex mixtures. However, the molecular identification is usually limited to the lipid class and fatty acid identities, which belies the actual number of isomers hidden underneath.

2.2.2 | Advanced Techniques for In-Depth Lipid Analysis

Over the last 15 years, an increasing variety of advanced tandem mass spectrometric techniques have been developed to investigate lipid isomers that remain unresolved by ESI-CID-MS/MS lipidomics workflows.[9–16] They can be divided into two different approaches.[11] One strategy is to employ alternative ion activation techniques based on higher-energy collisions, photons, or electrons, which generate other types of fragment ions than CID. The alternative is to use conventional CID in conjunction with chemical derivatization to promote the formation of structurally diagnostic fragments by charge and/or ion-type manipulation. In other words, advanced tandem MS approaches change either the dissociation technique or the nature of the analyte.[13] Chemical derivatization can be further divided into derivatization of the neutral analyte before or during ionization, and gas-phase derivatization of the ionized analyte inside the mass spectrometer. The advantages of gas-phase reactions include a high degree of control, fast reaction kinetics, and unique reactivity due to the absence of solvents and counterions; however, ion/ion or ion/molecule reactions require instrument modification, whereas condensed-phase derivatization is generally compatible with commercial mass spectrometers.[13] In practice, multistage tandem MS workflows combining lipid derivatization and different ion activation techniques are often used to increase the structural coverage. The most recent and promising strategies for in-depth lipid analysis are presented in the following and summarized in Table 2.1.

Alternative ion activation techniques are used to generate diagnostic lipid fragments that are not accessible by CID. In the past, higher-energy collisional dissociation (HCD) was employed to fragment lipids on sector-based mass spectrometers.[117–119] High collision energies of > 1 keV dissociate C—C bonds along the alkyl chains and reveal the position of C=C bonds by gaps in the CH_2 fragmentation series. HCD has recently experienced a renaissance when it was integrated into modern mass spectrometers.[120–122] However, the extensive fragmentation decreases the sensitivity and makes the analysis of complex lipid extracts difficult because the ion signal is diluted over many product ions. Therefore, more selective fragmentation techniques yielding fewer but more diagnostic fragments are increasingly used for lipid analysis.[123]

Ultraviolet photodissociation (UVPD) employs UV photon absorption instead of collisional activation to dissociate ions, and has shown great potential for the structural analysis of lipids.[124,125] Allylic C—C bonds are preferentially cleaved, which allows to determine the position of C=C bonds in unsaturated lipids with a much better sensitivity than HCD.[126,127] The assignment of C=C bond positions is based on pairs of fragment ions spaced by 24 Da that are observed for each C=C bond in the UVPD spectrum. Similarly, C—C bonds adjacent to hydroxyl groups, cyclopropane modifications, or chain branching sites are easily broken.[78,128,129] Furthermore, by combining HCD with UVPD, not only the C=C bond position but also the *sn*-positions of the acyl chains in glycerol-based lipids can be determined.[130] Native lipids can be modified with UV chromophores to increase the UV absorption or induce alternative fragmentation pathways. For example, radical precursors can be introduced to trigger a radical-directed dissociation (RDD) mechanism.[131] RDD requires covalent or non-covalent modification of the lipid with a bifunctional molecule containing a radical precursor and a variable group for attachment to the target lipid.[132–136] The radical is formed in the mass spectrometer by homolytic cleavage of an aryl-iodide or another suitable chemical bond by UVPD or, less commonly, by CID.[137] The resulting lipid-radical complex then undergoes radical-directed fragmentation upon CID. RDD was used to identify the location of C=C bonds, hydroxyl groups, chain branching, and cyclopropanation in lipids.[132,133,137–141]

Electron-induced dissociation (EID) triggers extensive fragmentation by bombarding the precursor ions with high-energy electrons (> 10 eV).[142] The technique was used to localize C=C bonds in fatty acids[143] and to analyze more complex phospholipids, glycerolipids, and sphingomyelins.[144–150] EID generates a series of fragment ions for each of the two fatty acids in glycerophospholipids, which allows to determine their respective position on the glycerol backbone, the C=C bond position and geometry.[144,151] Overall, EID enables near-complete structural identification of complex lipids, but suffers from low and analyte-dependent fragmentation efficiencies as well as high spectral complexity.

Online or offline lipid derivatization increases the gain in structural information from a tandem MS experiment by promoting the formation of diagnostic fragments. The simplest way to modify lipids is to form non-covalent metal adducts, which can be easily produced by ESI of lipids in metal salt solutions.[152] Several alkali, alkaline earth, and transition metal ions have been used to distinguish *sn*-isomers[116,152–159] and double bond isomers.[153–155,160,161] However, empirical studies are required to identify the best metal cation for each specific application. Furthermore, fragment ion abundances of metal-adducted lipids are often highly instrument-dependent. As a consequence, more selective covalent derivatization strategies have been developed, particularly for the selective modification of C=C bonds.[74] The most commonly used techniques at present are ozonolysis, the Paternò-Büchi reaction, and epoxidation.

Ozonolysis is a well-known reaction in organic synthesis, which leads to oxidative cleavage of C=C bonds in unsaturated compounds.[162] The first step of the reaction is a [2+3] cycloaddition between the C=C bond and ozone, which yields a primary ozonide and subsequent cleavage products. In early studies, lipids were treated with ozone vapor and then analyzed by MS.[163] However, ozonolysis can also be initiated directly during the ESI process by ozone electrospray mass spectrometry (OzESI-MS),[164,165] in a low temperature plasma,[166] in solution,[167,168] or on tissue.[169,170] All these methods have one common drawback: the intact lipids cannot be *m/z*-selected before the reaction with ozone. As a result, ozonides, fragments, and underivatized lipids overlap in the mass spectrum, and the fragments often cannot be assigned to their precursors. Therefore, the technique is not well suited for shotgun analysis.

Another popular derivatization technique for pinpointing C=C bonds is the photochemical Paternò-Büchi reaction between a C=C bond and a carbonyl compound, which can be achieved by UV irradiation of the ESI spray containing lipids and a carbonyl compound.[171] C=C Bonds are thus converted into oxetane rings, which dissociate into an alkene and a carbonyl fragment upon ion activation. A widely used Paternò-Büchi reagent is acetone,[4,172–174] which can be added to the mobile phase in LC to enable post-column Paternò-Büchi derivatization.[175–177] By combining the Paternò-Büchi reaction with other derivatization strategies, the *sn*- and C=C bond position can be identified simultaneously.[5] In recent years, various Paternò-Büchi reagents have been developed to enhance the ionization efficiency,[178,179] increase the photochemical conversion yield,[180] modify the absorption wavelength,[181–183] and change the ion mobility of derivatized lipids.[184] In particular, acetylpyridine was successfully employed to locate C=C bonds, hydroxylation sites, and *sn*-positions in complex lipids.[6,185–187] By coupling the photochemical reaction with LC or high-resolution IMS, both the C=C bond location and geometry of unsaturated lipids were determined.[188,189]

Epoxidation is another common derivatization strategy for unsaturated lipids, which transforms C=C bonds into epoxides that yield a pair of fragment ions separated by 16 Da. Epoxidation of unsaturated lipids can be performed online or offline in solution or on tissue using, for example, a low-temperature plasma[190,191] or peroxy acids.[192–194] Several experimental variants with potential for clinical applications have been developed.[195–198] Instead of using classical solution-phase organic chemistry, epoxidation can also be achieved electrochemically by using the ESI emitter as an electrochemical cell to switch the epoxidation reaction on and off on demand by regulating the applied voltage.[199–202] Epoxidation achieves much higher reaction yields than the Paternò-Büchi reaction, but is less suitable for the analysis of complex mixtures due to the small mass shift of 16 Da between epoxidized and underivatized lipids.[11]

Ion/molecule and ion/ion reactions enable lipid derivatization in the gas phase with a high degree of reaction control. Ozone-induced dissociation (OzID) is an ion/molecule reaction between a charged alkene and neutral ozone, which has a major advantage over OzESI-MS: the precursor lipid can be m/z-selected before reacting with ozone.[203,204] Activation of the resulting ozonides by CID yields a pair of diagnostic aldehyde and Criegee ions separated by 16 Da. Ion/molecule reactions like OzID are relatively slow, but can be significantly accelerated by increasing the number densities of reagents[205–209] or by increasing the effective temperature of the ions using radio frequency (RF) activation.[210] Although the ozonolysis reaction rates depend on the C=C bond geometry and the *sn*-positions, the differences are not sufficient to distinguish *sn*-isomers and C=C stereoisomers.[205] However, *sn*-isomers can be distinguished by a combination of CID and OzID.[75,211,212] The miniaturization of mass spectrometers combining OzID and CID makes clinical applications conceivable that identify lipid biomarkers directly from patient samples.[213]

Contrary to ion/molecule reactions, ion/ion reactions are highly efficient and fast.[214] Applications of ion/ion reactions for lipid analysis involve charge transfer dissociation[215] and charge inversion reactions between two oppositely charged low-energy ions.[216] Simultaneous trapping of deprotonated fatty acids and doubly charged tris-phenanthroline magnesium complexes results in a singly charged fatty acid-magnesium complex, which yields CID fragments that are diagnostic of the C=C bond position.[87,217–220] Charge inversion of positively charged phospholipids can be achieved by reaction with doubly deprotonated 1,4-phenylenedipropionic acid,[87,221,222] and is frequently used in combination with other modification strategies[223–225] or MS imaging.[226] Charge inversion is also a valuable technique to identify glycan headgroups and the glycosidic linkage (α or β) in isomeric glycosphingolipids.[227–229] The main advantage of charge switching in the gas phase over solution-phase charge inversion reactions[230–232] is that the derivatization and ionization steps are decoupled. The charge can thus be switched according to the desired ion mode for fragmentation, independent of the ionization conditions.[216]

Table 2.1: Advanced tandem mass spectrometric techniques for in-depth lipid analysis. The main application of each technique for lipid analysis is specified and schematically illustrated.

Ion activation techniques	
Higher-energy collisional dissociation (HCD) Dissociation of lipid ions by collisional activation > 1 keV	C=C bond position [117–122]
Ultraviolet photodissociation (UVPD) Dissociation of lipid ions by UV photon absorption 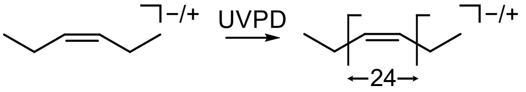	chain modifications [78, 124–130]
Radical-directed dissociation (RDD) Dissociation of a lipid-radical complex 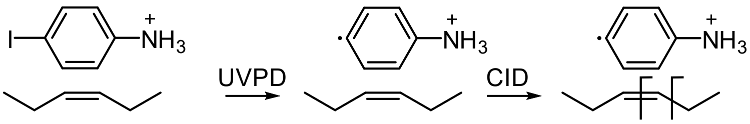	chain modifications [132–141]
Electron-induced dissociation (EID) Bombardment of lipid ions with high-energy electrons > 10 eV 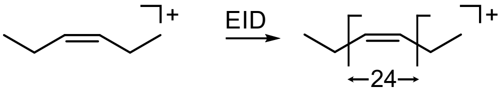	C=C bond position, geometry, *sn*-position [143–151]

Lipid derivatization

Metal cation adduction
sn-position

Cationization of lipids using metal salt solutions
[116, 152–161]

Ozonization before or during ionization (OzESI)*
C=C bond position

[2+3] cycloaddition of ozone to C=C bonds
[164–170]

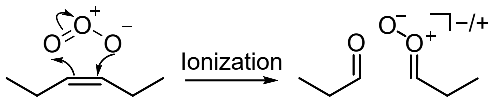

Paternò-Büchi reaction
C=C bond position

Photochemical [2+2] cycloaddition using a ketone or aldehyde
[3–6, 172–189]

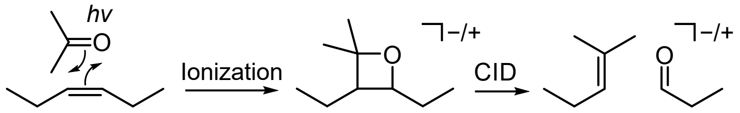

Epoxidation
C=C bond position

Epoxidation of C=C bonds, *e.g.*, using peroxy acids
[190–202]

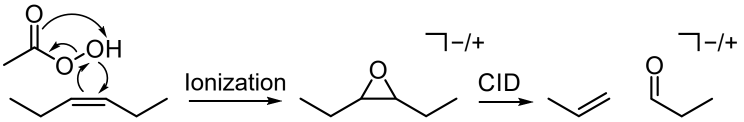

Ion/molecule and ion/ion reactions

Ozone-induced dissociation (OzID)
C=C bond position

Gas-phase [2+3] cycloaddition of ozone to C=C bonds
[75, 203–209, 211–213]

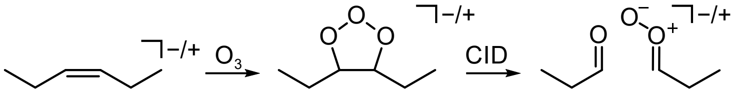

Charge inversion
chain modifications

Ion/ion reaction of charged lipids with oppositely charged ions
[87, 217–229]

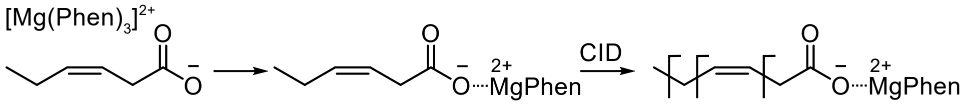

* The ozonide can be cleaved before the ionization, during ionization, or in the mass spectrometer.

Mass spectrometry-based spectroscopic approaches (action spectroscopy) have gained increasing importance for the structural analysis of biomolecules.[22–25] The first gas-phase UV action spectra of lipids were recently recorded using UVPD spectroscopy in a cryogenic ion trap.[233] Aromatic amino acids or dipeptides were non-covalently attached to the lipids as UV chromophores to induce spectral differences between isomeric lipids. Action spectroscopy in the infrared (IR) range, on the other hand, does not require lipid modification and has already yielded promising results for metabolite analysis.[234–236] Many of the previously discussed advanced tandem MS-based strategies have been designed for a specific application, such as C=C bond localization, and do not yet provide the ease of use and automated data analysis of established LC-MS/MS methods. IR action spectroscopy is a universal technique with a high potential to solve some of the remaining challenges in lipidomics.

2.3 | Gas-Phase Infrared Spectroscopy

Spectroscopic methods investigate the interaction of matter with electromagnetic radiation, which excites different transitions depending on the radiation frequency. The energy of electromagnetic radiation in the mid-IR range (400–4000 cm^{-1}) corresponds to the energy difference between vibrational levels in molecules, and the absorption of resonant IR photons thus excites molecular vibrations. IR spectroscopy is a very powerful technique to analyze chemical structures, as the vibrations of specific functional groups are located in well-defined frequency regions. The IR spectrum not only confirms the presence or absence of certain functional groups, but also contains information about intramolecular interactions such as hydrogen bonds. To avoid interactions with surrounding molecules that interfere with its intrinsic vibrations, the analyte can be transferred into the gas phase to be probed in the clean room environment of a mass spectrometer.

2.3.1 | Theory of Molecular Vibrations

The stretching and compression of a spring connecting point masses is classically described by Hooke's law, which states that the restoring force acting on the spring is proportional to its displacement and stiffness.[237] The concept can be transferred to atoms connected by a chemical bond of a certain stiffness or bond strength that oscillate around the equilibrium bond length. The quantum theoretical treatment of Hooke's law yields the quantum harmonic oscillator, which is the simplest model to describe molecular vibrations in diatomic molecules.[237] The vibrational energy levels E_υ are quantized according to

$$E_\upsilon = (\upsilon + \frac{1}{2})h\nu, \tag{2.1}$$

where υ is the vibrational quantum number that can be zero or a positive integer, h is Planck's constant, and ν the frequency of the harmonic oscillator. The specific selection rule for the harmonic oscillator is $\Delta \upsilon = \pm 1$; however, overtone transitions with $\Delta \upsilon = \pm 2$ or ± 3 are observed in vibrational spectra because molecular vibrations are anharmonic.[237] It is important to note that the zero-point energy in the ground vibrational state (*i.e.*, υ = 0) of the harmonic oscillator is not zero but $\frac{1}{2}h\nu$ as a consequence of the uncertainty principle. All energy levels E_υ and $E_{\upsilon+1}$ are equally spaced by the value of $h\nu$. Because h is a constant, the energy difference between two vibrational levels is solely determined by the frequency ν, which depends on the reduced mass μ of the vibrating atoms and the force constant k of the chemical bond. The frequency increases with increasing bond strength and decreasing reduced mass:

$$\nu = \frac{1}{2\pi}\sqrt{\frac{k}{\mu}}. \tag{2.2}$$

The harmonic oscillator has a parabolic potential that is proportional to the square of the atomic displacement. The parabolic shape is a reasonable theoretical approximation of the potential energy close to the potential minimum; however, the model fails to describe the system as the vibrational quantum number and the oscillation amplitude increase because it allows infinite atomic displacement without bond dissociation. A more accurate description of vibrations in diatomic molecules is given by the Morse potential, which takes anharmonicities into account.[238] In the Morse potential, the spacing between vibrational energy levels decreases with increasing υ until the molecule dissociates.

Non-linear molecules consisting of N atoms have three translational and three rotational modes, resulting in $3N - 6$ normal modes of vibration, whereas linear molecules have $3N - 5$ vibrational modes. However, not all vibrational modes can be excited by IR light. For a vibrational mode to be IR active, the electric dipole moment of the molecule must change during the course of the vibration. Because most biomolecules have a low symmetry and permanent dipole moment, most normal modes are IR active.[239] In general, there are two different types of vibrations that can be stimulated by IR light: stretching (ν) and bending (δ) vibrations. Stretching vibrations are excited at higher frequencies than the bending modes, and thus the two types are usually well-separated in the vibrational spectrum. If more than two atoms are involved, the vibrations can be further specified, for example, as symmetric or antisymmetric stretching vibrations.

Because vibrational frequencies reflect the energy of transitions between quantum states, they can be computed using quantum chemical methods.[240] IR spectra of isolated analytes in the gas phase can be directly compared with computed IR spectra of candidate structures to determine the chemical structure and obtain detailed information about the gas-phase conformation, charged sites, and intramolecular interactions.[234] This is a major advantage over MS/MS, which requires reference spectra for structural assignment, because computational methods used to predict fragment spectra still lack reliability.[241] Vibrational frequencies can be computed by various quantum chemistry methods including density functional theory (DFT), which is used in this work (*cf.* Section 3.4).[242] To compute IR spectra, the candidate structure must first undergo a geometry optimization to determine the equilibrium interatomic distances and potential energy minimum of the system. Subsequently, the second derivatives of the energy with respect to the atomic displacement from the equilibrium geometry are computed to determine the vibrational eigenfrequencies. Because they are systematically overestimated in the harmonic approximation, computed harmonic frequencies must be corrected by appropriate scaling factors depending on the computational level to improve the agreement between experiment and theory.[242] In some systems, however, anharmonic effects cannot be neglected in the quantum chemical treatment, which is computationally demanding and thus restricted to relatively small molecules.[240]

2.3.2 | Action Spectroscopy

Vibrational spectroscopy holds great potential for lipid analysis. In the condensed phase, Fourier-transform IR spectroscopy allows to distinguish and quantify *cis* and *trans* C=C bonds,[92] and surface-enhanced Raman spectroscopy provides deep structural insight into fatty acids and triacylglycerols.[243] While vibrational spectroscopy yields direct structural information, it requires very pure samples or measures averaged spectra of a molecular ensemble. In contrast, MS is blind to the molecular structure, but enables the separation of analytes according to their *m/z*. Consequently, MS and IR spectroscopy are perfectly complementary techniques that in combination provide structural information about *m/z*-selected, isolated ions in the gas phase, free from interactions with surrounding molecules, solvents, or counterions.

Despite these obvious advantages, coupling MS and IR spectroscopy is not straightforward due to the space-charge limit: Coulombic repulsion between ions of the same polarity in the vacuum restricts their maximum number density to 10^6–10^7 ions per cm^3.[239,244] However, classical absorption spectroscopy requires a minimum number density of 10^{10} molecules per cm^3.[245] That is because absorption spectroscopy is based on measuring the attenuation of incident light by the sample. The photon absorption is governed by the Lambert-Beer law, which describes the transmitted intensity $I(\nu)$ of light with the frequency ν as

$$I(\nu) = I_0 \cdot e^{-\sigma(\nu) \cdot l \cdot n}, \tag{2.3}$$

where I_0 is the intensity of the incident light, $\sigma(\nu)$ the absorption cross section, l the pathlength of the light traversing the sample, and n the particle density.[244] Because the number density of ions in the vacuum of a mass spectrometer is several orders of magnitude lower than the density required to induce a measurable difference between I_0 and $I(\nu)$, one must turn to more sensitive spectroscopic methods united under the term *action spectroscopy* (Figure 2.5).[239] Action spectroscopy measures the impact of the light absorption on the analyte by monitoring

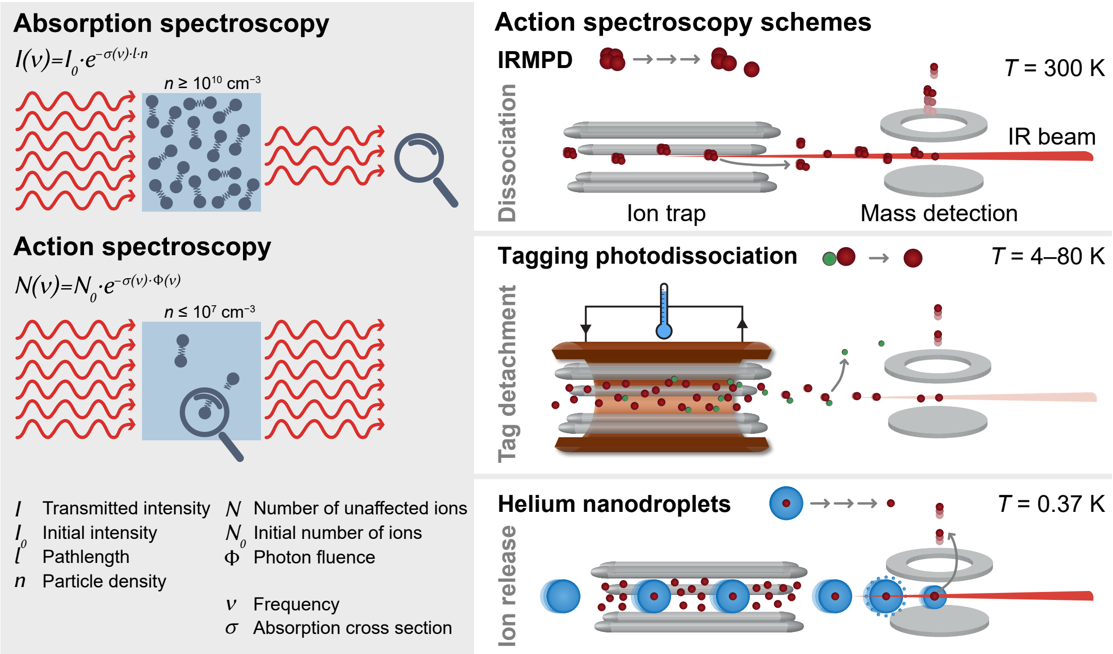

Figure 2.5: Absorption spectroscopy and action spectroscopy. The effect of photon absorption on the probed ions in action spectroscopy can be quantified by a similar equation as the Lambert-Beer law used in absorption spectroscopy. Common implementations of action spectroscopy include infrared multiple photon dissociation (IRMPD) spectroscopy, tagging photodissociation spectroscopy, and infrared action spectroscopy in helium nanodroplets. Figure adapted from Grabarics *et al.*[69]

an *action* as a function of the light frequency. This approach can be described by a very similar equation as absorption spectroscopy if one assumes a linear dependence between the photon fluence and the number of affected ions.[244] Instead of the transmitted light intensity, the equation describes the number of ions $N(\nu)$ that remain unaffected by the light absorption as a function of the initial number of ions N_0, their absorption cross section $\sigma(\nu)$, and the photon fluence $\Phi(\nu)$:

$$N(\nu) = N_0 \cdot e^{-\sigma(\nu)\cdot\Phi(\nu)}. \tag{2.4}$$

There are different ways to implement action spectroscopy, depending on the type of action that is monitored. The most common IR action spectroscopy techniques used for biomolecular analysis are infrared multiple photon dissociation (IRMPD) spectroscopy, tagging photodissociation spectroscopy, and IR action spectroscopy in helium nanodroplets.[22,23,244] IRMPD spectroscopy is the most straightforward method to implement in commercial mass spectrometers, as it simply requires an ion trap with optical access for a tunable IR laser.[246] Trapped ions are irradiated with IR light and fragment after the sequential absorption of multiple photons. The wavelength-dependent photofragmentation yield is monitored by MS as an indirect measure for IR absorption. Because IRMPD is based on a multiple photon absorption process, powerful lasers with a wide spectral tunability and high photon flux are required. IR free-electron lasers (FEL) are most widely used, although commercial tabletop optical parametric oscillator/amplifier systems (OPO/OPA) can be employed in the 3 µm (2500–4000 cm^{-1}) range.[247,248] Another drawback of IRMPD spectroscopy is that the ions heat up during photon absorption. After each photon absorption event, the vibrational energy is randomized over the entire molecule *via* intramolecular vibrational redistribution,[249] which results in broadening and red-shifting of the absorption bands.[245] Higher spectral resolution can be achieved by cryogenic methods, which require additional instrumentation.[24,250] In tagging photodissociation spectroscopy, the ions are trapped in a cryogenic ion trap, where a weakly interacting tag (H_2, D_2, N_2, or a noble gas) is condensed onto them.[251] Because a single photon is usually sufficient to dissociate the weakly bound ion-messenger tag complex, tabletop lasers can be used in the whole mid-IR range.[239] The third approach, IR action spectroscopy in helium nanodroplets, is similar to tagging photodissociation spectroscopy. Instead of tagging the ion with a single or few tags, the ions are embedded in superfluid helium droplets.[252] The sequential absorption of multiple photons by the ion inside the droplet leads to stepwise evaporation of the helium shell until the bare ion is released in a non-thermal process.[253] Like IRMPD spectroscopy, the technique requires powerful IR lasers. However, ion heating is prevented by the evaporation of helium atoms after each photon absorption event, which dissipates the vibrational energy and maintains the equilibrium droplet temperature of 0.37 K.

In summary, IRMPD spectroscopy measures photodissociation of chemical bonds, tagging photodissociation spectroscopy measures the detachment of a weakly bound tag from the analyte ion, and IR action spectroscopy in helium nanodroplets measures the release of analyte ions from superfluid helium droplets. All these actions involve a change in *m/z* and can therefore be monitored by MS. In the following, the use of helium for spectroscopy and the experimental details for IR action spectroscopy in helium nanodroplets are explained in greater detail.

2.3.3 | Superfluid Helium

Helium is the second most abundant element in the universe and occurs in the Earth's atmosphere in the form of two stable isotopes, bosonic ^{4}He and fermionic ^{3}He, at a ratio of 1:10^{-6}.[254] The low atomic mass of helium induces a high zero-point energy and low density, which, in combination with very weak interatomic van der Waals forces, prevent condensation of helium at low temperatures.[255] As a consequence, helium has the lowest boiling point of all elements (4.2 K for ^{4}He at ambient pressure) and is the only element that remains fluid at 0 K below pressures of 25 bar (Figure 2.6a). Instead of solidifying at cryogenic temperatures, ^{4}He undergoes a unique phase transition from normal fluid He I to superfluid He II at the transition temperature T_λ, which is 2.18 K at ambient pressure.[256] This so-called λ-transition owes its name to the concomitant discontinuity of the specific heat capacity curve, the shape of which resembles the Greek letter λ (Figure 2.6b). The transition from He I to He II is believed to be

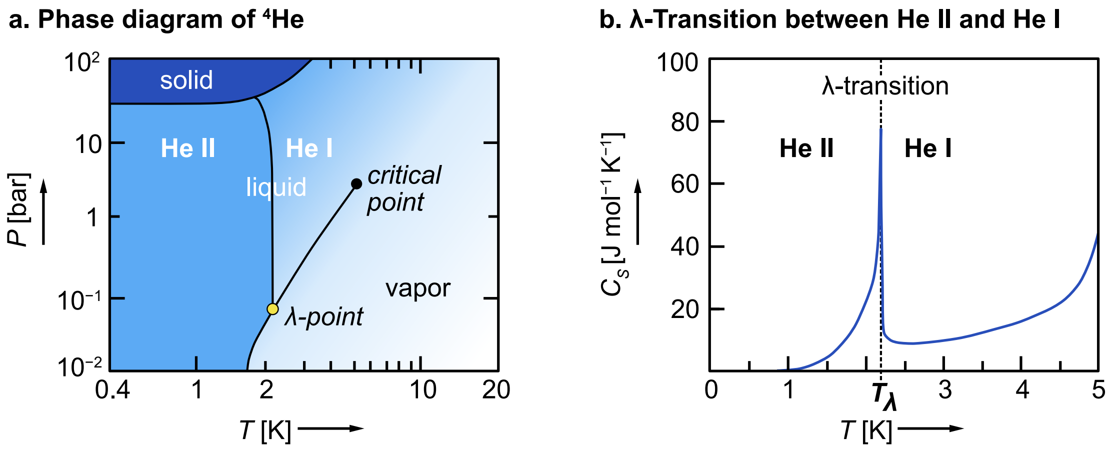

Figure 2.6: Phase transitions of helium. **a.** The temperature-pressure phase diagram of ^{4}He illustrates the phase transition from fluid He I to superfluid He II below 2.2 K. Figure adapted from Toennies *et al.*[258] **b.** The λ-transition is characterized by a steep increase of the specific heat capacity C_S at the transition temperature T_λ. Figure adapted from Donnelly *et al.*[259]

related to Bose-Einstein condensation, *i.e.*, a macroscopic number of atoms crowd into the same quantum state.[255,257] A remarkable consequence of the unusual phase behavior of ^{4}He is the absence of a triple point in its phase diagram. ^{3}He becomes superfluid below 3 mK[256] and will not be further discussed, because it has no relevant application for spectroscopy.

Superfluid helium is characterized by a high heat conductivity and a vanishingly small viscosity, which manifests itself by frictionless flow of He II through narrow channels or tubes. Superfluidity exhibits striking parallels to superconductivity, the frictionless flow of electrical charges through solid materials.[255,260] Both phenomena are manifestations of macroscopic quantization, and the discovery of both was preceded by the first liquefaction of helium in 1908.[261] The peculiar properties of superfluid helium have been extensively investigated, and researchers soon came across unexpected effects such as the thermomechanical helium fountain,[262] helium crawling up the walls of containers,[263] or forming quantized vortices in rotating bulk helium[264] and in helium droplets.[265] The initially contradictory observation that He II provides no viscous resistance to flow, but does exert a viscous drag on objects moving through the liquid was resolved by the today well-accepted two-fluid model.[266,267] The model describes He II as a mixture of a superfluid component carrying neither viscosity nor entropy, and a normal fluid component. At 0 K, the normal fluid component is absent and its ratio increases with increasing temperature until the superfluid component vanishes at T_λ.[268] The first evidence for superfluidity on a microscopic scale was obtained in 1996 from the electronic excitation spectrum of glyoxal embedded in finite-sized helium droplets,[269] and was shortly afterwards confirmed by the observation that OCS molecules rotate freely in ^{4}He droplets but not in normal fluid-like ^{3}He droplets.[270]

2.3.4 | Action Spectroscopy of Biomolecules in Helium

Helium is *"the gentlest and coldest of all matrices used for molecular spectroscopy"*,[271] which has been employed to study atoms and molecules since the early 1990s.[272] The spectroscopic investigation of a chemical species embedded in superfluid helium is similar to classical matrix isolation spectroscopy, which enables trapping of otherwise inaccessible species such as radicals in a solid arrangement of a condensed noble gas.[273] However, the rigid lattice of a solid matrix exhibits different sites, leading to inhomogeneous spectral line broadening. Helium atoms, on the other hand, form perfectly tailored voids to host analytes of any shape. The analytes are highly mobile inside the weakly interacting helium matrix, which allows for molecular vibrations, rotations, and even chemical reactions.[258,274] Furthermore, the helium matrix is transparent from the far IR to deep UV range. Matrix effects are thus significantly reduced compared with solid matrices, and the spectra of isolated analytes in superfluid helium are comparable to gas-phase spectra of the free atoms, molecules, or ions.[258] An initial problem preventing the isolation of analytes in helium was caused by the much stronger interactions of the analytes with each other or with the container walls than with the helium matrix. Instead of becoming solvated in bulk helium, the analytes thus agglomerate and precipitate on the walls.[275] This obstacle was overcome by the advent of droplet sources producing helium clusters of 10^3–10^{10} helium atoms by a free jet expansion.[256] Gaseous analytes are readily picked up by collisions with the helium droplets with a pick-up cross section close to the geometrical droplet cross section.[258,272] Upon immersion in the helium droplet, the analyte is cooled down to the intrinsic droplet temperature, which is 0.37 K for ^{4}He droplets in vacuum (0.15 K for mixed ^{3}He/^{4}He droplets).[276,277] Cooling occurs *via* evaporation of helium atoms with a very high cooling rate (10^{10}–10^{11} K s^{-1}) owing to the large effective heat capacity of He II.[278] Any excess energy is rapidly dissipated by evaporative cooling, and the isothermal helium droplets can therefore be regarded as almost perfect cryostats for the embedded analytes. Overall, helium droplets combine the advantages of classical cryogenic matrix isolation spectroscopy and gas-phase spectroscopy.

The first IR spectrum of a molecule in superfluid helium droplets was reported for SF_6 in 1992.[279] Molecular ions, however, were not investigated in helium droplets until almost two decades later.[253] The discovery that ions are released by a non-thermal ejection mechanism from helium nanodroplets upon vibrational or electronic excitation led to the development of experiments for ion spectroscopy in superfluid helium.[253,280] In particular, the coupling of IR spectroscopy with ESI allowed for the first time to incorporate non-volatile biomolecules into helium droplets.[281] In the first setup used for IR spectroscopy of biomolecular ions, the molecules are ionized by ESI and trapped in a linear ion trap.[282] Superfluid helium droplets traverse the trap coaxially, pick up ions, and transport them to the interaction region, where the doped droplet beam overlaps with an IR beam generated by a FEL. After each photon absorption event, evaporative cooling dissipates any excess energy, and the ions relax back into their vibrational ground state. After the absorption of multiple resonant photons, they are released from the droplets and detected by MS. The technique is universally applicable to investigate biomolecules such as peptides,[282] proteins,[283] carbohydrates,[284,285] and nucleic acids.[286] An extended version of this first experimental setup was used in the present work to study *m/z*-selected lipids. The instrument is described in detail in Section 3.1.

3 | Experimental

This chapter presents the experimental methods and instruments used in this work for the structural analysis of lipids and glycolipids. First, the custom-built instrument for infrared action spectroscopy in helium nanodroplets is described, followed by an overview of the components and operating principle of the Fritz Haber Institute free-electron laser. In addition, the setups of two drift tube ion mobility-mass spectrometers and the procedure for deriving collision cross sections from the experimental data are outlined. The chapter concludes with an overview of computational methods used to identify the gas-phase structures of lipids and to predict their vibrational frequencies and collision cross sections. Further experimental details can be found in Chapters 4–6.

3.1 | Infrared Action Spectroscopy in Helium Nanodroplets

The custom-built instrument for IR action spectroscopy in helium nanodroplets (Figure 3.1) is at the core of this thesis and will be described in the following.[282–284,286–288] The front end of the instrument is a Waters Ultima quadrupole time-of-flight mass spectrometer (Waters Corporation, Manchester, UK) equipped with a Z-spray nano-ESI source. The needles required for nano-ESI are prepared in-house from borosilicate capillaries pulled by a P-1000 micropipette puller (Sutter Instrument, Novato, USA), and coated with Pd/Pt (80:20, w:w) by a sputter coater 108auto (Cressington Scientific Instruments, Watford, UK). Lipid samples were dissolved in organic solvents and diluted to final concentrations of 100–500 µM, according to the experimental details given in Chapters 4–6. The lipids were ionized by applying a positive or negative voltage between 0.6–1.1 kV to the electrically conducting needle containing the sample solution. The generated ions are guided from ambient conditions in the ion source into the high-vacuum region *via* two ring-electrode ion guides. At the next stage, a quadrupole enables *m/z*-selection of the ions of interest. These are then transferred through a hexapole (not shown in Figure 3.1) to a quadrupole bender, which can be switched between two states: the electrodes are either electrically grounded to let the ions pass straight into the time-of-flight mass analyzer, or opposing direct current (DC) voltages of ±33 V are applied to neighboring quadrupole rods to deflect the ions by 90° into a hexapole ion trap. The time-of-flight mass analyzer is used to monitor and optimize the ion signal coming from the nano-ESI source. In this work, it was operated in W-mode, *i.e.*, the ions follow a W-shaped path before they hit the detector. Because the flight time of the ions is proportional to the square root of their *m/z*, the measured time of flight can be converted into *m/z* after calibration.

In operating mode, the voltage applied to the quadrupole bender is periodically switched between 0 V and ±33 V to alternately monitor the quality of the electrospray or deflect the ions into the hexapole ion trap. The ion trap is enclosed in a copper housing, which enables filling of the trap with helium to thermalize incoming ions by buffer gas cooling. The thermalized ions are radially confined by a RF potential on the rods of the hexapole operating at 1.1 MHz. Axial trapping is achieved by applying a DC potential to the two endcap electrodes that is 3–5 V above the offset voltage of the hexapole. The temperature in the trap can be varied by pre-cooling or pre-heating of nitrogen gas flowing through channels in the copper housing.[288] The spectra shown in this thesis were recorded at a trap temperature around 90 K, which is achieved by cooling of the nitrogen gas with liquid nitrogen. The heat transfer between the ions at room temperature and the cold copper housing is mediated by the helium buffer gas, which collides with the walls and with the trapped ions. Cooling of the ions eliminates higher-energy conformers that would otherwise be kinetically trapped upon shock freezing in the helium droplets.[286] The trap is filled with ions for 2.5 seconds, after which the space-charge limit is reached and the buffer gas is pumped out of the trap.

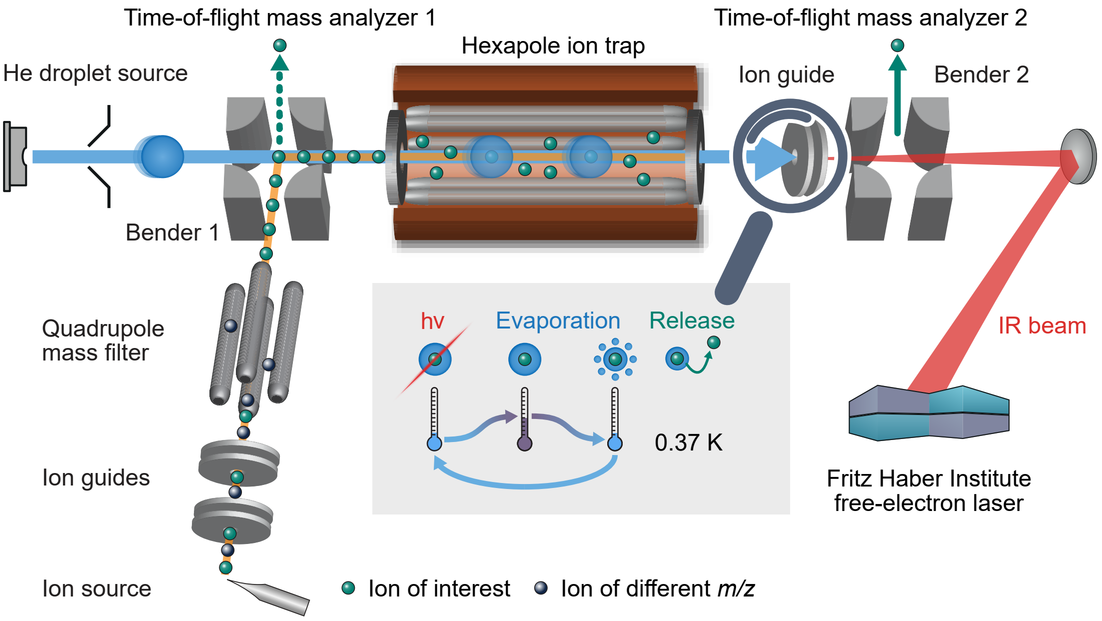

Figure 3.1: Setup for infrared action spectroscopy in helium nanodroplets. Ions are generated by nano-electrospray ionization, *m/z*-selected in a quadrupole, and deflected into a hexapole ion trap. Superfluid helium droplets pick up ions from the trap and transport them to the interaction region, where the absorption of multiple resonant IR photons provided by the Fritz Haber Institute free-electron laser leads to release of the ions. The ion signal is monitored on a time-of-flight mass analyzer.

Superfluid helium droplets are generated by the expansion of pressurized helium (60–80 bar) into the vacuum through the cryogenic nozzle of a pulsed Even–Lavie valve[289] at a repetition rate of 10 Hz. The valve body is cooled by a closed-cycle helium cryocooler, and the temperature of the nozzle is precisely adjusted by a resistive heating element. In this work, the nozzle temperature was kept between 19–21 K, resulting in an average droplet size of 10^5 helium atoms and a mean droplet velocity of approximately 450 $\mathrm{m\,s^{-1}}$.[287] The helium droplet beam passes through a beam skimmer into the ion trap, where each droplet usually picks up a maximum of one ion.[287] The ion-doped droplets coaxially traverse the trap and overcome the longitudinal trapping potential due to their high kinetic energy. They travel further downstream towards the interaction region, which is on the level of a third ring-electrode ion guide. Here, the pulsed beam of doped droplets overlaps with the pulsed beam of IR photons generated by the Fritz Haber Institute free-electron laser (FHI FEL).[290] The exact position of the focal point of the IR beam can be adjusted by a pneumatically controlled adaptive mirror. A wire-grid polarizer between the ion trap and the interaction region prevents the IR beam from entering the ion trap where it could induce ion fragmentation by IRMPD processes. In this work, the FHI FEL was operated at a macro-pulse repetition rate of 10 Hz with typical macro-pulse energies between 60–120 mJ. Each macro-pulse contains 10^4 micro-pulses at a frequency of 1 GHz, which enables rapid sequential absorption of IR photons by the ions inside the helium droplets. The multiple photon absorption process results in multiple cycles of vibrational excitation, evaporative cooling, and relaxation back into the vibrational ground state until the ions are released from the droplets.

The cloud of released ions is compressed along the flight axis by increasing the DC offset on the endcap electrode of the ion guide by about 5 V, which pushes the ions towards a second quadrupole bender. The bender deflects the ions by 90° into the second time-of-flight mass analyzer, which is technically identical to the first mass analyzer, but is operated in V-mode to increase the sensitivity. The ion signal is averaged over 25 FEL macro-pulses per datapoint before the wavenumber is shifted 2 cm^{-1} forward. The IR spectrum is generated by plotting the ion signal at the *m/z* of interest as a function of the wavenumber. Each spectrum shown in this work is averaged from at least two full scans over the entire spectral range, which is typically between 900 and 1800 cm^{-1}. The spectra were averaged and plotted using the OriginPro software package (OriginLab Corporation, Northampton, USA).

3.2 | Fritz Haber Institute Free-Electron Laser

IR action spectroscopy in helium droplets requires intense, monochromatic mid-IR radiation, which must be tunable over a wide spectral range. In the molecular fingerprint region that contains most stretching and bending vibrations (approx. 600–2000 cm^{-1}), a sufficient photon flux for the multiple photon absorption process is provided only by free-electron lasers.[291] As the name suggests, the lasing medium of FELs is formed by relativistic free electrons, which emit radiation as they move through a periodic magnetic field in a vacuum.[292] Because FELs do not rely on discrete energy transitions in atomic or molecular gain media like conventional lasers, they are continuously tunable by varying either the kinetic energy of the relativistic electrons or the strength of the magnetic field.

The FHI FEL is a mid-IR FEL that provides pulsed IR radiation from 200 to 3400 cm^{-1}.[290] A second, recently installed beamline will extend into the far-IR range (60–2000 cm^{-1}), and will be usable simultaneously with the current mid-IR beamline owing to a kicker cavity that splits the electron beam between the two beamlines (Figure 3.2). In this work, only the original mid-IR branch was used. In the accelerator system, electron bunches are generated by a gridded thermionic gun operating at a bunch repetition rate of 1 GHz. These micro-bunches are compressed by a 1 GHz subharmonic buncher cavity before entering the first linear accelerator (LINAC), which accelerates the electrons to a constant energy of 20 MeV. Subsequently, the second LINAC further accelerates or decelerates the electrons to reach final kinetic energies between 15–50 MeV (36–37 MeV in this work). In this way, 10 μs long macro-bunches consisting of 10^4 micro-bunches are produced at a macro-pulse repetition rate of 10 Hz. The pulsed infrared radiation generated by the FHI FEL inherits this characteristic time structure from the electrons, as illustrated in the inset of Figure 3.2. Downstream of the second LINAC, the relativistic

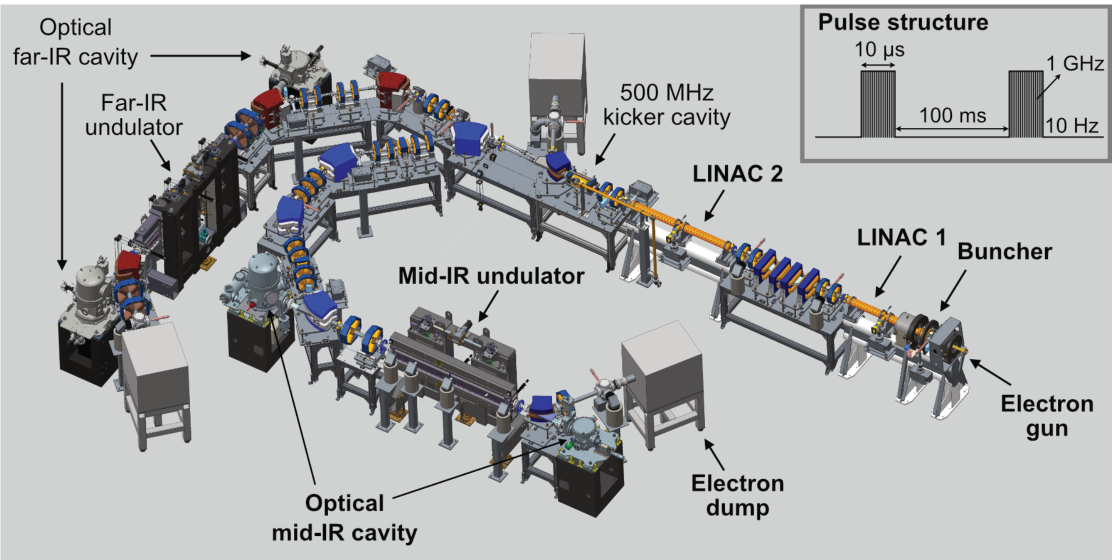

Figure 3.2: Overview of the Fritz Haber Institute free-electron laser. Electron bunches are generated by a thermionic electron gun, compressed by a buncher, and accelerated by two consecutive linear accelerators (LINACs), before they enter the mid-IR cavity. The electrons emit radiation in the magnetic field of the undulator and are dumped, whereas the light remains captured in the optical cavity. The characteristic time structure of the light pulses is shown in the inset. The far-IR cavity was not used in this work. Image provided by Dr. Wieland Schöllkopf.

electrons are transferred into the optical mid-IR cavity by two 90°-isochronous achromatic bends. The cavity is formed by two concave gold-plated copper mirrors: an end-mirror and an out-coupling mirror, which are mounted 5.4 m apart from each other. The centerpiece of the cavity is an undulator, which consists of two periodic arrays of permanent magnets above and below the beamline. The magnets are arranged such that on-axis a strong vertical magnetic field of periodically alternating polarity is formed. Once the relativistic electrons enter the magnetic field of the undulator, they are forced into a sinusoidal motion during which they emit incoherent radiation in the forward direction. Downstream of the undulator, the electrons are steered sideways into an electron-beam dump, while the radiation is captured between the two cavity mirrors. The electromagnetic field interacts with the next electron bunch entering the cavity, which leads to micro-bunching of the electrons and stimulated emission of coherent radiation. It is thus the interaction between the electromagnetic wave, the electron beam, and the magnetic field that makes the light coherent and monochromatic—two key properties of laser radiation.[292] A fraction of the beam is transmitted through a hole in the out-coupling mirror and guided to the experiment *via* an evacuated beamline.

At a given kinetic energy of the free electrons, the photon energy is determined by the magnetic field strength that is changed by adjusting the undulator gap: the smaller the distance between the upper and lower magnet arrays, the stronger the magnetic field, and the longer the wavelength of the emitted radiation. The full width at half maximum (FWHM) of the spectrum of the IR beam is influenced by several factors, and can be controlled in particular by the *detuning* factor. Detuning reduces the length of the cavity by a constant factor multiplied with the current wavelength λ. In this work, the detuning was usually set to 5–6 λ to decrease the FWHM to as low as 0.3–0.5 % of the central wavelength.

3.3 | Drift Tube Ion Mobility-Mass Spectrometry

Collision cross sections help to gain a deeper understanding of the three-dimensional gas-phase structures of lipids and glycolipids. In this work, they provide substantial support for the assignment of fragment structures reported in Chapter 6. The CCSs were determined by drift tube ion mobility-mass spectrometry (DT-IM-MS). DT-IMS separates ions according to their mass, charge, size, and shape in a gas-filled drift tube under the influence of a constant electric field. In this work, two different instruments were used to measure CCSs: a modified Synapt G2-S HDMS instrument (Waters Corporation, Manchester, UK) and a custom-built ion mobility-mass spectrometer described previously.[293,294] The latter was used to study non-covalent complexes of fatty acids described in Chapter 5, which require particularly gentle source conditions to remain intact. The instrument will be presented briefly at the end of this section.

The majority of CCS values in this work were determined using a modified Synapt G2-S HDMS ion mobility-mass spectrometer, which contains a drift tube instead of the commercial traveling wave ion mobility cell (Figure 3.3).[295] The instrument is equipped with a Z-spray nano-ESI source, which is operated similarly to the instrument described in Section 3.1, with typical sample concentrations in the range of 10 µM. The ions are guided into the high-vacuum region *via* a stepwave ion guide, which rejects neutral molecules and transfers the ions to a quadrupole used for *m/z*-selection. Before the ions enter the drift tube, they can optionally be fragmented by CID in the argon-filled trap cell to measure the mobility of fragments. In contrast to the original traveling wave ion mobility setup,[296] the helium cell in front of the drift tube is not in operation and only used for ion transfer. The 25.05 cm long drift tube has the same dimensions and electrical inputs as the traveling wave cell. It consists of stacked ring-electrodes that generate a constant axial electric field and radially confine the ion cloud by RF potentials. In this work, the drift tube was filled with helium at a pressure of 2.2 Torr (2.9 mbar). The temperature was measured by a Pt100 resistance thermometer attached to the housing. After traversing the drift tube, the ions pass through the transfer cell, which, like the trap cell, consists of an argon-filled ring-electrode ion guide and can be employed as a second collision cell. The ions are then guided to the time-of-flight mass analyzer that was operated in *Sensitivity mode* (V-mode). Because the mass analysis occurs on the timescale of microseconds, whereas the mobility separation requires several milliseconds, a number of mass spectra are recorded for each section of the arrival time distribution (ATD). The ATD of every *m/z* can thus be extracted from the averaged mass spectrum and *vice versa*.

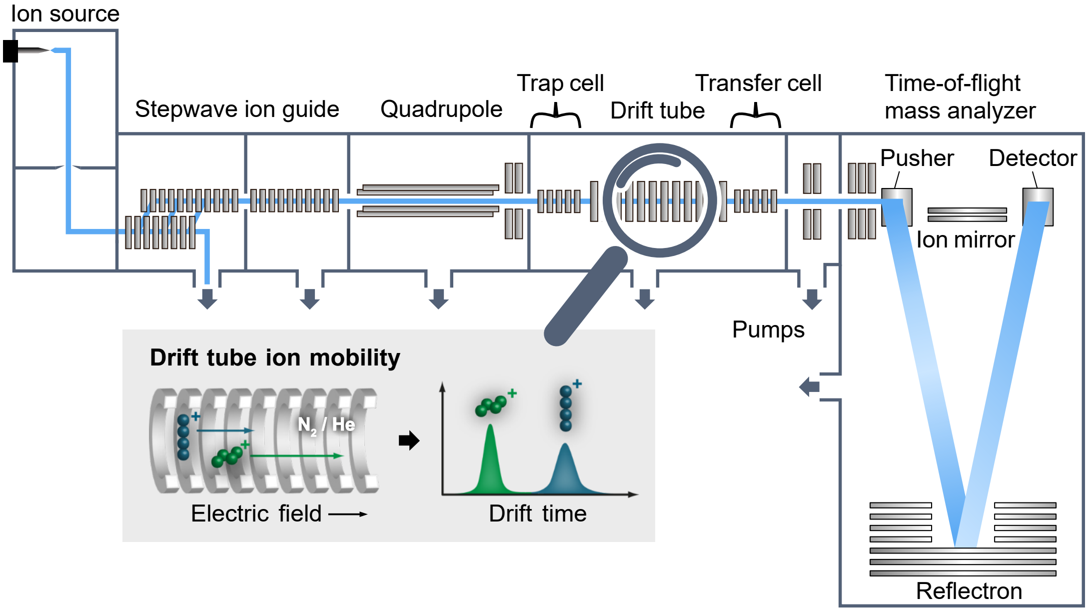

Figure 3.3: Schematic setup of the modified Synapt G2-S HDMS ion mobility-mass spectrometer. Ions are generated by nano-electrospray ionization and can be *m/z*-selected in a quadrupole and fragmented in the trap cell before entering the drift tube. Here, the ions traverse a buffer gas-filled cell under the influence of a constant electric field, which separates ions based on their mass, charge, size, and shape. The ions are then transferred into a time-of-flight mass analyzer.

DT-IMS employs a constant electric field, which allows the straightforward determination of ion mobilities and their conversion into CCSs using the Mason-Schamp equation:[297]

$$\mathrm{CCS} = \frac{3ze}{16n}\sqrt{\frac{2\pi}{\mu k_B T}} \cdot \frac{1}{K}, \tag{3.1}$$

where z and e are the charge state of the ion and the elementary charge, respectively, n is the number density of the buffer gas, μ is the reduced mass of the analyte ion and the buffer gas, k_B is the Boltzmann constant, T is the temperature, and K is the ion mobility. All values in the Mason-Schamp equation except for K are either constants or parameters that are fixed by the experimental conditions and can be measured or calculated. To determine the ion mobility K, the arrival times of the ion of interest were measured at 10 different drift voltages. The drift voltage V_D in the modified Synapt G2-S HDMS instrument depends on four individual voltages that are multiplied by a factor to correct for two resistors:[295]

$$V_D = (He\,Cell\,DC + He\,Exit + IMS\,Bias - Transfer\,DC\,Entrance) \cdot (1 - \frac{2}{170}) \tag{3.2}$$

(Figure 3.4a). The drift voltage was varied by changing the *IMS Bias* while keeping the other voltages constant. The ATD of the ion of interest was extracted at each drift voltage and fitted

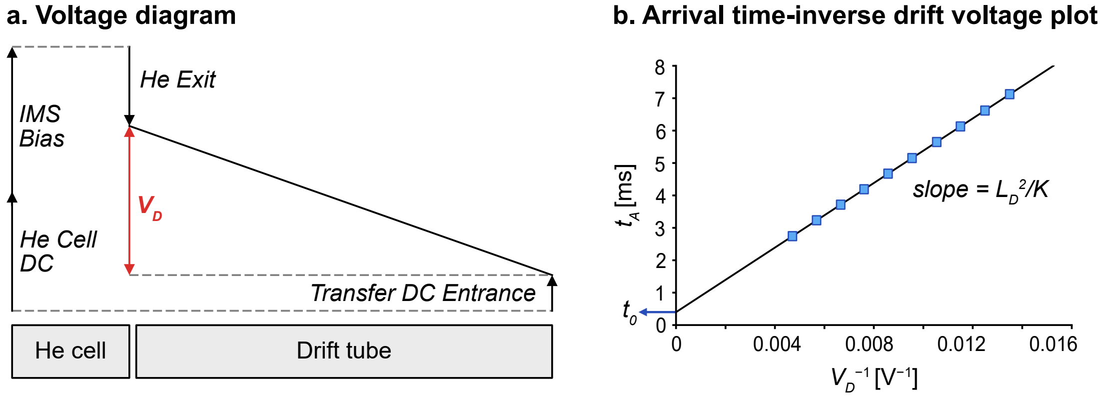

Figure 3.4: Determination of collision cross sections from arrival times measured on the modified Synapt G2-S HDMS instrument. **a.** The drift voltage V_D is determined by four individual voltages. **b.** The arrival times are recorded at 10 different drift voltages and plotted against the inverse drift voltage. The ion mobility K is derived from the slope of the linear fit function.

with a Gaussian in OriginPro to obtain the centroid arrival times. The drift velocity v_D of the ions is proportional to the ion mobility K and the electric field E_D:

$$v_D = \frac{L_D}{t_D} = K \cdot E_D, \tag{3.3}$$

where L_D is the length of the drift tube and t_D is the drift time that the ions need to traverse the drift tube. Because the electric field is constant in DT-IMS, it corresponds to the quotient of the drift voltage and the length of the drift tube, so that the drift time can be expressed as:

$$t_D = \frac{L_D}{K \cdot E_D} = \frac{L_D^2}{K} \cdot \frac{1}{V_D}. \tag{3.4}$$

According to Equation 3.4, the drift time t_D is inversely proportional to the ion mobility K and the drift voltage V_D. Hence, by plotting the 10 arrival times as a function of $1/V_D$, the ion mobility K can be determined from the slope of the linear fit function, which is L_D^2/K (Figure 3.4b). The curve is shifted on the y-axis by t_0, which corresponds to the time that the ions need to reach the detector after exiting the drift tube. The drift time t_D thus corresponds to the measured arrival time t_A minus t_0. For the obtained CCS to be reliable, the R^2 value of the linear fit must be ≥ 0.9999. The temperature in the drift tube, which is required to convert the ion mobility into the CCS using Equation 3.1, was determined as the average temperature of the 10 individual measurements. To ensure reproducibility, the measurement was repeated on at least two different days, and the CCS values shown in this work correspond to the averaged values. The uncertainty of the measured CCS values is in the range of 1–2 % of the absolute CCS. The recommended nomenclature for reporting CCS values, which includes the method (DT) as superscript and the drift gas (He or N_2) as subscript, is used throughout this work.[298]

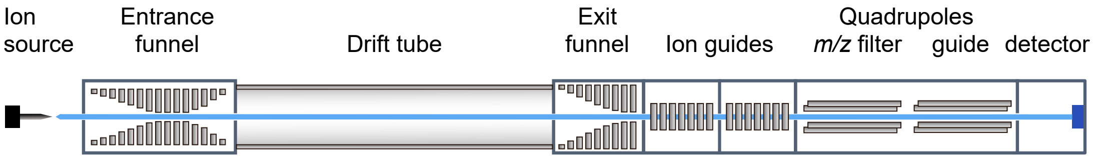

Figure 3.5: Simplified representation of the custom-built ion mobility-mass spectrometer used to determine collision cross sections of non-covalent complexes. After nano-electrospray ionization, the ions are transferred into a 161.2 cm long drift tube filled with helium. The mobility-separated ions are transferred to an electron multiplier detector *via* two ring-electrode ion guides and two quadrupoles.

For the analysis of non-covalent lipid adducts, a custom-built DT ion mobility-mass spectrometer was employed (Figure 3.5).[293,294] The instrument is equipped with a slightly off-axis linear nano-ESI source that is compatible with the needles prepared in-house as described in Section 3.1. In comparison to the Synapt G2-S HDMS instrument, fewer in-source fragmentation of the analyte ions is observed in this instrument because the ions are not directly transferred from ambient conditions into the high vacuum. Instead, the gas-filled mobility region is placed before the high-vacuum part, which enables a more gentle transfer of non-covalent lipid adducts into the gas phase. The ions are accumulated in an electrodynamic entrance funnel before they are injected in packages into the 161.2 cm long drift region at a rate of 10 Hz. The drift tube consists of conductive lead glass tubes and is filled with helium at a pressure of 4.1–4.2 mbar. After traversing the drift tube, the ions are transferred into the high vacuum *via* a second ion funnel and two consecutive ring-electrode ion guides. They are *m/z*-selected in a quadrupole and detected using an electron multiplier detector (ETP Ion Detect, Sydney, Australia) to record the ATD. CCSs were determined by measuring the arrival times of *m/z*-selected ions at 11 different drift voltages from 2110–1110 V in steps of 100 V while monitoring the temperature and pressure in the drift tube. The resulting mobilities were converted into CCSs according to the Mason-Schamp equation using a software developed in our group (https://github.com/jeriedel/CCS).

3.4 | Computational Methods

The computation of lipid structures and comparison of predicted vibrational frequencies with experimental IR spectra constitutes an essential part of this work. Some structural information, such as the presence or absence of certain functional groups, can be read directly from the IR spectrum; however, computational methods are needed to extract in-depth structural information including the position and orientation of functional groups and their interactions. These structural details and intramolecular interactions influence the global appearance of the IR spectrum in a way that is challenging to predict rationally. With computational methods, gas-phase IR spectra can be assigned to specific isomers or conformers from a range of structural candidates. DFT is the method of choice for electronic structure calculations of medium-sized biomolecules because it describes the electronic ground state energy by the total electron density, which is a function of three coordinates regardless of the size of the molecule.[240]

The general workflow for generating a pool of candidate structures and predicting their vibrational spectra *in silico* consists of a conformational search at a comparably inexpensive level of theory, followed by geometry optimization and harmonic frequency analysis of several low-energy conformers using DFT. Because lipids are mostly flexible molecules that can adopt a large number of conformations in the gas phase, their potential energy hyper-surface needs to be sampled in the first step to generate a set of low-energy structures for the subsequent geometry optimization.[299] In this work, the conformational space of lipids and glycolipids was sampled using CREST, which is an acronym for *Conformer-Rotamer Ensemble Sampling Tool.*[300] CREST was employed with the semiempirical tight-binding method GFN2-xTB[301] to generate a conformational ensemble of relevant minimum energy structures and an initial energetic ranking. Furthermore, the sampling tool was used to determine the most favorable sites for protonation, deprotonation, or attachment of a metal cation prior to the main conformational search. Before CREST was released, other sampling tools were employed: the glycosylceramide structures shown in Chapter 4 were sampled in Maestro (Schrödinger Release 2019), which relies on classical molecular dynamics simulations. Sphingolipid structures reported in Chapter 5 were sampled using the genetic algorithm-based search tool Fafoom.[302] Both Maestro and Fafoom were interfaced with FHI-aims[303] to optimize the generated structures at the PBE+vdW$^{\mathrm{TS}}$/light[304,305] level of theory. The calculations for sphingolipids and glycolipids were performed by Kim Greis (Freie Universität Berlin, Berlin, Germany) and Prof. Mateusz Marianski (Hunter College, New York, USA).

Following the conformational search, the most stable conformers were subjected to geometry optimization. To obtain a maximum variety of structures, a certain number of conformers below a defined energy threshold were selected using principal component analysis of the distances between all atoms except hydrogen, and clustering by k-means clustering in Python.[306] The selected conformers were then optimized in Gaussian 16[307] using DFT. The DFT calculations in this work were performed using the hybrid functionals PBE0[308,309] and B3LYP[310,311] with D3 dispersion correction.[312] B3LYP was only employed for the non-covalent fatty acid adducts investigated in Chapter 5 due to a better overall spectral match. The 6-311+G(d,p) basis set was used throughout and was extended with an SDD effective core potential for silver to investigate silver-adducted lipids (*cf.* Chapter 6). The harmonic frequency analysis of the optimized structures was performed at the same level of theory as the optimization, and the vibrational frequencies were scaled by an empirical factor of 0.965 to match the experimental spectra.[285,286,313] To establish energy rankings of the optimized structures, their relative free energies ΔF were calculated at 90 K, according to the temperature in the ion trap. ΔF was used rather than the Gibbs energy ΔG because the volume of the ion trap is constant.

Once an energetically reasonable structure with a well-matching IR spectrum has been found, the calculation of its CCS and comparison with the experimental value provides an additional parameter to support the structural identification. CCSs were computed using HPCCS,[314] which is based on the trajectory method (TM).[315] The computation was based on Merz-Singh-Kollman charges[316] that were determined at the same level of theory as the previous structure optimization. The temperature and drift gas were selected according to the respective experimental conditions.

In addition to harmonic IR spectra and CCSs, reaction profiles for lipid fragmentation mechanisms were computed by DFT. The computation of bond-cleaving or bond-forming events allows to verify whether an experimentally observed fragmentation reaction can proceed *via* a proposed mechanism and whether it is energetically reasonable. Before computing the fragmentation mechanism, the structure of the resulting fragment was confirmed by comparison of its IR spectrum and CCS with computed data, as described in the previous paragraphs. In the case of entirely unknown fragmentation pathways, reasonable candidate fragment structures were generated with the aid of the QCxMS program, which simulates fragmentation in Born-Oppenheimer molecular dynamics employing the semiempirical method GFN2-xTB.[317–321] After confirming the structure of the fragment ion, a transition state connecting the precursor and fragment ion was searched by scanning the potential energy surface (PES) of the bond to be broken or formed in Gaussian 16. The structure at the saddle point of the PES was then optimized as a transition state at the PBE0+D3/6-311+G(d,p) level of theory. To verify that the obtained structure is indeed a transition state, a harmonic frequency analysis was performed at the same level of theory to prove the existence of one imaginary frequency along the reaction coordinate. The transition state was then linked to a precursor and product by an intrinsic reaction coordinate calculation. Because the fragmentation reaction occurs in the source region of the mass spectrometer, ΔG was calculated at 298 K (25 °C) to indicate activation energies and the energy differences between precursors and product ions.

4 | Unravelling the Structural Complexity of Glycolipids

Glycolipids are complex glycoconjugates composed of a glycan headgroup and a lipid moiety. Their modular biosynthesis creates a vast amount of diverse and often isomeric structures which fulfill highly specific biological functions. To date, there is no gold-standard analytical technique that can provide a comprehensive structural elucidation of complex glycolipids, and insufficient tools for isomer distinction can lead to wrong assignments. In this chapter, infrared action spectroscopy is used to systematically investigate different kinds of isomerism in immunologically relevant glycolipids. All structural features, including isomeric glycan headgroups, different lipid moieties, and the configuration of the glycosidic bond connecting the glycan and lipid moieties were unambiguously resolved by diagnostic spectroscopic fingerprints in a narrow spectral range. Their unique fingerprints enabled the identification and quantification of individual glycolipids in isomeric mixtures by spectral deconvolution, making the technique highly valuable for biological applications.

This chapter is based on the following reference:

[322] C. Kirschbaum *et al.*, Unravelling the Structural Complexity of Glycolipids with Cryogenic Infrared Spectroscopy, *Nat. Commun.* **2021**, *12*, 1201.

4.1 | Introduction

Glycolipids are glycoconjugates composed of a hydrophilic glycan headgroup and a hydrophobic lipid moiety. They are ubiquitous in the cell membranes of all kinds of organisms ranging from bacteria to humans.[20] The opposite nature of the two components enables glycolipids to fulfill essential biological functions at cellular interfaces. The hydrophobic lipid tail anchors the glycolipid in the cell membrane, while the glycan headgroup protrudes into the extracellular medium for cellular communication and signaling. Playing key roles in cellular interactions and signal transduction, glycolipids are essential for the development and function of multicellular organisms.[55,323,324] Furthermore, immune responses can be modulated by α-linked glycolipid antigens such as α-GalCer. In case of microbial infections, they trigger the activation of natural killer T (NKT) cells, a T cell subset sitting at the interface between innate and adaptive immunities.[72,325–327] α-GalCer was first isolated as an antitumor agent from marine sponge[328] and was thought to be produced exclusively by bacteria and porifera.[329] In mammalian cells, however, only β-isomers were detected, which raised the question how NKT cells are triggered in mammals.[325,330] At the end of more than a decade of controversial debates, the presence of low-abundant, endogenous α-GalCer in mammalian cells was finally revealed using a combination of biological, enzymatic, and immunological assays,[325,331] and was later confirmed by direct biochemical evidence.[332] On the other hand, established analytical techniques failed to detect α-GalCer in the presence of highly abundant, non-antigenic β-GalCer, which caused severe confusion.[333]

The cumbersome search for endogenous antigens of NKT cells in mammals illustrates a general issue in glycolipid research: the lack of techniques for accurate analysis of glycolipids and limited availability of isomerically pure standards.[63,329] Classical (tandem-) MS workflows are highly sensitive but unable to distinguish the anomeric configuration of GalCer. Nuclear magnetic resonance (NMR) spectroscopy is considered the gold standard for molecular identification and yields comprehensive stereochemical information;[334] however, it requires comparably large sample amounts and cannot ensure the detection of low-abundant isomers in mixtures.[235] Hundreds of different glycosphingolipids were identified in nature based upon sugar heterogeneity, without taking into account the structural diversity of lipid moieties.[55] However, as illustrated by the example of GalCer, minute alterations of the glycolipid structure can completely eradicate its function. Isomer distinction is thus a highly relevant issue in glycolipidomics that requires novel analytical approaches. Here, we investigate consistent sets of synthetic glycolipid isomers using cryogenic IR action spectroscopy in helium nanodroplets. The technique allows to distinguish not only between α-GalCer and β-GalCer, but also between regio- and stereoisomeric glycan headgroups and different lipid moieties. The identification and relative quantification of glycolipid isomers in mixtures is demonstrated using synthetic two-, three-, and four-component mixtures and two biological lipid extracts from mice.

4.2 | Experimental Details

Sample preparation. An overview of the glycolipid samples included in this work is provided in Figure 4.1. The investigated glycan headgroups are Glc, Gal, globotriose (Gb3; α-Gal-(1→4)-β-Gal-(1→4)-Glc), and iso-Gb3 (iGb3; α-Gal-(1→3)-β-Gal-(1→4)-Glc) attached to sphingosine, phytosphingosine, ceramides (d18:1/24:1(15*Z*)) and (d18:1/26:0), and diacylglycerol (14:0/14:0). β-GlcCer, β-Gb3 sphingosine, and β-iGb3 sphingosine were purchased from Avanti Polar Lipids (Alabaster, USA). The other samples were synthesized in the laboratories of Prof. Paul B. Savage (Brigham Young University, Utah, USA) and Prof. Luc Teyton (Scripps Research, California, USA). Synthesis routes for the investigated glycosyl (phyto-)sphingosines[325] and α-Gb3Cer[335] were described previously. α-GalCer and β-GalCer,[336] α-GlcCer,[336] α-GalDAG,[337] and β-GalDAG[338] were synthesized by following published procedures and adapting the lipid residues. Solutions containing 100 µM and 10 µM of each glycolipid were prepared for IR spectroscopy and DT-IM-MS, respectively. β-Gb3 sphingosine and β-iGb3 sphingosine were dissolved in methanol. α-Gb3Cer was dissolved in dimethyl sulfoxide and diluted with methanol. The other glycolipids were dissolved in dimethyl sulfoxide (1–15 mM) and diluted in a 1:1 (v:v) mixture of acetonitrile and chloroform to obtain 1 mM stock solutions. Prior to measurements, the stock

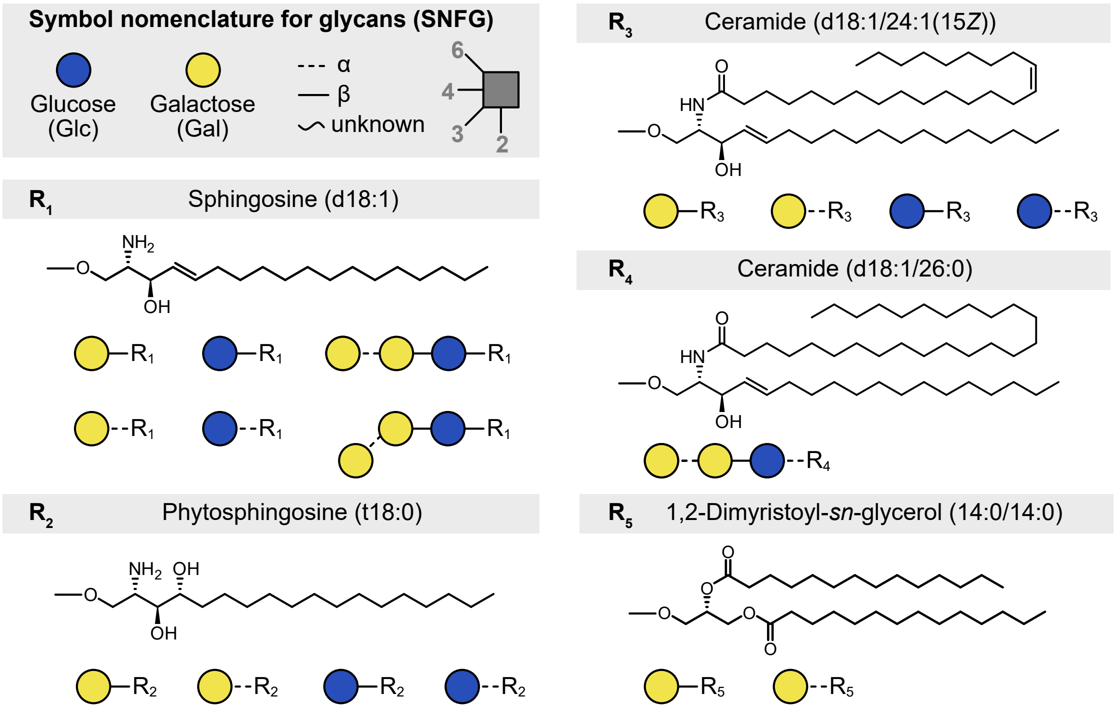

Figure 4.1: Overview of the investigated synthetic glycolipids. The symbol nomenclature for glycans (SNFG)[67,68] is used to represent the glycan structures. The investigated lipid moieties include sphingosine, phytosphingosine, ceramide (d18:1/24:1(15*Z*)) and (d18:1/26:0), and diacylglycerol (14:0/14:0).

solutions were diluted in a 2:2:1 (v:v:v) acetonitrile/methanol/water mixture. Silver adducts were prepared by mixing a 17 mᴍ solution of $Ag[PF_6]$ in acetonitrile with 100 µᴍ glycolipid solutions in a 1:10 (v:v) ratio. All chemicals were purchased from Sigma-Aldrich (Taufkirchen, Germany). The solutions were stored at −32 °C until use.

Synthetic isomeric mixtures of GalCer were prepared by mixing 100 µᴍ solutions of α-GalCer and β-GalCer with different mixing ratios: 50:50, 75:25, 90:10, 95:5, and 99:1 (β:α). Mixtures of Glc/Gal phytosphingosines were obtained by mixing 100 µᴍ solutions of the respective isomers to obtain any possible combination of two-component mixtures (1:1), three-component mixtures (1:1:1), and a four-component mixture (1:1:1:1).

Folch's extraction, liquid chromatography, and hydrolysis. Biological lipid extracts were prepared in the laboratory of Prof. Luc Teyton by standard extraction procedures:[339,340] Thymi and spleen from α-galactosidase (GLA) and α-glucosidase (GAA) knockout mice (Jackson Laboratory, California, USA) were harvested from 8- to 12-week-old mice in compliance with ethical regulations and with the approval of the Institutional Animal Care and Use Committee (protocol # 09-0057-4). The samples were frozen at −80 °C until use. Eight samples were pooled for a Folch's extraction that proceeded in four successive steps after homogenization of the tissue using a Polytron: 2:1, 1:1, 1:2 (v:v) chloroform/methanol, and finally a 1:1:1 (v:v:v) chloroform/methanol/water mixture. The four 20 mL fractions were pooled and lyophilized. The extraction was repeated on the dry pellet before a final lyophilization.

After inter-laboratory shipment, the crude lipid extract was purified by reversed-phase HPLC using a Dionex Ultimate 3000 LC system. A Supelco C18 column (2.1 mm x 250 mm, 5 µm) at a constant temperature of 60 °C was used for lipid separation. The mobile phase consisted of 70 % isopropanol/22 % water/8 % methanol, and the system was operated at a flow rate of 0.4 mL min^{-1}. The detection was carried out with a UV detector at 205 nm. A total of four measurements with an injection volume of 4 µL were carried out for each sample. Several fractions were collected and examined for the presence of glycolipids by MS and MS/MS. The chromatograms and mass spectra can be found in the supporting material of the original publication.[322] Prior to IR spectroscopy, the dried fractions were redissolved in 100 µL acetonitrile/methanol/water (2:2:1; v:v:v), and phosphatidylcholines were removed by adding 1.5 µL of a 1 ᴍ aqueous NaOH solution per 50 µL glycolipid solution. Gas-phase IR spectra were recorded when the hydrolysis was completed after 1–2 h (monitored by the disappearance of carbonyl stretching vibrations).

IR action spectroscopy. IR spectra of protonated and sodiated glycolipids were measured from 100 µᴍ solutions using the instrument described in Section 3.1. IR spectra of synthetic glycolipid mixtures (GalCer $[M+H]^+$ *m/z* 810.7; Glc/Gal phytosphingosines $[M+H]^+$ *m/z* 480.4) and natural glycosylceramides extracted from mice ($[M+Na]^+$ *m/z* 832.7) were recorded in the diagnostic fingerprint region (1000–1150 cm^{-1}). The individual measurements were performed during one day, and a constant laser focus was applied to reduce variations of the laser fluence. The experimental spectra of synthetic α- and β-GalCer with different mixing ratios were compared to simulated spectra, which were generated by averaging the spectra of the pure isomers with the expected ratios (1:1, 1:3, 1:9, 1:19, and 1:99) using OriginPro. The simulated and experimental spectra were normalized to the same surface area.

MS and DT-IM-MS. MS and DT-IM-MS measurements were performed on the modified Synapt G2-S HDMS instrument described in Section 3.3. In addition to protonated and sodiated glycolipids, silver adducts were also investigated by DT-IM-MS because silver adduction was shown to enable isomer distinction in several lipids based on their ion mobilities,[159] and silver ion chromatography is commonly employed to separate lipids due to the preference of Ag^+ ions to coordinate C=C bonds in hydrocarbon chains.[341,342] The CCSs were determined in helium at a pressure of 2.2 Torr. The ion mobility measurements were repeated on three different days, and the double standard deviation of the individual measurements is in all cases $\leq 1\,\%$ of the absolute CCS.

Non-negative matrix factorization (NMF). NMF factorizes an input matrix into two matrices containing the basis vectors and weighting factors, respectively. In contrast to other factorization methods, such as principal component analysis, NMF forces all matrix elements to be non-negative—which is an inherent property of IR spectra—and therefore only allows for additive combinations of single components.[286,343] In the present work, the input matrix contains experimental IR spectra of glycolipid mixtures, which are deconvolved into the component spectra and their relative abundance. Before applying NMF, the x-axis of the experimental spectra obtained from synthetic glycolipid mixtures was binned into 76 data points from 1000 to 1150 $\mathrm{cm^{-1}}$ (2 $\mathrm{cm^{-1}}$ steps) in OriginPro using the 1D binning application. The input matrices were normalized before applying NMF. The spectra of the biological glycolipids were binned into 100 datapoints from 952 to 1150 $\mathrm{cm^{-1}}$ (2 $\mathrm{cm^{-1}}$ steps) and normalized. The factorization was carried out using the NMF python module sklearn.decomposition.NMF[306] with the following arguments: *init = "random"*, *random_state=0*, *max_iter=2000*, *alpha=1*, and *n_components=2* or *4* (number of isomers contained in the input matrix). The output weighting factors were subsequently converted into percentages. All input and output matrices can be found in the supporting material of the original publication.[322]

Computational methods. The conformational space of sodiated glycolipids was sampled using Maestro (Schrödinger Release 2019) and CREST.[300] To save computational time and render the conformational search tractable, the lipid chains were truncated to feature the glycan moiety and relevant functional groups of the lipid. The sampling of sodiated α-GalCer and β-GalCer was performed using low-mode molecular dynamics sampling in Maestro with the Amber* force field, and the resulting structures were reoptimized in FHI-aims[303] using PBE+vdW^{TS} dispersion-corrected density-functional approximation and light basis set settings. This method has shown chemical accuracy for a large carbohydrate benchmark set.[285,344,345] The sampling of sodiated α-GalDAG and β-GalDAG was done using CREST with GFN2-xTB[301] and default settings. A series of low-energy conformers below a threshold of 20 kJ mol^{-1} were reoptimized at the PBE0+D3/6-311+G(d,p) level of theory followed by a harmonic frequency analysis, as described in Section 3.4. To determine whether truncation of the lipid chains affects the IR signature, full lipid chains were added to one of the low-energy conformers of truncated α-GalCer. The force field-based conformational search was repeated with restraints on atoms of the truncated parent cation. A compact structure with multiple van der Waals contacts between the lipid chains and the galactose moiety was selected and reoptimized using the same DFT level of theory and followed by computation of a harmonic spectrum. In addition, anharmonic spectra of four low-energy conformers of sodiated α-GalCer were derived using the GVPT2 method implemented in Gaussian 16 Rev. B01.[346,347] These calculations were performed at the same PBE0+D3/6-311+G(d,p) level of theory and using ultrafine grid settings for modes 68–88 (1000–1200 cm^{-1} region) and 128–130 (amide II, amide I, and C=C vibrations, respectively), which correspond to the vibrations in the experimental window. The resulting anharmonic spectrum was shifted by a constant factor of 20 cm^{-1}. The calculations were performed by Prof. Mateusz Marianski (Hunter College, New York, USA) and Kim Greis (Freie Universität Berlin, Berlin, Germany). Structure coordinate files of the computed glycolipids can be found in the supporting material of the original publication.[322]

4.3 | Results and Discussion

4.3.1 | Fingerprints of Isomeric Glycolipids

Galactosylceramides. This study was initiated by investigating α-GalCer and β-GalCer. This pair of stereoisomers is not distinguishable by IM-MS (Table A1), and tandem MS relies on relative ion intensities at different collision energies to resolve α-GalCer and β-GalCer.[332] In contrast, cryogenic gas-phase IR spectroscopy probes the ion's structure directly, including the stereochemistry of the glycosidic bond.[284] The IR spectra of α-GalCer and β-GalCer [M+Na]$^+$ ions feature distinct spectroscopic signatures in the 1000–1150 cm^{-1} region (Figure 4.2). The theoretical spectra of the lowest-energy structures of [α-GalCer+Na]$^+$ and [β-GalCer+Na]$^+$ with truncated lipid chains were derived using harmonic approximation, and revealed that this diagnostic fingerprint region is composed of C−O and C−C stretching vibrations of the sugar ring. However, while the absorption frequencies of the non-diagnostic N−H bending vibration (amide II) and the C=O stretching vibration (amide I) are in good agreement with the experimental values, the shape of the spectra in the diagnostic 1000–1150 cm^{-1} region

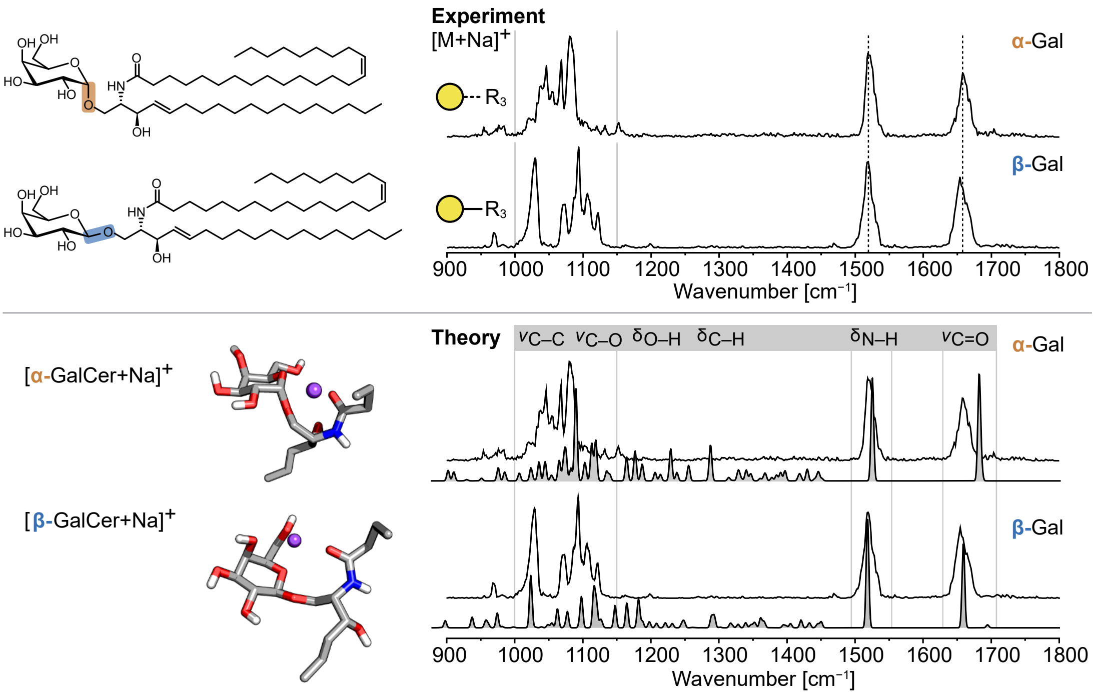

Figure 4.2: Structures and gas-phase IR spectra of α-GalCer and β-GalCer (d18:1/24:1(15*Z*)). Sodium adducts of α-GalCer and β-GalCer yield unique fingerprints in the 1000–1150 cm^{-1} region. The assignment of vibrational bands is based on computed harmonic IR spectra (gray) of the lowest-energy conformers of [α-GalCer+Na]$^+$ and [β-GalCer+Na]$^+$ with the lipid chains trimmed to four heavy atoms.

differs. Reattachment of the lipid chains to a conformer of [α-GalCer+Na]$^+$ resulted in only minor changes in the diagnostic region of the theoretical spectrum (Figure A1). The mismatch originates from the harmonic molecular potential[348] derived using an approximate density functional.[349] The inclusion of anharmonic effects in the theoretical IR spectrum improves the agreement between the spectra in the fingerprint region (Figure A2).[346] The region between 1150–1450 cm^{-1} is dominated by C−H and O−H bending vibrations and shows a very low intensity in the experimental spectra. In summary, the spectroscopic signatures of α-GalCer and β-GalCer demonstrate that the assignment of the anomeric configuration can be accomplished based on the merely 150 cm^{-1} wide fingerprint region.

Stereoisomeric monosaccharides. The ability to distinguish α-GalCer and β-GalCer entailed a more systematic study of isomeric glycolipids, starting with glycosylsphingosines as the simplest possible glycolipids and then gradually increasing size and complexity. The glycosylsphingosines α-Gal and β-Gal sphingosine are the primary degradation products of α-GalCer and β-GalCer that are formed by the enzymatic removal of the fatty acyl chain.[325,350] It was recently shown that α-Gal sphingosine shows antigenic activity towards NKT cells despite the missing lipid chain.[350] In addition to α-Gal and β-Gal sphingosine, the corresponding Glc

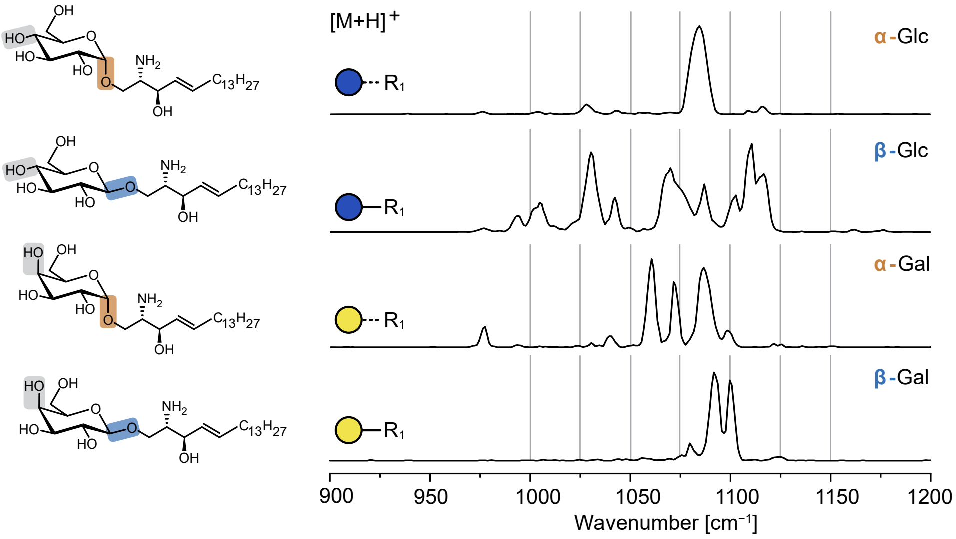

Figure 4.3: Spectroscopic fingerprints of protonated isomeric Glc and Gal sphingosines. The well-resolved absorption patterns of each permutation are diagnostic for both the monosaccharide and the configuration of the glycosidic bond.

epimers were investigated, as either Glc or Gal are typically linked as first monosaccharide in mammalian glycolipids.[20] Glc and Gal sphingosine are distinguishable after offline[136] or online[227] modification by MS/MS, but their distinction relies only on relative intensity differences of generated fragments. Without modification, MS/MS and IM-MS provide no stereochemical information. In contrast, gas-phase IR spectra of the protonated species yield diagnostic, baseline-resolved absorption patterns in the fingerprint region (Figure 4.3). The spectra are unique for each combination of monosaccharide (Glc or Gal) and anomeric configuration (α or β). Some absorption bands are so unique that the corresponding structure could be distinguished from the others by only monitoring the absorption at one specific wavenumber, for example 1065 cm^{-1} for α-Gal sphingosine. Besides the diagnostic fingerprint region between 1000–1150 cm^{-1}, the spectra display only weak absorption bands associated with the umbrella motion of NH_3^+ between 1400–1500 cm^{-1} (*cf.* Figure 4.5).

Regioisomeric trisaccharides. With increasing glycan size, the number of possible glycan isomers rises exponentially[66] while the resolution of the gas-phase IR spectra generally deteriorates.[284] To test the influence of the glycan size on the information content of the IR spectra, globotriose (Gb3) was selected as a common, naturally occurring trisaccharide headgroup consisting of two Gal and one Glc unit. The ability to resolve subtle structural differences in the trisaccharide was tested by including iso-globotriose (iGb3), the first reported endogenous NKT cell antigen.[351,352] The chemical structures of Gb3 and iGb3 differ by the connectivity between the two Gal building blocks (1→3 *vs.* 1→4) (Figure 4.4). This difference in

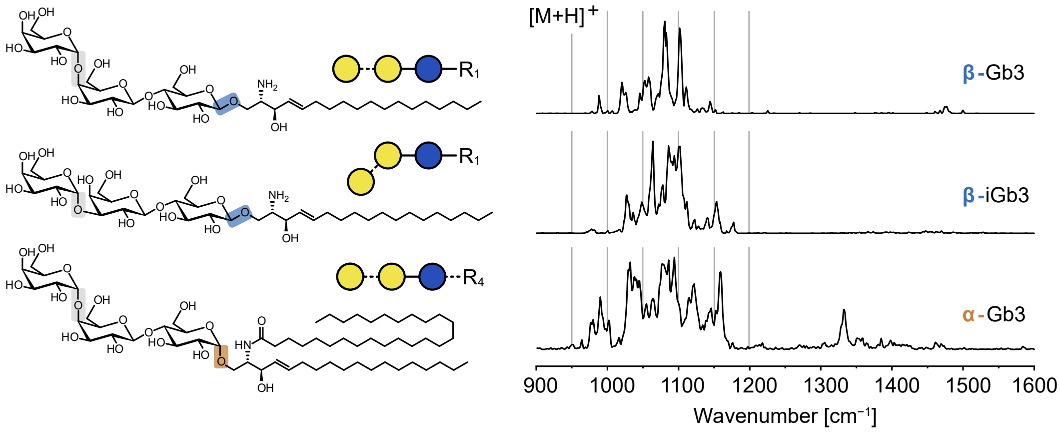

Figure 4.4: IR spectra of β-Gb3 sphingosine, β-iGb3 sphingosine, and α-Gb3Cer (d18:1/26:0). The regioisomeric trisaccharides in β-Gb3 sphingosine and β-iGb3 sphingosine yield distinguishable and well-resolved absorption patterns in the fingerprint region (950–1200 cm^{-1}). The spectrum becomes more congested with increasing size of the molecule, as shown for α-Gb3Cer (d18:1/26:0).

the molecular geometry causes slightly different ion mobilities of sodiated β-Gb3 sphingosine and β-iGb3 sphingosine (Table A1); however, the ATDs of the isomers in a mixture are not separated. Cryogenic IR spectroscopy allows for a much clearer isomer distinction. Even though the IR spectra of β-Gb3 sphingosine and β-iGb3 sphingosine are more congested than the spectra of the previously investigated monoglycosylsphingosines, they are still well-resolved, and the unique fingerprints demonstrate that the connectivity between monosaccharide building blocks can be determined by IR spectroscopy. Finally, the glycolipid size was further increased by replacing sphingosine by a ceramide. The IR spectrum of protonated α-Gb3Cer (d18:1/26:0) displays distinct absorption bands, but the spectrum is more congested in the fingerprint region (Figure 4.4, bottom), suggesting that the size limit for glycolipids is almost attained.

Lipid residues. So far, the investigated glycolipid structures were restricted to sphingolipids based on sphingosine. However, the sphingolipid backbones in nature are not exclusively relying on sphingosine, and a smaller number of glycolipids in mammals are not at all based on a sphingolipid, but on a glycerol backbone.[20,55] For example, several glycerolipids bearing α-linked Gal[353] or Glc[354] headgroups were identified as bacterial ligands of NKT cells. The influence of different lipid moieties on the IR spectra is shown on the example of α-Gal attached to sphingosine, phytosphingosine, Cer (d18:1/24:1(15*Z*)), and DAG (14:0/14:0) (Figure 4.5). The formal addition of water to the C=C bond of mammalian sphingosine to generate its plant analog phytosphingosine does not significantly alter the fingerprint region. The frequencies of the three main bands are identical, whereas a weak absorption at 950 cm^{-1} is only visible in the spectrum of α-Gal sphingosine. Ceramide yields a significantly different absorption pattern in the diagnostic fingerprint region and can be readily distinguished from other lipid residues by

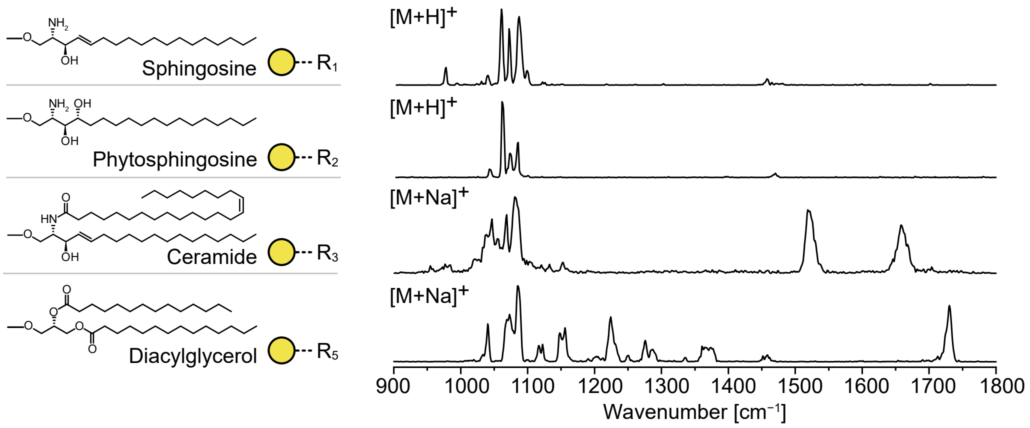

Figure 4.5: Influence of different lipid moieties on the IR spectra of α-Gal lipids. The exchange of sphingosine for phytosphingosine leads to subtle differences in the spectroscopic fingerprint, whereas ceramide (d18:1/24:1(15*Z*)) and diacylglycerol (14:0/14:0) considerably alter the fingerprint region. The amide- and ester groups yield additional bands beyond 1450 cm^{-1}.

the characteristic amide vibrations above 1450 cm^{-1}. The spectrum of α-GalDAG displays a less defined fingerprint region and more prominent C−H bending vibrations. The ester groups yield additional C=O stretching vibrations above 1700 cm^{-1}. Calculations revealed substantial mixing of the stretching of the two carbonyl groups resulting in in-phase and out-of-phase vibrational modes (Figure A3). The two modes are, however, not resolved in the experimental spectrum. Overall, these examples highlight the fact that, despite their exceptional resolution, cryogenic IR spectra are challenging to deconvolve using known increments. As a result, routine analyses will require spectral libraries containing distinct glycolipid reference data.

4.3.2 | Deconvolution of Isomeric Mixtures

Reference spectra of glycolipid standards can be used to study more complex isomeric mixtures and quantify the contributions of individual isomers. To test the utility of this approach, a proof-of-concept study on several glycolipid mixtures was performed. Three different aspects were addressed: (1) variation of mixing ratios in binary synthetic mixtures to evaluate the dependence of the absorption intensities on the relative concentrations and to determine the limit of detection, (2) deconvolution of more complex synthetic mixtures composed of up to four isomeric glycolipids, and (3) application to biological lipid extracts.

Synthetic glycolipid mixtures. At first, binary mixtures of α-GalCer and β-GalCer with defined mixing ratios were investigated. The experimental spectra of the protonated ions were compared with theoretical spectra obtained by weighting and averaging the two reference spectra of pure α-GalCer and β-GalCer $[\mathrm{M+H}]^+$ ions according to their mixing ratios. Even

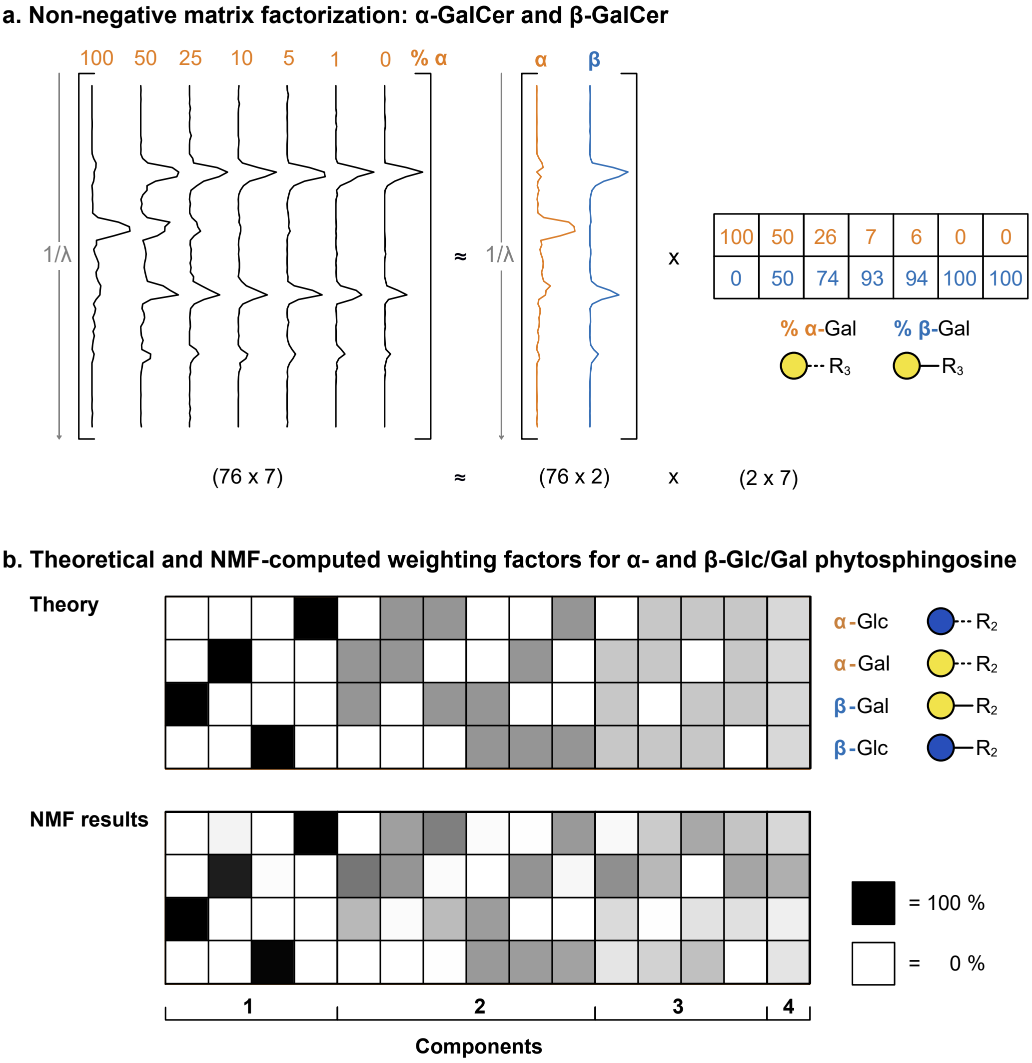

Figure 4.6: Deconvolution of IR spectra of synthetic glycolipid mixtures by non-negative matrix factorization (NMF). **a.** Deconvolution of the IR spectra of synthetic mixtures of α- and β-GalCer (d18:1/24:1(15*Z*)). The (76 x 7) input matrix contains the binned experimental spectra from 1000 to 1150 cm^{-1}. The expected ratio of α-GalCer is indicated on top. The output contains the two spectra of pure α- and β-GalCer in a (76 x 2) matrix multiplied by their relative contributions to each of the input spectra. **b.** Heatmap representation of the weighting factors predicted by the mixing ratios (top) and calculated by NMF from the 15 experimental spectra (bottom) of four glycosylphytosphingosines. The weighting factors are encoded in the corresponding ratio of black and white (white = 0 %, black = 100 % glycolipid).

though this simple mathematical approach assumes a strictly linear decrease of intensity with decreasing relative concentration, which is not necessarily given due to potentially different ionization efficiencies and the non-linear photon absorption process, the theoretical spectra model the experimental spectra very well (Figure A4). This finding implies that the relative intensities scale roughly linearly with the molar ratio over a wide range of mixing ratios. The respective contributions of the pure compounds to the mixtures were also quantitatively determined with an exceptional accuracy by non-negative matrix factorization (Figure 4.6a).[343,355] This factorization method deconvolves the spectra of isomeric mixtures into the spectra of α-GalCer and β-GalCer (basis vectors), and their relative contribution to each of the mixtures (weighting factors). The weighting factors were found to be accurate within an error range of less than 5 %. NMF is thus a well-suited method for spectral deconvolution of binary glycolipid mixtures, provided that the abundance of the minor isomer is not much below 5 %. In accordance with this limit of reliable detection, α-GalCer could be detected and quantified in a 5:95 (α:β) mixture, but was not detectable in a 1:99 mixture. This detection limit for minor species in isomeric mixtures is within the same order of magnitude as that of NMR spectroscopy.[65]

More complex ternary and quaternary mixtures of isomeric glycolipids were investigated to assess if spectral deconvolution is still possible at increasing spectral congestion. For this purpose, the four isomers α-Gal/Glc and β-Gal/Glc phytosphingosine were mixed in any possible combination of two-, three-, and four-component mixtures with equal concentrations. NMF correctly retrieves which isomer is present in which of the 11 mixtures (Figure 4.6b). Due to the increased complexity of the mixtures (four instead of two possible compounds), the mixing ratios predicted by NMF are not as exact as in the case of binary GalCer mixtures, but still sufficiently accurate. Slight deviations of the predicted weighting factors from the actual mixing ratios can be partly ascribed to the fact that the result obtained by NMF is not unique.[355] The single component spectra of each of the four isomers exhibit slightly different absolute intensities. Consequently, a low intensity of a specific absorption band in the mixture spectra can indicate either a low relative abundance of the respective isomer or a higher abundance but low absolute intensity. Because the absolute intensities of the pure spectra are not perfectly modeled by NMF, the relative abundance of some isomers is systematically overestimated (see α-Gal in Figure 4.6b), whereas others are underestimated (see β-Gal in Figure 4.6b); however, within well-acceptable limits. Another reason for systematic over- or underestimation of relative abundances are possible differences in the ionization efficiencies and charge competition between isomers during the ESI process.[356] As a consequence, the ion abundance in the gas phase does not necessarily reflect the solution-state distribution, which impedes accurate quantification by gas-phase techniques. However, this constraint is expected to play a minor role in the case of the glycolipid isomers studied here, which should ionize with similar efficiencies due to their high structural similarity.

Biological glycolipid extracts. Having established the utility of IR spectroscopy and NMF for the identification and relative quantification of isomers in synthetic glycolipid mixtures, the method was applied to biological lipid extracts. Two lipid extracts **1** and **2** were prepared from cells of GLA and GAA knockout mice, respectively.[339,340] After reversed-phase HPLC separation, glycosylceramides (monoisotopic mass = 809.7 Da) were detected in both samples

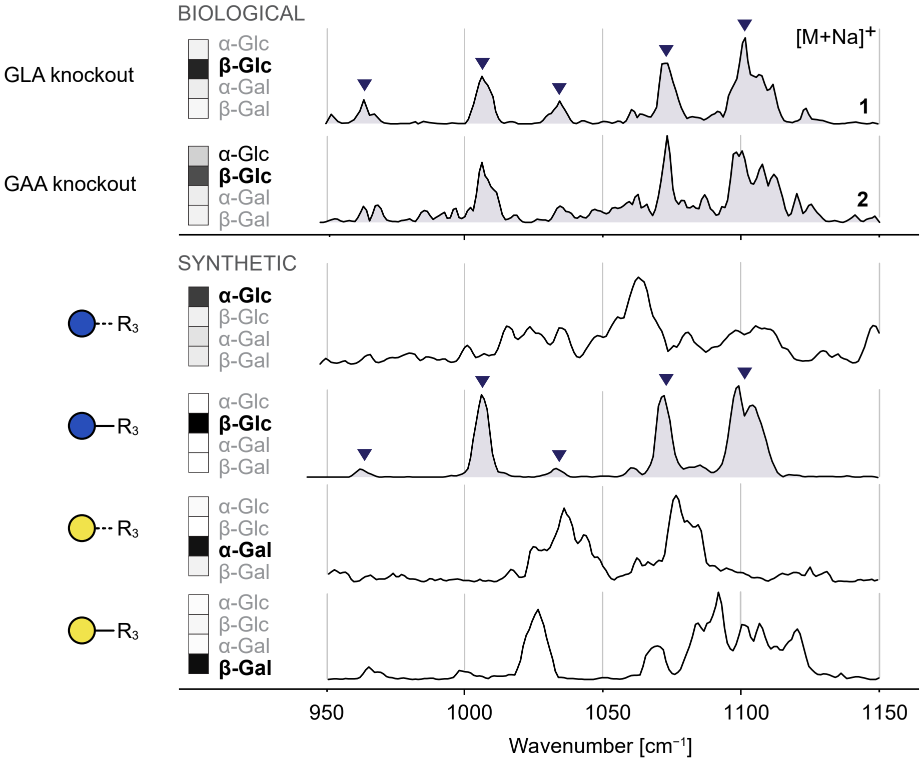

Figure 4.7: IR spectra of sodiated glycosylceramides (m/z 832.7) from biological lipid extracts and from synthetic α-Glc/GalCer and β-Glc/GalCer (d18:1/24:1(15*Z*)) standards. The five main absorption bands found in both spectra of biological glycolipids are equally present in the spectrum of β-GlcCer. In addition, α-GlcCer contributes to the spectrum of Folch extract **2** isolated from spleen of GAA knockout mice. The isomer contributions are derived from spectral deconvolution by non-negative matrix factorization.

by MS and MS/MS. Isobaric phosphatidylcholines were removed by treatment with NaOH, and the remaining sodiated glycosylceramides were investigated without further purification by IR spectroscopy. The successful removal of phosphatidylcholines was confirmed by the absence of characteristic ester carbonyl stretching vibrations between 1700–1800 cm^{-1}. To assign the isomers present in the biological samples, IR spectra of α-GlcCer and β-GlcCer (d18:1/24:1(15*Z*)) standards were recorded (Figure 4.7). Both biological samples display very similar spectroscopic fingerprints with β-GlcCer as predominant isomer. However, the results from NMF clearly indicate that extract **2**, contrary to extract **1**, also contains a considerable fraction of α-GlcCer. This finding agrees with the fact that extract **2** was obtained from GAA knockout mice which lack an enzyme cleaving alpha-glucosidic bonds. In Folch extract **1** from GLA knockout mice, the presence of α-GalCer could, however, not be confirmed. In fact, only GlcCer, but not GalCer, was reliably detected in the biological samples. In general, the accuracy of weighting factors obtained by NMF is higher in the case of synthetic mixtures than for deconvolution of biological mixtures. This can be partly attributed to the lower signal-to-noise (*s*/*n*) ratio of the IR spectra caused by a lower glycolipid concentration in the biological extracts. The spectrum of extract **1** displays a higher *s/n* ratio than the spectrum of extract **2**.

This exemplary investigation of two biological lipid extracts demonstrates that IR action spectroscopy can provide informative spectra despite low sample concentration and interferences from the biological matrix, while requiring only few basic purification steps. As the number of possible monoglycosyl lipid isomers underlying a certain *m/z* peak is restricted (usually Glc or Gal), the isomers in question can be unambiguously identified with the help of a small set of reference spectra. The sensitivity of the technique is sufficient to identify certain changes in the isomer distribution, as shown by the example of GAA knockout mice. In contrast to NMR spectroscopy—the gold standard for direct structure assignment of molecules in solution—IR spectroscopy is furthermore compatible with the small glycolipid quantities typically found in biological samples. Assuming sample concentrations of 0.1–1 mᴍ required for NMR spectroscopy *vs.* 0.01–0.1 mᴍ for IR spectroscopy, and sample volumes of 1 mL and 10 µL for a complete measurement, respectively, NMR spectroscopy requires a 100–1000 fold larger total sample amount (0.1–1 µmol) than IR action spectroscopy (0.1–1 nmol). Furthermore, and again contrary to NMR, MS-based IR spectroscopy does not require pure samples; the quality of IR spectra is not impaired by impurities from biological matrices present in solution, because the glycolipid of interested is isolated in the gas phase by a *m/z* filter prior to the measurement.

4.4 | Conclusions

This comprehensive spectroscopic study demonstrates the potential of cryogenic IR action spectroscopy for the characterization of glycolipid isomers. The technique overcomes substantial analytical difficulties previously encountered in immunological studies, where *"the anomeric identity of the isolated compound could not be probed directly by MS given that alpha- and beta-anomers are isobaric species or by NMR because quantities were so limiting"*.[325] Using IR action spectroscopy, all investigated structural features including the anomeric configuration, regioisomeric and stereoisomeric glycan headgroups, and different lipid classes were unambiguously resolved. Major advantages of the MS-based detection scheme over other structure-sensitive techniques, in particular NMR spectroscopy, are indeed a 100–1000-fold reduction in sample consumption and tolerance towards non-isobaric impurities. These virtues of IR action spectroscopy pave the way for biological applications without extensive sample purification and enrichment. The practical application is further facilitated by the narrow spectral range covering only 150–200 cm^{-1}, in which most of the structural information is condensed. The high sensitivity of the technique enables the characterization of low-abundant glycolipids from biological lipid extracts and monitoring of changes in the isomer distribution. The detection limit for minor isomers in a mixture was found to be within 1–5 %, which is consistent with a similar spectroscopic study on glycans that reported a detection limit of 3 %.[357]

Despite the obvious advantages of IR action spectroscopy, several challenges must be overcome before it can be integrated into standard analytical workflows. First of all, the spectral deconvolution of glycolipid mixtures requires reference spectra, which implies prior knowledge about the isomers potentially contained in the mixture and the availability of isomerically pure standards. This problem is not unique to IR spectroscopy, but is also known for other MS-based methods resolving isomers based on HPLC,[358] high-resolution IMS,[108–110] UVPD,[359] and solution-phase[136] or gas-phase[227–229] derivatization. However, as the number of possible glycan structures in natural glycolipids is restricted, this limitation is expected to resolve over time. Another problem is the size limit above which spectral congestion prevents unambiguous assignment of isomers by IR spectroscopy. A possible solution for biological glycolipids with large glycan headgroups could be fragmentation prior to the spectroscopic interrogation, as has been repeatedly demonstrated for the analysis of large glycans.[360] Finally, a major drawback of IR action spectroscopy is the need for expensive, custom-made instrumentation and a powerful light source. The prospects for implementing IR action spectroscopy in a benchtop experiment to make the technique more widely available are discussed in more detail in Chapter 7.

5 | Resolving Double Bond Isomers by Chemical Sensors

Determining the position and configuration of C=C bonds in unsaturated lipids is of paramount importance in deciphering metabolic pathways and monitoring disease development and progression. In this chapter, different strategies are explored to visualize the position and geometry of C=C bonds in unsaturated fatty acids and sphingolipids using infrared action spectroscopy. In the first part, it is demonstrated that the NH_3^+ group in protonated sphingolipids interacts with the electron-rich C=C bond and thereby induces diagnostic frequency shifts in the N−H bending vibrations. This frequency shift makes C=C regio- and stereoisomers distinguishable, such that the protonated amine can be regarded as an intrinsic double bond sensor of sphingolipids. Because fatty acids bear no comparable electrophilic functional group, extrinsic double bond sensors are introduced either by non-covalent modification with ammonium derivatives or by covalent modification with pyridinium derivatives. While the non-covalent derivatization approach yields only minor differences in the infrared spectra of isomeric fatty acids, the conversion of fatty acids into 3-pyridylcarbinol esters results in diagnostic spectroscopic fingerprints for each isomer. The approach allowed quantification of double bond regio- and stereoisomers in fatty acid mixtures and differentiation of two human cancer cell lines. In particular, the technique enabled the first unambiguous identification of 6Z-octadecenoic acid in a human-derived cell line, providing insight into the underlying aberrant lipid metabolism in cancer cells.

This chapter is based on the following references:

[361] C. Kirschbaum *et al.*, Resolving Sphingolipid Isomers using Cryogenic Infrared Spectroscopy, *Angew. Chem. Int. Ed.* **2020**, *59*, 13638–13642.

[362] C. Kirschbaum *et al.*, Non-Covalent Double Bond Sensors for Gas-Phase Infrared Spectroscopy of Unsaturated Fatty Acids, *Anal. Bioanal. Chem.* **2021**, *413*, 3643–3653.

Early version of C. Kirschbaum, R. S. E. Young, K. Greis, J. P. Menzel, S. Gewinner, W. Schöllkopf, G. Meijer, G. von Helden, T. Causon, V. R. Narreddula, B. L. J. Poad, S. J. Blanksby, K. Pagel, Establishing Carbon-Carbon Double Bond Position and Configuration in Unsaturated Fatty Acids by Gas-Phase Infrared Spectroscopy, *under review.*

5.1 | Introduction

Fatty acids and sphingoid bases are fundamental building blocks of more complex lipids. The number, position, and geometry of the carbon-carbon double bonds in these building blocks are crucial for the biological function of the assembled lipids and influence health and disease (*cf.* Section 2.1).[74] To understand how the position and geometry of C=C bonds affect biological function and to examine how the ratio of specific double bond isomers changes in disease, reliable analytical techniques that can both locate C=C bonds and determine their geometry are required (*cf.* Section 2.2).[9–16]

The *de novo* biosynthesis of sphingoid bases is initiated by the condensation of palmitoyl-CoA and L-serine, which is catalyzed by serine palmitoyl transferase.[55] One major reason for the structural diversity of natural sphingoid bases is that serine palmitoyl transferase can accept other fatty acyl substrates than palmitoyl-CoA and can even use glycine and L-alanine instead of L-serine.[363,364] The condensation of L-alanine or glycine with fatty acyl-CoA yields 1-deoxysphingolipids and 1-deoxymethylsphingolipids, respectively. They lack the terminal hydroxyl group and can therefore neither be converted to more complex phospho- or glycosphingolipids, nor degraded *via* the canonical pathway which requires phosphorylation of the 1-hydroxyl group.[363,365] Since their first discovery in marine clams[366] and recent detection in mammals,[364,367] 1-deoxysphingolipids have moved into the focus of interest. Their accumulation and resulting neurotoxic effects are observed after anoxia-associated injuries,[368] in hereditary sensory neuropathy type 1,[364] and in clinically similar diabetic sensory neuropathy.[369] Furthermore, 1-deoxysphingolipids are potential plasma markers for predicting the outbreak of diseases such as type 2 diabetes.[370] Despite their seemingly simple structure, the analysis of 1-deoxysphingolipids is challenging due to the occurrence of different kinds of isomerism. Those include ketone/alkenol isomers, hydroxylation regioisomers, and in particular C=C regio- and stereoisomers. The predominant C=C bond position and configuration in 1-deoxysphingosine was only recently identified as 14*Z*, in contrast to the 4*E* double bond in canonical sphingosine.[371] Here, we show that all types of isomerism in 1-deoxysphingolipids can be resolved by cryogenic IR action spectroscopy. In particular, the position and geometry of C=C bonds can be determined due to charge-olefin interactions between the protonated amine and the C=C bond, leading to isomer-specific frequency shifts in the N−H bending vibrations.

Fatty acids, on the other hand, do not contain a primary amine or a comparable electrophilic functional group that could potentially interact with the C=C bond. However, the unambiguous assignment of the regio- and stereochemistry of C=C bonds in unsaturated fatty acids is crucial for the discovery of unknown metabolic pathways leading to unusual fatty acids, such as those synthesized by cancer cells *via* alternative desaturation pathways. In the canonical view of mammalian cellular metabolism, the action of stearoyl-CoA desaturase 1 on palmitic acid (FA 16:0) and stearic acid (FA 18:0) gives rise to the monounsaturated FAs palmitoleic acid (FA 16:1(9*Z*)) and oleic acid (FA 18:1(9*Z*)), respectively.[372,373] Intriguingly, however, human sebum and sebocytes have been found to be rich in sapienic acid (FA 16:1(6*Z*)) and its elongation product 8*Z*-octadecenoic acid (FA 18:1(8*Z*)), ascribed to the activity of fatty acid desaturase 2.[374,375] Both FAs have recently been discovered in cancer-derived cells and tissues, suggesting that the non-canonical activity of fatty acid desaturase 2 may afford the cancer cells alternative pathways to lipid synthesis and modification.[7] These findings have triggered reinvestigation of monounsaturated fatty acid families in cancer cells, particularly in instances where the canonical pathways are unavailable.[8] Such investigations highlight the potential for further divergence from canonical metabolism, with the putative identification of a 6-octadecenoic acid (FA 18:1(Δ6)) of unknown double bond stereochemistry. The *Z* isomer, petroselinic acid (FA 18:1(6*Z*)), is frequently found in the plantae kingdom,[376] however, its presence in human-derived cells is intriguing as it has only been reported once prior in human sebum.[374] While human desaturase enzymes are known to install C=C bonds in the *Z* configuration by convention, abnormalities in the natural pathways of β-oxidation (*e.g.*, 3,2-*trans*-enoyl-CoA isomerase[377] and leaky β-oxidation[378]) or free radical stress[92,379] create the possibility for the formation of endogenously derived *trans* FA species. Indeed, elaidic acid (FA 18:1(9*E*)) and other common *trans* FAs have previously been reported in prostate cancer cell lines.[380] Thus, the appearance of the unusual FA 18:1(Δ6) in human cells warrants rigorous structure elucidation including the assignment of double bond position and stereochemistry.

Motivated by the finding that 1-deoxysphingolipids carry an intrinsic double bond sensor for gas-phase IR spectroscopy, we extended the concept to FAs by non-covalent and covalent modification with electrophilic functional groups to induce charge-olefin interactions. Non-covalent complexes of monounsaturated FAs with sodium, pyridinium, trimethylammonium, dimethylammonium, and ammonium cations were investigated using a combined approach of cryogenic IR action spectroscopy, IM-MS, and quantum chemical calculations. 3-Pyridinemethanol and 3-aminomethylpyridine were used for covalent modification. These pyridine derivatives are established derivatization reagents that enhance the ionization efficiency of FAs in positive ion mode and induce diagnostic fragmentation in tandem MS.[381–383] IR action spectroscopy of synthetic 3-pyridylcarbinol esters yields unique spectroscopic fingerprints, which were used to determine the relative abundance of FA 18:1 isomers in synthetic mixtures by computational deconvolution. Semi-quantitative analysis of two human prostate cancer cell lines (PC-3 and LNCaP) demonstrated that the unusual FA 18:1(Δ6) present in the PC-3 cell line is in the *Z* configuration. The results were independently confirmed by LC-OzID-MS.

5.2 | Experimental Details

Sample preparation. An overview of the 1-deoxysphingolipids and fatty acids investigated in this work is provided in Figure 5.1. 4*E*-1-Deoxysphingosine (SO) was purchased from Avanti

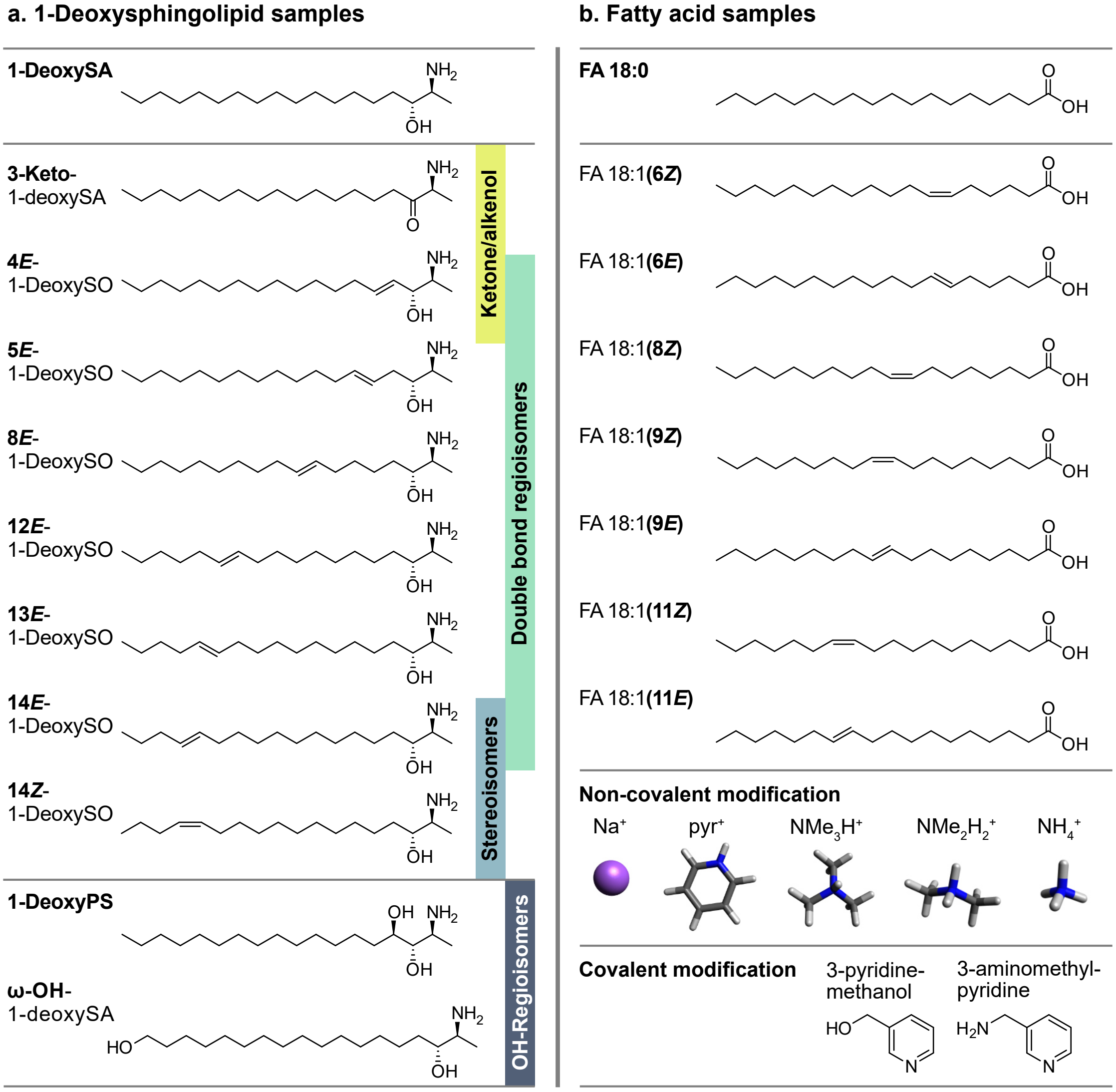

Figure 5.1: Overview of the investigated 1-deoxysphingolipids and fatty acids. **a.** The 1-deoxysphingolipid samples include ketone/alkenol isomers, double bond regio- and stereoisomers, and hydroxylation regioisomers. **b.** Stearic acid (FA 18:0) and several double bond isomers of FA 18:1 were non-covalently modified with sodium, pyridinium, trimethylammonium, dimethylammonium, and ammonium cations. Covalent modification with 3-pyridinemethanol and 3-aminomethylpyridine was achieved by esterification and amidation of the fatty acids, respectively.

Polar Lipids (Alabaster, USA). 3-Keto-1-deoxysphinganine (SA), 8*E*-1-deoxySO, 12*E*-1-deoxySO, 13*E*-1-deoxySO, 14*E*-1-deoxySO, 14*Z*-1-deoxySO, 1-deoxyphytosphingosine (PS), and ω-OH-1-deoxySA were synthesized in the laboratory of Prof. Christoph Arenz (Humboldt-Universität zu Berlin, Berlin, Germany), as reported previously.[371,384,385] The synthesis of 1-deoxySA and 5*E*-1-deoxySO was carried out according to largely analogous synthesis routes.[386] Detailed synthesis data can be found in the supporting material of the original publication.[361] In addition to the 1-deoxysphingolipids shown in Figure 5.1, the 3-deoxysphingolipid 4*E*-3-deoxySO was purchased from Avanti Polar Lipids. The deoxysphingolipids were dissolved in methanol (Sigma-Aldrich, Taufkirchen, Germany) and diluted to final concentrations of 10–100 µM for DT-IM-MS and IR spectroscopy.

Oleic acid (FA 18:1(9*Z*)), elaidic acid (FA 18:1(9*E*)), *cis*-vaccenic acid (FA 18:1(11*Z*)), and *trans*-vaccenic acid (FA 18:1(11*E*)), trimethylammonium chloride, dimethylammonium chloride, ammonium acetate, pyridinium chloride, water, methanol, and acetonitrile were purchased from Sigma-Aldrich for the formation of non-covalent fatty acid adducts. Aqueous stock solutions (100 mM) of each salt were prepared and the FAs were dissolved in methanol or acetonitrile (1 mM). Sodium and ammonium adducts were formed from 100 µM FA solutions in methanol containing 10 mM ammonium acetate. Trimethylammonium, dimethylammonium, and pyridinium adducts were generated from 500 µM solutions of FAs in acetonitrile containing 1 mM of the respective chloride salt.

Covalent modification of fatty acids with 3-pyridinemethanol and 3-aminomethylpyridine was carried out in the laboratory of Prof. Stephen Blanksby (Queensland University of Technology, Brisbane, Australia) as follows. The C18:1 fatty acid standards FA 18:1(11*Z*) and FA 18:1(9*Z*) were purchased from Sigma-Aldrich, FA 18:1(11*E*) was purchased from Matreya (Pennsylvania, USA), FA 18:1(9*E*) and FA 18:1(6*Z*) from TCI (Sydney, Australia), FA 18:1(6*E*) from Nu-Chek Prep (Minnesota, USA), FA 18:1(8*Z*) from Larodan (Solna, Sweden), and the Food Industry FAME mix of 37 fatty acid methyl esters including FA 18:1(9*Z*) and FA 18:1(9*E*) were obtained from Restek (Pennsylvania, USA). Biological lipids were extracted from PC-3 and LNCaP (TOFA) cells using methods similar to those described by Matyash *et al.*[387] as documented in detail in Young *et al.*[8] with no amendments. The procedure involves the addition of a mixture of deuterated lipids as an internal standard (SPLASH Lipid-o-mix, Avanti Polar Lipids). Fatty acids were hydrolyzed from intact lipids extracted from approximately 350,000 cells using 200 µL of methanol (Fisher Scientific, Scorseby, Australia) and 200 µL of 1.75 M aqueous KOH. The vials were lightly agitated for 30 s, heated at 75 °C for two hours using a dry block heater (Ratek, Saratoga, United States), and cooled to room temperature. The reaction was quenched using 800 µL of water and acidified to pH 1.5 using 120 µL of 5 M HCl. 500 µL of *n*-hexane was added and the vials were vortexed for 30 s. The supernatant was collected before the biphasic extraction process was repeated with an additional 500 µL of *n*-hexane. The obtained fatty acids in *n*-hexane were dried under N_2 gas.

Synthetic and extracted fatty acids were derivatized with 3-pyridinemethanol to yield 3-pyridylcarbinol esters. For lipid extract samples, 250 µL acetonitrile, 50 µL 3-pyridinemethanol in acetonitrile at a concentration of 110 mM, 50 µL *N*,*N*-diisopropylethylamine (DIPEA) in acetonitrile (350 mM), and 50 µL of (2-(1*H*-benzotriazol-1-yl)-1,1,3,3-tetramethyluronium hexafluorophosphate (HBTU) in acetonitrile (110 mM) were added to each vial before a 30 s vortex. For fatty acid standard samples, 50 µL of the fatty acid in acetonitrile (35 mM), 200 µL acetonitrile, 50 µL 3-pyridinemethanol in acetonitrile (110 mM), 50 µL DIPEA in acetonitrile (350 mM), and

50 µL of HBTU in acetonitrile (110 mM) were added to each vial before 30 s vortex. Samples were heated at 50 °C for 17 hours using a dry heat block. After cooling to room temperature, 1 mL of water was added along with 200 µL saturated aqueous NaCl solution and 2 mL of methyl *tert*-butyl ether. The samples were vortexed for 30 s before the supernatant was collected, dried under N_2 gas, and washed with an additional 200 µL water, 200 µL saturated aqueous NaCl solution, and 750 µL methyl *tert*-butyl ether. The supernatant was collected, dried, and capped with N_2 gas in the head space prior to inter-laboratory shipment.

For the conversion of fatty acids into 3-picolylamides, 133 µL of 3-aminomethylpyridine (2.67 µmol, 3 equiv.) in dimethylformamide (20 mM) was added to the C18:1 fatty acid (0.889 µmol, 1 equiv.) before 30 s vortex. 26 µL 1-[bis(dimethylamino)methylene]-1H-1,2,3-triazolo[4,5-b]pyridinium 3-oxide hexafluorophosphate (HATU; 2.67 µmol, 3 equiv.) in dimethylformamide (0.1 M) and 44 µL DIPEA (4.44 µmol, 5 equiv.) in dimethylformamide (0.1 M) were added before 1 min vortex. The resulting mixture was heated at 65 °C for 30 min. After cooling to room temperature, the mixture was diluted with 1.5 mL water and 1.5 mL methyl *tert*-butyl ether. 100 µL of saturated NH_4Cl solution was added before 30 s vortex. The layers were separated, and the aqueous layer was again extracted with 1.5 mL methyl *tert*-butyl ether. The organic layers were combined and dried under N_2 gas. After inter-laboratory shipment, the 3-pyridylcarbinol esters and 3-picolylamides were redissolved in methanol to a concentration of 100 µM for IR action spectroscopy. Synthetic mixtures of 3-pyridylcarbinol esters of FA 18:1(8*Z*), FA 18:1(9*Z*), and FA 18:1(11*Z*) were obtained by mixing the 100 µM solutions in defined ratios.

IR action spectroscopy. IR spectra of protonated deoxysphingolipids, fatty acid adducts, and protonated 3-pyridylcarbinol esters and 3-picolylamides were measured using the custom-built instrument described in Section 3.1.

DT-IM-MS. DT-IM-MS measurements were performed on three different instruments as follows. CCSs of protonated deoxysphingolipids were measured in helium using the modified Synapt G2-S HDMS instrument described in Section 3.3. The non-covalent fatty acid adducts were investigated in helium using the custom-built DT ion mobility-mass spectrometer described at the end of Section 3.3. CCSs of protonated 3-pyridylcarbinol esters and 3-picolylamides were recorded in nitrogen in the laboratory of Prof. Tim Causon (Universität für Bodenkultur Wien, Vienna, Austria) using an Agilent 6560 IM-QTOFMS (Agilent Technologies, California, USA) equipped with a Dual JetStream ESI source. Each isomer was injected separately and eluted from a Zorbax Eclipse Plus C18 column (50 mm x 2.1 mm, 1.8 µm) using a linear gradient (solvent A: 0.1 % formic acid in water; solvent B: 0.1 % formic acid in acetonitrile) and a flow rate of 200 µL min^{-1}. The instrument was operated in the 1700 Extended Dynamic Range mode with positive polarity. The trapping funnel fill time was set to 1 ms, and the 78 cm long drift tube was operated using a field strength of 10.9 V cm^{-1} (entrance 1074 V, exit 224 V). The maximum drift time was set to 50 ms and the trap release time to 150 µs. An acquisition rate of 1.1 frames per second was realized by summing 14 ion mobility transients per frame. For secondary (single-field) $^{DT}CCS_{N2}$ calibration, an infusion of ESI Tune Mix ESI-L (G1969-85000, Agilent Technologies) was used to determine a linear calibration function using the method and $^{DT}CCS_{N2}$ values reported in Stow *et al.*[388] The calibration parameters were subsequently applied to all measurement files in a single sequence. All data processing for $^{DT}CCS_{N2}$ determination was performed using the Agilent MassHunter IM-MS Browser (10.0, Build 10.0.100027.0).

UPLC-OzID-MS. Ultra-high performance liquid chromatography-ozone-induced dissociation-mass spectrometry (UPLC-OzID-MS) of derivatized C18:1 fatty acids was performed in the laboratory of Prof. Stephen Blanksby. The fatty acids were derivatized with 1-(4-(aminomethyl)phenyl)-pyridinium as described previously in Young *et al.*[8] 5 µL of the Restek 37 mix of fatty acid methyl esters and blanks were derivatized using the same method. Analysis was performed using a Waters Acquity (UPLC i-Class; CSH, C18 reverse phase column; 100 mm x 2.1 mm, 1.7 µm) LC system coupled with a Waters Synapt G2-Si ion mobility-mass spectrometer previously modified to allow introduction of ozone into the IMS cell.[207] Liquid chromatography was performed at a column temperature of 60 °C using a linear gradient at a flow rate of 0.4 mL min^{-1} (solvent A: 0.1 % formic acid in water; solvent B: 0.1 % formic acid in acetonitrile). Initially, the mobile phase consisted of 10 % B, and was increased to 20 % B at 0.5 min, then linearly increased from 0.5 min to 18 min to 100 %. The mobile phase was then kept isocratic until 20 min, and was reduced to 10 % B at 22 min to 25 min to recondition the column. Using positive polarity, the mass spectrometer was operated in *Sensitivity mode.*

For OzID, the ion mobility cell was filled with a mixture of nitrogen, ozone, and oxygen. Ozone was produced from high purity oxygen using a corona discharge-based high-concentration ozone generator (Ozone Solutions TG-40, Iowa, USA), producing a flow of 400 mL min^{-1} with 200–250 g cm^{-3} ozone in oxygen. Ozone in oxygen was introduced to the IMS gas flow through a needle valve that was adjusted to yield an ultimate pressure of 3 mbar in the IMS cell. Ozone was catalytically destroyed using a manganese dioxide-based catalyst. A solution of leucine enkephalin in a 1:1 (v:v) mixture of acetonitrile and water with 0.1 % formic acid was used as a Lockmass solution, and Lockmass correction was performed upon loading of the raw LC-MS dataset into Skyline. Data analysis was performed with Skyline MS.

The presence of characteristic fragments associated with cleavage of double bonds during ozonolysis (leading to aldehyde and Criegee fragments) provides evidence of the position of the double bond. The associated extracted ion chromatograms provide further evidence for correct identification (coelution of associated aldehyde and Criegee fragments). Relative quantification was performed by integration of the extracted ion chromatograms of both precursor and associated fragment chromatograms. The extracted ion chromatogram of the precursor were deconvolved as a sum of Gaussians to determine the contribution of each isomer. The retention time of the characteristic fragments was used to inform the retention time position of the Gaussians used for deconvolution. Apart from the aldehyde and Criegee fragmentation pathways, no other fragmentation pathways were detectable. The *E/Z* configuration was determined employing UPLC-OzID-MS data of photochemically isomerized fatty acid standards.

Linear regression analysis of mixtures. IR spectra of synthetic and biological mixtures of FA 18:1 3-pyridylcarbinol esters were deconvolved using reference IR spectra of standard substances. Mixture spectra and reference spectra were binned in 2 cm^{-1} steps using the 1D binning application, and then deconvolved using linear regression in OriginPro to yield the relative abundance of each isomer contained in the mixtures. The IR spectra of isomeric mixtures were simulated by linear combination of the reference spectra using the factors obtained from the linear regression analysis. The R^2 values are > 0.91 for the synthetic mixtures in a reduced wavenumber range covering 300 cm^{-1}, and > 0.83 for the biological samples (1000–1800 cm^{-1}).

Computational methods. The conformational space of deoxysphingolipids was sampled using Fafoom,[302] followed by optimization at the PBE+vdW^{TS}/light level of theory in FHI-aims.[303] The conformational search included rotation of all rotatable bonds. A subset of the energetically most stable structures were reoptimized at the PBE0+D3/6-311+G(d,p) level of theory followed by a frequency analysis in Gaussian 16,[307] as described in Section 3.4. The calculations for deoxysphingolipids were done by Kim Greis (Freie Universität Berlin, Berlin, Germany).

The non-covalent fatty acid adducts, protonated 3-pyridylcarbinol esters, and protonated 3-picolylamides were sampled in CREST[300] using GFN2-xTB.[301] 15–25 Conformers below a threshold of 15 kJ mol^{-1} relative to the lowest-energy conformer were selected using principal component analysis of all atomic distances excluding hydrogen atoms and k-means clustering, followed by optimization of the selected conformers at the B3LYP+D3/6-311+G(d,p) level of theory for non-covalent lipid adducts, and PBE0+D3/6-311+G(d,p) level of theory for 3-pyridylcarbinol esters and 3-picolylamides, as described in Section 3.4. CCSs of the optimized conformers were computed using HPCCS[314] with DFT-computed Merz-Singh-Kollman charges[316] at a temperature of 298 K (25 °C) in helium for the non-covalent fatty acid adducts, and in nitrogen for 3-pyridylcarbinol esters and 3-picolylamides. The predicted CCSs correspond to the average CCS value of all computed conformers below a threshold of ΔF= 10 kJ mol^{-1}. The ΔF values refer to the lowest-energy DFT-optimized conformer for each isomer. The conformers are numbered according to their position in the CREST output file from the conformational search. Lists and xyz files of all computed conformers can be found in the supporting material of the original publications.[361,362]

5.3 | Results and Discussion

5.3.1 | Natural Double Bond Sensors in Deoxysphingolipids

The basis of this investigation is a consistent set of synthetic 1-deoxysphingolipids (*cf.* Figure 5.1). 3-Keto-1-deoxySA is the primary condensation product of L-alanine and palmitoyl-CoA, which is subsequently reduced to 1-deoxySA. Desaturation of 1-deoxySA yields 1-deoxySO, which is an alkenol isomer of 3-keto-1-deoxySA. The predominant C=C bond position and configuration in 1-deoxySO is 14*Z*, in contrast to the 4*E* double bond in canonical SO.[371] Apart from 4*E*- and 14*Z*-1-deoxySO, the double bond isomers 5*E*-, 8*E*-, 12*E*-, 13*E*-, and 14*E*-1-deoxySO are included in this study. Hydroxylation regioisomers are represented by ω-OH-1-deoxySA and 1-deoxyPS, the deoxy analogue of the most abundant sphingoid base in plants.[56] Furthermore, the 3-deoxysphingolipid 4*E*-3-deoxySO is investigated as a hydroxylation regioisomer of 4*E*-1-deoxySO.

Double bond regio- and stereoisomers. The ketone/alkenol isomers 3-keto-1-deoxySA and 4*E*-1-deoxySO are readily distinguishable based on the gas-phase IR spectra of the protonated ions. The assignment of the absorption bands is exemplarily shown in Figure 5.2a and relies on computed IR spectra of low-energy conformers. Computations suggest that in both isomers the ammonium proton coordinates preferentially to the oxygen of the adjacent hydroxyl- or keto group (Figure B1). The ketone and alkenol are readily distinguishable by IR spectroscopy not only because of the characteristic carbonyl stretching vibration, but also by other diagnostic bands. Below 1150 $\mathrm{cm^{-1}}$, weak to medium intensity C−O and C−C stretching vibrations of the lipid chain are located. A weak band corresponding to the O−H bending vibration in 4*E*-1-deoxySO is found below 1400 $\mathrm{cm^{-1}}$, whereas the spectra are clearly dominated by the symmetrical NH_3^+ umbrella bending modes between 1400 and 1500 $\mathrm{cm^{-1}}$. The antisymmetric NH_3^+ bending vibrations are located at higher wavenumbers (1550–1650 $\mathrm{cm^{-1}}$) and are less intense. The C=C stretching vibration of the double bond in the spectrum of 4*E*-1-deoxySO around 1700 $\mathrm{cm^{-1}}$ is intrinsically weak, whereas the C=O stretching vibration of the ketone above 1700 $\mathrm{cm^{-1}}$ is clearly distinguishable.

It is important to note that the relative intensities of absorption bands are not reliable due to the nonlinear multiple photon absorption process. The evaporation of helium atoms resulting in the release of ions from the helium droplets scales nonlinearly with the photon flux. In addition, the regions from 900 to 1150 $\mathrm{cm^{-1}}$ and 1550 to 1800 $\mathrm{cm^{-1}}$ were measured with a tighter laser focus (increased photon fluence) to enhance the visibility of low-intensity bands. As a consequence, the experimentally observed and the predicted intensities do not coincide perfectly. For example, the predicted relative intensities of antisymmetric NH_3^+ bending vibrations are higher than observed throughout all experimental spectra.

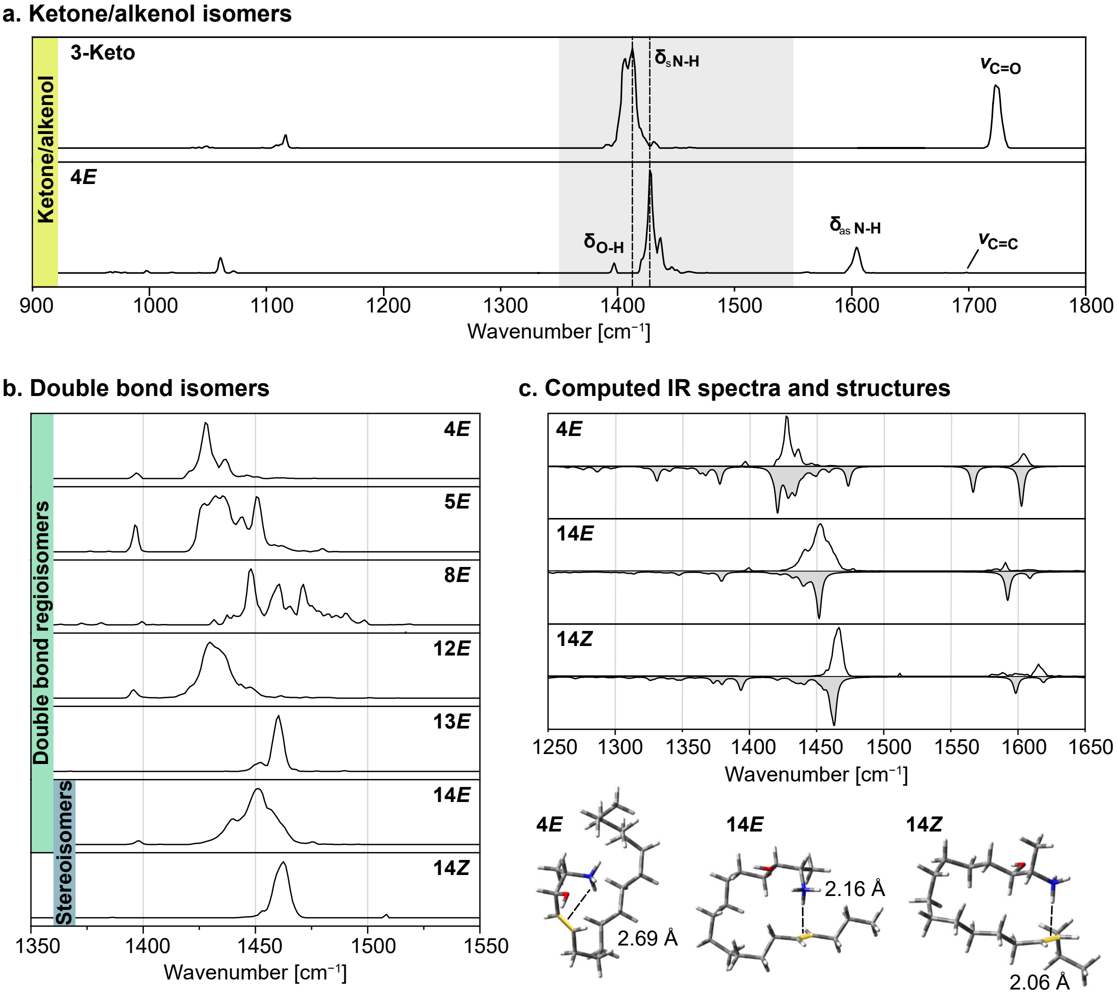

Figure 5.2: Gas-phase IR spectra and low-energy structures of 1-deoxysphingolipids. **a.** Isomeric 3-keto-1-deoxySA and 4*E*-1-deoxySO are distinguishable by diagnostic stretching (ν) and bending (δ) vibrations. The most intense bands in the gray region are assigned to NH_3^+ umbrella vibrations. **b.** IR spectra of 1-deoxySO double bond regio- and stereoisomers in the region of NH_3^+ umbrella vibrations (1350–1550 cm^{-1}). The vibrational frequencies depend on the position and configuration of the C=C bond. **c.** Spectral matches of 4*E*-, 14*E*-, and 14*Z*-1-deoxySO with computed IR spectra (gray) of DFT-optimized structures in the region of NH_3^+ bending vibrations. The corresponding computed structures depicted below highlight the different geometries due to intramolecular charge-olefin interactions. The charge-olefin interactions are indicated by dashed lines and the C=C bonds are highlighted in yellow.

In contrast to ketone/alkenol isomers that can also be differentiated by conventional LC-MS, double bond isomers are more challenging to distinguish. 1-Deoxysphingolipids differing by the position of the C=C bond were previously separated by differential-mobility spectrometry, but were found to be indistinguishable by classical DT-IMS.[389] This finding was confirmed by our DT-IMS measurements yielding identical collision cross sections for all investigated double bond isomers within the error limits (Table B1). Intuitively, the difficulty in distinguishing double bond isomers is also expected to apply to IR spectroscopy, as C=C stretching vibrations are intrinsically weak. However, as shown in Figure 5.2b, the frequencies of the NH_3^+ umbrella modes are significantly shifted depending on the position and configuration of the C=C bond. These frequency shifts are rather surprising, but can be explained by a charge-olefin interaction between the protonated amine and the C=C bond, which was predicted in a previous study by Poad *et al.*[389] and confirmed by our DFT calculations. The best spectral matches for the NH_3^+ bending vibrations are shown in Figure 5.2c for the representative double bond regio- and stereoisomers 4*E*-, 14*E*-, and 14*Z*-1-deoxySO, and in Figure B1 for the other isomers. A charge-olefin interaction was shown to be energetically favored for all three samples. However, substantial differences in the interaction geometry are observed, which is mainly dictated by the distance between the amine and the C=C bond. For example, in 4*E*-1-deoxySO, the ammonium proton cannot be centered directly above the C=C bond and the distance between the proton and the C=C bond is longer than in the 14*E* and 14*Z* structures. This difference was already reported by Poad *et al.*, who furthermore observed a deviating behavior of 8*E*-1-deoxySO that showed no preference for the charge-olefin interaction. DFT calculations reveal that several low-energy conformers of 8*E* favor an interaction between the C=C bond and the hydroxyl proton instead of the ammonium proton or no specific interaction at all. Accordingly, the crowdedness of the IR spectrum of 8*E*-1-deoxySO suggests the presence of more than one conformer. Another interesting observation is the similarity between the IR spectra of 13*E*- and 14*Z*-1-deoxySO despite the different double bond position and configuration. For both isomers, good qualitative matches with computed harmonic IR spectra were obtained (Figure B1).

Hydroxylation regioisomers. Another important source of isomerism arises from hydroxylation of 1-deoxysphingolipids, which is particularly relevant in the context of their biochemical degradation. The non-canonical sphingolipids are catabolized by successive steps of hydroxylation and desaturation.[365] Several structures of hydroxylated intermediates have been proposed; however, the positions of hydroxylation remain elusive. 1-DeoxyPS and ω-OH-1-deoxySA were thus investigated as a representative pair of isomers with one fixed and one varying OH position. Their IR spectra show significant differences in the N−H bending and C−C and C−O stretching regions (Figure 5.3a). In addition, DT-IMS measurements yield CCS differences between the hydroxylation regioisomers, which could be an indication of different conformations in the gas phase (Table B1). The conformational analyses suggest that in both cases the NH_3^+ group coordinates to both hydroxyl oxygen atoms. The terminal OH group of ω-OH-1-deoxySA has a large motional freedom and can interact with the protonated amine over a short distance in different geometries, whereas the interaction geometry is restricted in the rigid structure of 1-deoxyPS. Accordingly, the computed harmonic IR spectrum of the depicted DFT-optimized 1-deoxyPS conformer matches reasonably well with the experimental spectrum, whereas the spectrum of ω-OH-1-deoxySA cannot be explained with one single conformer (Figure B2).

a. IR spectra and computed structures of dihydroxylated 1-deoxysphingolipids

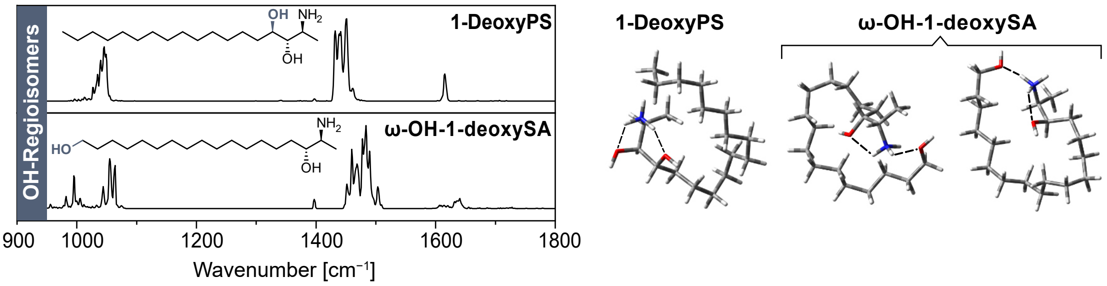

b. IR spectra and computed structures of 1- and 3-deoxysphingolipids

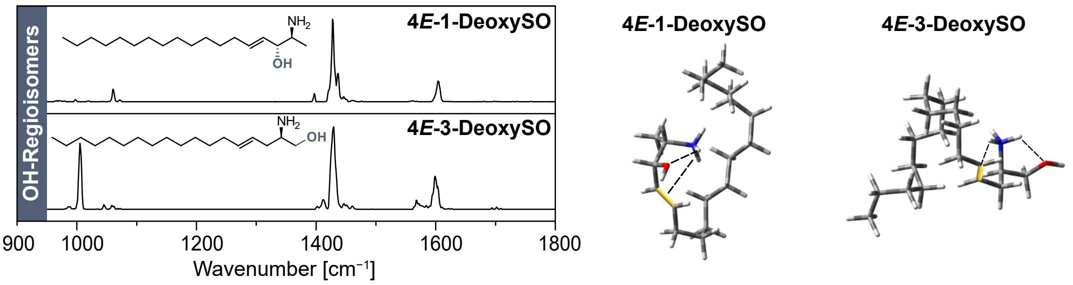

Figure 5.3: IR spectra and optimized structures of hydroxylation regioisomers. **a.** The IR spectra of the hydroxylation regioisomers 1-deoxyPS and ω-OH-1-deoxySA differ in the regions of scaffold vibrations and NH_3^+ umbrella vibrations. The computed low-energy structures show simultaneous coordination of the NH_3^+ group to both hydroxyl groups. Several conformers coexist in the case of ω-OH-1-deoxySA. **b.** The IR spectra of 4*E*-1-deoxySO and 4*E*-3-deoxySO are clearly distinguishable, although the hydroxyl group is shifted by only two carbons. The NH_3^+ group interacts with the hydroxyl oxygen and the C=C bond in both computed structures. The C=C bonds are highlighted in yellow.

A second pair of OH regioisomers with one varying hydroxyl group are 4*E*-1-deoxySO and 4*E*-3-deoxySO (Figure 5.3b). Interestingly, the region of NH_3^+ umbrella vibrations is almost identical, whereas scaffold vibrations and antisymmetric N—H bending frequencies render the isomers distinguishable. The computed conformers of 4*E*-1-deoxySO and 4*E*-3-deoxySO feature interactions of the NH_3^+ group with both the C=C bond and the hydroxyl oxygen. In view of the shift of the hydroxyl group by only two carbon atoms, similar intramolecular interaction patterns, and similar CCSs (Table B1), the ability to distinguish 4*E*-1-deoxySO and 4*E*-3-deoxySO by IR spectroscopy demonstrates the power of the technique and its sensitivity towards subtle structural changes. Gas-phase IR spectroscopy could thus help to identify hydroxylated intermediates formed during the 1-deoxysphingolipid catabolism.

In summary, we show here that all types of 1-deoxysphingolipid isomers, particularly double bond isomers, can be unambiguously resolved as protonated ions using cryogenic gas-phase IR spectroscopy. The results demonstrate the importance of the intramolecular coordination of NH_3^+ to electron-rich functional groups in the gas phase. These interactions enable indirect discrimination of double bond regio- and stereoisomers. Although the charge-olefin interactions are limited to sphingolipids, the concept can be extended to other lipids, for example, by adduct formation or wet-chemical derivatization of fatty acids with amine-functionalized conjugates, which are common strategies to enhance the ionization of neutral lipids.[383,390]

5.3.2 | Non-Covalent Double Bond Sensors for Fatty Acids

For the investigation of non-covalent FA adducts, a consistent set of four monounsaturated FAs (18:1) was selected: oleic acid (FA 18:1(9*Z*)), elaidic acid (FA 18:1(9*E*)), *cis*-vaccenic acid (FA 18:1(11*Z*)), and *trans*-vaccenic acid (FA 18:1(11*E*)). The most abundant isomer of 18:1 FAs in mammalian cells is FA 18:1(9*Z*), followed by FA 18:1(11*Z*).[4,175] The corresponding *trans* isomers FA 18:1(9*E*) and FA 18:1(11*E*) are not naturally synthesized by mammalian enzymes but taken up from various food sources: elaidic acid belongs to the main *trans* FAs formed during partial hydrogenation of oil in industrial food processing and is therefore elevated in margarine, fried goods, and bakery products.[391] *trans*-Vaccenic acid is naturally produced by bacterial fermentation in ruminants and therefore taken up with dairy products and meat.[391]

Five cations were selected for adduct formation with the monounsaturated FAs: sodium, pyridinium, trimethylammonium, dimethylammonium, and ammonium. The cations differ by the number of electrophilic hydrogen atoms (0–4), size, and shape (*cf.* Figure 5.1). Depending on the number of electrophilic hydrogens, the cation can either only interact with the carboxyl group or with both the carboxyl group and the C=C bond of the FA. The cation's size and shape should further influence the overall size and geometry of the corresponding non-covalent complex. In general, the efficiency of adduct formation during the nano-ESI process decreases with increasing size of the coordinating cation. The observation of pyridinium, tri-, and dimethylammonium adducts requires dissolution of the fatty acid in pure acetonitrile. In contrast, protic solvents such as methanol promote the formation of ammonium and alkali metal adducts. The adducts were studied by IR action spectroscopy and DT-IM-MS.

Sodium adducts $[FA+Na]^+$. Alkali metal adducts are usually the most abundant species generated during nano-ESI of FAs in positive ion mode. Accordingly, sodium adducts of 18:1 FAs are readily formed without the addition of sodium salts from methanolic solutions, and observed at *m/z* 305 in positive ion mode by MS. DT-IM-MS measurements yield almost identical CCSs of the $[FA+Na]^+$ ions with a difference of only 1.5 % between stereoisomers (Table B2). The *E* configuration yields more extended lipid chains and therefore slightly increased CCSs compared to the *Z* isomers. According to its small size, the impact of the sodium cation on the global size and shape of the adduct seems to be limited, and the observation of comparable CCSs is an indication of similar three-dimensional geometries of the isomeric adducts. The geometry of the [FA 18:1(11*Z*)+Na]$^+$ adduct was investigated as a representative example of sodiated FAs by conformational sampling and DFT optimization. All computed low-energy

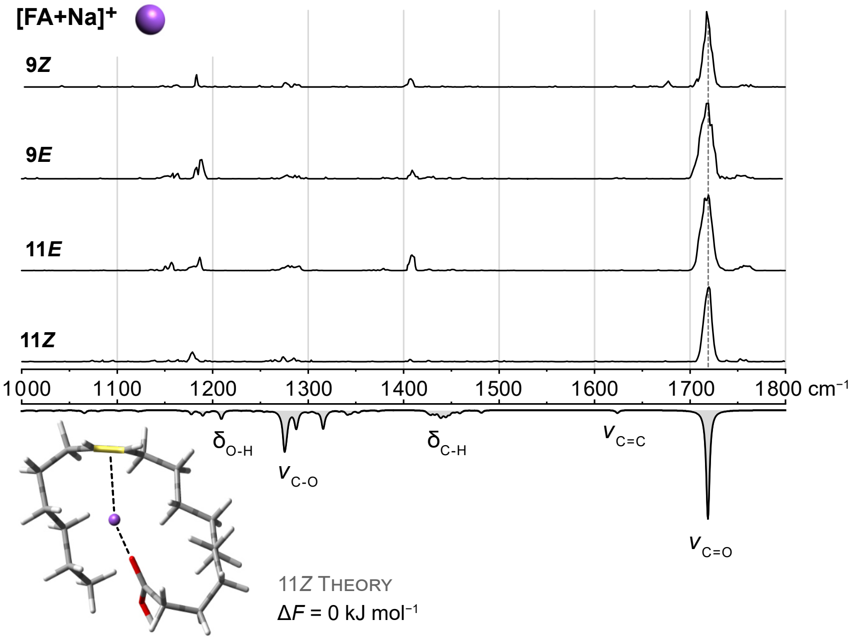

Figure 5.4: IR spectra of sodium adducts of FA 18:1 double bond isomers. Experimental spectra are stacked above the wavenumber scale and a computed spectrum of [FA 18:1(11*Z*)+Na]$^+$ is shown as inverted gray trace at the bottom. The frequency of the intense carbonyl stretching vibration is not influenced by the C=C bond position and configuration. The region between 1100 and 1300 cm^{-1} displays weak, non-diagnostic bands derived from coupled vibrations of the lipid chain. Selected vibrational modes are annotated in the computed IR spectrum of sodiated FA 18:1(11*Z*). Non-covalent interactions are depicted by dashed lines and the C=C bond is highlighted in yellow.

conformers display a common structural motif: the Na$^+$ cation coordinates both the carbonyl oxygen of the carboxyl group and the C=C bond. However, the expected and desired charge-olefin interaction does not lead to diagnostic vibrations (Figure 5.4). The predominant vibration in the IR spectra of the [FA 18:1+Na]$^+$ adducts is the intense carbonyl stretching vibration at the same frequency for all isomers. Other absorption bands derived from C−H bending vibrations of the hydrocarbon chain, O−H bending, and C−O stretching vibrations are comparably weak. The C=C stretching vibration is predicted between 1600 and 1650 cm^{-1} but not visible in the experimental spectra. In summary, the formation of sodium adducts does not lead to distinct geometries or distinguishable vibrational modes of C=C regio- and stereoisomers in monounsaturated FAs. Therefore, inspired by the previous study on sphingolipids, several amines were tested for adduct formation with the expectation that they would have a greater effect on the FA geometries.

Pyridinium [FA+pyr]$^+$ and trimethylammonium adducts [FA+NMe$_3$H]$^+$. Despite their significantly different shapes, pyridinium and trimethylammonium share two common characteristics: both cations contain a protonated tertiary amine and have a similar mass. [FA+pyr]$^+$

and $[FA+NMe_3H]^+$ adducts are observed upon nano-ESI of acetonitrile solutions at *m/z* 362 and 342, respectively. The single proton on the tertiary amines can interact with the carboxyl group or the C=C bond of the FA, but not with both simultaneously. Sampling of the conformational space confirmed unambiguously that both pyridinium and trimethylammonium interact exclusively with the carbonyl oxygen and not with the less nucleophilic C=C bond. However, both theory and the experimental IR spectra confirm that a small fraction of conformers displays an indirect hydrogen–C=C interaction. While the cation is coordinated to the carbonyl oxygen, the carboxyl proton interacts with the C=C bond (distance 2.1–2.5 Å). This interaction induces a significant red-shift of the carbonyl stretching frequency of 20–30 cm^{-1} that can be observed as an additional shoulder next to the dominant C=O band in the experimental spectra (Figures 5.5a and b). The pyridinium adducts of the 9*Z* and 11*Z* regioisomers display only a weak side band besides the main carbonyl vibration. The main vibration frequency is slightly shifted between the isomers, but otherwise the spectra are not distinguishable.

In the case of trimethylammonium adducts, a difference between conformer distributions can be observed. While the 9*Z* and 9*E* isomer only show a carbonyl stretching vibration at the expected frequency, the spectrum of the 11*Z* isomer also displays a pronounced, red-shifted side band attributed to the OH–C=C interaction as observed for pyridinium adducts. Compared to the spectra of sodiated FAs, the relative intensities of lipid chain vibrations are increased for both cations, but the N–H bending frequencies and vibrations in the lower wavenumber region are not diagnostic for C=C isomers. Also, the region below 1200 cm^{-1} is not well modeled by the employed level of theory. CCSs are identical for isomeric pyridinium or trimethylammonium adducts within the accuracy of the measurement (Table B2). The ATDs of the adducts are broad compared to the ATDs of sodium adducts, which agrees with the assumption that the dangling lipid chain has a large conformational freedom if there is only one point of interaction with the cation. In conclusion, the investigation of pyridinium and trimethylammonium adducts yielded interesting results that contradict the previous assumption that both cations only interact with the carbonyl oxygen and therefore cannot influence the overall conformation of the FA significantly. Instead, an interaction of the carboxyl OH with the C=C bond is observed, which gives rise to a characteristic red-shift of the C=O stretching vibration. In addition, the broad ATDs show that a multitude of conformers are present at room temperature.

Dimethylammonium adducts $[FA+NMe_2H_2]^+$. Advancing from trimethyl- to dimethylammonium increases the number of electrophilic hydrogen atoms that can possibly interact with the lipid chain by one. In principle, the cation should be able to interact with two nucleophilic groups at the same time. This assumption was confirmed by theoretical modeling, which yielded a simultaneous interaction of the cation with the C=C bond and carbonyl oxygen as the main and energetically most favorable structural motif. To confirm the computational predictions, IR spectra of $[FA+NMe_2H_2]^+$ adducts (*m/z* 328) were measured for all four isomers (Figure 5.5c).

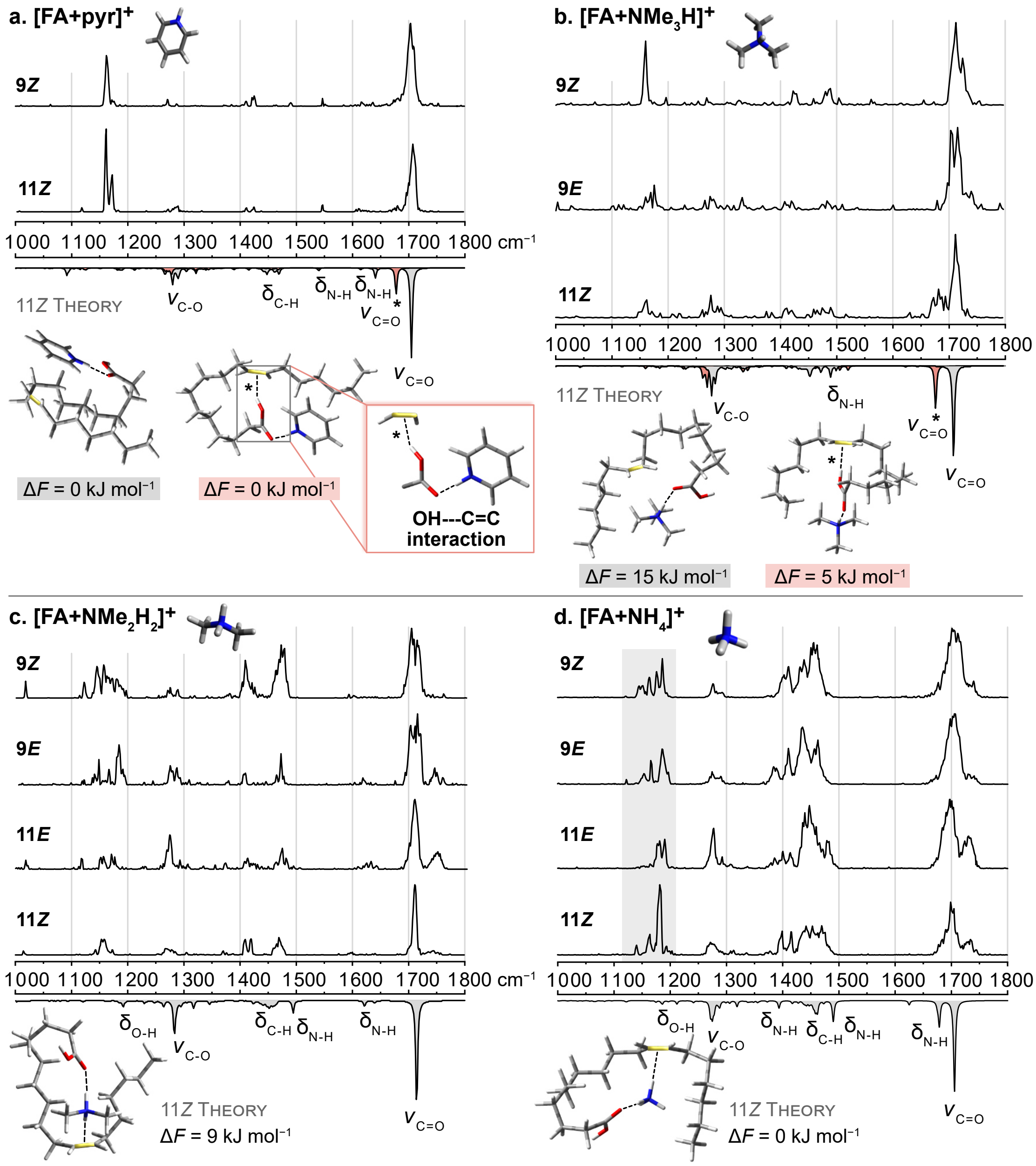

Figure 5.5: IR spectra of non-covalent adducts of FA 18:1 double bond isomers with ammonium derivatives. Experimental IR spectra are stacked above the wavenumber scale and a computed spectrum of the 11*Z* isomer (gray) is shown for each adduct. **a.** Pyridinium adducts $[FA+pyr]^+$ favor NH−O=C interactions. Red-shifted carbonyl bands suggest a carboxylic acid-C=C bond interaction in some conformers. **b.** For trimethylammonium adducts $[FA+NMe_3H]^+$, the red-shift is only observed for the 11*Z* isomer. **c.** Dimethylammonium adducts $[FA+NMe_2H_2]^+$ yield an increased wealth of absorption bands. Computed structures display mainly a bridged motif. **d.** The carbonyl stretching frequency of $[FA+NH_4]^+$ adducts is slightly shifted depending on the C=C position, and the isomers display distinct band patterns between 1100 and 1200 cm^{-1}. The computed conformers exhibit a bridged motif. Non-covalent interactions are depicted by dashed lines and the C=C bond is highlighted in yellow.

The wealth of spectral features clearly increases compared to the previous spectra. In particular, intense C−H and N−H bending vibrations are present between 1400 and 1500 cm^{-1}, and the fingerprint region below 1200 cm^{-1} exhibits distinct absorption patterns. The spectral region which is most apparently affected by the C=C location and configuration is the region of carbonyl stretching vibrations. The shape of the carbonyl band is different for the C=C positions 9 and 11. Moreover, in contrast to the *Z* isomers, the *E* isomers display a clearly blue-shifted side band adjacent to the main carbonyl band. Computational sampling of low-energy conformers does not lead to structures with such blue-shifts. Instead, these structures are probably derived from higher-energy conformers on the PES resulting from incomplete lipid folding. The difference between *E* and *Z* fits with the observation that some *E* isomers sampled by CREST are not completely folded into the bridged motif. It could be that *Z* isomers are more easily pre-folded due to the bend in the lipid chain, which facilitates wedging in the cation between the carbonyl oxygen and the C=C bond.

Differences between *E* and *Z* isomers were also confirmed by DT-IM-MS. The CCSs of *E* isomers are 2–4 % larger than those of *Z* isomers (Table B2). In addition, the regioisomers 9*Z* and 11*Z* show a CCS difference of 3 Å^2, which is in perfect agreement with theoretical predictions. Overall, dimethylammonium adducts of C=C isomers can be better distinguished by IR spectroscopy and IMS than trimethylammonium adducts. Regioisomers can be discriminated by the different shapes of the carbonyl band, whereas stereoisomers differ by the intensity of a blue-shifted side band and exhibit a significant CCS difference. However, the spectra and CCSs are too similar to allow an unambiguous identification of individual FAs in isomeric mixtures.

Ammonium adducts $[FA+NH_4]^+$. Ammonium adducts of C18:1 FAs (*m/z* 300) are readily formed from methanolic solutions containing ammonium acetate. The ammonium cation is considerably smaller than tri- and dimethylammonium, which leads to a significant reduction of the CCSs. Sampling of the conformational space yielded bridged motifs for all isomers, in which ammonium interacts with both the carbonyl oxygen and the C=C bond *via* two of the four available electrophilic hydrogens. Similar to $[FA+Na]^+$ adducts, the CCSs of $[FA+NH_4]^+$ adducts are identical between regioisomers but slightly different between stereoisomers: the CCSs of *E* isomers are roughly 2 % larger than the CCSs of *Z* isomers (Table B2). Overall, the CCSs are very similar because of the identical coordination geometry for all isomers.

In contrast to the sodium adducts, the IR spectra of the ammonium adducts show a multitude of vibrational modes (Figure 5.5d). The carbonyl stretching vibration is no longer the dominant vibration, but many other spectral features such as C−H and N−H bending vibrations are visible. The most diagnostic vibrations are located between 1100 and 1200 cm^{-1}. The absorption band patterns in that region enable the assignment of single isomers, but the band positions are not distinct enough to deconvolve IR spectra of isomeric mixtures. The carbonyl bands are very broad, indicating that multiple conformers contribute to the spectra. This is in agreement with the conformational flexibility and absence of bulky methyl groups in the ammonium adducts. The C=O stretching frequency is slightly shifted between position 9 and 11. Computed spectra for all four isomers are exemplarily shown in Figure B3.

As previously observed for dimethylammonium adducts, the isomers exhibit a blue-shifted band adjacent to the main carbonyl band with varying intensity. Its origin was exemplarily explored for the [FA 18:1(11*E*)+NH_4]$^+$ adduct because the band is most intense in the corresponding experimental spectrum. As all conformers generated by CREST exhibit the same interaction motif and their C=O stretching frequencies coincide with the main experimental absorption band, other conformers were generated on an empirical basis to test the influence of different interaction motifs on the carbonyl band (Figure B4). If the ammonium cation interacts only with the carbonyl oxygen, the carbonyl band is red-shifted, and even more so if the OH group simultaneously interacts with the C=C bond, as observed for trimethylammonium and pyridinium adducts. Blue-shifted carbonyl bands above $1800\,\mathrm{cm}^{-1}$ are obtained if the ammonium cation donates electron density into the C=O bond by interacting with the OH group. The experimentally observed, less drastic blue-shift coincides with a conformer in which the ammonium cation interacts with the C=C bond but not with the carboxyl group. However, all empirically generated conformers are significantly higher in energy than the dominant bridged structural motif. Accordingly, no conformer with a blue-shifted carbonyl stretching vibration was found for any kind of FA adduct during the automated conformer sampling.

One explanation for the experimental observation of energetically unfavored conformers can be kinetic trapping of conformers in which the lipid chains are not yet ideally folded. Kinetically trapped conformers cannot reach the global minimum of the PES due to insufficient internal energy to overcome energetic barriers after cooling in the ion trap. This effect is most noticeable for *trans*-vaccenic acid. In the spectra of dimethylammonium, ammonium, and even sodium adducts, blue-shifted side bands next to the main C=O stretching vibration are clearly visible for this isomer. One possible explanation is that the lipid chains of *E* isomers are not pre-folded as the hydrocarbon chains of *Z* isomers, which are already naturally bent. In addition, the distance between the carbonyl oxygen and C=C bond, which must approach each other to form bridged structures, is larger than in oleic and elaidic acid. The relative intensity of the blue-shifted band thus depends on both C=C bond location and configuration, and consequently facilitates discrimination of C=C isomers.

In summary, the impact of non-covalent adduct formation with several cations on the gas-phase structures of isomeric monounsaturated FAs was examined in this study. The results demonstrate that coordinating cations induce specific three-dimensional conformations of the lipid chains. Those conformational differences result in distinct vibrational modes observable by IR spectroscopy and different overall shapes translating into different CCSs. The geometry of the non-covalent complex depends on the nature of the cation, particularly on the number of available protons that interact with the carboxyl group and the C=C bond *via* intermolecular charge-olefin interactions. Interestingly, the N−H bending vibrations of interacting amines are not diagnostic for double bond isomers, in contrast to the results observed for sphingolipids. However, the position and geometry of the C=C bond can influence the carbonyl stretching vibrations. The observed spectral differences include red-shifted carbonyl bands in $[FA+NMe_3H]^+$ adducts due to distinct structural motifs in low-energy conformers, different shapes and blue-shifts of the carbonyl bands in $[FA+NMe_2H_2]^+$ complexes, and frequency shifts of the C=O stretching vibration in $[FA+NH_4]^+$ adducts depending on the C=C bond location. Overall, the spectral wealth and thus the information content increases from sodium adducts, which show no characteristic absorptions, to ammonium adducts that yield spectroscopic fingerprints with distinguishable band patterns for each C=C bond position and geometry. However, the IR spectra are not sufficiently different to identify individual isomers in isomeric mixtures from biological sources. Therefore, further studies are needed to improve the discrimination of isomeric FAs by gas-phase IR spectroscopy.

5.3.3 | Covalent Double Bond Sensors for Fatty Acids

For the investigation of covalently modified FAs, a set of FA 18:1 double bond regio- and stereoisomers (6*Z*, 6*E*, 8*Z*, 9*Z*, 9*E*, 11*Z*, and 11*E*) along with a FA 18:0 reference sample were derivatized with 3-pyridinemethanol. FA 18:1(8*Z*), FA 18:1(9*Z*), FA 18:1(9*E*), FA 18:1(11*Z*), and FA 18:1(11*E*) were additionally derivatized with 3-aminomethylpyridine. The resulting FA 18:1 3-pyridylcarbinol esters and 3-picolylamides serve to enhance ionization in positive ion mode *via* protonation of the pyridyl-nitrogen, and were investigated here as potential double bond sensors for gas-phase IR spectroscopy.

3-Pyridylcarbinol esters and 3-picolylamides. Covalent modification of FAs with pyridinium derivatives is expected to impose more rigid constraints on the conformation of the lipid chain than non-covalent modification with pyridinium cations discussed in the previous section. Reducing the number of conformers should result in a reduced band width and number of absorption bands, which could improve the discrimination of double bond isomers. Indeed, derivatization of FAs with 3-pyridinemethanol enables a much clearer distinction between FA 18:1 isomers by gas-phase IR spectroscopy in the 1000–1800 cm^{-1} region than observed for non-covalent complexes (Figure 5.6a). In particular, the fingerprint region (1050–1250 cm^{-1}) offers unique absorption patterns for each isomer. In addition, the C=O stretching frequency of the ester is shifted depending on the C=C bond position and configuration.

Computation of gas-phase structures using DFT at the PBE0+D3/6-311+G(d,p) level of theory reveals charge-olefin interactions between the protonated 3-pyridylcarbinol moiety and the C=C bond, as previously observed for sphingolipids and cationic FA complexes. For comparison, an IR spectrum of the FA 18:0 3-pyridylcarbinol ester was recorded, in which the absence of

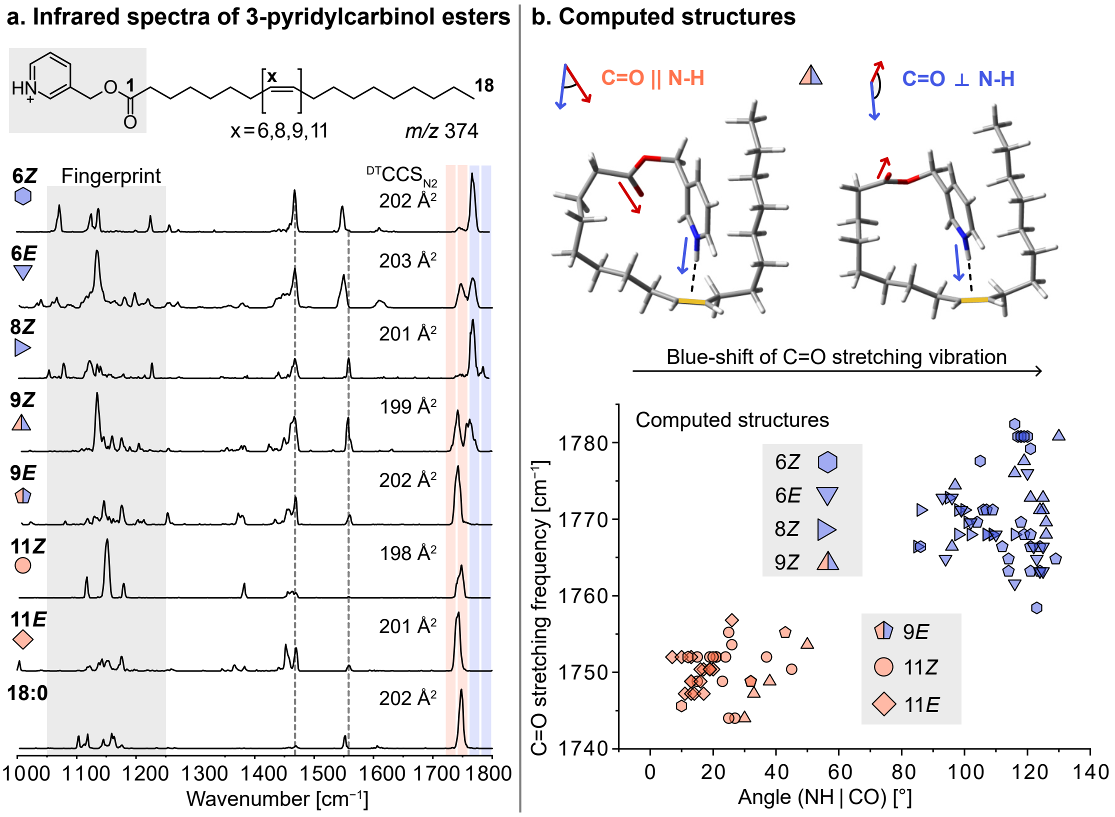

Figure 5.6: Gas-phase IR spectra, collision cross sections ($^{DT}CCS_{N2}$), and structures of FA 18:1 double bond isomers derivatized with 3-pyridinemethanol. **a.** The position and configuration of the C=C bond influence the frequency of the carbonyl stretching vibration and the diagnostic fingerprint region (1050–1250 cm^{-1}). **b.** The predicted carbonyl stretching frequency correlates with the relative orientation of the C=O and the N−H bonds, as shown for two computed conformers of the FA 18:1(9*Z*) 3-pyridylcarbinol ester with the C=C bond highlighted in yellow. Large angles (> 80°) in the computed structures induce a blue-shift of the predicted carbonyl stretching frequency, which is indicated by blue filling of the respective symbol. Mixed-color symbols show that a splitting of the C=O band is predicted.

charge-olefin interactions translates into a reduced signal intensity in the N-H bending region between 1350–1500 cm^{-1} (Figure 5.6a, bottom). Upon further investigation of the computed conformers featuring charge-olefin interactions, a correlation was found between the C=O stretching frequency and the angle between the N−H and the C=O vectors (Figure 5.6b). If the two vectors have cosine similarity (< 60°), C=O stretching frequencies below 1760 cm^{-1} are predicted, whereas computed structures with angles larger than 80° display a significant blue-shift of the carbonyl stretching vibration. The predicted frequencies match remarkably well with the experimental spectra. The only exceptions are FA 18:1(6*E*) and FA 18:1(9*E*) 3-pyridylcarbinol esters, which are predicted to yield a single blue-shifted and a split C=O band, respectively, which is clearly not reflected in the experiment. Computed conformers and spectra are exemplarily shown for the FA 18:1(9*Z*) 3-pyridylcarbinol in Figure B5.

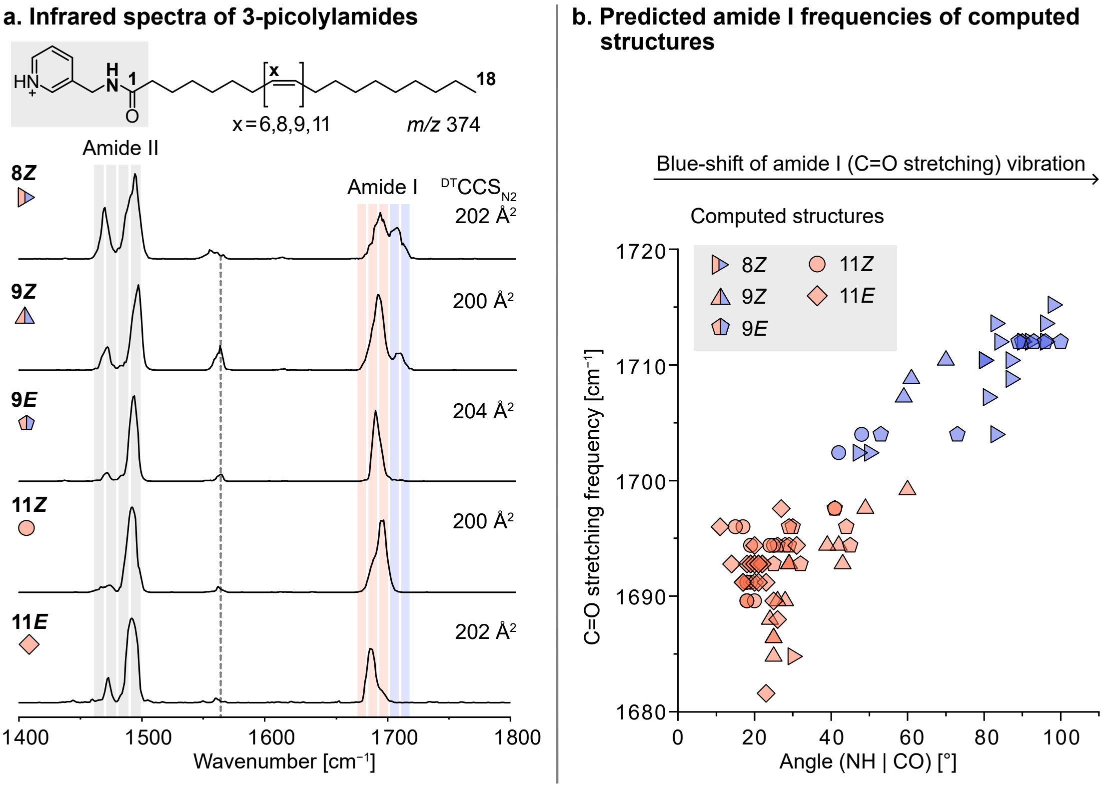

a. Infrared spectra of 3-picolylamides

b. Predicted amide I frequencies of computed structures

Figure 5.7: Gas-phase IR spectra, collision cross sections ($^{\text{DT}}\text{CCS}_{\text{N2}}$), and computed structures of protonated FA 18:1 double bond isomers derivatized with 3-aminomethylpyridine. **a.** The frequencies and relative intensities of the amide vibrations are influenced by the double bond position and configuration. **b.** The conformational search yields two groups of conformers based on the relative orientation of the C=O and the pyridinium N—H bonds and the resulting predicted amide I frequency. Red-shifted amide I vibrations are predicted for isomers marked by orange symbols. Mixed-color symbols show that a split C=O band is predicted based on the IR spectra of computed conformers.

As charge-olefin interactions determine the conformation of 3-pyridylcarbinol esters in the gas phase, they also influence the ion mobility of double bond isomers. The CCSs determined by DT-IM-MS increase with decreasing distance of the C=C bond from the charge group and are larger for *E* than for *Z* isomers, in agreement with previous reports.[108] The CCSs of the computed structures are consistently underestimated, but their trends are in general agreement with the measured values (Table B3). However, the CCS differences are too small to enable the analysis of isomeric mixtures by DT-IM-MS. On the contrary, IR spectroscopy yields sufficiently diagnostic absorption bands for each regio- and stereoisomer to enable mixture analysis.

3-Picolylamides were investigated as an alternative modification strategy for unsaturated FAs. The gas-phase IR spectra of FA 18:1 isomers modified with 3-aminomethylpyridine feature no absorption bands except for the N—H bending (amide II) and C=O stretching (amide I) vibrations (Figure 5.7a). The lack of absorption bands below 1400 cm^{-1} is in agreement with computed IR spectra, which predict only modes of very low intensity in that region (Figure B6).

Compared with the spectra of 3-pyridylcarbinol esters, the spectra of 3-picolylamides thus carry less structural information, as they are restricted to the amide vibrations. Interestingly, the amide vibrations are affected in a similar way as the C=O stretching frequency of the 3-pyridylcarbinol esters. The IR spectrum of FA 18:1(8*Z*) 3-picolylamide features a strong blue-shifted amide I band, which is less intense in the spectrum of the 9*Z* isomer and absent in the spectra of the other isomers. The computed structures show a similar relationship between the C=O stretching frequency and the angle between the N−H bond of protonated pyridine and the C=O bond of the amide as previously observed for the ester derivatives (Figure 5.7b). The shifts are well predicted by theory, except for the 9*E* isomer, which should feature a split C=O band according to the computations. Because 3-picolylamides are largely outperformed by 3-pyridylcarbinol esters in terms of isomer distinction, they are not further considered in the following.

Deconvolution of isomeric mixtures. In order to benchmark the ability to analyze isomeric mixtures of FAs by IR spectroscopy, synthetic binary and ternary mixtures of FA 18:1(8*Z*), FA 18:1(9*Z*), and FA 18:1(11*Z*) 3-pyridylcarbinol esters were prepared. FA 18:1(9*Z*) and (11*Z*) are the two most abundant isomers in mammalian cells, whereas the 8*Z* isomer has only recently been discovered in cancer cells.[7] IR spectra of isomeric mixtures were recorded in the fingerprint region and C=O stretching region, and were deconvolved by linear regression using the three reference spectra (Figure 5.8). As all isomers are modified with the same charge carrier, ionization efficiencies are expected to be comparable, and the isomer distribution in the gas phase should hence reflect the distribution in solution. Previous reports from other compound classes have revealed that relative isomer abundances of 3–5 % can be determined in isomeric mixtures,[322,357] while the present work demonstrates measured isomeric ratios to be within ± 8 % of the known FA isomer composition. This value is not universal, but varies with the length of the probed wavenumber range and the similarity of the component spectra in that range. Overall, the results demonstrate that linear regression of composite IR spectra enables identification and accurate relative quantification of double bond isomers in mixtures. In the case of the synthetic binary and ternary mixtures, a spectral range of only 300 $\mathrm{cm^{-1}}$ is sufficient for isomer identification and relative quantification.

After the successful validation of the linear regression approach for synthetic mixtures of biologically relevant isomers, the derivatization procedure was optimized for biological lipid extracts to eliminate isobaric impurities. The technique was tested on a commercially available reference mixture (Restek 35077 Food Industry FAME mix), which contains FA 18:1(9*Z*) and (9*E*) isomers. The IR spectrum of the FA 18:1 mixture after derivatization is shown in Figure 5.9a. Linear regression yielded a ratio of approximately 3:1 9*Z*:9*E*. As a control experiment, ultra-high performance liquid chromatography-ozone-induced dissociation-mass spectrometry was used to determine isomer ratios by integration of the chromatogram (Figure 5.9b). Both

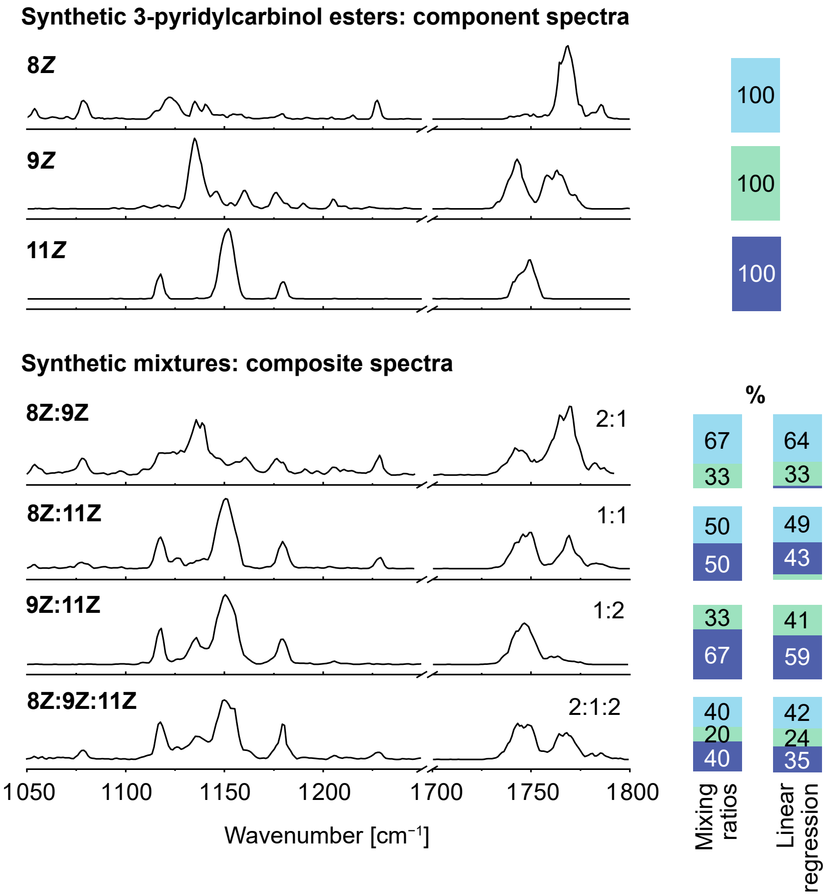

Figure 5.8: Gas-phase IR spectra of synthetic FA 18:1(8*Z*), (9*Z*), and (11*Z*) 3-pyridylcarbinol ester standards and synthetic binary and ternary mixtures of known composition. Linear regression of the IR spectra obtained from synthetic mixtures in the fingerprint and carbonyl stretching regions yields values close to the expected isomer contributions.

techniques yield similar isomer ratios (Figure 5.9c). Subsequently, hydrolyzed lipid extracts from two human cancer cell lines, LNCaP (treated with TOFA, a dual inhibitor of stearoyl-CoA desaturase 1 and acetyl-CoA carboxylase 1) and PC-3, were derivatized with 3-pyridinemethanol and measured by IR spectroscopy. Linear combination of the component spectra of FA 18:1(6*Z*), (8*Z*), (9*Z*), and (11*Z*) using the isomer ratios determined by linear regression (gray trace) shows a reasonable agreement between the predicted and the experimental spectra. UPLC-OzID-MS yields comparable ratios of isomers. Both methods provide evidence for significant differences between the two cancer cell lines. Most importantly, the presence of FA 18:1(6*Z*)—previously reported in PC-3 cells[8]—was confirmed by two entirely orthogonal approaches with IR action spectroscopy enabling explicit determination of the C=C bond geometry. In the IR spectrum of PC-3, the red-shifted peak at 1550 $\mathrm{cm^{-1}}$ is diagnostic for position 6 (*cf.* Figure 5.6a), and the *Z* configuration was verified by linear regression, yielding a contribution of 0 % from the

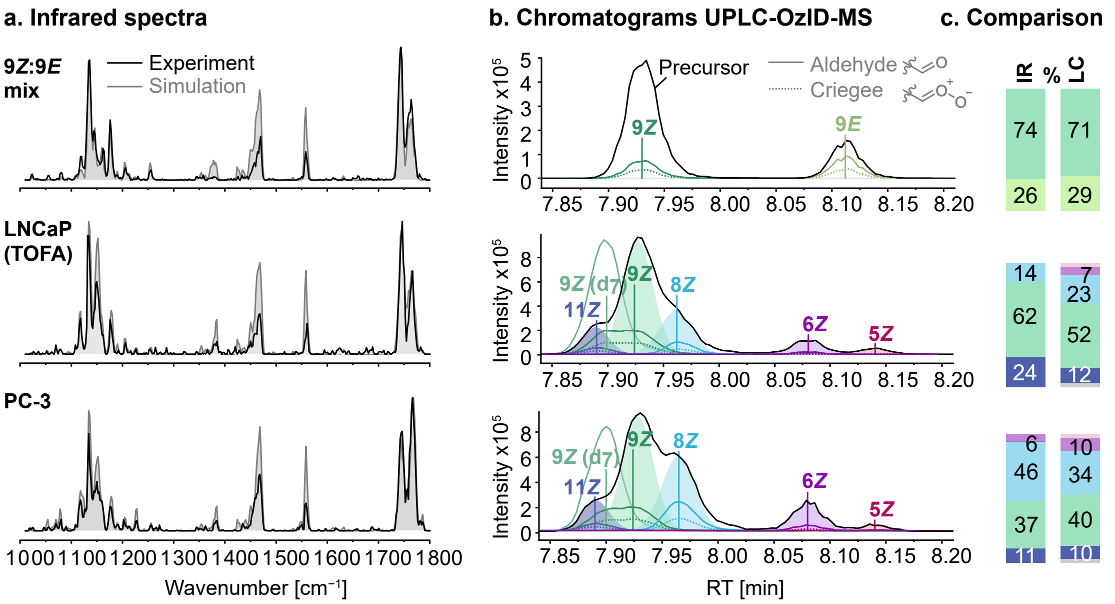

Figure 5.9: Gas-phase IR spectra and chromatograms of FA 18:1 derivatized with 3-pyridinemethanol from a synthetic standard mix (37 mix Restek) and two lipid extracts from cancer cell lines, LNCaP (TOFA) and PC-3. **a.** IR spectra were deconvolved by linear regression using reference spectra. **b.** Relative quantification of isomers by ultra-high performance liquid chromatography-ozone-induced dissociation-mass spectrometry was performed by summing the integrals of OzID product chromatograms (aldehyde and Criegee; colored and dotted lines) and the associated deconvolved precursor chromatogram (shaded Gaussian peak area) for each isomer. Heptadeuterated oleic acid (9*Z*-d7) is derived from the SPLASH Lipid-o-mix analytical standard that was added to the cancer cell samples prior to lipid extraction. **c.** Deconvolution of IR spectra and UPLC-OzID-MS yield similar isomer ratios.

6*E* standard. Furthermore, a significant amount of the 8*Z* isomer was found in the PC-3 lipid extract, in accordance with previous findings.[380] The increased amount of FA 18:1(8*Z*) in PC-3 cells can be seen in the increased intensity of the blue-shifted C=O band. The analysis of two hydrolyzed lipid extracts of biological origin showcases the power of gas-phase IR spectroscopy for the analysis of isomeric mixtures, even in the most complex matrices.

In conclusion, the modification of FAs with 3-pyridinemethanol constitutes an innovative approach to determine the C=C bond position and geometry in monounsaturated FAs by gas-phase IR spectroscopy. 3-Pyridylcarbinol esters serve as double bond sensors that engage in charge-olefin interactions with the C=C bonds. The technique was employed to detect altered isomer ratios in cancer cells by deconvolution of mixture spectra and confirm the C=C bond geometry in FA 18:1(Δ6) from PC-3 cancer cells as being *cis*. Gas-phase IR spectroscopy enables sensitive and explicit assignment of the position and configuration of C=C bonds for individual unsaturated FAs in the presence of multiple isomeric variants. Such detailed structure elucidation of *m/z*-selected lipids is a powerful and complementary approach to LC-MS to empower lipid discovery and reveal otherwise-invisible changes in the lipidome in response to disease states.

5.4 | Conclusions

The present studies demonstrate that IR action spectroscopy is capable of determining the position and stereochemistry of C=C bonds in unsaturated fatty acids and deoxysphingolipids. While the stretching vibrations of C=C bonds are inherently weak and uninformative, structural information can be gained by exploiting intrinsic or extrinsic double bond sensors. The double bond sensors developed here for the structural analysis of unsaturated fatty acids are protonated amines that engage in a charge-olefin interaction with the C=C bond and thereby constrain the gas-phase conformation of the lipid chain in an isomer-specific manner. These conformational differences lead to distinct N−H bending frequencies in natural 1-deoxysphingolipids and shifts in the C=O stretching vibration and other low-frequency vibrations of modified fatty acids.

The non-covalent attachment of pyridinium and ammonium derivatives does not lead to sufficiently strong differences in the IR spectra of isomeric FAs, probably because of the large conformational flexibility of the bimolecular complexes. On the contrary, the covalent modification of FAs with 3-pyridinemethanol yields diagnostic spectroscopic fingerprints that enable deconvolution of isomeric mixtures by linear regression. An obvious drawback of the strategy is that only those isomers can be analyzed for which reference spectra have been recorded. Moreover, the technique has only been tested for monounsaturated FAs, and the gas-phase structures of polyunsaturated FA 3-pyridylcarbinol esters remain to be investigated. However, a major strength of IR action spectroscopy is that it not only distinguishes between different C=C bond positions, but also determines the double bond geometry, which is not achieved by most MS-based techniques (*cf.* Section 2.2). Furthermore, the harmonic frequency calculations predict isomer-dependent frequency shifts of the N−H and O−H stretching vibrations located above 2500 cm^{-1}, which would make the modification strategy amenable to tagging photodissociation IR spectroscopy using less powerful benchtop lasers in the 3 μm range.

Recently, similar approaches have been reported using derivatization strategies to influence the conformation of lipids and discriminate between isomers. For example, the non-covalent complexation of isomeric lipids with aromatic amino acids was found to affect the lipid conformation such that distinguishable gas-phase UV spectra were obtained for several kinds of isomers.[233] Furthermore, non-covalent modification of short-chain fatty acids with metal cations and crown ethers allowed to separate double bond regioisomers by IMS.[161] The derivatization of FAs with charge tags has a long history and has been used in particular to distinguish double bond isomers by charge-remote fragmentation.[232] Overall, lipid modification strategies have great potential to aid in the discrimination of isomeric lipids. As shown in this and other works, manipulating the three-dimensional gas-phase structures of lipids can greatly increase the information gain by structure-sensitive techniques such as action spectroscopy and IMS.

6 Investigating Lipid Fragmentation Mechanisms

Tandem mass spectrometry is the principal analytical technique for the structural elucidation of lipids and other metabolites. However, the interpretation of fragment spectra is often hampered by poor understanding of the underlying fragmentation mechanisms that occur in the black box of the mass spectrometer. In this chapter, infrared action spectroscopy is used in tandem with quantum chemistry to elucidate the structures of lipid fragments and thus gain insights into lipid fragmentation mechanisms. The investigation of phospholipid headgroup loss, the most important fragmentation reaction for lipid class assignment, confirms the long-standing hypothesis of an *sn*-specific mechanism leading to dioxolane fragments. Subsequently, it is shown that this knowledge helps to rationalize isomer-dependent intensity differences in the fragment spectra of silver-adducted phospholipids. In the final part, the fragmentation of vitamin E derivatives is investigated, demonstrating that high-resolution infrared spectroscopy can reveal unknown fragmentation mechanisms and unexpected fragment structures without the need for reference substances. Overall, this chapter expands the scope of infrared action spectroscopy from an analytical technique for structural analysis to a functional tool for understanding fragmentation mechanisms that form the basis of contemporary lipidomics.

This chapter is based on the following references:

[392] C. Kirschbaum *et al.*, Unveiling Glycerolipid Fragmentation by Cryogenic Infrared Spectroscopy, *J. Am. Chem. Soc.* **2021**, *143*, 14827–14834.

[393] C. Kirschbaum *et al.*, Cryogenic Infrared Spectroscopy Provides Mechanistic Insight into the Fragmentation of Phospholipid Silver Adducts, *Anal. Bioanal. Chem.* **2022**, *414*, 5275-5285.
Part of the topical collection *Promising Early-Career (Bio)Analytical Researchers.*

Early version of C. Kirschbaum, K. Greis, A. Y. Torres-Boy, J. Riedel, S. Gewinner, W. Schöllkopf, G. Meijer, G. von Helden, K. Pagel, Studying the Intrinsic Reactivity of Chromanes by Gas-Phase Infrared Spectroscopy, *in preparation.*

6.1 | Introduction

Tandem mass spectrometry is the dominating technology in lipidomics and metabolomics.[12] However, structural analysis is frequently thwarted by unexpected rearrangement reactions including the migration of atom groups[394,395] or intramolecular cyclization[396] upon ion activation in the mass spectrometer. Gaining fundamental understanding of fragmentation reactions can help to interpret tandem mass spectra, improve the rule-based prediction of fragmentation patterns,[397,398] and validate quantum chemical or machine learning-based methods that predict fragment spectra *in silico*.[399–401] In the field of proteomics, gas-phase IR spectroscopy has been successfully applied to determine peptide fragment structures and thereby establish pivotal dissociation mechanisms,[402,403] whereas lipid fragmentation mechanisms are still largely unknown. A few lipid and metabolite fragments have been studied using IRMPD spectroscopy, demonstrating that fragment structures can be assigned in a reference-free approach based on computed IR spectra of candidate structures.[404–407] However, the resolution of IRMPD spectra proved to be insufficient in several cases.[404,407] Cryogenic spectroscopic methods can drastically improve the resolution and increase the confidence in structural assignment.[24]

One of the most important fragmentation reactions for the structural analysis of phospholipids is the loss of the phosphate-containing headgroup in positive ion mode.[98] For example, protonated and alkali metal-adducted phosphatidylethanolamines yield abundant fragments resulting from neutral headgroup loss (141 Da) (Figure 6.1a). On the contrary, collision-induced dissociation of protonated phosphatidylcholines results in a single phosphocholine fragment at *m/z* 184 because of the permanent positive charge on the quaternary amine (Figure 6.1b). Fragmentation of alkali metal-adducted PC yields $[PC+M-59]^+$ ions resulting from the neutral loss of trimethylamine. At higher collision energies, $[PC+H/M-183]^+$ ions are generated that exhibit identical *m/z* as the corresponding $[PE+H/M-141]^+$ ions.[98]

The headgroup loss from glycerophospholipids has been thought to occur *via* a beta-elimination involving a glycerol hydrogen at the *sn*-2 carbon, which is eliminated together with the headgroup.[408,409] The resulting fragment features a C=C bond between the *sn*-2 and *sn*-3 carbons of the glycerol backbone. In 2003, Hsu and Turk proposed an alternative fragmentation mechanism that involves the transfer of an alpha-hydrogen from one fatty acyl to the leaving headgroup, leading to intramolecular cyclization (Figure 6.1c).[410] The resulting ring is either a six-membered 1,3-dioxane if the fatty acyl at the *sn*-1 position participates, or a five-membered 1,3-dioxolane in the case of *sn*-2 acyl participation. The crucial role of alpha-hydrogens was later confirmed,[212] and experimental evidence from OzID,[211] Paternò-Büchi reaction,[6] UVPD,[130] and CID[202] supported the formation of dioxolanes from alkali metal-adducted glycerophospholipids. Spectroscopic investigations of phospholipid precursor ions explained the preferred formation of dioxolanes by strong interactions between the *sn*-1 ester and the cation, promoting intramolecular cyclization of the less strongly bound *sn*-2 ester.[407]

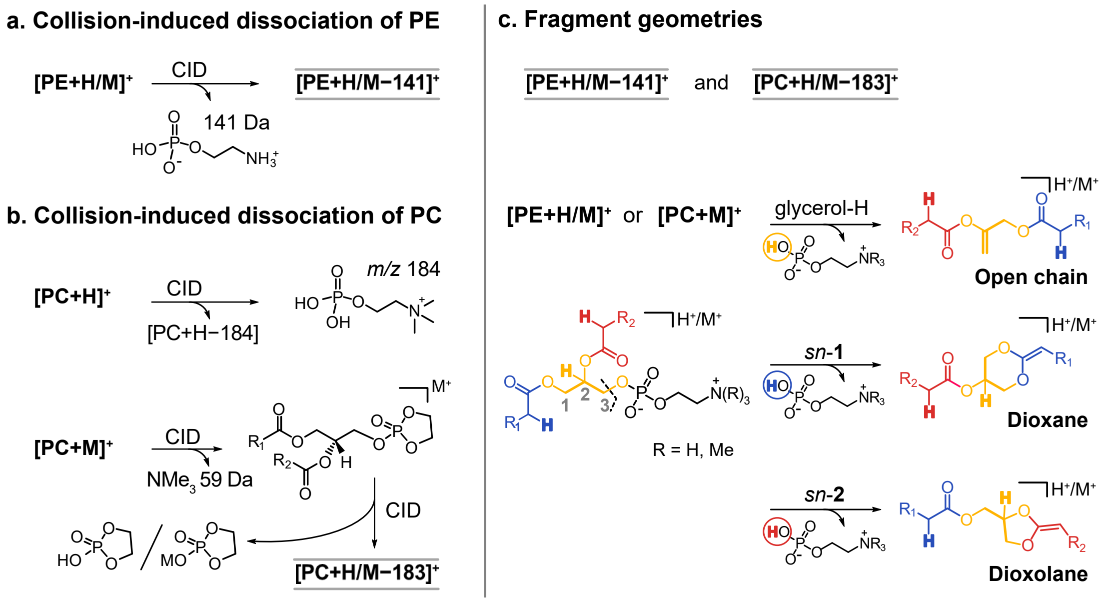

Figure 6.1: Collision-induced dissociation of glycerophospholipids in positive ion mode. **a.** CID of protonated and alkali metal-adducted PE induces neutral loss of phosphoethanolamine. **b.** Protonated PC generates phosphocholine fragments, whereas alkali metal adducts yield fragments analogous to PE. **c.** Proposed fragment structures resulting from neutral headgroup loss from PE and PC. Participation of the glycerol hydrogens leads to a beta-elimination resulting in an open chain fragment. Participation of the alpha-hydrogens at *sn*-1 or *sn*-2 yields six-membered dioxane or five-membered dioxolane rings, respectively. The glycerol backbone (yellow) and fatty acids (red and blue) are colored for visual clarity.

In the cyclic dioxane and dioxolane structures, the fatty acyls occupy different chemical positions, either being part of the ring or next to the ring. Using silver instead of alkali metal cations, further fragmentation of these primary fragments leads to inverse ratios of ketene and acid fragments in the MS/MS/MS (MS^3) spectra of *sn*-isomers.[156,159] Historically, silver ions have played an important role in lipid analysis and separation because the Ag^+ ions bind not only lone pairs of heteroatoms but also pi-bonds.[341,342] Cation-pi interactions also exist in the gas phase and allow the separation of glycerophospholipid *sn*-[159] and double bond isomers[208] by IMS. However, the intensity differences of acid and ketene fragments observed in the MS^3 spectra of silver-adducted *sn*-isomers have never been rationalized.

Here, we fill two gaps in the understanding of glycerolipid and glycerophospholipid fragmentation in the positive ion mode. First, the structure of protonated fragments resulting from neutral headgroup loss, which cannot be studied by any of the techniques that were used to unveil the structure of metal-adducted fragments, was identified by IR action spectroscopy. The results provide direct and conclusive evidence that the protonated fragments contain dioxolane rings, in which the positive charge is stabilized between the two ring oxygens. The results further confirm that the intermediate fragment resulting from neutral loss of trimethylamine from PC contains indeed a cyclic phosphate. Moreover, the influence of silver adduction on

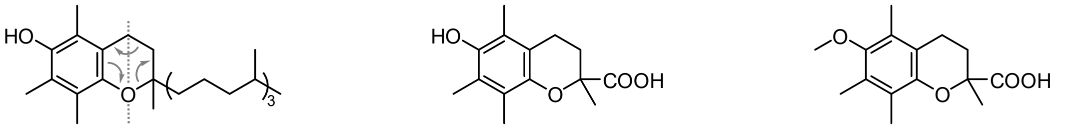

α-Tocopherol (vitamin E)
+/− Retro-Diels-Alder reaction

Trolox
+/− Decarboxylation

Methyltrolox
+ Decarboxylation
− Radical fragmentation

Figure 6.2: Structures and collision-induced dissociation reactions of α-tocopherol (vitamin E), Trolox, and Methyltrolox in positive (+) and negative (−) ion mode. The retro-Diels-Alder reaction is exemplarily sketched for vitamin E. The fragmentation reactions of Trolox and Methyltrolox are studied here.

phospholipid fragmentation was investigated. The gas-phase structures of dioxolane fragments derived from silver-adducted phospholipids were found to depend on the nature of the lipid chains and the resulting coordination geometry of silver. Based on the results, the ratios of acid and ketene fragments previously noted in the MS^3 spectra of phospholipid isomers can be explained qualitatively.

In addition to glycerol-based lipids, the fragmentation mechanisms of two chromane-derived antioxidants, Trolox and Methyltrolox, are investigated to demonstrate that IR spectroscopy can help to elucidate entirely unknown fragmentation mechanisms. As a water-soluble analog of vitamin E, Trolox is routinely employed in Trolox Equivalent Antioxidant Capacity assays as a reference standard for quantification of the antioxidant capacity of other substances.[411] α-Tocopherol (vitamin E), Trolox, and Methyltrolox share one common fragmentation pathway, which is the mechanistically well-understood retro-Diels-Alder reaction resulting in cleavage of the dihydropyrane ring (Figure 6.2).[412] Although Trolox and Methyltrolox are based on the same chromane scaffold as vitamin E, alternative fragmentation routes dominate their fragment spectra.[413,414] Due to the presence of a carboxylic acid, protonated Trolox and Methyltrolox show abundant decarboxylation upon collisional activation in positive ion mode. In negative ion mode, Trolox decarboxylates, whereas Methyltrolox yields a series of radical fragments through the loss of methyl radicals and CO_2, which is intriguing and not well understood from a mechanistic perspective.

Here, we investigate the collision-induced dissociation of Trolox and Methyltrolox in positive and negative ion polarities to shed light on unknown fragmentation mechanisms of small metabolites. We show that fragment structures can be unambiguously assigned without reference standards by matching the high-resolution gas-phase IR spectra with computed IR spectra of candidate structures. Based on the confirmed fragment structures, fragmentation pathways are proposed that include unexpected intramolecular rearrangement reactions. We show that high-resolution cryogenic IR spectroscopy and computational chemistry form a powerful couple to gain mechanistic insights and a fundamental understanding of the fragmentation of lipids and other small organic molecules.

6.2 | Experimental Details

Sample preparation. PE (6:0/6:0), PE (16:0/18:1(9*Z*)), PE (d31-16:0/18:1(9*Z*)), PE (18:1(9*Z*)/16:0), PC (16:0/18:1(9*Z*)), PC (18:1(9*Z*)/18:1(9*Z*)), PC (18:1(6*Z*)/18:1(6*Z*)), and 1,2-DAG (16:0/18:1(9*Z*)) were purchased from Avanti Polar Lipids (Alabaster, USA). 1,2-DAG (18:1(9*Z*)/18:1(9*Z*)) and 1,3-DAG (18:1(9*Z*)/18:1(9*Z*)), methanol, sodium acetate, and silver hexafluorophosphate were obtained from Sigma-Aldrich (Taufkirchen, Germany). Stock solutions (10–100 mM) of phospholipids were prepared in methanol and diluted to 100 µM for measurements. DAG solutions were freshly prepared before each measurement. Silver adducts were formed from 100 µM solutions of phospholipids in methanol containing 1.7 mM Ag[PF_6].

The dehydroxyl DAG derivatives 1,2-propylene glycol dioleate and 1,3-propylene glycol dioleate were synthesized according to published protocols.[415,416] All reagents were purchased from Sigma-Aldrich, and the reaction was carried out under nitrogen atmosphere. 1,2- or 1,3-propylene glycol (0.25 mmol) was dissolved in dry dichloromethane (20 mL). *N,N'*-Dicyclohexylcarbodiimide (0.6 mmol) and 4-dimethylaminopyridine (0.05 mmol) were added under nitrogen flow at 0 °C. Oleic acid (0.55 mmol) in dry dichloromethane (2 mL) was added in excess, and the mixture was stirred at 0 °C for 5 min and then for 3 h at room temperature. The solution was washed with 0.5 M HCl (20 mL) and saturated sodium hydrogen carbonate solution (20 mL), and dried with sodium sulfate. After filtration, the remaining urea precipitate was removed by centrifugation, the solvent was evaporated under nitrogen flow, and the solid was redissolved in methanol.

(±)-6-Hydroxy-2,5,7,8-tetramethylchromane-2-carboxylic acid (Trolox) and (*S*)-6-Methoxy-2,5,7,8-tetramethylchromane-2-carboxylic acid (Methyltrolox) were purchased from Sigma-Aldrich. Stock solutions of Trolox and Methyltrolox (10 mM) were prepared in methanol and diluted to 50–200 µM before the measurement. All samples were stored at −25 °C until use.

MS/MS and DT-IM-MS. CID spectra and CCSs of fragments were obtained by fragmenting the precursor ions in the trap cell of the Synapt G2-S HDMS instrument described in Section 3.3. To generate pseudo-MS^3 spectra of silver-adducted glycerophospholipids, the intact lipids were fragmented in the ion source, and the fragments resulting from neutral headgroup loss were *m/z*-selected in the quadrupole before being subjected to CID in the trap cell.

IR action spectroscopy. Gas-phase IR spectra of fragments generated from glycerolipids, glycerophospholipids, Trolox, and Methyltrolox were measured using the custom-built instrument described in Section 3.1. The fragments were formed by in-source fragmentation, which is based on collisions between the molecular ions and residual gas in the source region, and is thus equivalent to CID. In-source fragmentation was achieved by applying appropriate voltages to the source block and the two ring-electrode ion guides to accelerate the ions (*cf.* Figure 3.1).

Computational methods. Fragment structures were computed by sampling the conformational space, followed by DFT optimization of selected structures at the PBE0+D3/6-311+G(d,p) level of theory (including an SDD effective core potential for silver) and harmonic frequency calculations, as described in detail in Section 3.4. Prior to the conformational sampling, preferred sites for protonation and silver adduction were identified using the protonation tool implemented in CREST[300] (keywords *-protonate* and *-protonate -swel Ag+*, respectively). For chromane fragments, a list of candidate structures corresponding to the *m/z* of each investigated fragment was generated manually as well as with the aid of QCxMS[317] using the CID[320,321] and the dissociative electron attachment (DEA)[318] modes. For CID simulations, the input parameters were set to *xtb2*, *cid*, *elab 60*, *fullauto*, and, only for anions, *charge* -1. For the DEA mode, the input commands *xtb2* and *dea* were used. For visualization of the results, the entirety of xyz structure output files were analyzed to extract the exact masses and abundance of all generated fragments, both charged and neutral. It was manually confirmed whether the structures with the searched atomic composition indeed correspond to the proposed fragment structure. CCSs of DFT-optimized Trolox and Methyltrolox fragments were computed using HPCCS[314] with DFT-computed Merz-Singh-Kollman charges[316] at a temperature of 298 K (25 °C) in helium. The ΔF values refer to the lowest-energy DFT-optimized structure for each isomer. Transition states of fragmentation mechanisms were obtained by scanning the PES, as described in Section 3.4. Glycerolipid structures were truncated to three carbon atoms per lipid chain to speed up the computation. Lists and xyz files of all computed structures can be found in the supporting material of the original publications.[392,393]

6.3 | Results and Discussion

6.3.1 | Headgroup Loss from Protonated Glycerolipids

Protonated dioxolane fragments. In this study, protonated fragments resulting from neutral loss of the headgroup from PE and PC, as well as complementary DAG fragments were investigated. First, the fragmentation of protonated PE was studied using the model lipid PE (6:0/6:0). In-source fragmentation of the protonated precursor yields $[\mathrm{PE{+}H{-}141}]^+$ ions in high abundance. The IR spectrum of $[\mathrm{PE\,(6{:}0/6{:}0){+}H{-}141}]^+$ is depicted in Figure 6.3. The spectrum displays two bands of high relative intensity between 1500 and 1550 cm^{-1} and a well-defined band at 1750 cm^{-1} derived from the carbonyl stretching vibration. The presence of only one carbonyl band instead of two provides a first indication that the fragment structure features one free carbonyl group, whereas the second has engaged in cyclization.

In order to interpret the IR spectrum, DFT calculations at the PBE0+D3/6-311+G(d,p) level of theory were carried out for all three candidate structures depicted in Figure 6.1: open chain, dioxane, and dioxolane structures. The preferred sites of protonation were determined by

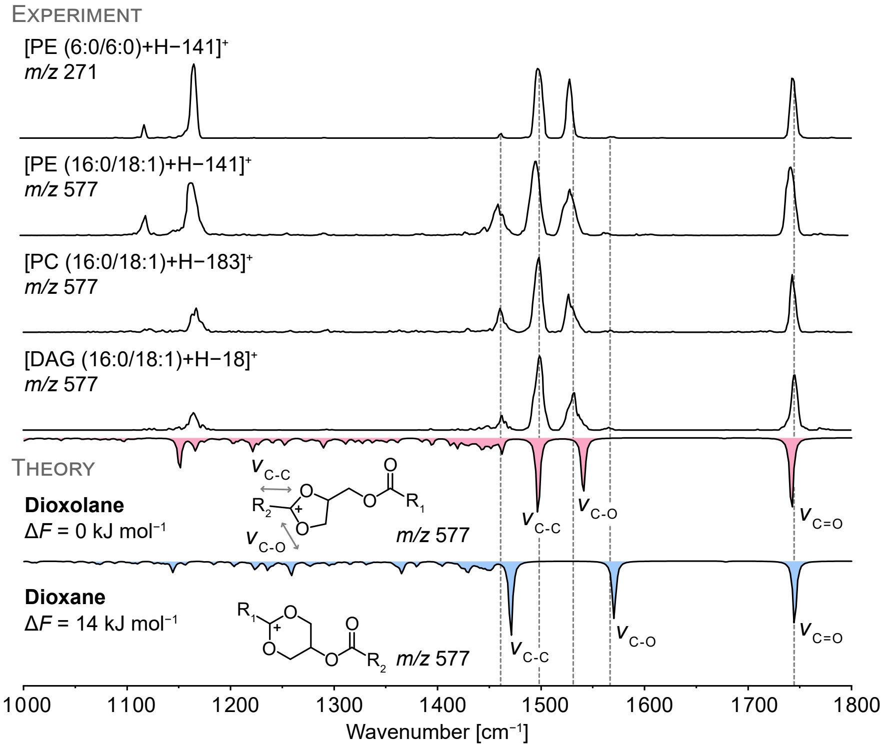

Figure 6.3: Gas-phase IR spectra of protonated PE, PC, and DAG fragments resulting from neutral headgroup loss. The spectroscopic signatures are mainly determined by the core ring structure and less by the fatty acid chain length. The fragments derived from PE, PC, and DAG (16:0/18:1(9*Z*)) yield identical spectra. DFT calculations (PBE0+D3/6-311+G(d,p)) of dioxolane and dioxane (16:0/18:1(9*Z*)) structures show that the dioxolane structure is energetically favored and is in good agreement with the experimental spectra.

calculations on model structures, which unambiguously confirmed that protonation of the C=C bond is energetically most favorable in all cases (Figure C1). The positive charge is located at the sp^2 carbon and stabilized by the two ring oxygens. This fixed charge location and concomitant absence of a C=C bond next to the ring explains the different dissociation behaviors of protonated glycerolipids *vs.* metal adducts. The carbonyl group of the second fatty acid furthermore interacts with the charged site in the most stable structures. The dioxolane model structure featuring a non-covalent carbonyl oxygen-ring carbon interaction with a distance of 2.6 Å yields a very good match with the experiment (Figure C1). In the computed IR spectra of dioxane structures, the frequency of the carbonyl stretching vibration is in good agreement with the experiment, but the main vibration bands arising from the dioxane ring are significantly shifted. The computed dioxane structures are furthermore destabilized by $\geq 10\,\mathrm{kJ\,mol^{-1}}$ (ΔF at 90 K) compared to the most stable dioxolanes. The open chain structure was discarded due to the unsatisfactory spectral match. Combined with the computed spectra, IR spectroscopy provides clear evidence that almost exclusively dioxolane structures are formed. Throughout the remainder of this section, experimental IR spectra are transparent and computed spectra are colored (red = dioxolane, blue = dioxane).

In order to study the impact of the lipid chain length and degree of unsaturation on the spectroscopic signature, the IR spectrum of $[\mathrm{PE}\,(16{:}0/18{:}1(9Z))+\mathrm{H}-141]^+$ was recorded (Figure 6.3). The position of the main absorption bands is not affected by the extended lipid chains compared to the fragment generated from PE (6:0/6:0). However, different band intensities are discernible. In particular, the intensity of the band at $1450\,\mathrm{cm}^{-1}$ increases with increasing chain length because it arises mainly from CH_2 bending vibrations of the aliphatic chains. Overall, the fatty acids have no major impact on the IR spectrum. The positions of the main absorption bands remain largely unaffected by variation of the lipid chains, demonstrating that the dioxolane core structure determines the IR signature. As shown by the computed spectra of low-energy dioxolane and dioxane (16:0/18:1(9*Z*)) structures in Figure 6.3, the two absorption bands at 1500 and $1540\,\mathrm{cm}^{-1}$ originate from diagnostic C—C and C—O stretching vibrations of the dioxolane ring and dominate the spectrum. The weak band around $1570\,\mathrm{cm}^{-1}$ in all experimental spectra, which coincides with one of the two main bands in the computed dioxane spectra, points toward the presence of minor dioxane-type fragments. Computed spectra of dioxolane and dioxane structures suggest that the main band in the dioxolane spectra ($1500\,\mathrm{cm}^{-1}$) is of equal intensity as the band at $1570\,\mathrm{cm}^{-1}$ in the dioxane spectra. The relative abundance of dioxane was thus determined by dividing the area under the peak from 1560 to $1575\,\mathrm{cm}^{-1}$ by the area under the main peak from 1485 to $1510\,\mathrm{cm}^{-1}$. The ratio of dioxane fragments was determined to lie between 2–3 % for all fragment spectra depicted in Figure 6.3. CID of PE (d31-16:0/18:1(9*Z*)) featuring a perdeuterated *sn*-1 lipid chain yielded approximately the same ratio of dioxolanes as a control experiment (Figure C2).

In the next step, the structures of fragments generated from PE were compared with the corresponding fragments obtained from PC and DAG. $[\mathrm{PE}+\mathrm{H}-141]^+$, $[\mathrm{PC}+\mathrm{H}-183]^+$, and $[\mathrm{DAG}+\mathrm{H}-18]^+$ ions, which result from neutral loss of the headgroup from PE and PC or loss of water from DAG, exhibit identical *m/z* values for identical fatty acid composition of the precursor ions. As shown in Figure 6.3, the IR spectra of the fragment at *m/z* 577 are independent of the precursor, which suggests identical fragment structures. Minor differences concerning relative band intensities, bandwidths, and *s/n* arise from day-to-day fluctuations of the laser power and FWHM as well as varying abundance of the precursor ions depending on the lipid class. The $[\mathrm{PC}+\mathrm{H}-183]^+$ ions, for example, are formed in very low abundance because metal-adducted fragments dominate the mass spectrum.

The formation of protonated dioxolane-type structures can be regarded as a universal phenomenon in glycerolipid fragmentation. However, the results do not agree with the deuteration experiments by Hsu and Turk, which suggested a ratio of 2:3 (dioxane:dioxolane) for protonated PC resulting from more labile alpha-hydrogens at the *sn*-2 position.[410] Several explanations are possible. First, a different fragmentation mechanism has been studied in their work. Instead of probing protonated fragments generated from sodiated PC, protonated precursor ions with deuterated hydrocarbon chains were fragmented. Dioxane structures were thus indirectly quantified by determining H/D ratios in phosphocholine fragments. It is possible that the fragmentation of protonated PC involves stronger participation of *sn*-1 alpha-hydrogens. The exact structure of the fragment, however, cannot be probed by MS-based methods due to the absence of a charge. A second explanation might be that initially both dioxolanes and dioxanes are formed, which then interconvert in the gas phase and finally converge to the more stable dioxolane structure. This hypothesis was tested by computing transition states between dioxane and dioxolane model structures. As shown in Figure C3, the computed activation energy required for a dioxane-dioxolane conversion is well above 150 kJ mol^{-1} (ΔG) for model structures. Even though the activation energy can in principle be taken up by the fragments *via* ion-molecule collisions in the source region, it is rather unlikely that such high conversion barriers can be overcome in a secondary fragmentation reaction under the applied conditions. We therefore assume that dioxolanes are exclusively formed in the initial fragmentation process.

Cyclic phosphate intermediate. Alkali metal-adducted PC readily loses trimethylamine, resulting in $[\mathrm{PC+M-59}]^+$ fragments that are postulated to exhibit a cyclic phosphate (*cf.* Figure 6.1b).[410] To confirm the structure of this intermediate fragment, which can further dissociate to yield the dioxolane fragment discussed in the previous section, $[\mathrm{PC\,(16{:}0/18{:}1(9}Z\mathrm{))+Na}]^+$ ions (*m/z* 782) were generated by the addition of sodium acetate to the phospholipid solution. The IR spectrum of the $[\mathrm{PC\,(16{:}0/18{:}1(9}Z\mathrm{))+Na-59}]^+$ ion at *m/z* 723 is depicted in Figure 6.4 together with a computed spectrum of the suggested cyclic phosphate structure. Overall, the spectrum is in good agreement with the computed IR spectrum. The symmetric and antisymmetric stretching vibrations of the two carbonyl groups are at the correct positions and partly resolved. Another characteristic vibration is the P=O stretching vibration between 1200 and 1300 cm^{-1}, which is slightly shifted relative to the computed frequency. The most important vibrations providing evidence for the cyclic phosphate are located at lower wavenumbers: the C−C stretching vibration of the two ring carbons yields a characteristic, narrow band between 900 and 950 cm^{-1}. The C−O stretching vibrations of the ring are located at 1050 cm^{-1} and are of high relative intensity. The presence of these two characteristic bands as well as the overall good match between experiment and theory provide first direct experimental evidence that the sodiated intermediate fragment occurring in the phosphatidylcholine fragmentation pathway indeed features a five-membered phosphate ring.

Dioxolane and dioxane fragments from diacylglycerols. The enzymatic removal of the phosphate headgroup from glycerophospholipids results in 1,2-DAGs bearing a hydroxyl group at the *sn*-3 position. However, a smaller pool of DAGs in the human body is constituted by 1,3-DAGs, which are distinguished by processing enzymes and by shape-sensitive analytical

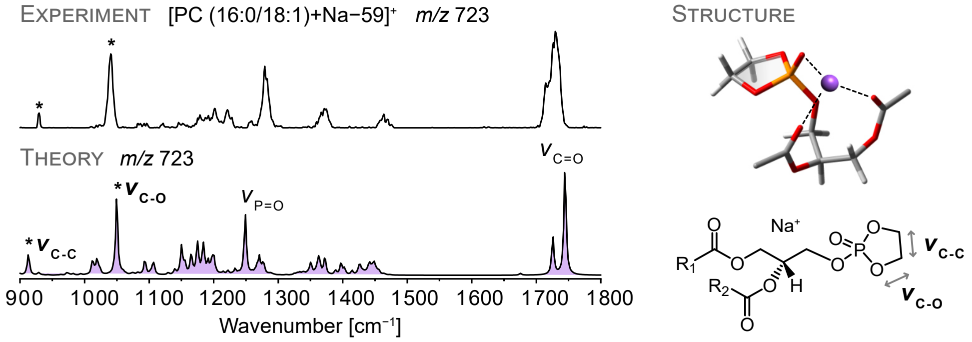

Figure 6.4: Gas-phase IR spectrum of the [PC (16:0/18:1(9*Z*))+Na−59]+ ion generated by neutral loss of trimethylamine from sodiated PC. The experimental spectrum features two diagnostic vibrations predicted by DFT calculations (PBE0+D3/6-311+G(d,p)) for a cyclic phosphate structure equipped with full-length fatty acid chains (16:0/18:1(9*Z*)). The depicted 3D structure is truncated to two carbon atoms per fatty acid to enhance visibility.

techniques such as ion mobility spectrometry.[42,105] 1,2- and 1,3-DAGs can interconvert by acyl chain migration, a process catalyzed by acidic and basic conditions.[417] Upon CID, protonated DAGs readily lose water or one of the two fatty acids. The fragments formed *via* neutral loss of a fatty acid provide a wealth of additional information on the formation of dioxolane and dioxane structures.

1,2-DAG (16:0/18:1(9*Z*)) can lose either palmitic acid or oleic acid, resulting in two different fragment ions at *m/z* 339 and *m/z* 313, respectively. Both fragments were studied by IR spectroscopy and yield very similar spectra (Figure 6.5), which suggest identical core structures. The absence of absorption bands above 1600 cm^{-1} witnesses the absence of a carbonyl group, indicating that the remaining fatty acid has engaged in an intramolecular cyclization reaction in the gas phase. The spectra display two main bands at 1500 and 1550 cm^{-1} that closely resemble the spectrum of [DAG (16:0/18:1(9*Z*))+H−18]+ resulting from water loss. From these observations, it is reasonable to assume the formation of a dioxolane ring upon neutral loss of one fatty acid. As shown in Figure 6.5, the geometry of 1,2-DAGs indeed imposes the formation of dioxolane rings because the fatty acids are located at neighboring positions on the glycerol backbone. The formation of dioxane rings, on the other hand, is precluded by the geometry of the precursor ion. The opposite is true for 1,3-DAGs, in which the two fatty acid substituents are separated by the *sn*-2 carbon on the glycerol backbone. From a geometrical point of view, the formation of dioxolanes is precluded in 1,3-DAGs, which raises the intriguing possibility to generate the less stable dioxane rings.

As shown in Figure 6.5, the IR spectra of the fragment ions at *m/z* 339 are indeed different for 1,2- and 1,3-DAG precursor ions. However, both spectra feature the same absorption bands, differing only in their relative intensity. As confirmed by DFT calculations, both dioxolane- and dioxane-type fragments are present in both spectra with the ratio of dioxane structures being

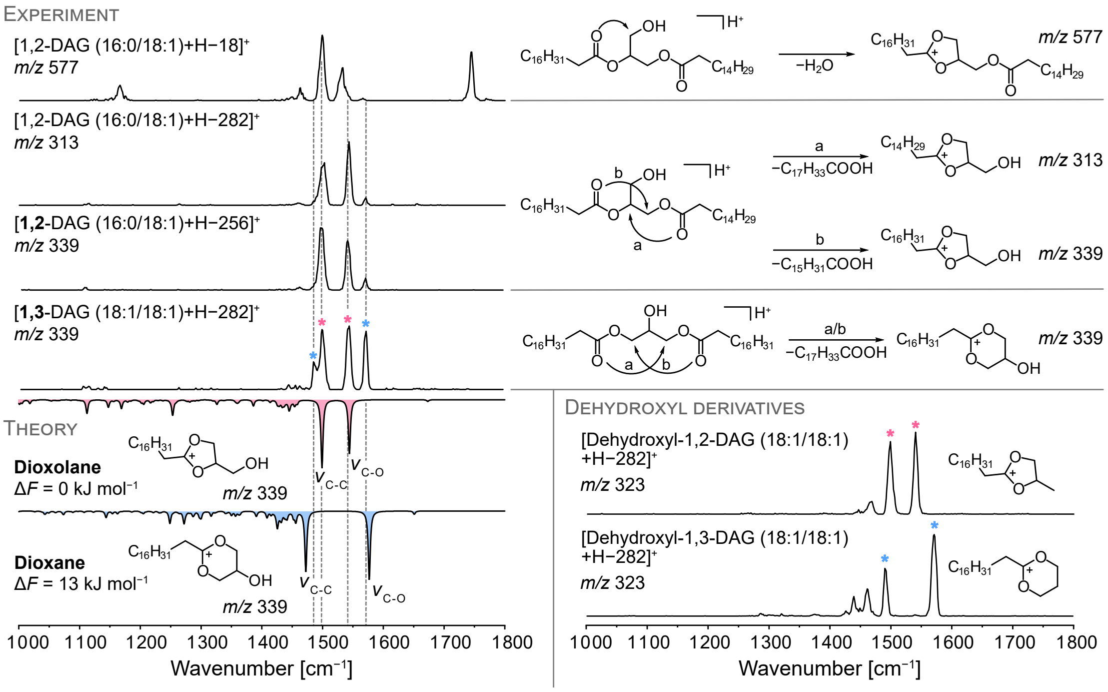

Figure 6.5: IR spectra and structures of fragments generated from protonated 1,2- and 1,3-DAGs. Protonated DAGs readily lose one fatty acid (FA 16:0 or FA 18:1(9*Z*)) to form fragment structures resembling the previously observed dioxolane resulting from water loss. In theory, 1,2-DAGs can only form dioxolanes and 1,3-DAGs can only form dioxanes upon neutral fatty acid loss. Both ring sizes are observed in both spectra due to acyl chain migration, as confirmed by DFT calculations (PBE0+D3/6-311+G(d,p)). Prevention of acyl chain migration in tailor-made dehydroxyl derivatives yields pure dioxolane and dioxane spectra.

significantly elevated in the spectrum of the fragments derived from 1,3-DAG. The most likely explanation for the observation of both structures in both spectra despite the contradicting geometrical assumptions is acyl chain migration. The transfer of an acyl moiety to a different position on the glycerol backbone is initiated by the hydroxyl group attacking the electrophilic carbonyl carbon.[418] This process can in principle occur in solution or in the source region of the instrument. Because acyl chain migration of DAGs in organic solvents is minimal at room temperature,[417] the rearrangement is suspected to occur in the source region of the instrument. Here, collisions with residual gas can induce rearrangement reactions which may be further promoted by methanol as a protic solvent.[419] Also, the observed ratios of dioxolanes and dioxanes in the IR spectra do not correspond to the typical 1:2 equilibrium of 1,2:1,3-DAG in solution.[417]

In order to suppress acyl chain migration, we chose to synthesize dehydroxyl derivatives of 1,2- and 1,3-DAG (18:1(9*Z*)/18:1(9*Z*)). 1,2- and 1,3-propylene glycol dioleate were synthesized by esterification of oleic acid with 1,2-propanediol and 1,3-propanediol, respectively, following published protocols.[415,416] The dehydroxyl derivatives were found to undergo neutral loss of one fatty acid, analogous to DAGs. The fragments at *m/z* 323 correspond to the fragments at *m/z* 339 obtained from DAGs lacking the hydroxyl group. In perfect agreement with the expectations, the protonated fragments obtained from the dehydroxyl derivatives 1,2- and 1,3-propylene glycol dioleate yield clean, distinguishable IR spectra matching the computed IR spectra of dioxolane and dioxane rings, respectively (Figure 6.5). Fragmentation of 1,3-propylene glycol dioleate allows the observation of dioxane-type fragments, which are energetically less favored than dioxolane structures and had not been observed before. This finding demonstrates that the preference of glycerolipids to form dioxolane fragments can be circumvented by rational design of the precursor ion structure.

In conclusion, IR action spectroscopy provided the first direct experimental evidence for protonated dioxolane fragments generated throughout different glycerol-based lipids and fragmentation routes. Even though not all phospholipid classes were studied, the consistency of their fragmentation behavior[98] suggests that the results are generally valid. The results are in good agreement with recent studies on metal adducts[6,130,202,211,212] and corroborate the previously proposed dissociation mechanism involving the participation of *sn*-2 alpha-hydrogens,[410] while excluding alternative reaction pathways resulting in dioxane or open chain fragments.

6.3.2 | The Influence of Silver Coordination

Silver-adducted dioxolane fragments. In positive ion mode, CID of silver-adducted glycerophospholipids yields abundant product ions resulting from neutral loss of the phosphate-containing headgroup. To determine whether silver adduction yields dioxolane structures like alkali metal-adducted and protonated phospholipids and to estimate the respective influence of the headgroup and the lipid chains on the fragment structure, silver-adducted PE and PC precursor ions were subjected to in-source fragmentation. The fragments generated by neutral headgroup loss were subsequently probed by cryogenic IR action spectroscopy. The IR spectra of the fragments derived from silver-adducted PC (16:0/18:1(9*Z*)), PE (16:0/18:1(9*Z*)), and PE (6:0/6:0) are shown in Figure 6.6. As the headgroup is cleaved during in-source fragmentation, the fragments resulting from PE and PC precursor ions with the same lipid chains are expected to be identical. Indeed, the IR spectra of $[\mathrm{PC}\,(16{:}0/18{:}1(9Z))+\mathrm{Ag}-183]^+$ and $[\mathrm{PE}\,(16{:}0/18{:}1(9Z))+\mathrm{Ag}-141]^+$ fragments are equal except for intensity differences in the lower wavenumber region that can be ascribed to day-to-day fluctuations of the laser power. The lipid chains, on the contrary, have a major influence on the IR spectrum, as illustrated by the model lipid PE (6:0/6:0) equipped with short, saturated hexanoic acid chains. One of the two main absorption bands is significantly shifted compared to the IR spectra of the fragments featuring significantly longer lipid chains.

In order to assign the vibration bands and determine the core fragment structure, DFT calculations were performed for both dioxolane and dioxane fragment structures. The preferred

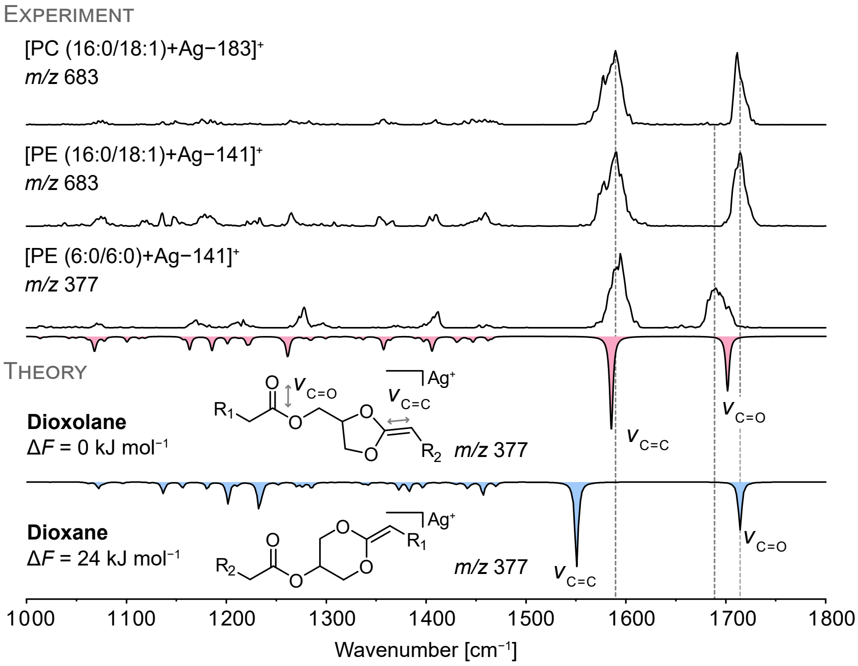

Figure 6.6: Experimental and computed IR spectra of silver-adducted phospholipid fragments generated by neutral headgroup loss. The band positions in the fragment spectra of PE and PC (16:0/18:1(9*Z*)) are not influenced by the different headgroups. The lipid chains have a major influence on the spectroscopic signature. Computed spectra for [PE (6:0/6:0)+Ag−141]$^+$ dioxolane and dioxane fragments (PBE0+D3/6-311+G(d,p)) show that the fragment features a dioxolane ring.

coordination geometry of silver ions was found to involve interactions with the carbonyl oxygen and the C=C bond adjacent to the ring (Figure C4). Geometry optimization and harmonic frequency calculation of [PE (6:0/6:0)+Ag−141]$^+$ ions featuring this favored interaction geometry were subsequently performed at the PBE0+D3/6-311+G(d,p), SDD (Ag) level of theory. As shown in Figure 6.6, the computed dioxolane fragment is energetically favored over the dioxane fragment and yields a satisfactory match with the experimental spectrum. The two main vibration bands are attributed to the stretching vibration of the C=C bond adjacent to the ring at 1600 cm^{-1} and to the C=O stretching vibration of the fatty acid next to the ring approximately at 1700 cm^{-1}. The computed IR spectrum of the dioxane fragment does not coincide with the experimental spectrum, as the C=C stretching frequency is red-shifted to 1550 cm^{-1} and the C=O vibration is blue-shifted to above 1700 cm^{-1}.

As a conclusion, fragments resulting from neutral headgroup loss from silver-adducted PE and PC yield dioxolane structures, in accordance with alkali metal adducts and protonated fragments. Truncation of the lipid chains leads to a red-shifted C=O stretching vibration in the spectrum of [PE (6:0/6:0)+Ag−141]$^+$ compared with the spectra of fragments featuring longer lipid chains. In addition, the vibration at 1600 cm^{-1} is broader and slightly shifted in the case of longer lipid chains. DFT calculations suggest that the stretching vibration of the

C=C bond in the lipid chain that interacts with the silver ion contributes to the vibration band at 1600 cm^{-1} and leads to broadening compared to the truncated lipid chains lacking double bonds. In the case of protonated dioxolane fragments that were studied in the previous section, the band positions are not affected by the nature of the lipid chains. Frequency shifts due to silver adduction are indicative of interactions between the silver ion and the fatty acids, which influence the conformation of the fragment ions and consequently the spectroscopic signature. In the following, silver-lipid interactions are studied in more detail to investigate the effects of lipid chain permutation and C=C bond position on the fragment geometry and fragmentation behavior.

***sn*-Isomers.** Silver adduction results in different relative intensities of second-generation product ions in the MS^3 spectra of *sn*-isomers. For example, phospholipids featuring palmitic acid (FA 16:0) and oleic acid (FA 18:1(9*Z*)) yield silver-adducted oleic acid fragments in the form of carboxylic acid (*m/z* 389) or ketene (*m/z* 371) with relative intensities depending on the positions of the fatty acids on the glycerol backbone.[156,159] In order to explain the observed intensity differences in the MS^3 spectra of *sn*-isomers, IR spectra of the first-generation fragment ions [PE (16:0/18:1(9*Z*))+Ag−141]$^+$ and [PE (18:1(9*Z*)/16:0)+Ag−141]$^+$ at *m/z* 683 were recorded (Figure 6.7a). The positions of the main absorption bands are identical, whereas minor but reproducible differences are discernible in the lower wavenumber region. The fragment geometry is expected to be the same for both isomers, but distinct coordination motifs between silver and the fatty acids could induce differences in the molecular conformation causing the minor differences in the lower wavenumber region. According to DFT calculations, the region below 1500 cm^{-1} is dominated by C−H bending vibrations of the lipid chains. However, the experimental differences between the *sn*-isomers cannot be assigned to specific vibrational modes due to the crowdedness of that spectral region and insufficient accuracy of computation for such large and flexible lipids. Interestingly, the computed coordination geometries of the two isomers are indeed clearly different (Figure 6.7b). As silver ions preferentially coordinate C=C bonds in fatty acids, the fragment geometry is adapted to enable an interaction between the C=C bond of oleic acid and the silver ion. In the (16:0/18:1(9*Z*)) isomer, oleic acid is attached to the *sn*-2 position and participates in the formation of the dioxolane ring. In the (18:1(9*Z*)/16:0) isomer, oleic acid is attached next to the dioxolane ring and interacts with silver *via* the C=C bond and the carbonyl oxygen.

These different coordination geometries and the dioxolane structure of the MS/MS fragments are key to explain the previously noted intensity differences between MS^3 ketene and acid fragments (Figure 6.7c). In the case of the (16:0/18:1(9*Z*)) isomer, the ketene motif is already pre-formed because oleic acid is part of the dioxolane ring and features a C=C bond between the original carbonyl carbon and the alpha-carbon. In contrast, in the (18:1(9*Z*)/16:0) isomer, oleic acid is esterified next to the dioxolane ring and the carboxylic acid motif is pre-formed.

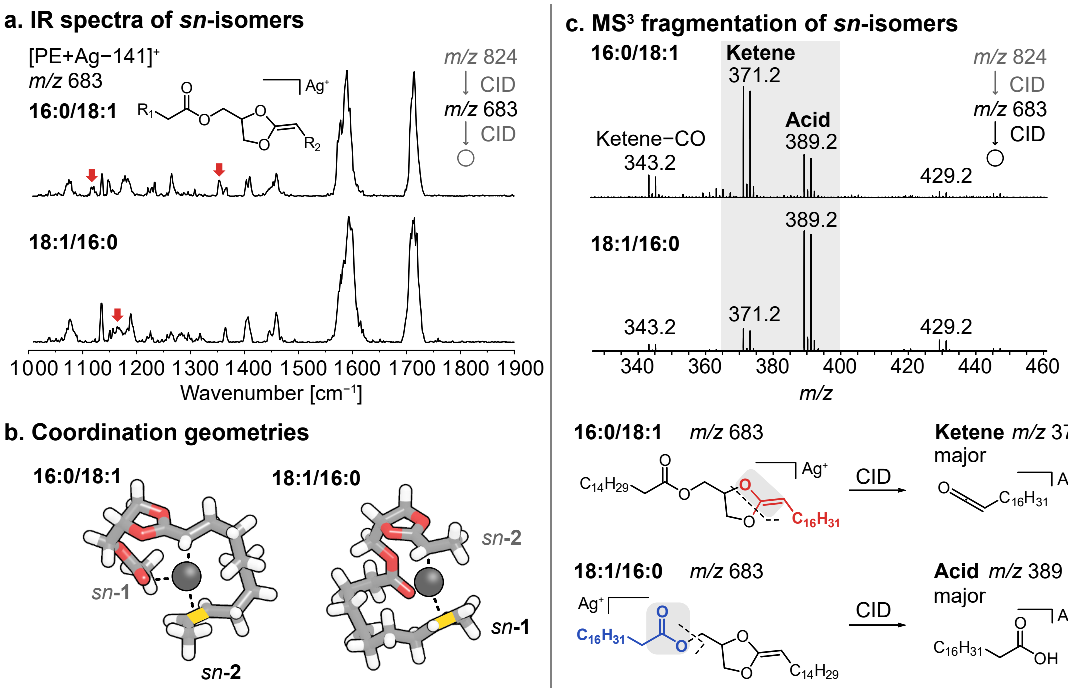

Figure 6.7: Collision-induced dissociation of silver-adducted PE *sn*-isomers. **a.** The IR spectra of dioxolane fragments generated from PE (16:0/18:1(9*Z*)) and PE (18:1(9*Z*)/16:0) display subtle differences between 1000 and 1500 cm^{-1}. **b.** Computed structures of dioxolane fragments show that silver interacts with the C=C bond in the oleic acid residue. The fatty acids are truncated for visibility and the double bond in oleic acid is highlighted in yellow. **c.** Inverse ratios of acid and ketene fragments in the MS^3 spectra of the isomers can be rationalized by the preferential coordination of silver to the oleic acid residue and the pre-formed acid and ketene motifs at the *sn*-1 and *sn*-2 positions, respectively.

The preferential loss of oleic acid as either ketene or carboxylic acid can thus be rationalized based on the structure and coordination geometry of the MS/MS intermediate fragment. In both cases, however, a small fraction of the other fragment ion is also present, showing that the formation of ketene and carboxylic acid fragments are competing.

Double bond isomers. The position of unsaturated lipid chains on the glycerol backbone influences the coordination geometry in silver-adducted glycerophospholipids and thus the fragmentation behavior of *sn*-isomers. As the coordination of silver is mainly dictated by interactions with C=C bonds of unsaturated lipid chains, the position of double bonds is equally expected to influence the coordination geometry and thus the fragmentation behavior. To test this hypothesis, the double bond isomers PC (18:1(9*Z*)/18:1(9*Z*)) and PC (18:1(6*Z*)/18:1(6*Z*)) were investigated. CID of the double bond isomers yields a striking difference in the MS^3 fragment spectra: the formation of ketene and ketene—CO fragments is suppressed in the case of the 6*Z* isomer (Figure 6.8c). As the fragment intensities are expected to be determined by the geometry of the intermediate dioxolane fragment, IR spectra of [PC (18:1(9*Z*)/18:1(9*Z*))+Ag−183]$^+$ and

[PC (18:1(6*Z*)/18:1(6*Z*))+Ag−183]$^+$ fragments (*m/z* 709) were measured (Figure 6.8a). Interestingly, the absorption band corresponding to the stretching vibration of the C=C bond adjacent to the dioxolane ring is blue-shifted by 50 cm^{-1} in the spectrum of the 6*Z* isomer compared to the 9*Z* isomer. Based on this significant spectral difference, fundamental conformational differences are expected between the double bond isomers.

DFT calculations were thus performed for both isomers, and the computed harmonic IR spectra reproduce the experimentally observed shift of the C=C stretching vibration conclusively (Figure C5). The computed low-energy conformers adopt clearly different conformations depending on the C=C bond position within the lipid chains (Figure 6.8b). In the 9*Z* isomer, the overall conformation and spectroscopic signature are very similar to the [PC (16:0/18:1(9*Z*))+Ag−183]$^+$ fragment (*cf.* Figures 6.7a and b). The silver ion coordinates to the carbonyl oxygen, the C=C bond next to the dioxolane ring, and the C=C bond of the oleic acid chain at the *sn*-2 position. The C=C bond of the second oleic acid chain is not involved. On the contrary, the C=C bonds in the petroselinic acid substituents of the [PC (18:1(6*Z*)/18:1(6*Z*))+Ag−183]$^+$ fragment are both interacting simultaneously with the silver ion due to their proximity to the glycerol backbone. The coordination of both lipid chains instead of one leads to an overall distortion of the chains in close proximity to the dioxolane core structure compared to the 9*Z* isomer.

The different conformations of silver-adducted dioxolane fragments depend on the proximity of C=C bonds to the glycerol backbone and are key to explain the fragmentation behavior of 6*Z* and 9*Z* double bond isomers. The MS^3 spectrum of the 9*Z* isomer shows the expected formation of both ketene and acid fragments because both oleic acid residues can be cleaved off (Figure 6.8c). However, in the 6*Z* isomer, ketene formation, which is associated with the loss of the fatty acid at the *sn*-2 position, is clearly reduced. It can be assumed that the fatty acid at the *sn*-1 position, which yields mainly acid fragments, is dissociated with high preference together with the silver cation. To provide an explanation, it is important to note that the fragments are only visible in the CID spectrum if they are associated with the positively charged silver ion. In the 6*Z* isomer, the fatty acid at the *sn*-1 position coordinates strongly to the silver ion *via* its carbonyl oxygen and the C=C bond, whereas in the case of the 9*Z* isomer, the C=C bond of the fatty acid at the *sn*-1 position does not participate in the silver coordination. Therefore, the silver ion is strongly localized at the *sn*-1 fatty acid in the 6*Z* isomer, which leads to a high ratio of acid fragments, whereas both fatty acids can be lost as silver adducts from the 9*Z* isomer. This example shows that cation-pi interactions strongly influence the fragmentation behavior of silver-adducted lipids.

Allylic dioxolane fragments. Another particularity in the CID spectra of silver-adducted phospholipids is the observation of abundant silver hydride loss from the dioxolane fragments, which does not occur in the case of alkali metal adduction. In order to propose a fragmentation mechanism for hydride abstraction from dioxolane fragments, silver-adducted PC (16:0/18:1(9*Z*))

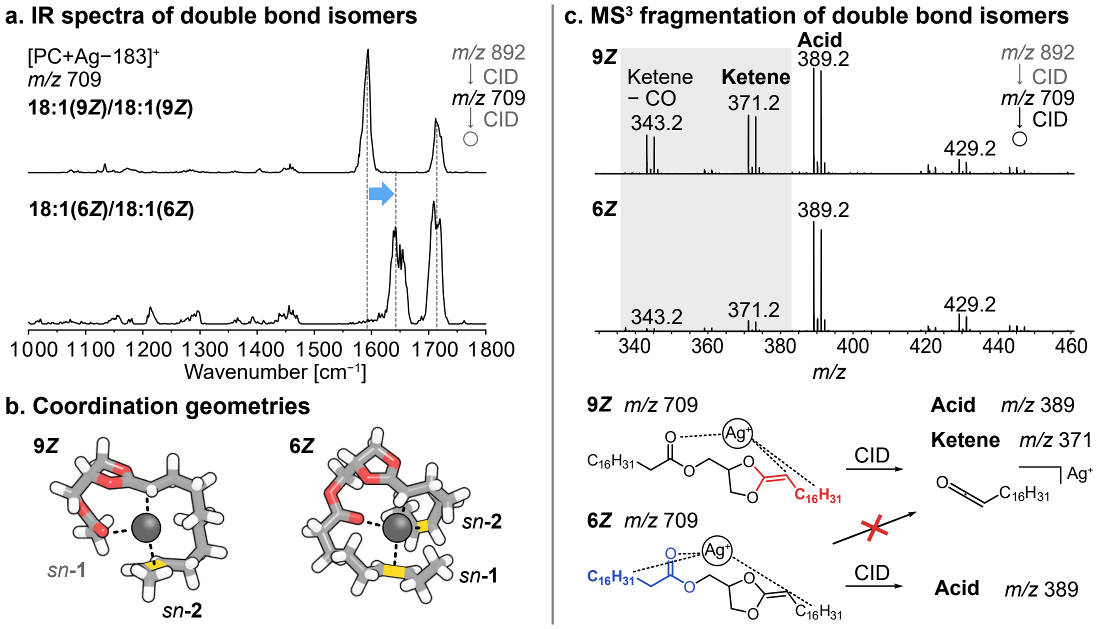

Figure 6.8: Influence of the double bond position on the collision-induced dissociation of silver-adducted phospholipids. **a.** The IR spectra of the dioxolane fragments generated from PC (18:1(9*Z*)/18:1(9*Z*)) and PC (18:1(6*Z*)/18:1(6*Z*)) show a significant band shift. **b.** Computed structures of dioxolane fragments confirm that silver interacts only with the fatty acid at the *sn*-2 position in the 9*Z* isomer, but with both lipid chains in the 6*Z* isomer. The fatty acids are truncated for visibility and double bonds are highlighted in yellow. **c.** Ketene formation is suppressed in the fragmentation of dioxolane fragments generated from the 6*Z* isomer. One possible explanation is the strong coordination of silver to the fatty acid at the *sn*-1 position, which preferentially yields acid fragments.

was subjected to neutral loss of phosphocholine and subsequent dissociation of silver hydride by applying a steep voltage gradient in the source region. The mass peak of the resulting $[\mathrm{PC}\,(16{:}0/18{:}1(9Z))+\mathrm{Ag}-183-\mathrm{AgH}]^+$ fragment (*m/z* 575) does not show the characteristic silver isotope pattern, providing clear evidence that the silver ion is lost upon fragmentation. The IR spectrum of the obtained fragment is shown in Figure 6.9a. It features a strong absorption at 1500 $\mathrm{cm^{-1}}$, two absorption bands of equal intensity between 1550 and 1650 $\mathrm{cm^{-1}}$, and a broad band between 1750 and 1800 $\mathrm{cm^{-1}}$, which is attributed to the C=O stretching vibration. The main absorption band at 1500 $\mathrm{cm^{-1}}$ coincides perfectly with the main absorption band of protonated dioxolane fragments, which stabilize the positive charge between the two ring oxygens (*cf.* Figure 6.3). The two absorption bands between 1550 and 1650 $\mathrm{cm^{-1}}$ are absent in the IR spectra of protonated fragments, but are highly diagnostic for the structural assignment of the fragment investigated here. Their position can only be explained by assuming an allylic dioxolane fragment, which is formed by hydride abstraction from the carbon atom next to the C=C bond (Figure 6.9b). Before the hydride abstraction, the C−C bond next to the C=C bond can rotate freely, but it is locked in a *cis* or *trans* configuration upon dissociation of silver hydride. The coexistence of *cis* and *trans* isomers explains the observation of two separate

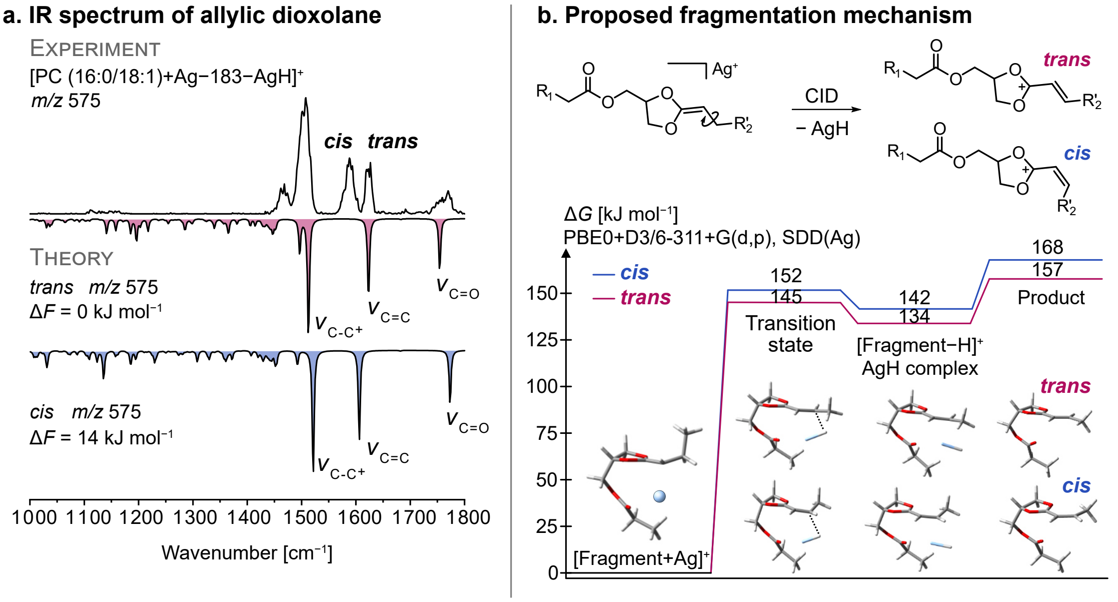

Figure 6.9: IR spectrum and proposed formation of allylic dioxolane fragments. **a.** Fragmentation of silver-adducted dioxolane fragments generated from PC (16:0/18:1(9*Z*)) results in neutral loss of silver hydride. Both *cis* and *trans* isomers contribute to the experimental IR spectrum of the allylic cation. **b.** The most stable fragment structure found by computation features an allylic cation. The residue R_2 is replaced by $R_2' = R_2{-}CH_2$ in the fragmentation scheme to illustrate the geometry of the allylic double bond. The energy diagram shows activation barriers for the formation of *cis* and *trans* allylic dioxolane fragments from a silver-adducted dioxolane model structure (3:0/4:0) computed at the PBE0+D3/6-311+G(d,p), SDD (Ag) level of theory. The activation barriers leading to *cis* and *trans* products are very similar.

bands corresponding to the C=C stretching vibration of the allylic cation.

The allylic structure is energetically favorable because of the mesomeric effect: the positive charge is well-stabilized by delocalization of electrons between the two ring oxygens and the allylic double bond. Computation of transition states for dioxolane model structures yielded an activation barrier for silver hydride abstraction of 150 kJ mol^{-1} (ΔG) (Figure 6.9b). In comparison to this value, the energy difference between the formation of *cis* and *trans* allylic fragments is small, and hence both isomers are observed in comparable quantities. Interconversion between *cis* and *trans* isomers under the activating conditions in the source region is conceivable as well, but rather unlikely because the computed activation barrier exceeds 200 kJ mol^{-1} (ΔG). This significant amount of energy would have to be transferred to the allylic cation in addition to the activation energy required for its initial formation. Therefore, the geometry of the C=C bond is assumed to be determined during hydride abstraction.

In conclusion, the influence of silver adduction on the fragmentation behavior of glycerophospholipids was investigated and rationalized by a combination of cryogenic IR action spectroscopy and computational chemistry. The approach was employed to determine the structures and coordination geometries of silver-adducted fragments, which, in turn, allow to

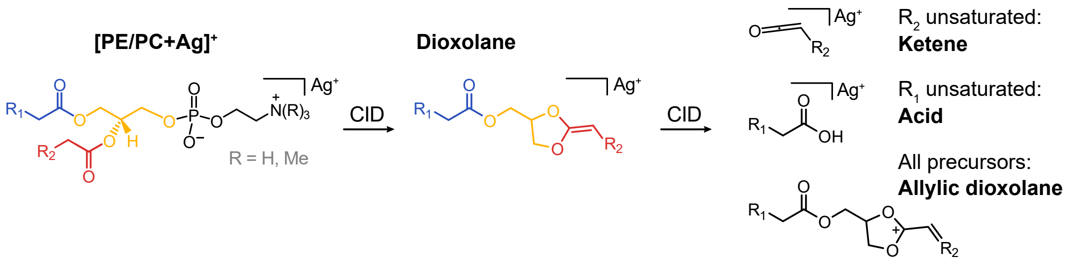

Figure 6.10: Overview of the collision-induced dissociation pathways of phospholipid silver adducts. Silver-adducted PE and PC yield dioxolane fragments upon neutral headgroup loss. The dioxolane dissociates into allylic dioxolane fragments as well as silver-adducted ketene and acid fragments. The relative abundance of ketene and acid fragments depends on the position of the unsaturated fatty acid.

draw conclusions about the fragmentation reactions and relative fragment ion abundances. Neutral headgroup loss from silver-adducted PE and PC was found to yield dioxolane structures featuring specific coordination geometries depending on the lipid chain positions and the position of C=C bonds within the lipid chains. Therefore, *sn*-isomers and double bond regioisomers yield distinguishable MS^3 spectra, which can be qualitatively explained based on the geometry of the dioxolane fragments. Furthermore, allylic dioxolane fragment structures resulting from silver hydride abstraction were proposed and confirmed for the first time. An overview scheme summarizing the fragmentation of phospholipid silver adducts studied in this work is shown in Figure 6.10.

6.3.3 | Reference-Free Assignment of Chromane Fragments

Positive ion mode: dehydration and decarbonylation. The structural difference between Trolox and Methyltrolox is subtle: it consists in a single methyl group attached to the phenol oxygen (*cf.* Figure 6.2). Not surprisingly, the fragmentation patterns in positive ion mode are identical for both precursor ions, shifted by 14 on the *m/z* scale. Protonated Trolox and Methyltrolox follow two major fragmentation pathways upon CID in positive ion mode: ring opening *via* a retro-Diels-Alder reaction and neutral loss of CO_2H_2 (Figures 6.11a and b). The well-understood retro-Diels-Alder reaction yields primary and secondary fragments at *m/z* 165 and *m/z* 137 for Trolox, and at *m/z* 179 and *m/z* 151 for Methyltrolox.[420]

To investigate the fragmentation reactions leading to a net loss of CO_2H_2 from the protonated precursor ions, gas-phase IR spectra of protonated Trolox (*m/z* 251) and the resulting fragment (*m/z* 205) were recorded. The methylated analogs were not analyzed, because the results are expected to be transferable due to identical fragmentation in positive ion mode. The IR spectrum of protonated Trolox was recorded in the 1000–1850 cm^{-1} range (Figure 6.11c). To identify the structure corresponding to the IR spectrum, all possible protonation sites were identified using CREST,[300] followed by geometry optimization and harmonic frequency analysis of the

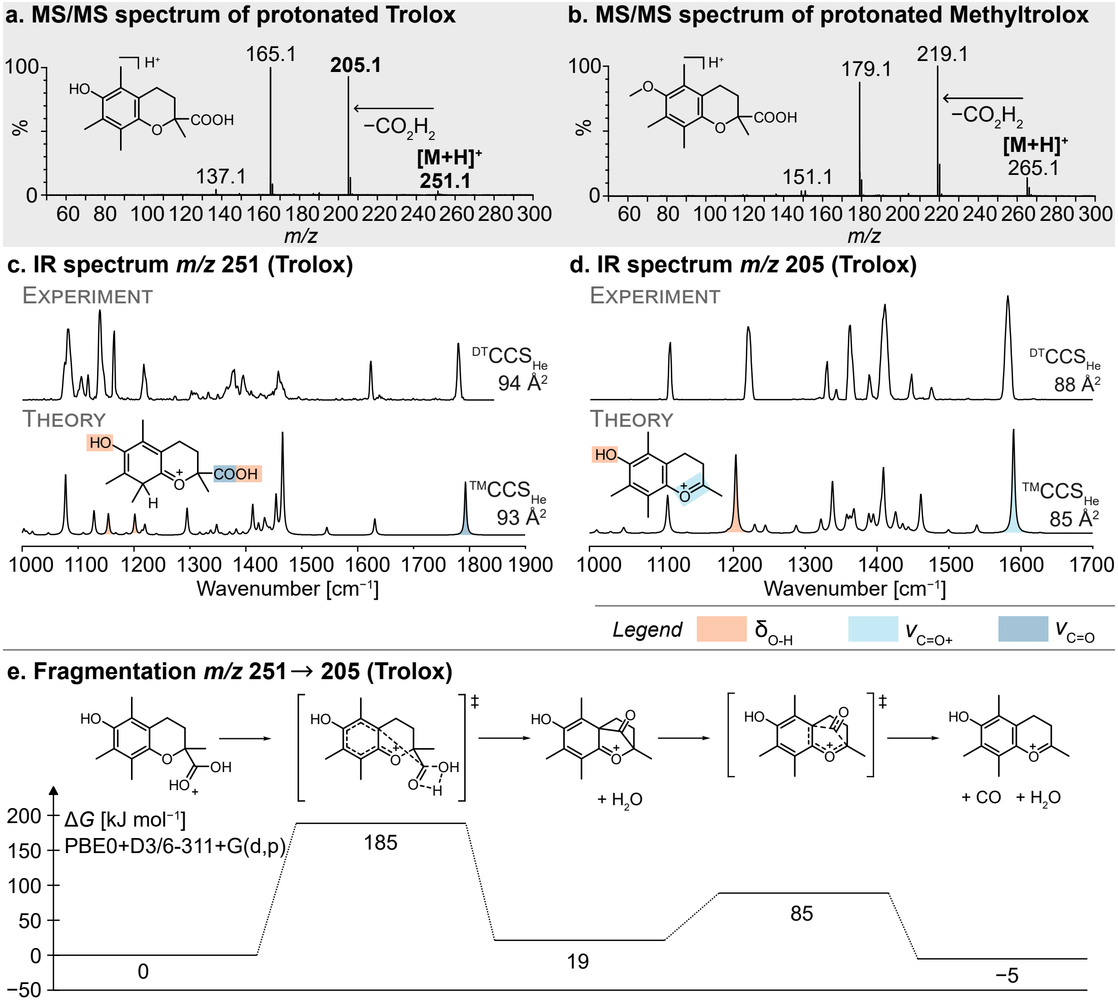

Figure 6.11: Collision-induced dissociation of protonated Trolox and Methyltrolox. **a,b.** Protonated Trolox and Methyltrolox yield the same fragmentation pattern. The fragment ions at *m/z* 165 (179) and *m/z* 137 (151) in the MS/MS spectra correspond to primary and secondary retro-Diels-Alder fragments of Trolox (Methyltrolox), which are not studied here. **c.** IR spectroscopy confirms that Trolox (*m/z* 251) is protonated on the aromatic ring. **d.** The net loss of CO_2H_2 yields a fragment at *m/z* 205, which features a closed-ring structure. **e.** The proposed fragmentation mechanism includes an initial proton transfer to the carboxylic acid (see text), followed by dehydration and decarbonylation.

protomers by DFT at the PBE0+D3/6-311+G(d,p) level of theory. Seven protomers corresponding to protonation of the phenol oxygen, ring oxygen, carboxyl oxygen, or the benzene ring at four possible positions were identified. Interestingly, the comparison of the experimental IR spectrum with the computed spectra clearly shows that Trolox is protonated on the benzene ring, whereas protonation of the oxygen atoms is improbable based on the spectral match and energetics (Figure C6). The band at 1800 cm^{-1} in the experimental spectrum is diagnostic for a C=O stretching vibration of the carboxylic acid. Protonation of the carboxylic acid can thus be ruled out because it would lead to the disappearance of the C=O band. Furthermore, the sharp band between 1600 and 1650 cm^{-1} in the experimental spectrum is present in all computed spectra of structures that are protonated on the aromatic ring. It corresponds to C=C vibrations of the non-aromatic carbon scaffold. The band above 1200 cm^{-1} was assigned to the O−H bending vibration of the phenol group, whereas the band below 1200 cm^{-1} might correspond to the O−H bending vibration of the carboxylic acid.

Based on the relative free energies and spectral match, the protomer shown in Figure 6.11c is the most probable structure. Its free energy is lowered by 11 kJ mol^{-1} relative to the energetically second lowest protomer. However, the presence of a second protomer cannot be ruled out, because the computed IR spectra of all four structures protonated on the aromatic ring match with the diagnostic bands. The ^{TM}CCS values computed based on the trajectory method for all four protomers (93–94 $Å^2$) also match very well with the experimental value (94 $Å^2$). In sum, the experimental data unambiguously show that Trolox is protonated on the benzene ring. Although protonation of the ring breaks its aromaticity, it is still energetically favored over protonation of the oxygen atoms because the positive charge is well-stabilized by the phenol and dihydropyrane oxygens.

The gas-phase IR spectrum of the fragment at *m/z* 205 was recorded in the 1000–1700 cm^{-1} range (Figure 6.11d). The most intense band is observed below 1600 cm^{-1}, which is indicative of a C−O stretching vibration with partial double bond character. Accordingly, the structure which provides the best spectral match features an intact chromane scaffold with the positive charge being stabilized on the ring oxygen (Figure C7). The phenol oxygen is protonated, which is reflected in the O−H bending vibration at 1200 cm^{-1}. Hence, the phenol oxygen does not participate in the fragmentation and charge transfer, whereas the ring oxygen stabilizes the positive charge upon neutral loss of CO_2H_2.

The net loss of CO_2H_2 could proceed *via* an initial loss of water followed by decarbonylation, as previously suggested for small organic carboxylic acids.[421] To confirm this hypothesis, transition states and activation barriers were computed by DFT. For the initial loss of water, the proton must be transferred from the aromatic ring to the carboxyl group. The computed activation barrier for the reaction is reasonably low (60 kJ mol^{-1}). Once the carboxyl group is protonated, water can be formed by a proton transfer between the two oxygen atoms (Figure 6.11e). The protonated carboxylic acid is approximately 30 kJ mol^{-1} higher in energy (ΔF) than the lowest-energy protomer, but provides the optimal geometry for the formation of water. The reaction mechanism includes the formation of a ketone, which readily dissociates in the form of CO to yield the spectroscopically observed product ion (*m/z* 205). The computed energy barriers are readily achievable in the ion source.

The proposed mechanism was further supported by a molecular dynamics simulation of the CID process using QCxMS.[317,320] The most stable protonated Trolox precursor from Figure 6.11c and the protonated carboxylic acid precursor (first structure in Figure 6.11e) were subjected to the CID simulation. The Trolox precursor protonated on the aromatic ring yields only few fragment ions of *m/z* 205, which do not correspond to the spectroscopically confirmed structure (Figure C8). In contrast, the protonated carboxylic acid yields abundant fragment ions with the correct structure resulting from the loss of CO_2H_2 (Figure C8).

This first example illustrates that functional groups and structural elements of fragments can be deduced from the position of diagnostic bands including O—H bending vibrations (approx. 1200 cm^{-1}), C—O stretching vibrations with double bond character (> 1550 cm^{-1}), and C=O stretching vibrations of carboxylic acids (approx. 1800 cm^{-1}). As will be shown in the following, the vibrational frequencies of specific functional groups are reproducible throughout different fragment structures and allow to reduce the pool of theoretical structures to a few eligible candidates featuring the required structural elements. Furthermore, the reaction studied in this section highlights that fragmentation does not necessarily start from the most stable precursor ion. The dynamics of mobile protons can generate higher-energy protomers that provide favorable geometrical conditions for subsequent fragmentation reactions.

Negative ion mode: decarboxylation and radical fragmentation. In contrast to the fragmentation in positive ion mode, the fragmentation behavior of Methyltrolox in negative ion mode is significantly affected by the additional methyl group on the phenol oxygen. The MS/MS spectra of deprotonated Trolox and Methyltrolox differ substantially (Figures 6.12a and b). Deprotonated Trolox yields one major fragment at *m/z* 205 resulting from decarboxylation. The second, minor fragment observed in the MS/MS spectrum corresponds to the retro-Diels-Alder product (*m/z* 163). On the contrary, deprotonated Methyltrolox yields a range of radical fragments by sequential neutral loss of methyl radicals and decarboxylation. Interestingly, decarboxylation of the $[M{-}H]^-$ ion only occurs with the simultaneous loss of a methyl radical. The fragments highlighted in bold in the MS/MS spectra are investigated in the following.

Intriguingly, neutral loss of CO_2 from deprotonated Trolox yields a fragment of identical *m/z* as the main fragment previously observed in positive ion mode. However, the CCS of the anion is 4 $Å^2$ larger than that of the cation, indicating that the structure is less compact than the closed-ring structure identified in positive ion mode. In the IR spectrum of the anion, the most intense vibration is observed below 1500 cm^{-1}, which corresponds to the C—O stretching vibration of a phenolate that involves C=C stretching vibrations of the aromatic ring (Figure 6.12c). A second diagnostic band is located below 1200 cm^{-1}, which is indicative of the O—H bending vibration of a hydroxyl group. Accordingly, the best match is obtained for a *para*-hydroxyl phenolate resulting from opening of the dihydropyrane ring (Figure C9). The ring opening reaction is consistent with the observed increase in CCS due to the formation of a flexible hydrocarbon chain which renders the structure less compact.

An energetic evaluation of deprotonated Trolox precursor ions suggests that the negative charge is initially localized at the carboxyl rather than the less acidic phenol group. Hence, the negative charge is expected to be transferred from the carboxylate to the ring oxygen, which is

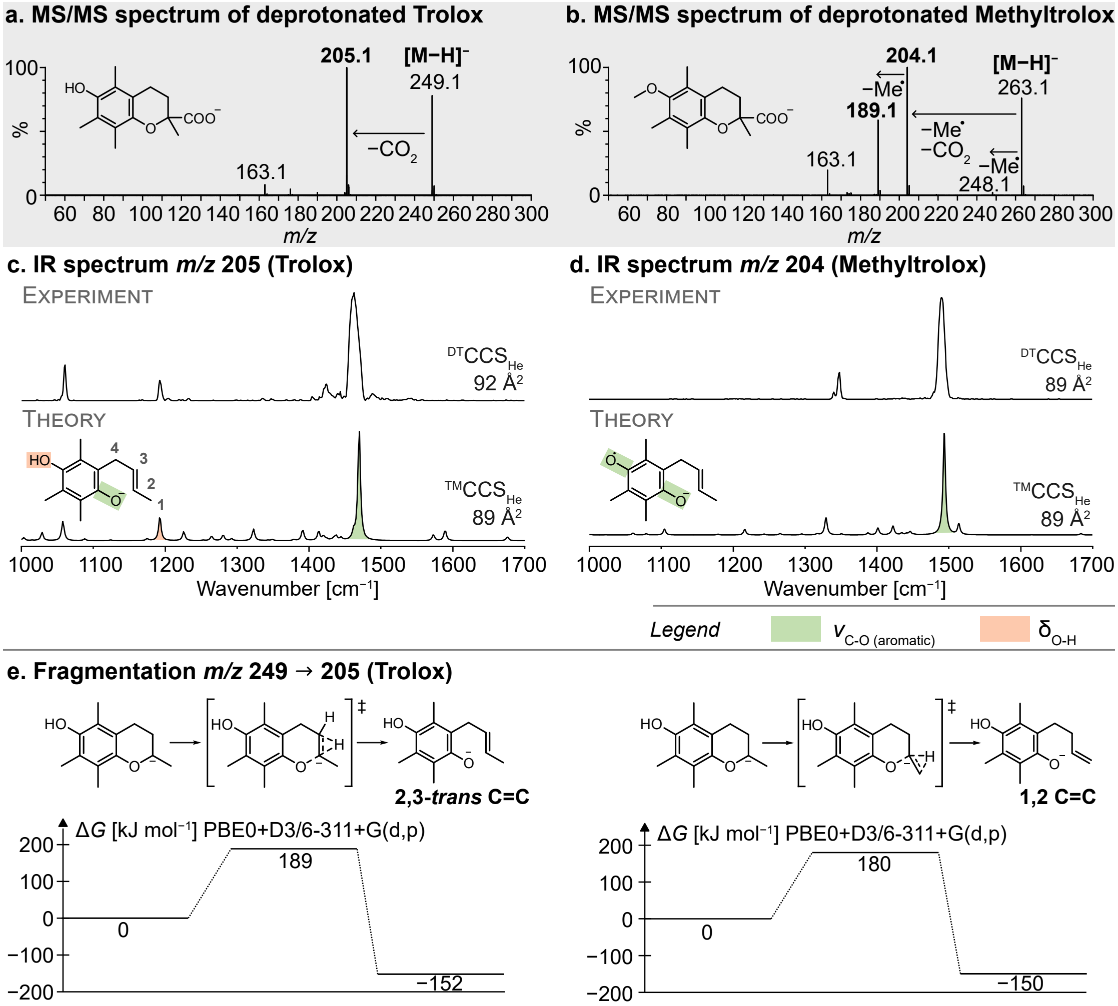

Figure 6.12: Collision-induced dissociation of deprotonated Trolox and Methyltrolox. **a.** Deprotonated Trolox undergoes neutral loss of CO_2. **b.** Deprotonated Methyltrolox undergoes radical fragmentation. The fragment at *m/z* 163 is derived from a retro-Diels-Alder reaction. **c,d.** The IR spectra of the fragments resulting from decarboxylation of Trolox and Methyltrolox are similar. The fragments feature the same basic structure and result from analogous dissociation reactions. **e.** The dissociation reactions involve the generation of a new C=C bond, which can be formed at two different positions (2,3 and 1,2). The corresponding reaction profiles are exemplarily shown for Trolox.

accompanied by ring opening. The CID simulation of deprotonated Trolox in QCxMS yields abundant fragment ions resulting from decarboxylation (Figure C10, top panel). The generated fragments feature an intact chromane scaffold with a tertiary carbanion at the original position of the carboxylic acid (first structure in Figure 6.12e). After proton transfer from either of the two neighboring carbon atoms, the dihydropyrane ring can open to stabilize the negative charge on the ring oxygen (Figure 6.12e). The emerging C=C bond in the aliphatic chain can thus be formed at two different positions to yield either a terminal (1,2) alkene or a 2,3-*cis* or -*trans* alkene (*cf.* Figure 6.12c for numbering of carbon atoms). The geometry of the 2,3 C=C bond depends on the ring conformation of the starting structure. As shown in Figure 6.12e, the formation of the product ions featuring a 1,2 or 2,3-*trans* C=C bond have comparable activation energies. The isomers cannot be distinguished based on their computed harmonic IR spectra and their coexistence is probable (Figure C9). The spectral match for the 2,3-*trans* isomer is shown in Figure 6.12c because it has the lowest computed free energy.

Methyltrolox features only one acidic proton at the carboxyl group that can be abstracted during ionization in negative ion mode, yielding a carboxylate. The energy required for the abstraction of a methyl radical from the phenol oxygen is reasonably low (ΔG = 125 kJ mol^{-1}) and can be followed by CO_2 abstraction (ΔG = 80 kJ mol^{-1}). Both fragmentation reactions proceed without a transition state. The sequential demethylation and decarboxylation of the deprotonated precursor ion result in an odd-electron fragment at *m/z* 204, which yields a similar IR spectrum as the decarboxylated Trolox fragment at *m/z* 205 (Figure 6.12d). Comparison with computed structures confirmed that the scaffold of the two fragment structures is identical. However, the phenol oxygen in the Methyltrolox fragment bears an unpaired electron instead of a hydrogen (Figure C11). The absence of a hydroxyl group translates into the absence of a vibrational band at 1200 cm^{-1}. It is important to note that the unpaired electron is well-stabilized between the two oxygens and the aromatic ring. The structure is strikingly similar to vitamin E phenoxyl radicals in solution, which stabilize unpaired electrons and thus break radical chain reactions to protect lipid membranes from oxidation.[422] The exceptional stability of the radical fragment explains why such an ion is formed by CID, which, unlike electron-based fragmentation methods, rarely yields radical fragments.

The molecular dynamics simulation of the CID process of deprotonated Methyltrolox does not reflect the experimentally observed behavior, but mainly yields decarboxylated even-electron fragments and low amounts of a decarboxylated and demethylated closed-ring radical anion at *m/z* 204 (Figure C10, middle panel). To investigate the radical fragmentation pathways, QCxMS was employed in the dissociative electron attachment mode, which was designed to simulate unimolecular dissociation of radical anions.[318] DEA of the decarboxylated and demethylated radical anion (*m/z* 204) yields abundant product ions at *m/z* 189 featuring an indanone scaffold (Figure C10, bottom panel). This even-electron fragment results from decarboxylation and loss of two methyl radicals. The computed IR spectrum and CCS of the indanone derivative are in good agreement with the experiment (Figure 6.13a, Figure C12). In particular, the C=O stretching vibration at 1650 cm^{-1} is diagnostic for the formation of a ketone. There are two additional bands at 1600 cm^{-1} and between 1500 and 1550 cm^{-1}, which can be assigned to the C=C stretching vibrations of the benzene ring and the C−O stretching vibration of the phenolate, respectively. The band at 1420 cm^{-1}, which should be present according to the computed spectrum, is only visible in the experiment at high laser energy (> 60 mJ macro-pulse energy). However, attenuated laser energy (30–40 mJ) was employed to record the IR spectrum to prevent saturation of the more intense bands.

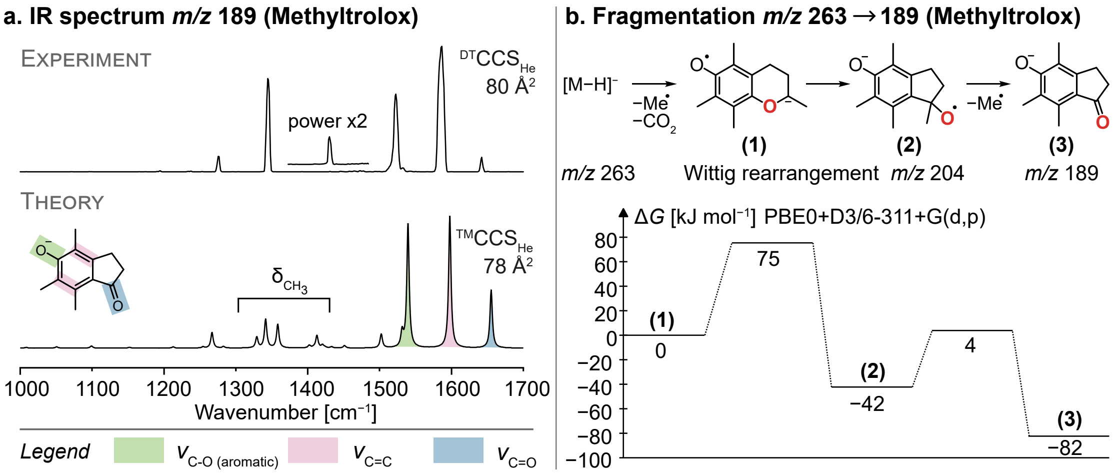

Figure 6.13: Investigation of the fragment at *m/z* 189 derived from deprotonated Methyltrolox. **a.** Gas-phase IR spectroscopy confirms that the even-electron fragment features an indanone scaffold. **b.** The proposed fragmentation mechanism involves a [1,2]-Wittig rearrangement reaction followed by the dissociation of a second methyl radical, which results in the formation of a cyclopentanone ring.

Despite the good match between experiment and theory for the fragment at *m/z* 189, the underlying rearrangement reaction is intriguing as it involves the dissociation of an aryl ether bond. Similar aryl migration reactions have been observed in solution, such as the rearrangement reaction of 6*H*-benzo[*c*]chromene to 9-fluorenol, which involves ring contraction similar to the reaction studied here.[423] The reaction is a [1,2]-Wittig rearrangement, *i.e.*, an isomerization reaction of α-deprotonated ethers to secondary or tertiary alcohols.[424] The migration of neutral and electron-poor aryl ethers in solution is thought to proceed *via* a concerted anionic intramolecular addition/elimination mechanism, in which the anion attacks the aryl group and the C−O bond is cleaved.[423]

To assess the possibility of an analogous reaction in the gas phase, the energetic profile was computed assuming a concerted addition/elimination mechanism (Figure 6.13b). The activation barriers of the two computed transition states are surprisingly low and readily achievable in the ion source (ΔG = 75 kJ mol^{-1} for the Wittig rearrangement and 46 kJ mol^{-1} for the methyl radical abstraction). Hence, the structure of the fragment has been clearly confirmed by IR spectroscopy, molecular dynamics, and DFT. This example shows that molecular dynamics simulations are highly useful to identify rearranged fragment ions that are challenging to derive by rational considerations. It is likely that the reaction shown in Figure 6.13b competes with the formation of the radical fragment at *m/z* 204 because both ions derive from the same, unstable because not spectroscopically observed, radical anion (1) by cleavage of either of the two ether bonds. An analogous Wittig rearrangement reaction cannot occur in Trolox because the phenol group cannot stabilize the negative charge. An overview of the investigated fragmentation reactions and fragment structures is provided in Figure 6.14.

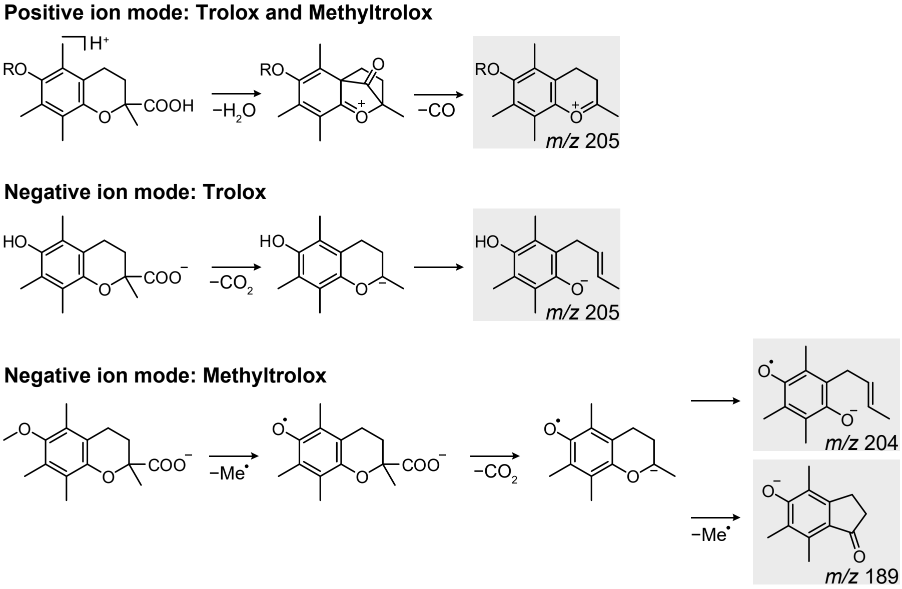

Figure 6.14: Overview of the fragmentation pathways and fragment structures identified in this work. Trolox (R = H) and Methyltrolox (R = Me) follow the same dissociation routes in positive ion mode, but their fragmentation behaviors differ significantly in negative ion mode. The fragment structures highlighted in gray were confirmed by cryogenic IR action spectroscopy.

In summary, this work demonstrates that cryogenic IR action spectroscopy is a powerful technique to gain insight into the fragmentation of small metabolites. Using a combination of IR spectroscopy, computational chemistry, and IM-MS, fragment structures and dissociation mechanisms of two chromane-derived antioxidants, Trolox and Methyltrolox, were elucidated. Due to the exceptional spectral resolution achieved by cryogenic cooling of the ions, computed structures were unambiguously matched with the experimental data without the need for reference standards. IR spectroscopy is particularly sensitive towards the oxidation state and chemical environment of oxygen in Trolox and Methyltrolox fragments and yields reproducible bands for specific functional groups. The identification of such diagnostic bands can reduce the pool of eligible candidate structures. Because isomeric computed structures can feature similar CCS, IM-MS is often not sufficiently diagnostic for structural assignment, but provides an additional structural parameter to support the spectroscopic data. Major structural differences, for example, between closed-ring and open-chain structures, were thus confirmed. In general, the results show that fragment structures do not necessarily correspond to the intuitively most straightforward or most stable candidate structure.

6.4 | Conclusions

Cryogenic IR action spectroscopy in combination with computational chemistry expands our understanding of lipid fragmentation in tandem MS by confirming, complementing, or discarding hypothetical dissociation mechanisms, which are more often than not based on rational considerations rather than experimental evidence. As shown in this work, short-lived fragments can be probed in the gas phase by high-resolution IR spectroscopy, and their structures can be assigned by comparison with computed IR spectra of candidate structures. Based on the confirmed structures, experimentally substantiated fragmentation mechanisms can be computed.

Here, we used this approach to investigate the fragmentation of glycerol-based lipids and found that they yield dioxolane fragments regardless of the nature of the headgroup and the lipid chains. Because the fragmentation behaviors differ only little between different glycerolipids, the findings obtained here for PE, PC, and DAG are likely to be transferable to other glycerol-based lipids.[98] First experimental evidence for the dioxolane structure of protonated and silver-adducted glycerolipid fragments was provided by gas-phase IR spectroscopy. Furthermore, the same technique was employed to gain further mechanistic insight into the fragmentation of silver-adducted phospholipids in order to explain intensity differences in the fragment spectra of *sn*- and double bond isomers. IR spectroscopy not only confirms proposed fragmentation mechanisms, but also reveals previously unknown intramolecular reactions leading to unexpected fragment structures, as was shown by the example of Trolox and Methyltrolox fragmentation. Fundamental understanding of fragmentation mechanisms can help to predict fragment spectra of structurally related compounds, validate predictive computational tools, and support the interpretation of fragment spectra. For example, the allylic dioxolane structure identified for the first time in this work serves to explain differences in the third-generation product ion (MS^4) spectra of silver-adducted phospholipid *sn*-isomers.[158]

While IR action spectroscopy in superfluid helium droplets cannot be easily integrated into analytical workflows for routine analysis, the technique is ideally suited for applications of fundamental interest, such as the determination of fragmentation mechanisms, where acquisition times are not a limiting factor and the highest possible resolution is desired. Contrary to other MS-based techniques, IR action spectroscopy does not rely on the presence of a specific structure motif such as $C{=}C$ bonds that are necessary, for example, for OzID and the Paternò-Büchi reaction. However, it is important to note that there is a size limit for fragments that can be investigated by IR action spectroscopy, as spectral congestion and the number of possible structures increase with the number of atoms. Furthermore, the assignment becomes exceedingly complex if two or more isomeric fragments are formed. Solutions for such challenging cases could be provided by IR-IR double resonance spectroscopy or SLIM IMS, which enable isomer- and conformer-selective gas-phase IR spectroscopy.[425,426]

7 | Summary and Future Perspectives

What is the potential of infrared action spectroscopy for future lipid analysis and what are the prospects for its integration into existing analytical workflows? This chapter summarizes the promising capabilities of infrared action spectroscopy for in-depth structural analysis of lipids demonstrated in this thesis, and points out current challenges as well as potential future applications of this technology. In particular, the latest technical innovations that bring infrared action spectroscopy closer to its establishment as an analytical technique will be highlighted.

This chapter is partly based on the following reference:

[427] C. Kirschbaum and K. Pagel, Lipid Analysis by Mass Spectrometry coupled with Laser Light, *Anal. Sens.* **2022**, e202200103.

Coupling mass spectrometry with infrared spectroscopy provides unprecedented insights into the structures of *m/z*-selected lipids. IR spectroscopy is a structure-sensitive technique that is universally applicable to all lipid classes, as it does not rely on the presence of specific functional groups like many other advanced MS-based approaches. The coupling of MS with a tunable IR laser combines the mass selectivity and sensitivity of MS with the valuable structural information obtained by IR spectroscopy. As a consequence, this approach offers significant advantages in terms of the required sample concentration and purity compared to condensed-phase analytical techniques such as NMR spectroscopy. In this thesis, IR action spectroscopy in helium droplets was used to distinguish isomeric glycolipids, determine the position and configuration of double bonds in sphingolipids and fatty acids, and reveal lipid fragmentation mechanisms in tandem MS.

Although IR action spectroscopy has demonstrated tremendous potential for the in-depth structural analysis of lipids, several technical limitations currently prevent its widespread use in analytical laboratories. The integration of IR action spectroscopy into existing analytical workflows requires considerable simplification of the instrumentation, the development of suitable turn-key benchtop light sources, and a significant reduction in acquisition times. These three key factors – instrumentation, light sources, and acquisition times – are the focus of current research and have been considerably improved recently. In terms of instrument size and complexity, IRMPD spectroscopy has clear advantages as it is straightforward to implement in commercial mass spectrometers.[246] However, the resolution of IRMPD spectra is insufficient for various applications, making the commercialization of cryogenic IR action spectroscopy highly desirable. IR action spectroscopy in helium droplets and tagging photodissociation spectroscopy require additional instrumentation for cryogenic cooling, which could be simplified by replacing two-stage closed cycle refrigerators by compact pressure-wave generators that currently reach temperatures as low as 40 K.[428]

While IR action spectroscopy in helium droplets is likely to remain a technology for fundamental research, tagging spectroscopy has the potential to be commercialized in the foreseeable future. The power of tagging photodissociation IR spectroscopy coupled with SLIM IMS has recently been impressively demonstrated with the development of a high-throughput instrument that relies on a turn-key fiber-pumped IR laser in the 3 μm range.[426] Other promising compact mid-IR light sources for tagging photodissociation spectroscopy include semiconductor-based quantum cascade lasers,[429] hybrid fiber-bulk chalcogenide-based laser systems,[430] and in particular OPO/OPA systems, which cover the entire spectral range from 800 to 4000 cm^{-1}, but require some expertise for operation.[239,248]

Using tagging photodissociation IR spectroscopy, multiple IR spectra can be recorded in parallel (multiplexing), which allows to reduce acquisition times to a few minutes or even down to seconds.[426,431] In general, acquisition times constitute a crucial bottleneck in IR action spectroscopy, preventing its integration into high-throughput LC-MS workflows. The time needed to record an IR spectrum depends on many factors including the spectral range, the scan step size, and the duty cycle of the instrument. Acquisition times usually range from a few minutes to hours, while LC separation is performed on the timescale of seconds. However, online coupling of IRMPD spectroscopy with LC-MS has recently been demonstrated by stopped-flow approaches combined with reduced irradiation times[432] or measurement of a reduced number of datapoints using kHz laser technology.[433] The reduction of datapoints is taken to the extreme by selecting only one or a few wavelengths, which allows LC-separated isomers to be probed by IR spectroscopy in an online workflow.[236] However, this approach is only applicable to known substances in targeted analyses. The separation of lipids by high-resolution IMS instead of LC is an attractive alternative because the ion mobility separation does not impose time constraints on the spectroscopic analysis. In particular, SLIM IMS has shown great potential for the separation of isomeric lipids.[108,109]

As has been repeatedly shown in this work, a major drawback of IR spectroscopy is that reference spectra are required to deconvolve IR spectra of isomeric mixtures. In other words, only those substances for which reference spectra are available can be identified in the mixture. Therefore, efforts are underway to establish a library of IR spectra that will allow targeted screening of samples for known compounds at only a few selected wavelengths.[236] For small molecules, unknown substances can be identified with some prior knowledge by computational chemistry.[405,406,434] However, in case of ambiguity, the most promising candidate structures still need to be purchased or synthesized for final structure confirmation.[313,434] Another strategy that can help in such cases is to record IR spectra of fragments instead of intact molecules to reduce spectral complexity.[405,435,436] The computational cost of predicting a large number of IR spectra *in silico* can be significantly reduced by machine learning approaches, which currently suffer from insufficient transferability to new molecule classes, but have the potential to become a game changer for computational spectroscopy.[437]

Establishing IR action spectroscopy as an analytical technique would greatly advance lipidomics and related research areas. In this thesis, IR action spectroscopy was shown to provide detailed structural information not only on isolated lipids but also on lipids in biological samples with low concentration and high mixture complexity. Therefore, the technique is particularly attractive in a clinical context, for example, for the identification of biomarkers directly from patient fluids.[405,438,439] Finally, IR action spectroscopy could also enable the identification of lipids assembled in complex conjugates with other biomolecules. For example, the identity of membrane protein-bound lipids could be determined by using hybrid ion activation techniques to dissociate the lipid from the protein-lipid complex,[440] followed by structural identification of the released lipid by IR action spectroscopy. With this approach, interactions between lipids and, for example, pharmaceutically highly relevant G protein-coupled receptors could be studied by MS and IR spectroscopy, with the ultimate goal of developing new therapeutic strategies.

Appendix A

Supplementary Material for Chapter 4: Structural Complexity of Glycolipids

Table A1: Collision cross sections of glycolipids obtained from DT-IM-MS measurements (helium, 2.2 Torr). The values are given in Å^2 (± 1 %). Only sodium adducts of β-Gb3 and β-iGb3 sphingosine and silver adducts of glycosylphytosphingosines exhibit distinguishable CCSs. Silver adduction of glycosylphytosphingosines enables the distinction of α- and β-glycosidic bonds.

Sample	**$^{DT}CCS_{He}$ [M+H]$^+$**	**[M+Na]$^+$**	**[M+Ag]$^+$**
α-GlcCer (d18:1/24:1(15*Z*))	234	233	233
β-GlcCer (d18:1/24:1(15*Z*))	235	233	233
α-GalCer (d18:1/24:1(15*Z*))	235	235	232
β-GalCer (d18:1/24:1(15*Z*))	234	235	233
α-Glc sphingosine	153	158	150
β-Glc sphingosine	152	157	153
α-Gal sphingosine	154	157	151
β-Gal sphingosine	153	158	150
α-Glc phytosphingosine	160	163	152
β-Glc phytosphingosine	161	164	157
α-Gal phytosphingosine	160	162	153
β-Gal phytosphingosine	161	164	156
β-Gb3 sphingosine	197	203	198
β-iGb3 sphingosine	199	198	196
α-Gb3Cer (d18:1/26:0)	281	283	280
α-GalDAG (14:0/14:0)	–	207	202
β-GalDAG (14:0/14:0)	–	210	204

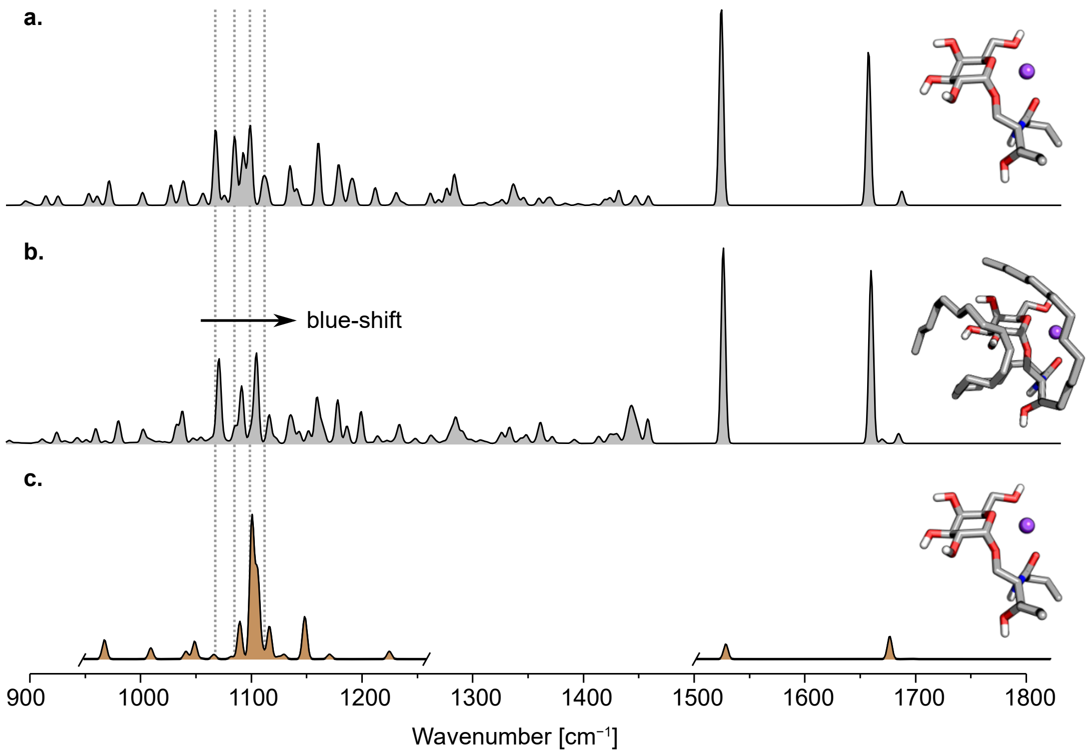

Figure A1: Comparison of the computed spectra of a low-energy conformer of [α-GalCer+Na]⁺ with **a.** lipid chains truncated to include only relevant functional groups of the lipid chain and calculated within harmonic approximation; **b.** with full lipid chains attached to the same core structure of the ion and calculated with harmonic approximation, and **c.** with lipid chains truncated and calculated including anharmonic effects. Attachment of the full lipid chains results in only minor changes to the diagnostic region (average blue-shift of 5 cm^{-1}) of the IR spectrum between 1000 and 1150 cm^{-1}. Anharmonicity of the potential has a larger impact on the IR spectrum than truncation of lipid chains.

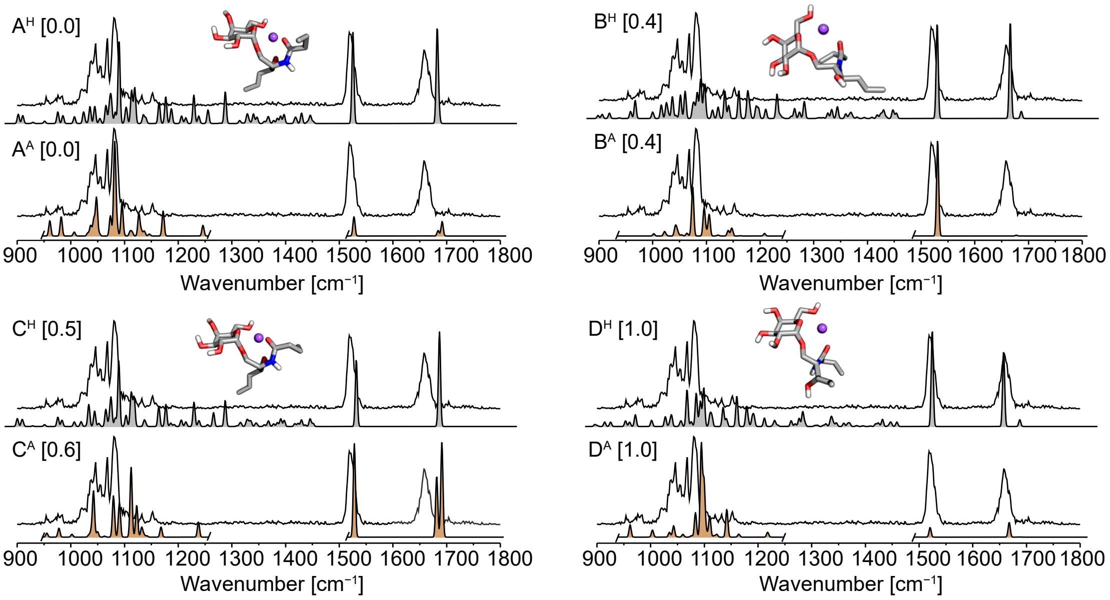

Figure A2: Comparison of the harmonic (gray, scaled by 0.965) and anharmonic (orange, red-shifted by 20 cm^{-1}) theoretical IR spectra of four low-energy conformers of $[\alpha\text{-GalCer+Na}]^+$ with lipid chains truncated to include only relevant functional groups. The experimental spectrum of the $[\alpha\text{-GalCer+Na}]^+$ cation is shown as black trace. The numbers next to the label indicate the relative electronic energy (in kcal mol^{-1}), including harmonic (H) or anharmonic (A) zero-point energy corrections. Evaluation of anharmonic vibrations only considered bands in the 1000–1150 cm^{-1} diagnostic region, amide I and II, and C=C stretching vibrations.

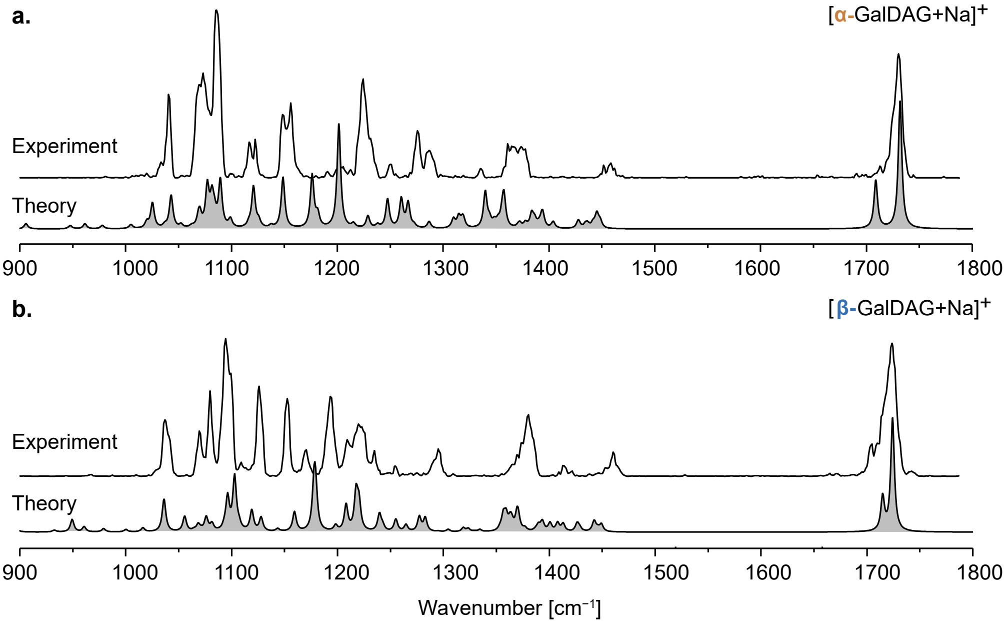

Figure A3: Experimental and computed harmonic IR spectra of $[M+Na]^+$ ions of **a.** α-GalDAG and **b.** β-GalDAG (14:0/14:0). The anomers are distinguishable by characteristic C—C, C—O, and C—H vibrations, which are difficult to model. The C=O frequencies are in good agreement with the experiment and consist of in- and out-of-phase vibrations of the two ester groups. The theoretical harmonic IR spectra were computed for lipid chains truncated to four heavy atoms and were scaled by 0.965.

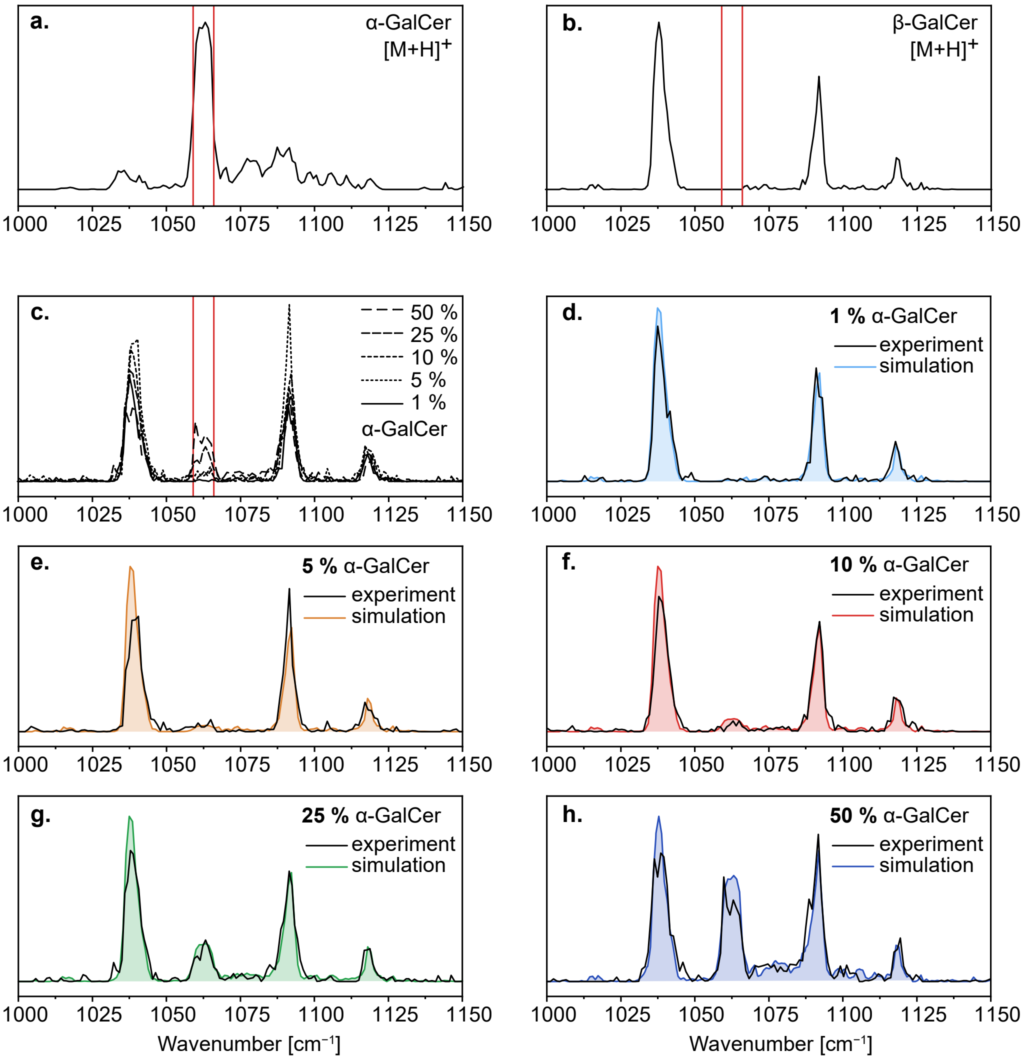

Figure A4: IR spectra of protonated α- and β-GalCer (d18:1/24:1(15*Z*)) in the fingerprint region (1000–1150 cm^{-1}). The main absorption bands of the pure isomers do not overlap (**a, b**). The decrease of α-GalCer from 50 % to 5 % is accompanied by a roughly linear decrease in the intensity of the absorption band within the set boundaries (1059–1066 cm^{-1}). At 1 %, α-GalCer cannot be detected anymore (**c**). The simulated mixture spectra generated by mathematically averaging the spectra of the pure isomers match the experimental spectra reasonably well (**d**–**h**). All spectra except for the spectra shown in panel **c** are normalized.

Appendix B

Supplementary Material for Chapter 5: Double Bond Isomers

Table B1: Collision cross sections of deoxysphingolipids obtained from DT-IM-MS measurements (helium, 2.2 Torr). The values are given in Å^{2} (± 1 %). The CCSs generally decrease with an increasing number of C=C bonds and are smaller for *Z* than for *E* double bonds.

Sample	$^{\mathrm{DT}}\mathrm{CCS}_{\mathrm{He}}$ **[M+H]**$^{+}$
1-Deoxysphinganine	120
3-Keto-1-deoxysphinganine	120
4*E*-1-Deoxysphingosine	118
5*E*-1-Deoxysphingosine	118
8*E*-1-Deoxysphingosine	117
12*E*-1-Deoxysphingosine	117
13*E*-1-Deoxysphingosine	116
14*E*-1-Deoxysphingosine	117
14*Z*-1-Deoxysphingosine	115
4*E*-3-Deoxysphingosine	120
1-Deoxyphytosphingosine	125
ω-OH-1-Deoxysphinganine	119

Table B2: Collision cross sections of non-covalent fatty acid adducts obtained from DT-IM-MS measurements (helium, 4.1–4.2 mbar). The values are given in Å^{2} (± 1 %). Predicted CCSs are indicated in brackets behind the experimental values. Some combinations were not measured (n.m.), and quantum chemical calculations of sodium adducts were only carried out for the 11*Z* isomer.

Sample	$^{\mathrm{DT}}\mathrm{CCS}_{\mathrm{He}}$				
	[FA+Na]$^{+}$	**[FA+pyr]**$^{+}$	**[FA+NMe$_{3}$H]**$^{+}$	**[FA+NMe$_{2}$H$_{2}$]**$^{+}$	**[FA+NH$_{4}$]**$^{+}$
FA 18:1(9*Z*)	120	135 (131)	136 (134)	133 (132)	124 (123)
FA 18:1(11*Z*)	120 (117)	136 (130)	135 (130)	130 (128)	124 (123)
FA 18:1(9*E*)	122	n.m.	136 (135)	136 (135)	127 (126)
FA 18:1(11*E*)	122	n.m.	n.m.	135 (135)	127 (125)

Table B3: Collision cross sections of 3-pyridylcarbinol esters and 3-picolylamides of FA 18:0 and FA 18:1 isomers. The CCSs were measured in the laboratory of Prof. Tim Causon by DT-IM-MS in nitrogen. The values are given in Å^{2} and predicted CCSs are indicated in brackets behind the experimental values. The CCSs generally decrease with increasing distance between the C=C bond and the amine and are smaller for *Z* than for *E* double bonds. Some combinations were not measured (n.m.).

Sample	$^{\mathrm{DT}}\mathrm{CCS}_{\mathrm{N2}}$	
	3-Pyridylcarbinol ester	**3-Picolylamide**
FA 18:0	202 (199)	n.m.
FA 18:1(6*Z*)	202 (194)	n.m.
FA 18:1(8*Z*)	201 (194)	202 (195)
FA 18:1(9*Z*)	199 (195)	200 (193)
FA 18:1(11*Z*)	198 (192)	200 (194)
FA 18:1(6*E*)	203 (195)	n.m.
FA 18:1(9*E*)	202 (195)	204 (198)
FA 18:1(11*E*)	201 (197)	202 (199)

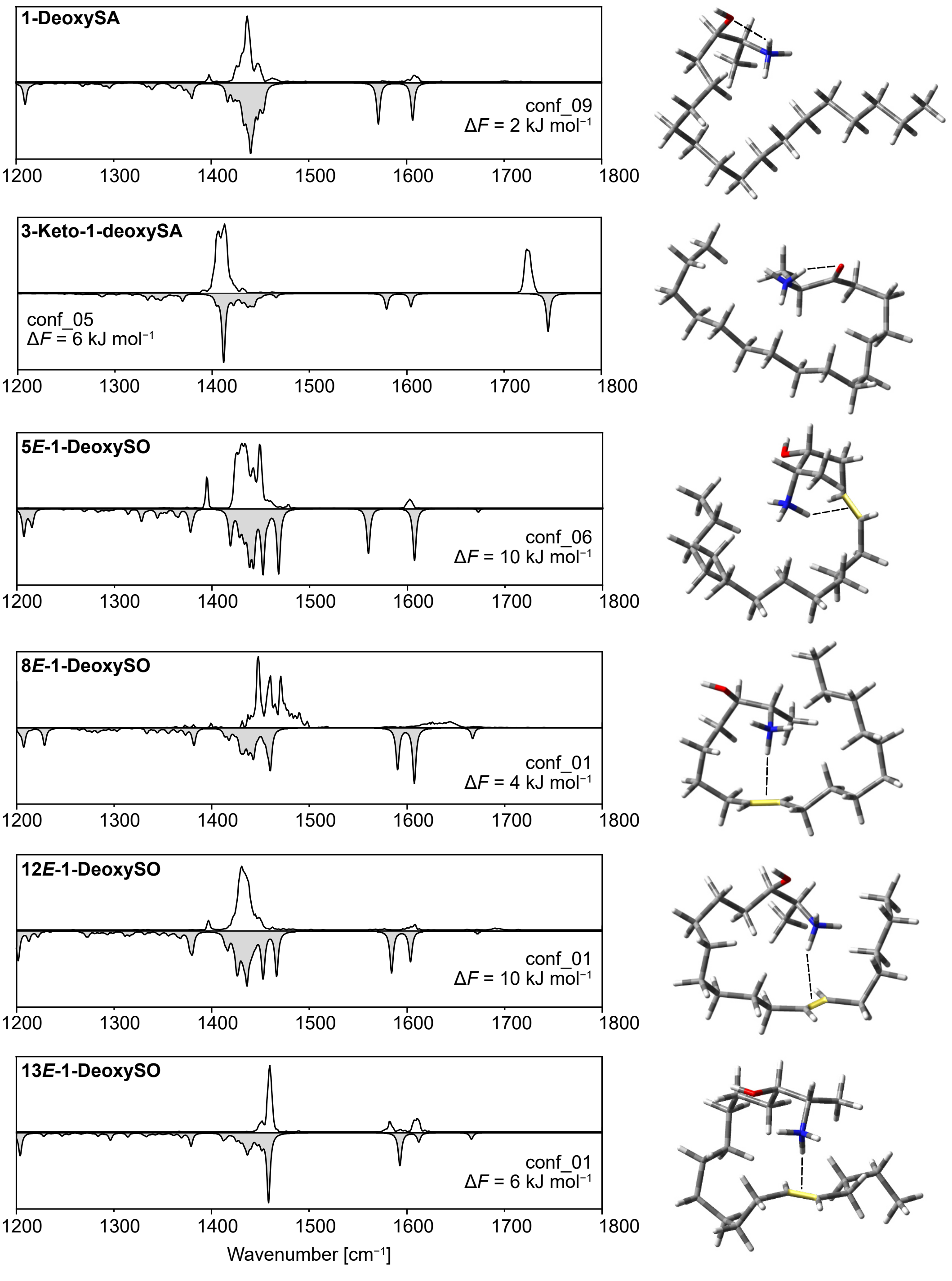

Figure B1: Experimental (transparent) and computed (gray) IR spectra and corresponding structures of 1-deoxySA, 3-keto-1-deoxySA, and several 1-deoxySO isomers with different C=C bond positions (1200–1800 cm^{-1}). The C=C bonds are highlighted in yellow and intramolecular interactions are indicated by dashed lines.

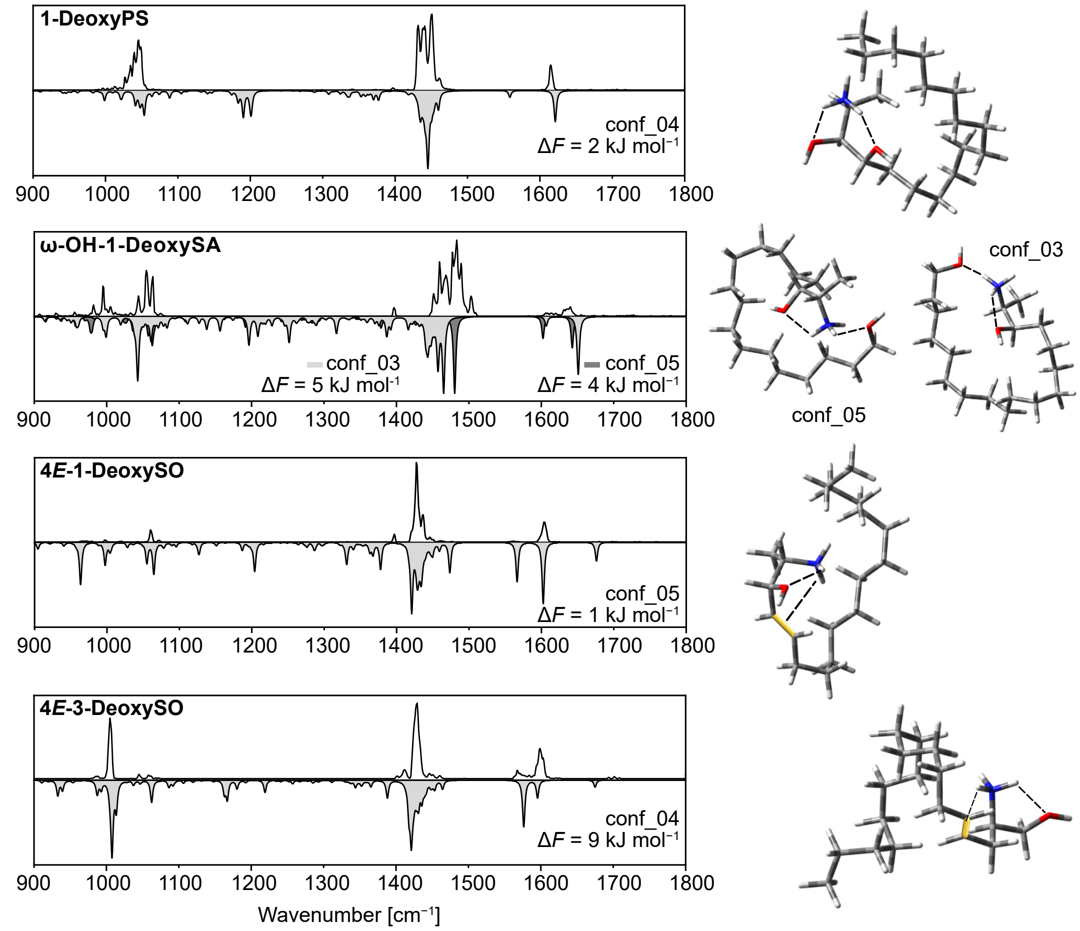

Figure B2: Experimental (transparent) and computed (gray) IR spectra and low-energy structures of deoxysphingolipids with varying hydroxylation positions. In the hydroxylation regioisomers 1-deoxyPS and ω-OH-1-deoxySA, the NH_3^+ group interacts with both hydroxyl groups. In the case of 4*E*-1-deoxySO and 4*E*-3-deoxySO, the NH_3^+ group interacts with the hydroxyl group and the C=C bond. The latter is highlighted in yellow in the computed structures.

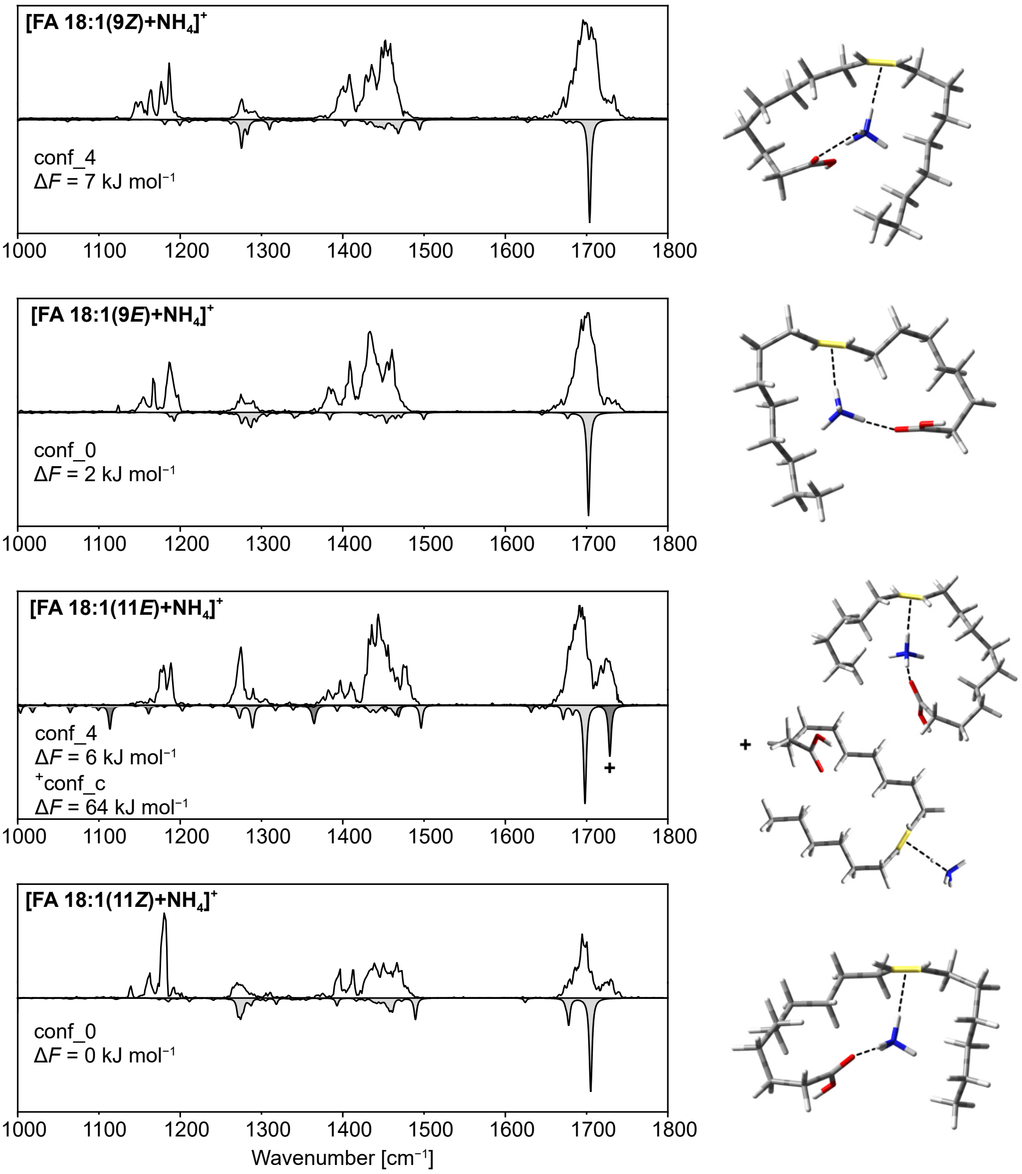

Figure B3: Experimental and computed IR spectra of non-covalent [FA 18:1+NH$_4$]$^+$ adducts. The computed IR spectra are shown as inverted traces below the experimental spectra and the three-dimensional structures of the computed conformers are depicted on the right. Interactions of the ammonium cation with the carbonyl oxygen and the C=C bond (yellow) are visualized by dashed lines. The blue-shifted carbonyl stretching vibrations (most prominent for FA 18:1(11*E*)) can be modeled only with energetically unfavored conformers.

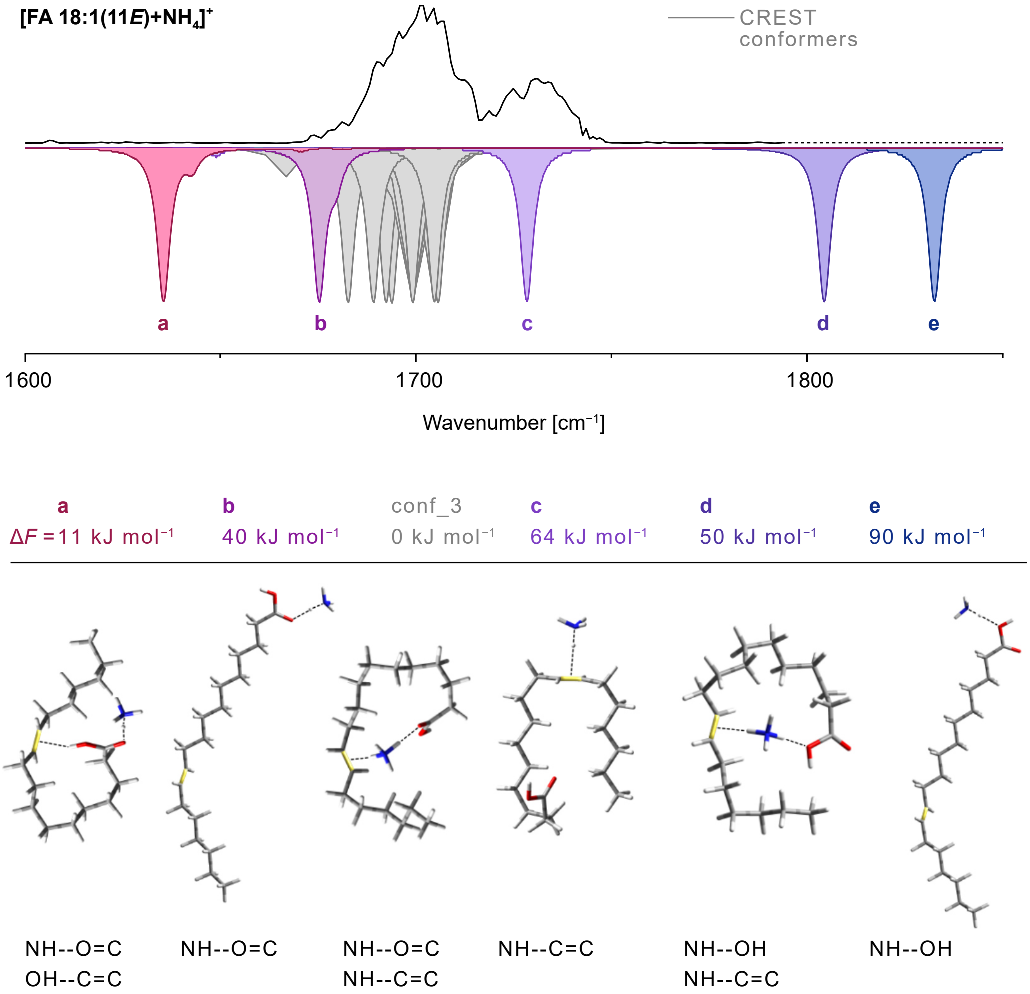

Figure B4: Empirical investigation of the influence of different structure motifs on the carbonyl stretching frequency of [FA 18:1(11*E*)+NH_4]$^+$ adducts. All conformers sampled by CREST (gray) coincide with the main absorption band in the experimental spectrum of [FA 18:1(11*E*)+NH_4]$^+$ (top). Interactions between the OH group and ammonium increase the electron density in the carbonyl bond and cause a significant blue-shift (d,e). The exclusive coordination of ammonium to the carbonyl oxygen causes a red-shift (b), which is increased by simultaneous interaction of the OH group with the C=C bond (a). The experimentally observed, blue-shifted carbonyl band probably derives from coordination of ammonium to the C=C bond (c), even though the depicted conformer is energetically unfavored. C=C bonds are highlighted in yellow, and relative free energies at 90 K refer to the lowest-energy conformer (conf_3) obtained from the CREST search.

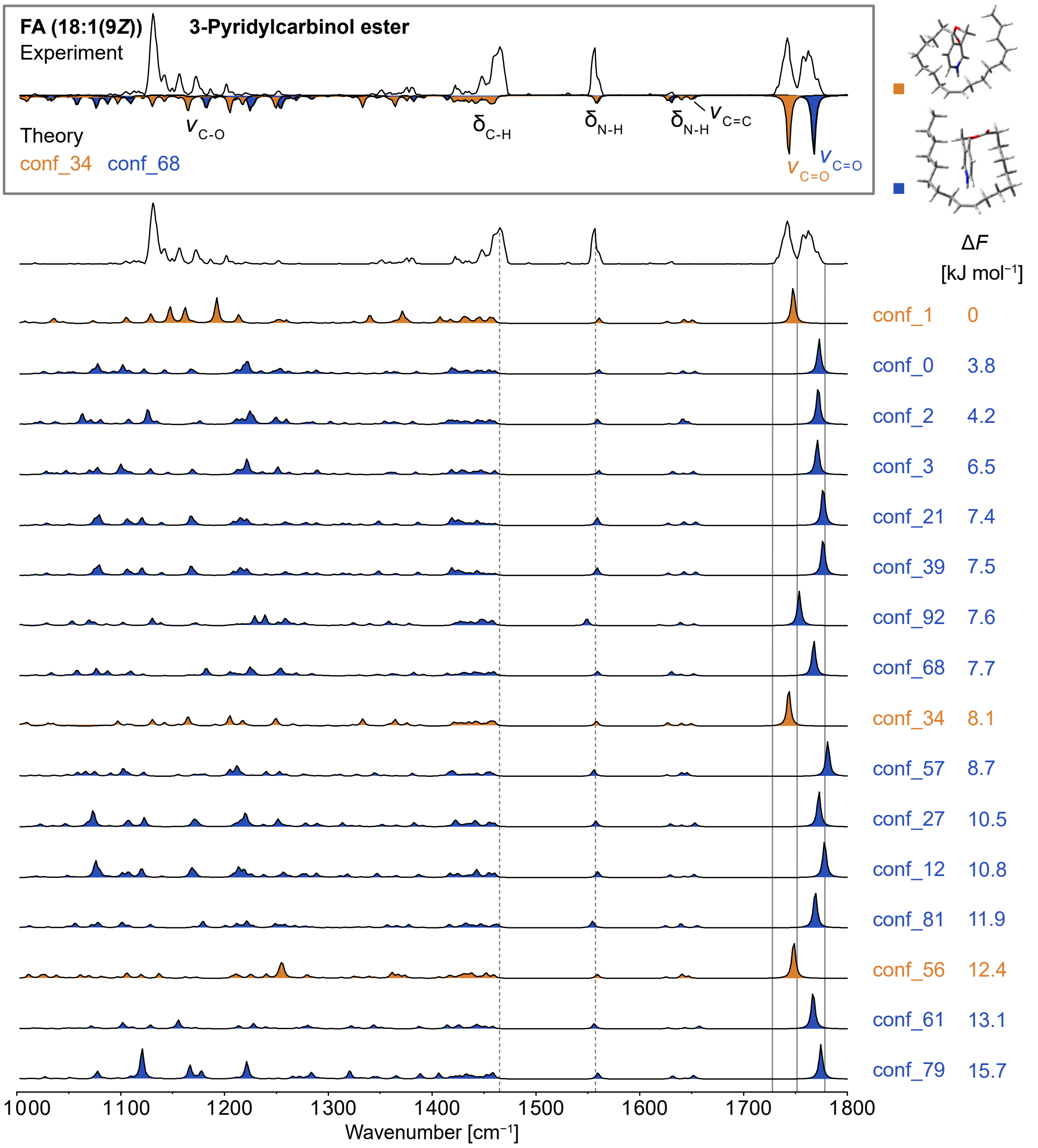

Figure B5: Gas-phase IR spectrum of the protonated FA (18:1(9*Z*)) 3-pyridylcarbinol ester (transparent) and harmonic IR spectra of computed conformers (colored). Several computed IR spectra exhibit a blue-shifted C=O stretching vibration (> 1760 cm^{-1}). The best match between the experimental and two computed spectra is shown on top with selected vibrations annotated.

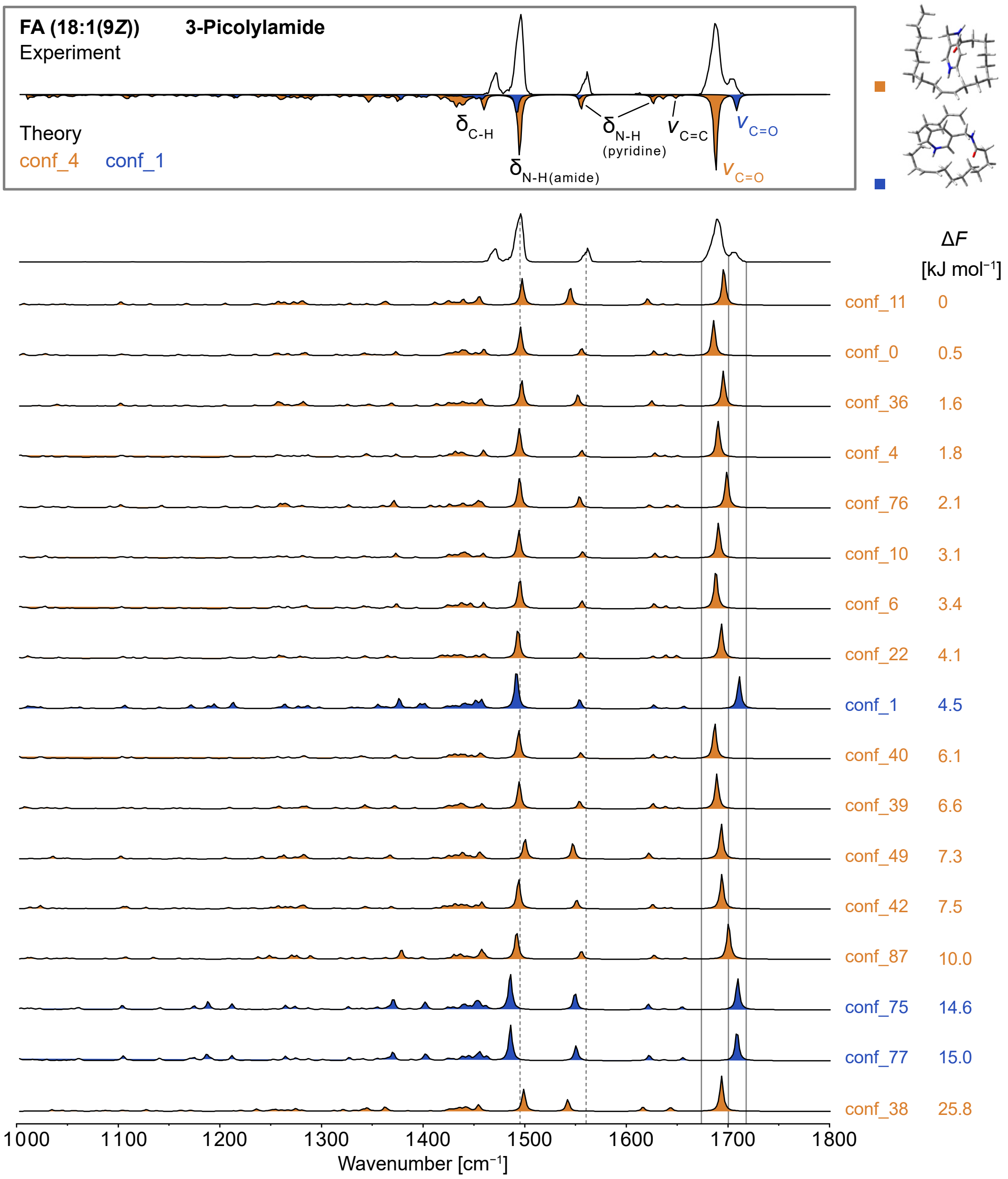

Figure B6: Gas-phase IR spectrum of the protonated FA (18:1(9*Z*)) 3-picolylamide (transparent) and harmonic IR spectra of computed conformers (colored). Several computed IR spectra exhibit a blue-shifted C=O stretching vibration (> 1700 cm^{-1}). The best match between the experimental and two computed spectra is shown on top with selected vibrations annotated.

Appendix C

Supplementary Material for Chapter 6: Lipid Fragmentation Mechanisms

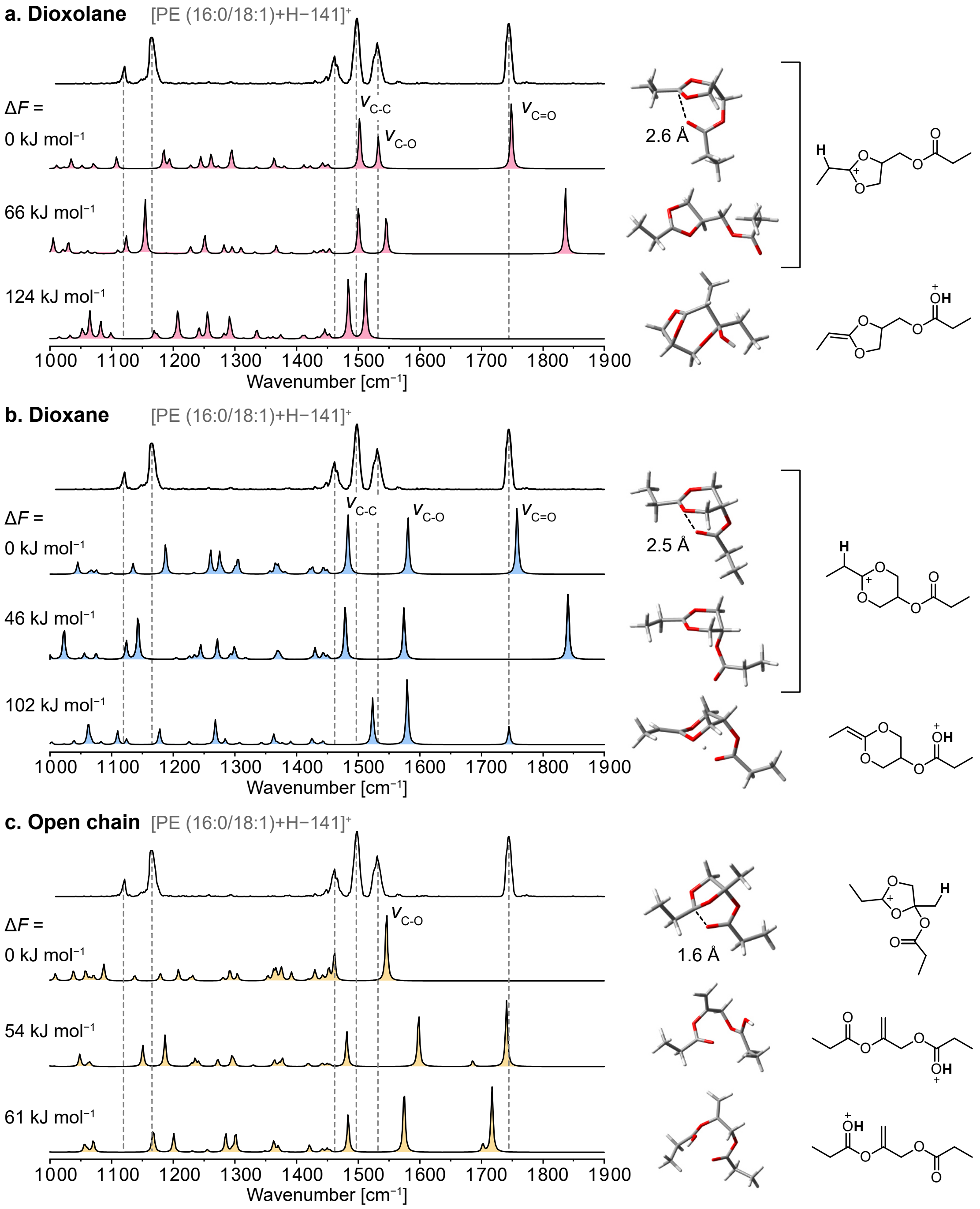

Figure C1: Experimental gas-phase IR spectrum of [PE (16:0/18:1(9*Z*))+H−141]$^+$ (transparent) and computed IR spectra (colored) of protomers of **a.** dioxolane, **b.** dioxane, and **c.** open chain model structures truncated to three carbons per fatty acid (3:0/3:0). In all cases, protonation of the C=C bond is energetically more favorable than protonation of a carbonyl oxygen. The best match with the experimental spectrum is obtained for dioxolanes that are protonated at the C=C bond and feature an interaction between the carbonyl oxygen and the positive charge. Spectra were computed at the PBE0+D3/6-311+G(d,p) level of theory, and relative free energies at 90 K refer to the most stable protomer of each fragment structure.

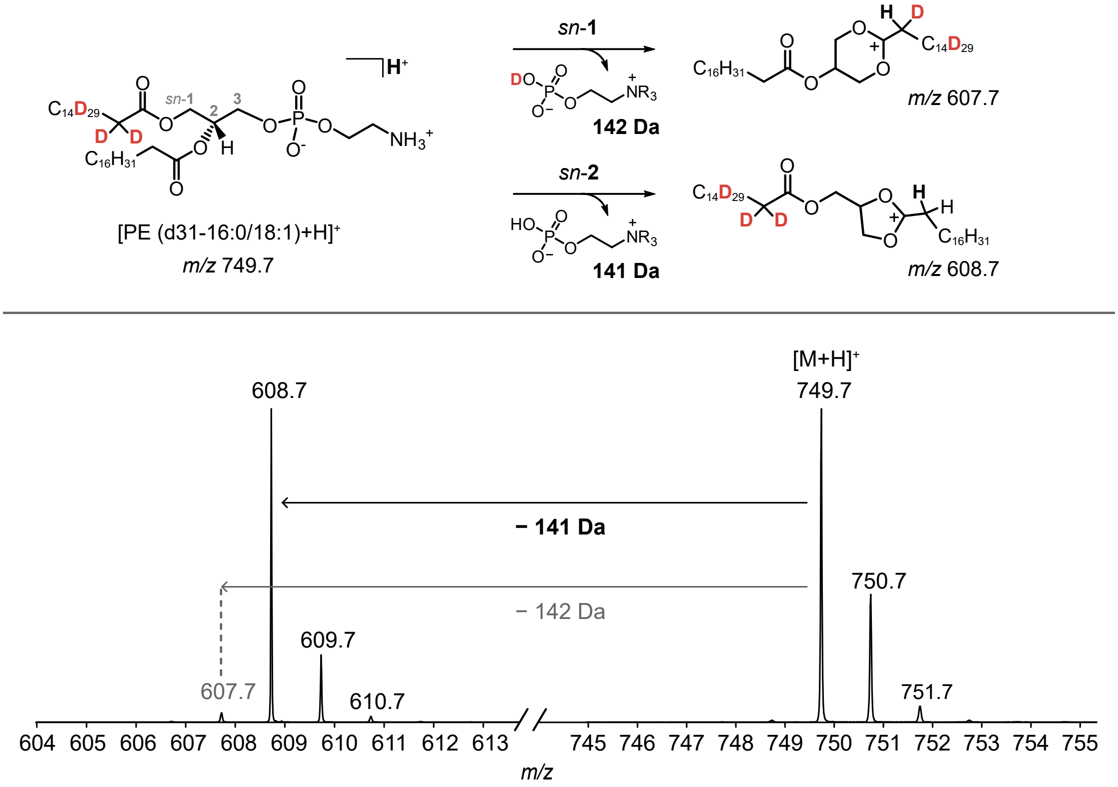

Figure C2: Collision-induced dissociation of protonated PE (d31-16:0/18:1(9*Z*)). The neutral loss of 141 Da corresponds to the formation of dioxolane fragments, whereas loss of 142 Da yields dioxane fragments *via* participation of the alpha-hydrogens of the fully deuterated *sn*-1 fatty acid. The relative fragment intensities suggest a dioxane ratio of around 3 %. The fragment spectrum was recorded on a Synapt G2-S HDMS instrument.

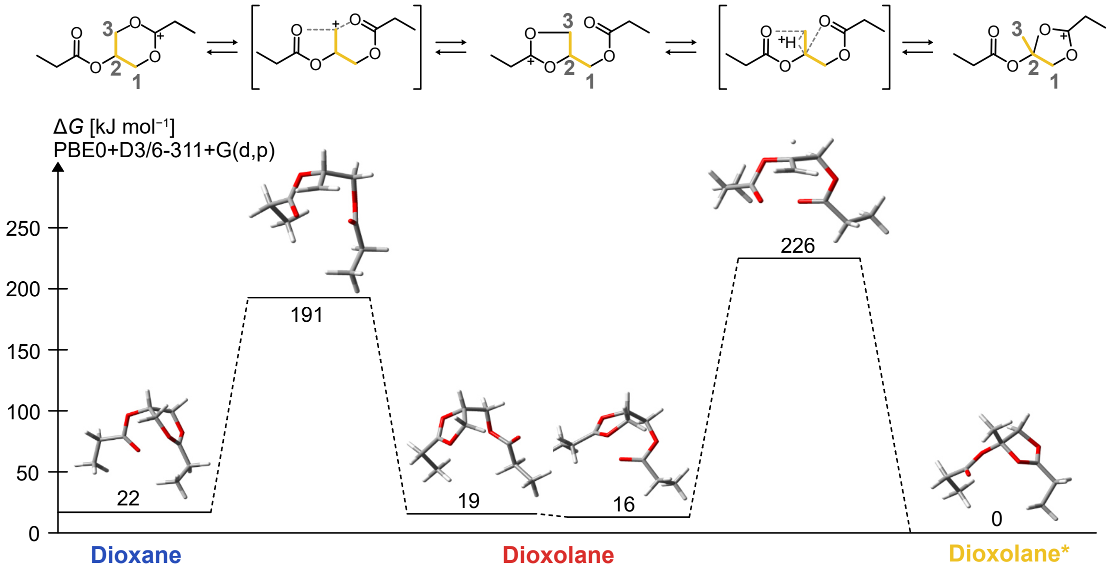

Figure C3: Energy diagram showing activation barriers (ΔG) for the interconversion between protonated dioxolane and dioxane rings computed at the PBE0+D3/6-311+G(d,p) level of theory. Bond rotation within the dioxolane marked by an asterisk yields the bicyclic structure obtained during the conformational sampling of open chain structures (*cf.* Figure C1). The dioxolane* structure is energetically favorable, but has not been observed experimentally.

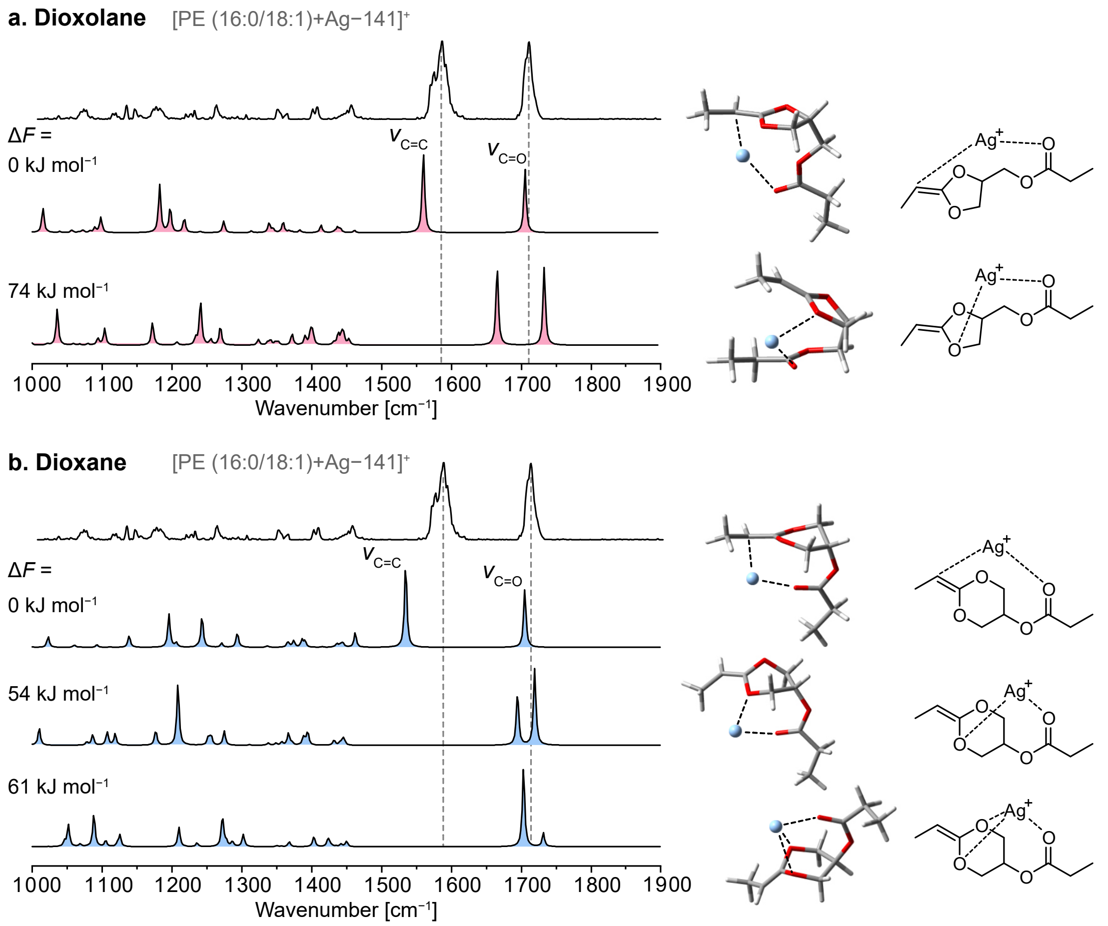

Figure C4: Experimental gas-phase IR spectrum of [PE (16:0/18:1(9*Z*))+Ag−141]+ (transparent) and computed IR spectra (colored) of **a.** dioxolane and **b.** dioxane model structures truncated to three carbons per fatty acid (3:0/3:0) with different silver coordination geometries. In the most stable conformers, the silver ion interacts with the carbonyl oxygen and the C=C bond adjacent to the ring. Spectra were computed at the PBE0+D3/6-311+G(d,p), SDD (Ag) level of theory, and relative free energies at 90 K refer to the most stable conformer of each fragment structure.

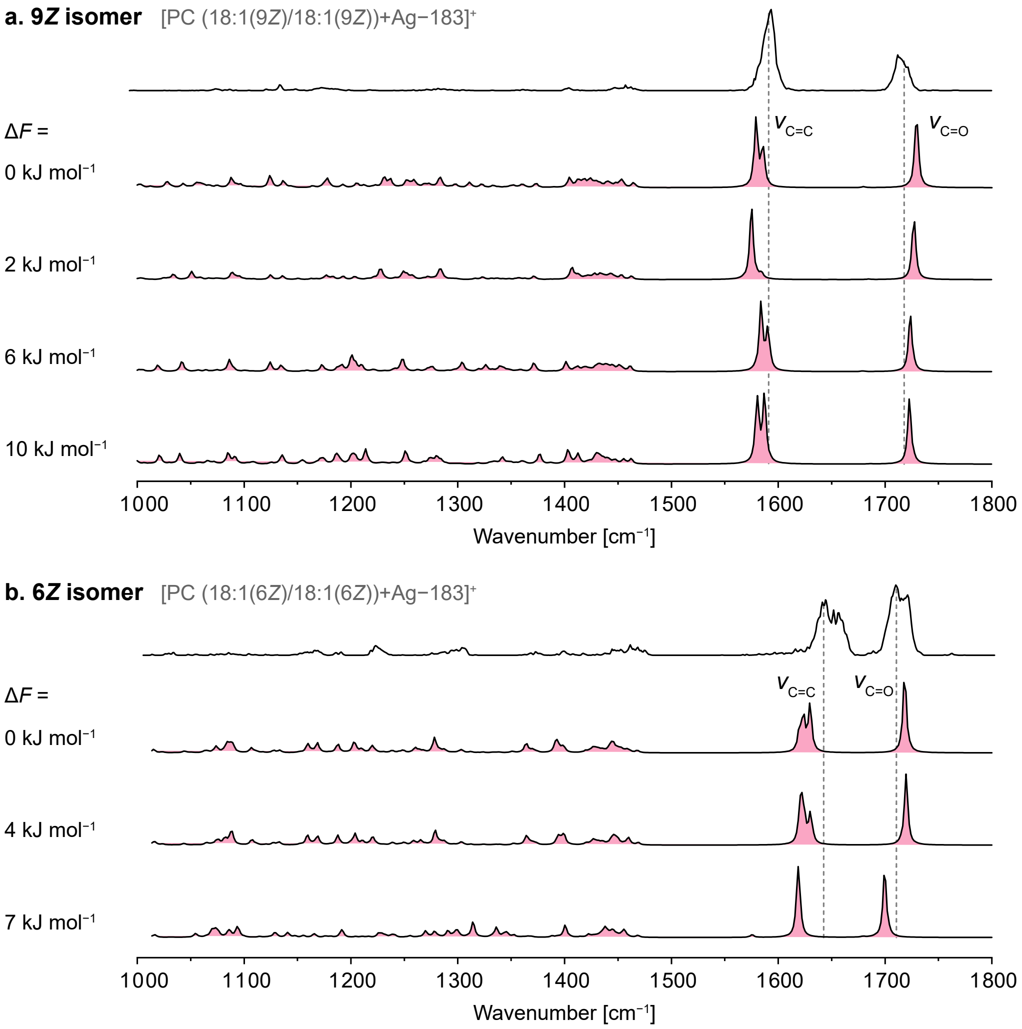

Figure C5: Experimental (transparent) and computed (colored) IR spectra of **a.** $[\mathrm{PC\,(18{:}1(9\mathit{Z})/18{:}1(9\mathit{Z}))+Ag-183}]^+$ and **b.** $[\mathrm{PC\,(18{:}1(6\mathit{Z})/18{:}1(6\mathit{Z}))+Ag-183}]^+$ fragments. The computed spectra model the band shifts depending on the position of the C=C bond reasonably well. Spectra were computed at the PBE0+D3/6-311+G(d,p), SDD (Ag) level of theory, and relative free energies at 90 K refer to the most stable conformer of each isomer.

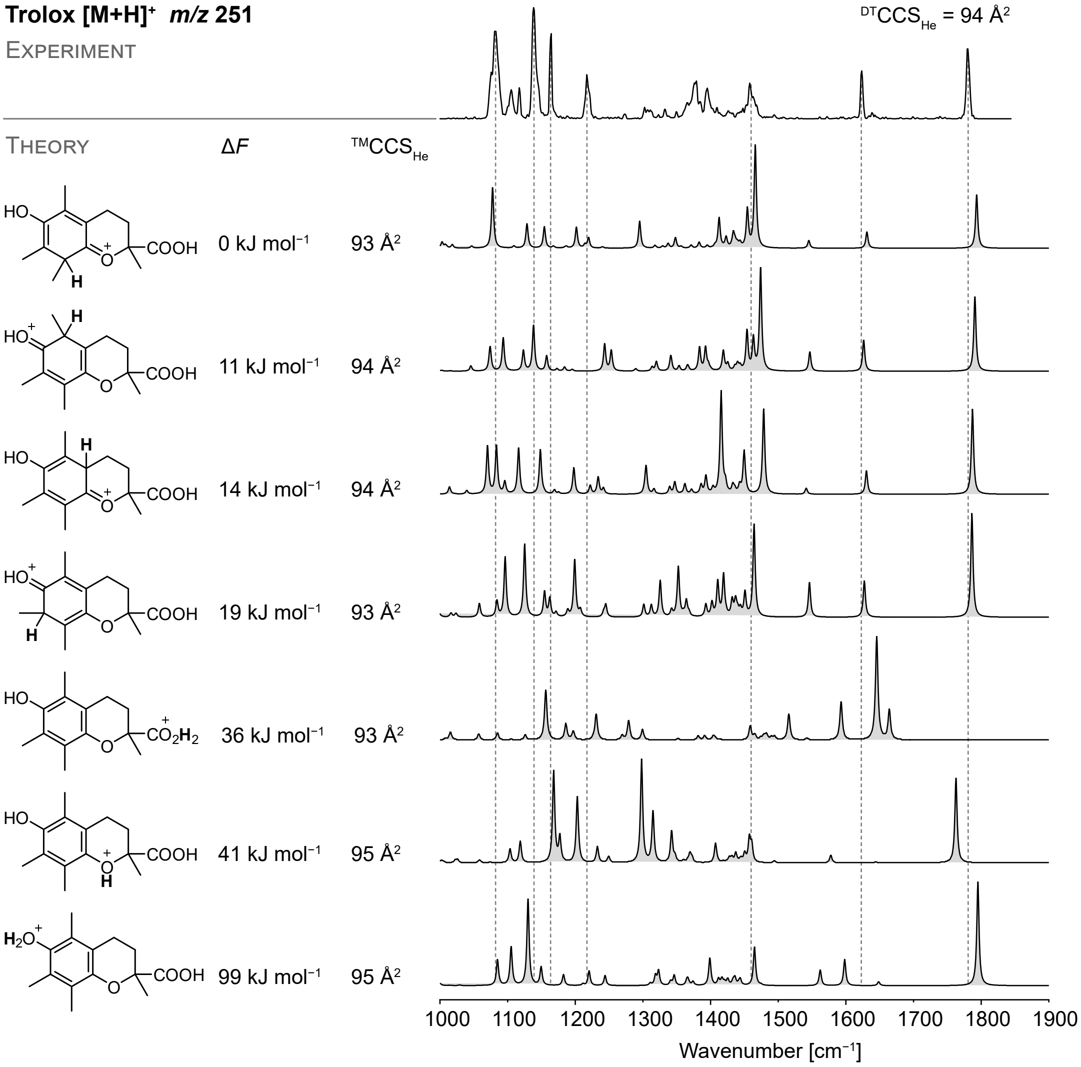

Figure C6: Experimental IR spectrum of protonated Trolox (*m/z* 251) and computed IR spectra of different protomers. The absorption bands at 1800 cm^{-1} and 1600 cm^{-1} are diagnostic for protonation of the aromatic ring. The computed structure shown on top yields the best match with the experiment. The relative free energies (90 K) and IR spectra were computed at the PBE0+D3/6-311+G(d,p) level of theory, and the CCSs were calculated based on the trajectory method (TM).

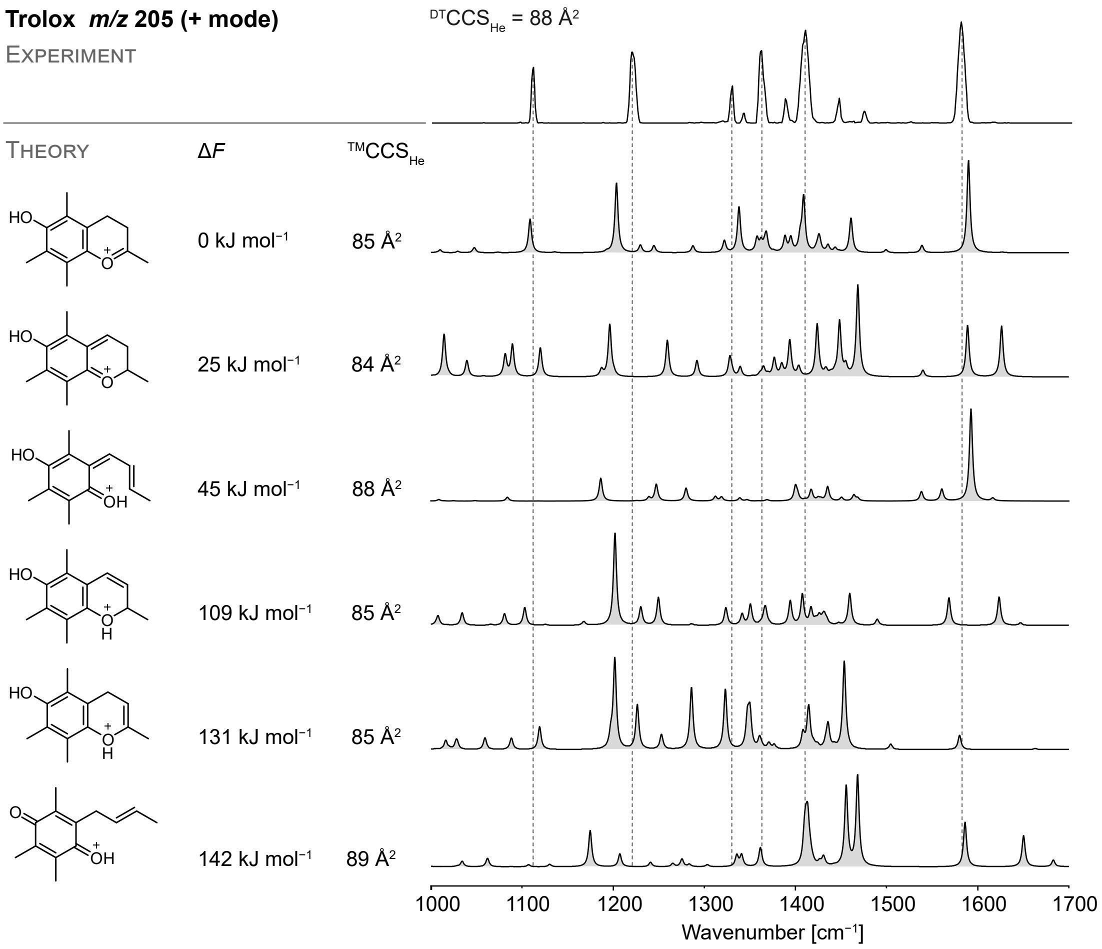

Figure C7: Experimental IR spectrum of the fragment at *m/z* 205 generated from protonated Trolox precursor ions and computed IR spectra of candidate structures. The band at 1200 cm^{-1} indicates the presence of a hydroxyl group, whereas the band at 1600 cm^{-1} corresponds to a C=O$^+$ stretching vibration. The best spectral match is shown on top. The relative free energies (90 K) and IR spectra were computed at the PBE0+D3/6-311+G(d,p) level of theory, and the CCSs were calculated based on the trajectory method (TM).

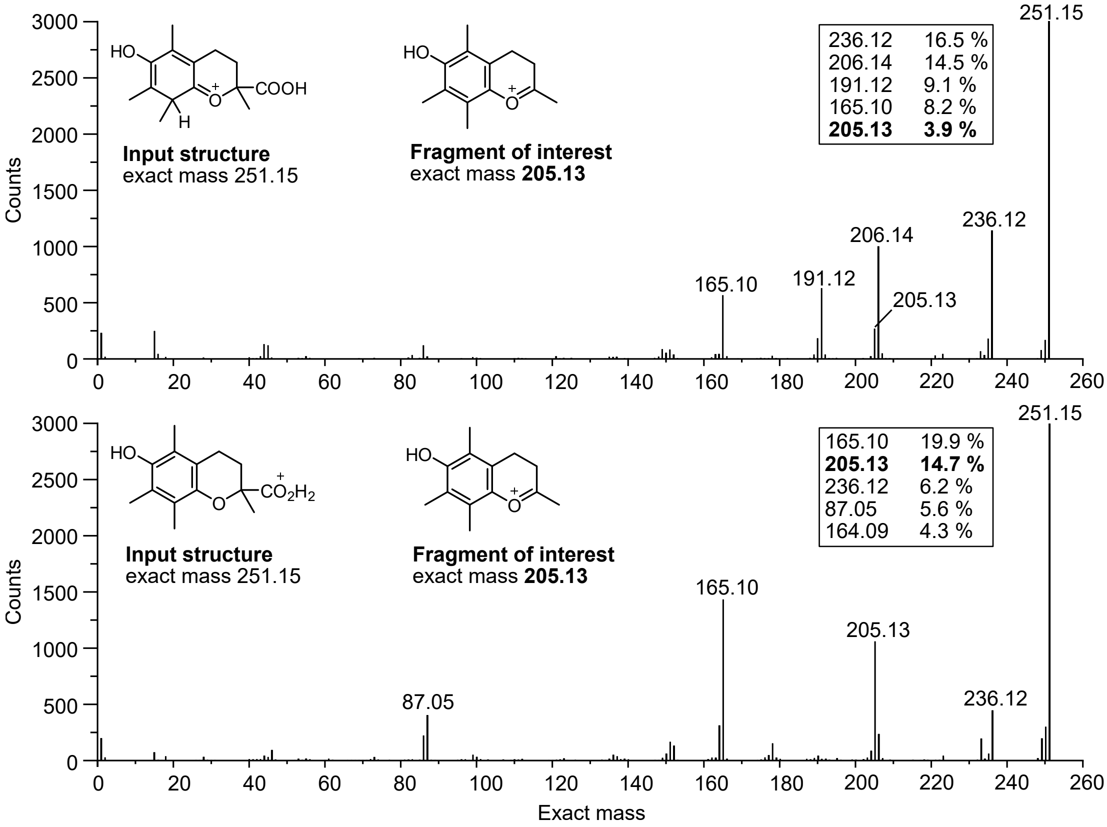

Figure C8: Simulation of collision-induced dissociation of the depicted protonated Trolox precursors in QCxMS. The exact masses of all generated structures were extracted and plotted against their abundance. The relative abundances of the most abundant fragments are shown and refer to the sum of all generated fragments (excluding the precursor). The fragment of interest (*m/z* 205) with the correct structure is only formed from the precursor structure featuring a protonated carboxylic acid (bottom panel).

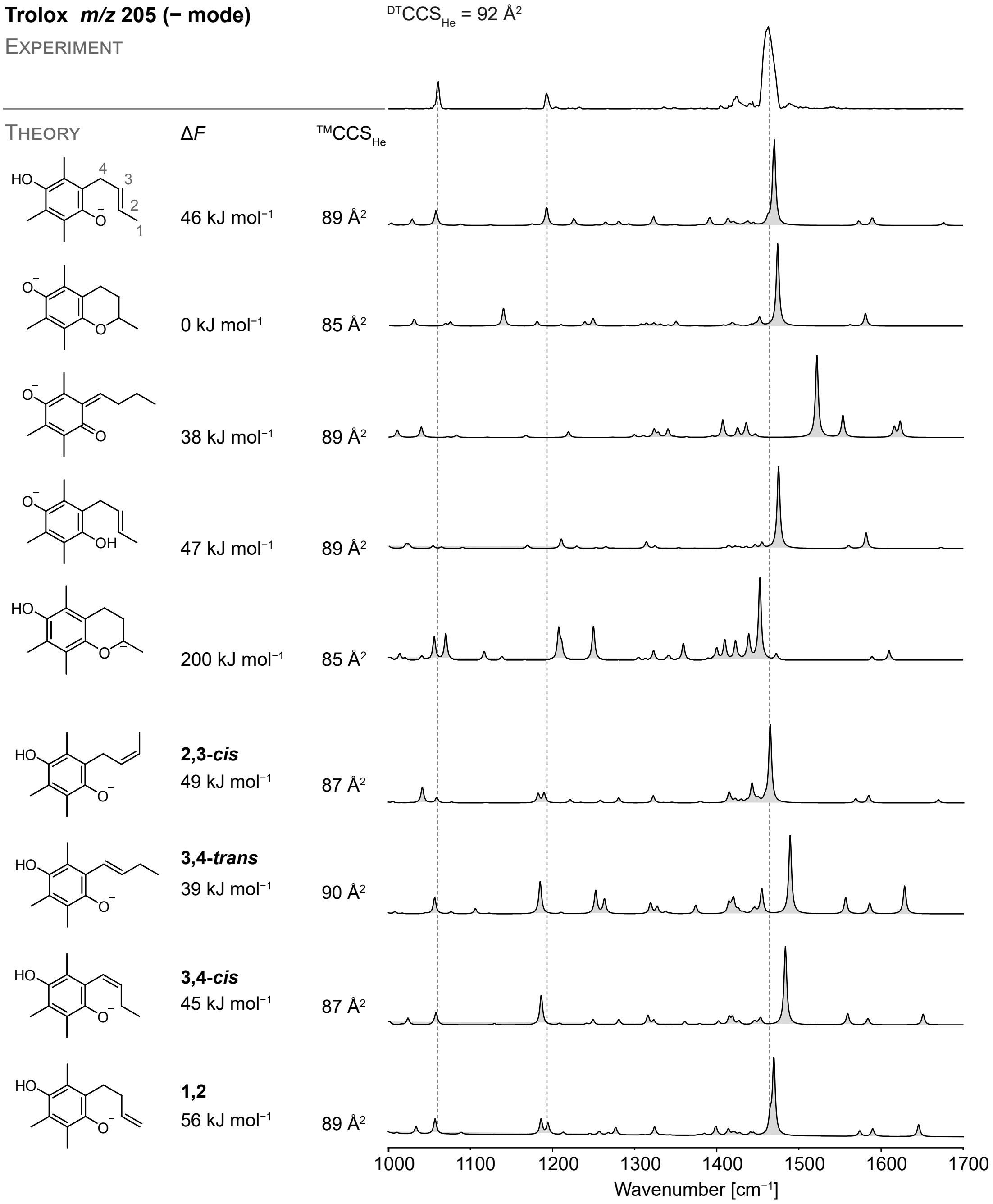

Figure C9: Experimental IR spectrum of the fragment at *m/z* 205 generated from deprotonated Trolox precursor ions and computed IR spectra of candidate structures. The band at 1200 cm^{-1} indicates the presence of a hydroxyl group, whereas the position of the main band corresponds to the frequency of a phenolic C—O stretch. The best spectral match is shown on top and does not correspond to the lowest-energy structure. Several double bond isomers of this structure are shown at the bottom. The relative free energies (90 K) and IR spectra were computed at the PBE0+D3/6-311+G(d,p) level of theory, and the CCSs were calculated based on the trajectory method (TM).

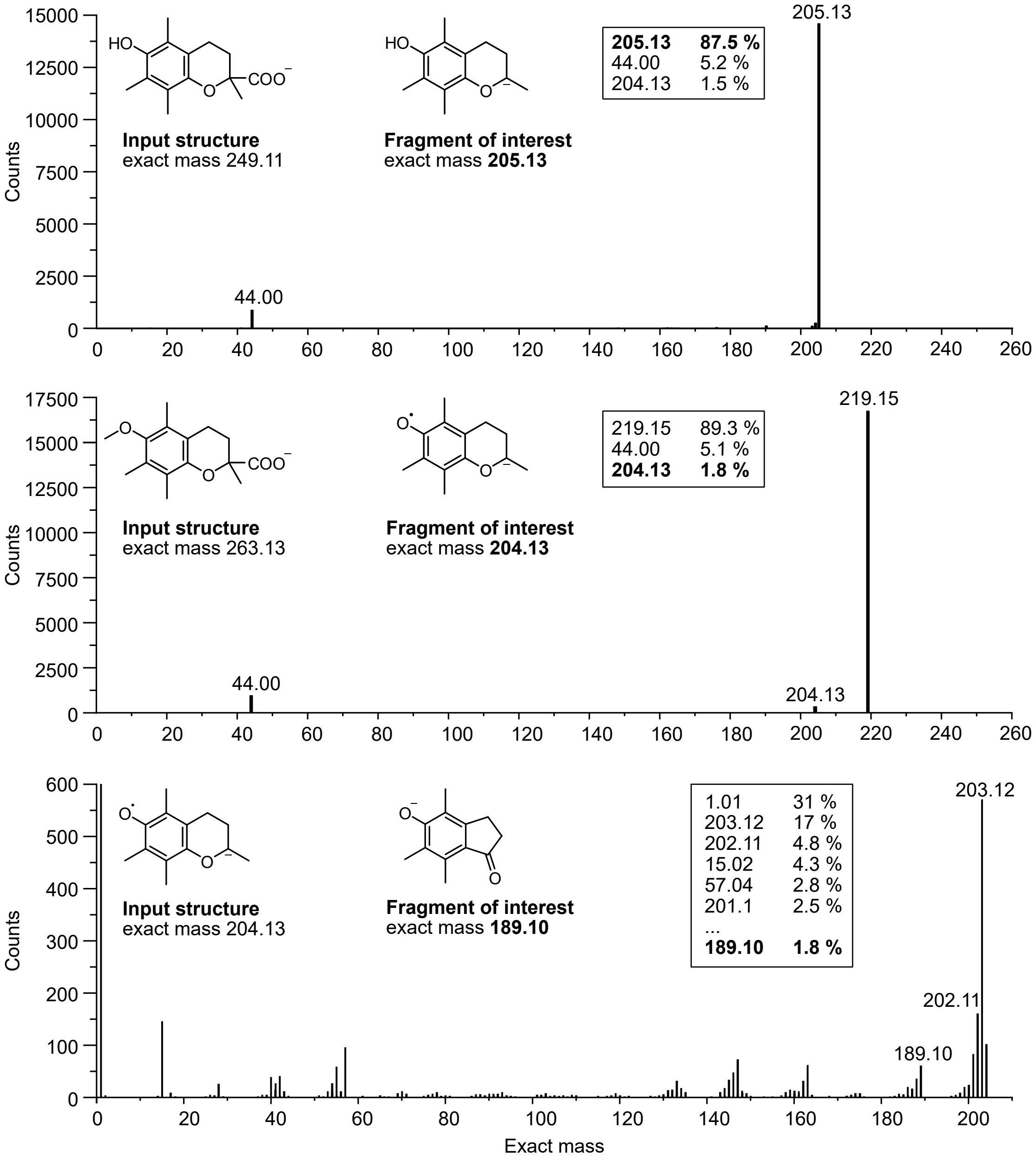

Figure C10: Simulation of the fragmentation of deprotonated Trolox and Methyltrolox in QCxMS. The exact masses of all generated structures were extracted and plotted against their abundance. Deprotonated Trolox (top panel) dissociates entirely in the CID simulation and yields the fragment of interest (exact mass = 205.13 Da) as the most abundant fragment corresponding to the depicted structure. The predominant fragmentation reaction of deprotonated Methyltrolox (middle panel) is decarboxylation without methyl radical abstraction yielding a fragment ion of *m/z* 219 and neutral CO_2 (exact mass = 44.00 Da). An additional fragment of *m/z* 204 corresponding to the depicted structure is formed in low abundance. DEA of the fragment at *m/z* 204 (bottom panel) yields the fragment of interest (*m/z* 189).

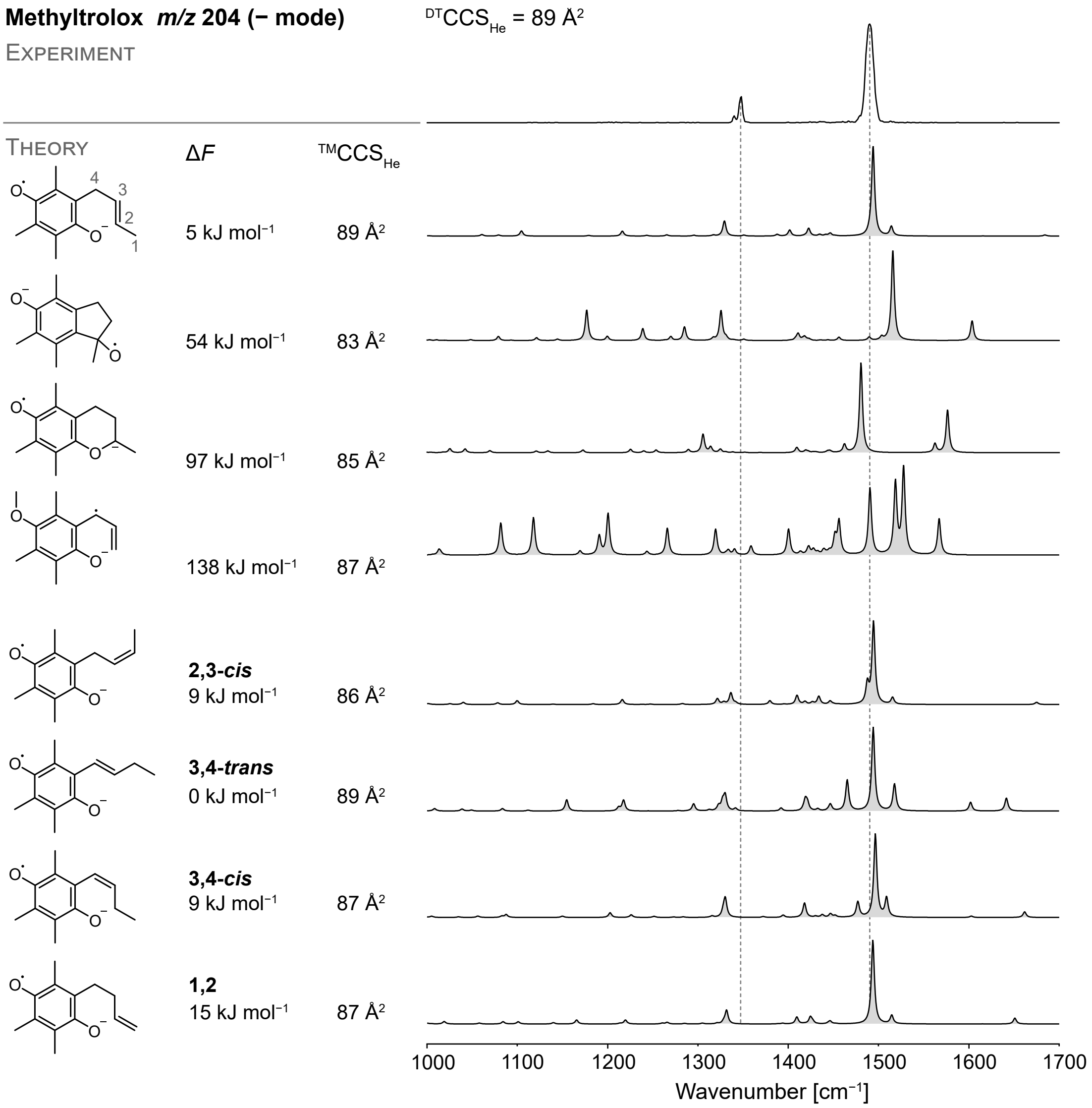

Figure C11: Experimental IR spectrum of the radical fragment at *m/z* 204 generated from deprotonated Methyltrolox precursor ions and computed IR spectra of candidate structures. The band at 1500 cm^{-1} coincides with the frequency of a phenolic C—O stretching vibration. The best spectral match is shown on top and corresponds to the most stable structure motif in which the radical and charge are delocalized in the aromatic ring. Several double bond isomers of this structure are shown at the bottom. The relative free energies (90 K) and IR spectra were computed at the PBE0+D3/6-311+G(d,p) level of theory, and the CCSs were calculated based on the trajectory method (TM).

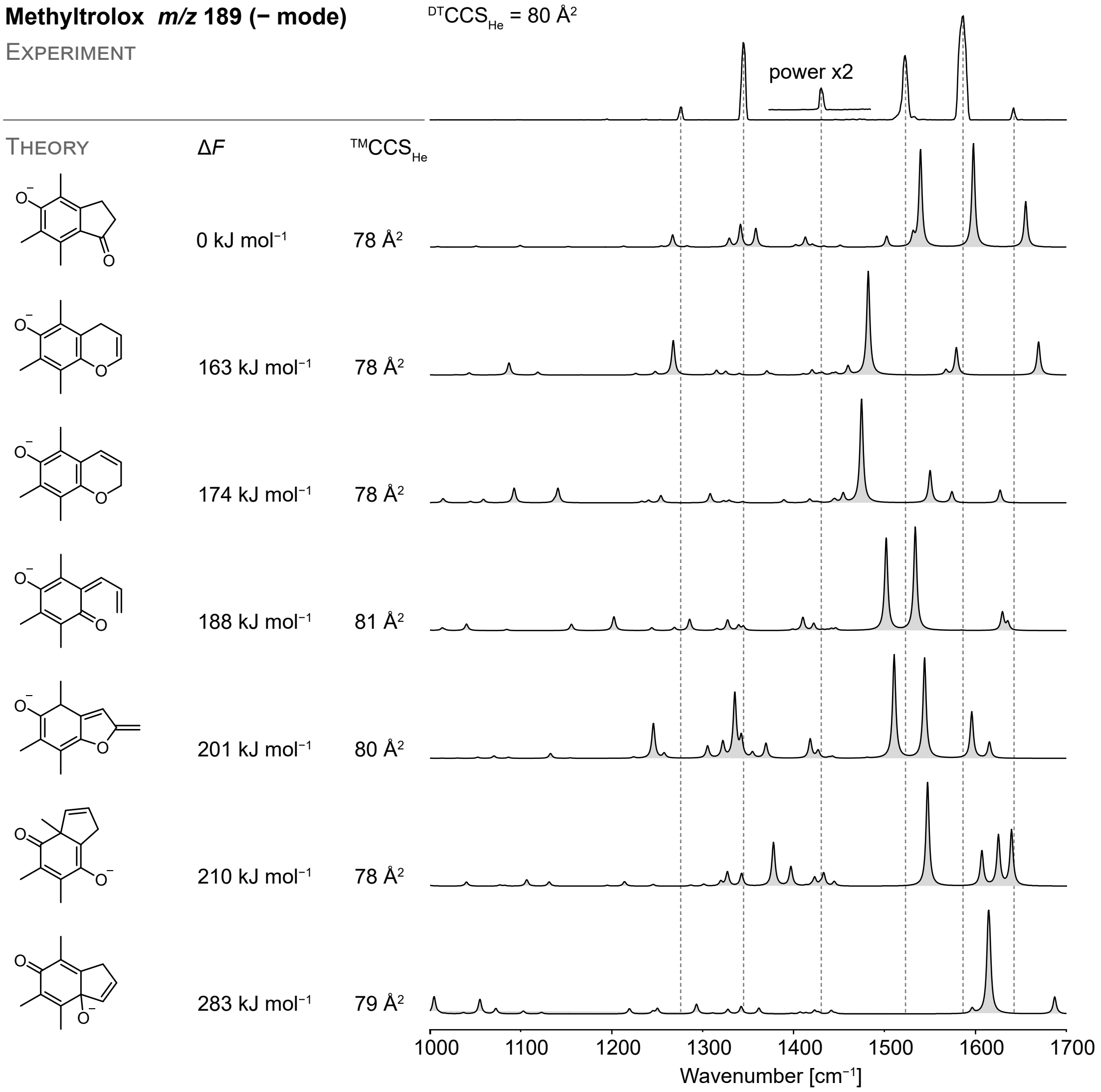

Figure C12: Experimental IR spectrum of the fragment at *m/z* 189 generated from deprotonated Methyltrolox precursor ions and computed IR spectra of candidate structures. The best spectral match is shown on top and corresponds to a rearranged structure featuring a cyclopentanone ring. By doubling the laser energy, an additional band becomes visible at 1420 cm^{-1}. The relative free energies (90 K) and IR spectra were computed at the PBE0+D3/6-311+G(d,p) level of theory, and the CCSs were calculated based on the trajectory method (TM).

Bibliography

[1] N. D. Ridgway, R. S. McLeod, *Biochemistry of Lipids, Lipoproteins and Membranes*, 6th Edition, Elsevier, Amsterdam, **2016**.

[2] J. M. Arbonés-Mainar, M. A. Navarro, M. A. Guzmán, C. Arnal, J. C. Surra, S. Acín, R. Carnicer, J. Osada, H. M. Roche, *Atherosclerosis* **2006**, *189*, 318–27.

[3] A. Bednařík, S. Bölsker, J. Soltwisch, K. Dreisewerd, *Angew. Chem. Int. Ed.* **2018**, *57*, 12092–6.

[4] X. Ma, L. Chong, R. Tian, R. Shi, T. Y. Hu, Z. Ouyang, Y. Xia, *Proc. Natl. Acad. Sci. U. S. A.* **2016**, *113*, 2573–8.

[5] X. Zhao, W. Zhang, D. Zhang, X. Liu, W. Cao, Q. Chen, Z. Ouyang, Y. Xia, *Chem. Sci.* **2019**, *10*, 10740–8.

[6] W. Cao, S. Cheng, J. Yang, J. Feng, W. Zhang, Z. Li, Q. Chen, Y. Xia, Z. Ouyang, X. Ma, *Nat. Commun.* **2020**, *11*, 375.

[7] K. Vriens, S. Christen, S. Parik, D. Broekaert, K. Yoshinaga, A. Talebi, J. Dehairs, C. Escalona-Noguero, R. Schmieder, T. Cornfield, C. Charlton, L. Romero-Perez, M. Rossi, G. Rinaldi, M. F. Orth, R. Boon, A. Kerstens, S. Y. Kwan, B. Faubert, A. Mendez-Lucas, C. C. Kopitz, T. Chen, J. Fernandez-Garcia, J. A. G. Duarte, A. A. Schmitz, P. Steigemann, M. Najimi, A. Hagebarth, J. A. Van Ginderachter, E. Sokal, N. Gotoh, K. K. Wong, C. Verfaillie, R. Derua, S. Munck, M. Yuneva, L. Beretta, R. J. DeBerardinis, J. V. Swinnen, L. Hodson, D. Cassiman, C. Verslype, S. Christian, S. Grunewald, T. G. P. Grunewald, S. M. Fendt, *Nature* **2019**, *566*, 403–6.

[8] R. S. E. Young, A. P. Bowman, E. D. Williams, K. D. Tousignant, C. L. Bidgood, V. R. Narreddula, R. Gupta, D. L. Marshall, B. L. J. Poad, C. C. Nelson, S. R. Ellis, R. M. A. Heeren, M. C. Sadowski, S. J. Blanksby, *Cell Rep.* **2021**, *34*, 108738.

[9] S. E. Hancock, B. L. Poad, A. Batarseh, S. K. Abbott, T. W. Mitchell, *Anal. Biochem.* **2017**, *524*, 45–55.

[10] Y. H. Rustam, G. E. Reid, *Anal. Chem.* **2018**, *90*, 374–97.

[11] S. Cheng, X. Zhao, X. Ma in *Advanced Fragmentation Methods in Biomolecular Mass Spectrometry*, *Vol. 9*, (Ed.: F. Lermyte), Royal Society of Chemistry, Cambridge, **2020**, pp. 209–34.

[12] S. Heiles, *Anal. Bioanal. Chem.* **2021**, *413*, 5927–48.

[13] J. R. Bonney, B. M. Prentice, *Anal. Chem.* **2021**, *93*, 6311–22.

[14] W. Zhang, R. Jian, J. Zhao, Y. Liu, Y. Xia, *J. Lipid Res.* **2022**, *63*, 100219.

[15] X. Zheng, R. D. Smith, E. S. Baker, *Curr. Opin. Chem. Biol.* **2018**, *42*, 111–8.

[16] T. Porta Siegel, K. Ekroos, S. R. Ellis, *Angew. Chem. Int. Ed.* **2019**, *58*, 6492–501.

[17] F. Spener, M. Lagarde, A. Géloên, M. Record, *Eur. J. Lipid Sci. Technol.* **2003**, *105*, 481–2.

[18] M. R. Wenk, *Nat. Rev. Drug Discov.* **2005**, *4*, 594–610.

[19] S. J. Blanksby, T. W. Mitchell, *Annu. Rev. Anal. Chem.* **2010**, *3*, 433–65.

[20] R. L. Schnaar, T. Kinoshita in *Essentials of Glycobiology*, (Eds.: A. Varki, R. D. Cummings, J. D. Esko, P. Stanley, G. W. Hart, M. Aebi, A. G. Darvill, T. Kinoshita, N. H. Packer, J. H. Prestegard, R. L. Schnaar, P. H. Seeberger), 3rd Edition, Cold Spring Harbor Laboratory Press, New York, **2015**, pp. 125–35.

[21] Z. D. Jiang, W. H. Gerwick, *Phytochemistry* **1990**, *29*, 1433–40.

[22] N. C. Polfer, J. Oomens, *Mass Spectrom. Rev.* **2009**, *28*, 468–94.

[23] C. N. Stedwell, J. F. Galindo, A. E. Roitberg, N. C. Polfer, *Annu. Rev. Anal. Chem.* **2013**, *6*, 267–85.

[24] T. R. Rizzo, O. V. Boyarkin, *Top. Curr. Chem.* **2015**, *364*, 43–97.

[25] O. V. Boyarkin, *Int. Rev. Phys. Chem.* **2018**, *37*, 559–606.

[26] A. O. Odegaard, M. A. Pereira, *Nutr. Rev.* **2006**, *64*, 364–72.

[27] J. Huang, J. Borensztajn, J. K. Reddy in *Molecular Pathology of Liver Diseases*, *Vol. 5*, (Ed.: S. P. S. Monga), Springer, New York, **2011**, pp. 133–46.

[28] A. Shevchenko, K. Simons, *Nat. Rev. Mol. Cell Biol.* **2010**, *11*, 593–8.

[29] D. A. Bender, S. P. Datta, A. D. Smith, *Oxford Dictionary of Biochemistry and Molecular Biology*, 2nd Edition, Oxford University Press, Oxford, **2000**.

[30] E. Fahy, S. Subramaniam, H. A. Brown, C. K. Glass, A. H. Merrill, R. C. Murphy, C. R. Raetz, D. W. Russell, Y. Seyama, W. Shaw, T. Shimizu, F. Spener, G. van Meer, M. S. VanNieuwenhze, S. H. White, J. L. Witztum, E. A. Dennis, *J. Lipid Res.* **2005**, *46*, 839–61.

[31] E. Fahy, S. Subramaniam, R. C. Murphy, M. Nishijima, C. R. Raetz, T. Shimizu, F. Spener, G. van Meer, M. J. Wakelam, E. A. Dennis, *J. Lipid Res.* **2009**, *50*, S9–14.

[32] G. Liebisch, E. Fahy, J. Aoki, E. A. Dennis, T. Durand, C. S. Ejsing, M. Fedorova, I. Feussner, W. J. Griffiths, H. Köfeler, A. H. Merrill, R. C. Murphy, V. B. O'Donnell, O. Oskolkova, S. Subramaniam, M. J. O. Wakelam, F. Spener, *J. Lipid Res.* **2020**, *61*, 1539–55.

[33] M. Sud, E. Fahy, D. Cotter, A. Brown, E. A. Dennis, C. K. Glass, A. H. Merrill, R. C. Murphy, C. R. Raetz, D. W. Russell, S. Subramaniam, *Nucleic Acids Res.* **2007**, *35*, D527–32.

[34] R. Lehner, A. D. Quiroga in *Biochemistry of Lipids, Lipoproteins and Membranes*, (Eds.: N. D. Ridgway, R. S. McLeod), Elsevier, Amsterdam, Netherlands, **2016**, pp. 149–84.

[35] A. B. Oteng, S. Kersten, *Adv. Nutr.* **2020**, *11*, 697–708.

[36] G. Liebisch, J. A. Vizcaino, H. Köfeler, M. Trotzmuller, W. J. Griffiths, G. Schmitz, F. Spener, M. J. O. Wakelam, *J. Lipid Res.* **2013**, *54*, 1523–30.

[37] S. M. Innis, *Prog. Lipid Res.* **1991**, *30*, 39–103.

[38] L. M. Bond, M. Miyazaki, L. M. O'Neill, F. Ding, J. M. Ntambi in *Biochemistry of Lipids, Lipoproteins and Membranes*, (Eds.: N. D. Ridgway, R. S. McLeod), 6th Edition, Elsevier, Amsterdam, **2016**, pp. 185–208.

[39] W. L. Smith, R. C. Murphy in *Biochemistry of Lipids, Lipoproteins and Membranes*, (Eds.: N. D. Ridgway, R. S. McLeod), 6th Edition, Elsevier, Amsterdam, **2016**, pp. 259–96.

[40] N. D. Ridgway in *Biochemistry of Lipids, Lipoproteins and Membranes*, 6th Edition, Elsevier, Amsterdam, **2016**, pp. 209–36.

[41] M. Hermansson, K. Hokynar, P. Somerharju, *Prog. Lipid Res.* **2011**, *50*, 240–57.

[42] T. O. Eichmann, A. Lass, *Cell. Mol. Life Sci.* **2015**, *72*, 3931–52.

[43] R. A. Coleman, D. G. Mashek, *Chem. Rev.* **2011**, *111*, 6359–86.

[44] H. Martinez-Seara, T. Róg, M. Pasenkiewicz-Gierula, I. Vattulainen, M. Karttunen, R. Reigada, *Biophys. J.* **2008**, *95*, 3295–305.

[45] G. van Meer, D. R. Voelker, G. W. Feigenson, *Nat. Rev. Mol. Cell Biol.* **2008**, *9*, 112–24.

[46] N. P. Barrera, M. Zhou, C. V. Robinson, *Trends Cell Biol.* **2013**, *23*, 1–8.

[47] M. Bogdanov, W. Dowhan, H. Vitrac, *Biochim. Biophys. Acta* **2014**, *1843*, 1475–88.

[48] W. Dowhan, H. Vitrac, M. Bogdanov, *Protein J.* **2019**, *38*, 274–88.

[49] M. D. Resh in *Biochemistry of Lipids, Lipoproteins and Membranes*, (Eds.: N. D. Ridgway, R. S. McLeod), 6th Edition, Elsevier, Amsterdam, **2016**, pp. 391–414.

[50] S. Chatterjee, S. Mayor, *Cell. Mol. Life Sci.* **2001**, *58*, 1969–87.

[51] K. Simons, E. Ikonen, *Nature* **1997**, *387*, 569–72.

[52] D. Lingwood, K. Simons, *Science* **2010**, *327*, 46–50.

[53] A. H. Futerman in *Biochemistry of Lipids, Lipoproteins and Membranes*, (Eds.: N. D. Ridgway, R. S. McLeod), 6th Edition, Elsevier, Amsterdam, **2016**, pp. 297–326.

[54] S. T. Pruett, A. Bushnev, K. Hagedorn, M. Adiga, C. A. Haynes, M. C. Sullards, D. C. Liotta, A. H. Merrill, *J. Lipid Res.* **2008**, *49*, 1621–39.

[55] A. H. Merrill, *Chem. Rev.* **2011**, *111*, 6387–422.

[56] K. Hanada, *Biochim. Biophys. Acta Mol. Cell Biol. Lipids* **2003**, *1632*, 16–30.

[57] Y. Chen, Y. Liu, M. C. Sullards, A. H. Merrill, *Neuromolecular Med.* **2010**, *12*, 306–19.

[58] A. H. Merrill, M. D. Wang, M. Park, M. C. Sullards, *Trends Biochem. Sci.* **2007**, *32*, 457–68.

[59] R. L. Schnaar in *Advances in Carbohydrate Chemistry and Biochemistry, Vol. 76*, (Ed.: D. C. Baker), Elsevier, Cambridge, **2019**, pp. 113–48.

[60] C. R. Raetz, C. Whitfield, *Annu. Rev. Biochem.* **2002**, *71*, 635–700.

[61] A. J. Brown, L. J. Sharpe in *Biochemistry of Lipids, Lipoproteins and Membranes*, (Eds.: N. D. Ridgway, R. S. McLeod), 6th Edition, Elsevier, Amsterdam, **2016**, pp. 327–58.

[62] S. S. Chandran, J. T. Kealey, C. D. Reeves, *Process Biochem.* **2011**, *46*, 1703–10.

[63] H. Farwanah, T. Kolter, *Metabolites* **2012**, *2*, 134–64.

[64] P. H. Seeberger in *Essentials of Glycobiology*, (Eds.: A. Varki, R. D. Cummings, J. D. Esko, P. Stanley, G. W. Hart, M. Aebi, A. G. Darvill, T. Kinoshita, N. H. Packer, J. H. Prestegard, R. L. Schnaar, P. H. Seeberger), 3rd Edition, Cold Spring Harbor Laboratory Press, New York, **2015**, pp. 19–30.

[65] J. Hofmann, H. S. Hahm, P. H. Seeberger, K. Pagel, *Nature* **2015**, *526*, 241.

[66] R. A. Laine, *Glycobiology* **1994**, *4*, 759–67.

[67] A. Varki, R. D. Cummings, M. Aebi, N. H. Packer, P. H. Seeberger, J. D. Esko, P. Stanley, G. Hart, A. Darvill, T. Kinoshita, J. J. Prestegard, R. L. Schnaar, H. H. Freeze, J. D. Marth, C. R. Bertozzi, M. E. Etzler, M. Frank, J. F. Vliegenthart, T. Lutteke, S. Perez, E. Bolton, P. Rudd, J. Paulson, M. Kanehisa, P. Toukach, K. F. Aoki-Kinoshita, A. Dell, H. Narimatsu, W. York, N. Taniguchi, S. Kornfeld, *Glycobiology* **2015**, *25*, 1323–4.

[68] S. Neelamegham, K. Aoki-Kinoshita, E. Bolton, M. Frank, F. Lisacek, T. Lutteke, N. O'Boyle, N. H. Packer, P. Stanley, P. Toukach, A. Varki, R. J. Woods, S. D. Group, *Glycobiology* **2019**, *29*, 620–4.

[69] M. Grabarics, M. Lettow, C. Kirschbaum, K. Greis, C. Manz, K. Pagel, *Chem. Rev.* **2022**, *122*, 7840–908.

[70] A. Varki, P. Gagneux in *Essentials of Glycobiology*, (Eds.: A. Varki, R. D. Cummings, J. D. Esko, P. Stanley, G. W. Hart, M. Aebi, A. G. Darvill, T. Kinoshita, N. H. Packer, J. H. Prestegard, R. L. Schnaar, P. H. Seeberger), 3rd Edition, Cold Spring Harbor Laboratory Press, New York, **2015**, pp. 77–88.

[71] P. B. Savage, L. Teyton, A. Bendelac, *Chem. Soc. Rev.* **2006**, *35*, 771–9.

[72] A. Bendelac, P. B. Savage, L. Teyton, *Annu. Rev. Immunol.* **2007**, *25*, 297–336.

[73] I. Brockhausen, P. Stanley in *Essentials of Glycobiology*, (Eds.: A. Varki, R. D. Cummings, J. D. Esko, P. Stanley, G. W. Hart, M. Aebi, A. G. Darvill, T. Kinoshita, N. H. Packer, J. H. Prestegard, R. L. Schnaar, P. H. Seeberger), 3rd Edition, Cold Spring Harbor Laboratory Press, New York, **2015**, pp. 113–23.

[74] T. W. Mitchell, H. Pham, M. C. Thomas, S. J. Blanksby, *J. Chromatogr. B Analyt. Technol. Biomed. Life Sci.* **2009**, *877*, 2722–35.

[75] M. R. L. Paine, B. L. J. Poad, G. B. Eijkel, D. L. Marshall, S. J. Blanksby, R. M. A. Heeren, S. R. Ellis, *Angew. Chem. Int. Ed.* **2018**, *57*, 10530–4.

[76] S. Liu, J. D. Brown, K. J. Stanya, E. Homan, M. Leidl, K. Inouye, P. Bhargava, M. R. Gangl, L. Dai, B. Hatano, G. S. Hotamisligil, A. Saghatelian, J. Plutzky, C. H. Lee, *Nature* **2013**, *502*, 550–4.

[77] R. R. Rando, N. Young, *Biochem. Biophys. Res. Commun.* **1984**, *122*, 818–23.

[78] M. S. Blevins, V. K. James, C. M. Herrera, A. B. Purcell, M. S. Trent, J. S. Brodbelt, *Anal. Chem.* **2020**, *92*, 9146–55.

[79] Y. Cao, X. Zhang, *Appl. Microbiol. Biotechnol.* **2013**, *97*, 3323–31.

[80] K. R. Kim, D. K. Oh, *Biotechnol. Adv.* **2013**, *31*, 1473–85.

[81] A. Kutschera, C. Dawid, N. Gisch, C. Schmid, L. Raasch, T. Gerster, M. Schaffer, E. Smakowska-Luzan, Y. Belkhadir, A. C. Vlot, C. E. Chandler, R. Schellenberger, D. Schwudke, R. K. Ernst, S. Dorey, R. Huckelhoven, T. Hofmann, S. Ranf, *Science* **2019**, *364*, 178–81.

[82] E. N. Frankel, *Prog. Lipid Res.* **1980**, *19*, 1–22.

[83] T. Kaneda, *Microbiol. Rev.* **1991**, *55*, 288–302.

[84] Y. M. Zhang, C. O. Rock, *Nat. Rev. Microbiol.* **2008**, *6*, 222–33.

[85] D. Poger, B. Caron, A. E. Mark, *J. Phys. Chem. B* **2014**, *118*, 13838–48.

[86] D. Poger, A. E. Mark, *J. Phys. Chem. B* **2015**, *119*, 5487–95.

[87] C. E. Randolph, D. M. Shenault, S. J. Blanksby, S. A. McLuckey, *J. Am. Soc. Mass Spectrom.* **2020**, *31*, 1093–103.

[88] M. S. Blevins, S. W. J. Shields, W. Cui, W. Fallatah, A. B. Moser, N. E. Braverman, J. S. Brodbelt, *Anal. Chem.* **2022**, *94*, 12621–9.

[89] C. R. Raetz, C. M. Reynolds, M. S. Trent, R. E. Bishop, *Annu. Rev. Biochem.* **2007**, *76*, 295–329.

[90] O. Quehenberger, A. M. Armando, A. H. Brown, S. B. Milne, D. S. Myers, A. H. Merrill, S. Bandyopadhyay, K. N. Jones, S. Kelly, R. L. Shaner, C. M. Sullards, E. Wang, R. C. Murphy, R. M. Barkley, T. J. Leiker, C. R. Raetz, Z. Guan, G. M. Laird, D. A. Six, D. W. Russell, J. G. McDonald, S. Subramaniam, E. Fahy, E. A. Dennis, *J. Lipid Res.* **2010**, *51*, 3299–305.

[91] M. R. Wenk, *Cell* **2010**, *143*, 888–95.

[92] C. Chatgilialoglu, C. Ferreri, M. Melchiorre, A. Sansone, A. Torreggiani, *Chem. Rev.* **2014**, *114*, 255–84.

[93] T. Züllig, H. C. Köfeler, *Mass Spectrom. Rev.* **2021**, *40*, 162–76.

[94] J. Fenn, M. Mann, C. Meng, S. Wong, C. Whitehouse, *Science* **1989**, *246*, 64–71.

[95] M. Karas, F. Hillenkamp, *Anal. Chem.* **1988**, *60*, 2299–301.

[96] R. C. Murphy, J. Fiedler, J. Hevko, *Chem. Rev.* **2001**, *101*, 479–526.

[97] J. B. Fenn, M. Mann, C. K. Meng, S. F. Wong, C. M. Whitehouse, *Mass Spectrom. Rev.* **1990**, *9*, 37–70.

[98] R. C. Murphy, P. H. Axelsen, *Mass Spectrom. Rev.* **2011**, *30*, 579–99.

[99] A. R. Buchberger, K. DeLaney, J. Johnson, L. Li, *Anal. Chem.* **2018**, *90*, 240–65.

[100] X. Han, *Lipidomics: Comprehensive Mass Spectrometry of Lipids*, Wiley, Hoboken, **2016**.

[101] C. Hu, Q. Duan, X. Han, *Proteomics* **2020**, *20*, e1900070.

[102] T. Cajka, O. Fiehn, *Trends Analyt. Chem.* **2014**, *61*, 192–206.

[103] G. Paglia, M. Kliman, E. Claude, S. Geromanos, G. Astarita, *Anal. Bioanal. Chem.* **2015**, *407*, 4995–5007.

[104] G. Paglia, A. J. Smith, G. Astarita, *Mass Spectrom. Rev.* **2022**, *41*, 722–65.

[105] A. A. Shvartsburg, G. Isaac, N. Leveque, R. D. Smith, T. O. Metz, *J. Am. Soc. Mass Spectrom.* **2011**, *22*, 1146–55.

[106] M. Groessl, S. Graf, R. Knochenmuss, *Analyst* **2015**, *140*, 6904–11.

[107] A. T. Kirk, A. Bohnhorst, C. R. Raddatz, M. Allers, S. Zimmermann, *Anal. Bioanal. Chem.* **2019**, *411*, 6229–46.

[108] R. Wojcik, I. K. Webb, L. Deng, S. V. Garimella, S. A. Prost, Y. M. Ibrahim, E. S. Baker, R. D. Smith, *Int. J. Mol. Sci.* **2017**, *18*, 183.

[109] J. C. May, K. L. Leaptrot, B. S. Rose, K. L. W. Moser, L. Deng, L. Maxon, D. DeBord, J. A. McLean, *J. Am. Soc. Mass Spectrom.* **2021**, *32*, 1126–37.

[110] T. Gao, A. A. Lott, F. Huang, R. Rohokale, Q. Li, H. J. Olivos, S. Chen, Z. Guo, *Analyst* **2022**, *147*, 3101–8.

[111] V. Gabelica, E. Marklund, *Curr. Opin. Chem. Biol.* **2018**, *42*, 51–9.

[112] C. Hinz, S. Liggi, J. L. Griffin, *Curr. Opin. Chem. Biol.* **2018**, *42*, 42–50.

[113] M. Pulfer, R. C. Murphy, *Mass Spectrom. Rev.* **2003**, *22*, 332–64.

[114] F. F. Hsu, J. Turk, *J. Chromatogr. B Analyt. Technol. Biomed. Life Sci.* **2009**, *877*, 2673–95.

[115] K. Ekroos, C. S. Ejsing, U. Bahr, M. Karas, K. Simons, A. Shevchenko, *J. Lipid Res.* **2003**, *44*, 2181–92.

[116] L. C. Herrera, M. A. Potvin, J. E. Melanson, *Rapid Commun. Mass Spectrom.* **2010**, *24*, 2745–52.

[117] K. B. Tomer, F. W. Crow, M. L. Gross, *J. Am. Chem. Soc.* **1983**, *105*, 5487–8.

[118] J. Adams, M. L. Gross, *Anal. Chem.* **1987**, *59*, 1576–82.

[119] C. Cheng, M. L. Gross, E. Pittenauer, *Anal. Chem.* **1998**, *70*, 4417–26.

[120] S. Trimpin, D. E. Clemmer, C. N. McEwen, *J. Am. Soc. Mass Spectrom.* **2007**, *18*, 1967–72.

[121] E. Pittenauer, G. Allmaier, *J. Am. Soc. Mass Spectrom.* **2009**, *20*, 1037–47.

[122] K. Schuhmann, R. Herzog, D. Schwudke, W. Metelmann-Strupat, S. R. Bornstein, A. Shevchenko, *Anal. Chem.* **2011**, *83*, 5480–7.

[123] S. H. Brown, T. W. Mitchell, S. J. Blanksby, *Biochim. Biophys. Acta* **2011**, *1811*, 807–17.

[124] J. S. Brodbelt, *Chem. Soc. Rev.* **2014**, *43*, 2757–83.

[125] J. S. Brodbelt, L. J. Morrison, I. Santos, *Chem. Rev.* **2020**, *120*, 3328–80.

[126] D. R. Klein, J. S. Brodbelt, *Anal. Chem.* **2017**, *89*, 1516–22.

[127] L. A. Macias, K. Y. Garza, C. L. Feider, L. S. Eberlin, J. S. Brodbelt, *J. Am. Chem. Soc.* **2021**, *143*, 14622–34.

[128] J. A. Madsen, T. W. Cullen, M. S. Trent, J. S. Brodbelt, *Anal. Chem.* **2011**, *83*, 5107–13.

[129] M. S. Blevins, D. R. Klein, J. S. Brodbelt, *Anal. Chem.* **2019**, *91*, 6820–8.

[130] P. E. Williams, D. R. Klein, S. M. Greer, J. S. Brodbelt, *J. Am. Chem. Soc.* **2017**, *139*, 15681–90.

[131] T. Ly, R. R. Julian, *J. Am. Chem. Soc.* **2008**, *130*, 351–8.

[132] H. T. Pham, T. Ly, A. J. Trevitt, T. W. Mitchell, S. J. Blanksby, *Anal. Chem.* **2012**, *84*, 7525–32.

[133] H. T. Pham, A. J. Trevitt, T. W. Mitchell, S. J. Blanksby, *Rapid Commun. Mass Spectrom.* **2013**, *27*, 805–15.

[134] H. T. Pham, R. R. Julian, *Anal. Chem.* **2014**, *86*, 3020–7.

[135] H. T. Pham, R. R. Julian, *Int. J. Mass Spectrom.* **2014**, *370*, 58–65.

[136] H. T. Pham, R. R. Julian, *Analyst* **2016**, *141*, 1273–8.

[137] Q. Lin, P. Li, R. Jian, Y. Xia, *J. Am. Soc. Mass Spectrom.* **2022**, *33*, 714–21.

[138] V. R. Narreddula, N. R. Boase, R. Ailuri, D. L. Marshall, B. L. J. Poad, M. J. Kelso, A. J. Trevitt, T. W. Mitchell, S. J. Blanksby, *Anal. Chem.* **2019**, *91*, 9901–9.

[139] V. R. Narreddula, P. Sadowski, N. R. B. Boase, D. L. Marshall, B. L. J. Poad, A. J. Trevitt, T. W. Mitchell, S. J. Blanksby, *Rapid Commun. Mass Spectrom.* **2020**, *34*, e8741.

[140] V. R. Narreddula, B. I. McKinnon, S. J. P. Marlton, D. L. Marshall, N. R. B. Boase, B. L. J. Poad, A. J. Trevitt, T. W. Mitchell, S. J. Blanksby, *Analyst* **2021**, *146*, 156–69.

[141] S. E. Hancock, R. Ailuri, D. L. Marshall, S. H. J. Brown, J. T. Saville, V. R. Narreddula, N. R. Boase, B. L. J. Poad, A. J. Trevitt, M. D. P. Willcox, M. J. Kelso, T. W. Mitchell, S. J. Blanksby, *J. Lipid Res.* **2018**, *59*, 1510–8.

[142] X. Chen, Z. Wang, Y. E. Wong, R. Wu, F. Zhang, T. D. Chan, *Mass Spectrom. Rev.* **2018**, *37*, 793–810.

[143] H. J. Yoo, K. Håkansson, *Anal. Chem.* **2010**, *82*, 6940–6.

[144] J. L. Campbell, T. Baba, *Anal. Chem.* **2015**, *87*, 5837–45.

[145] J. W. Jones, C. J. Thompson, C. L. Carter, M. A. Kane, *J. Mass Spectrom.* **2015**, *50*, 1327–39.

[146] T. Baba, J. L. Campbell, J. C. Le Blanc, P. R. Baker, *J. Lipid Res.* **2016**, *57*, 2015–27.

[147] T. Baba, J. L. Campbell, J. C. Le Blanc, P. R. Baker, *J. Lipid Res.* **2016**, *57*, 858–67.

[148] T. Baba, J. L. Campbell, J. C. Y. Le Blanc, P. R. S. Baker, K. Ikeda, *J. Lipid Res.* **2018**, *59*, 910–9.

[149] M.-E. N. Born, B. M. Prentice, *Int. J. Mass Spectrom.* **2020**, *452*, 116338.

[150] T. Yan, M.-E. N. Born, B. M. Prentice, *Int. J. Mass Spectrom.* **2023**, DOI: 10.1016/j.ijms.2022.116998.

[151] T. Baba, J. L. Campbell, J. C. Y. Le Blanc, P. R. S. Baker, *Anal. Chem.* **2017**, *89*, 7307–15.

[152] Y. P. Ho, P. C. Huang, K. H. Deng, *Rapid Commun. Mass Spectrom.* **2003**, *17*, 114–21.

[153] F. F. Hsu, J. Turk, *J. Am. Soc. Mass Spectrom.* **1999**, *10*, 587–99.

[154] F. F. Hsu, J. Turk, *J. Am. Soc. Mass Spectrom.* **2008**, *19*, 1681–91.

[155] F. F. Hsu, J. Turk, *J. Am. Soc. Mass Spectrom.* **2010**, *21*, 657–69.

[156] H. J. Yoo, K. Håkansson, *Anal. Chem.* **2011**, *83*, 1275–83.

[157] S. Becher, P. Esch, S. Heiles, *Anal. Chem.* **2018**, *90*, 11486–94.

[158] J. Lillja, I. Lanekoff, *Anal. Bioanal. Chem.* **2022**, *414*, 7473–82.

[159] A. T. Maccarone, J. Duldig, T. W. Mitchell, S. J. Blanksby, E. Duchoslav, J. L. Campbell, *J. Lipid Res.* **2014**, *55*, 1668–77.

[160] C. Afonso, A. Riu, Y. Xu, F. Fournier, J. C. Tabet, *J. Mass Spectrom.* **2005**, *40*, 342–9.

[161] F. Wu, X. Wu, C. Chi, C. F. Ding, *Anal. Chem.* **2022**, *94*, 12213–20.

[162] R. Criegee, *Angew. Chem. Int. Ed.* **1975**, *14*, 745–52.

[163] K. A. Harrison, R. C. Murphy, *Anal. Chem.* **1996**, *68*, 3224–30.

[164] M. C. Thomas, T. W. Mitchell, S. J. Blanksby, *J. Am. Chem. Soc.* **2006**, *128*, 58–9.

[165] M. C. Thomas, T. W. Mitchell, D. G. Harman, J. M. Deeley, R. C. Murphy, S. J. Blanksby, *Anal. Chem.* **2007**, *79*, 5013–22.

[166] J. I. Zhang, W. A. Tao, R. G. Cooks, *Anal. Chem.* **2011**, *83*, 4738–44.

[167] R. A. Harris, J. C. May, C. A. Stinson, Y. Xia, J. A. McLean, *Anal. Chem.* **2018**, *90*, 1915–24.

[168] C. A. Stinson, W. Zhang, Y. Xia, *J. Am. Soc. Mass Spectrom.* **2018**, *29*, 481–9.

[169] A. Bednařík, J. Preisler, D. Bezdeková, M. Machálková, M. Hendrych, J. Navrátilová, L. Knopfová, E. Moskovets, J. Soltwisch, K. Dreisewerd, *Anal. Chem.* **2020**, *92*, 6245–50.

[170] M. Koktavá, J. Valášek, D. Bezdeková, V. Prysiazhnyi, B. Adamová, P. Beneš, J. Navrátilová, M. Hendrych, P. Vlček, J. Preisler, A. Bednařík, *Anal. Chem.* **2022**, *94*, 8928–36.

[171] M. D'Auria, *Photochem. Photobiol. Sci.* **2019**, *18*, 2297–362.

[172] X. Ma, Y. Xia, *Angew. Chem. Int. Ed.* **2014**, *53*, 2592–6.

[173] X. Ma, X. Zhao, J. Li, W. Zhang, J. X. Cheng, Z. Ouyang, Y. Xia, *Anal. Chem.* **2016**, *88*, 8931–5.

[174] S. L. Xu, B. F. Wu, M. Orešič, Y. Xie, P. Yao, Z. Y. Wu, X. Lv, H. Chen, F. Wei, *Anal. Chem.* **2020**, *92*, 6446–55.

[175] W. Zhang, D. Zhang, Q. Chen, J. Wu, Z. Ouyang, Y. Xia, *Nat. Commun.* **2019**, *10*, 79.

[176] V. Jeck, A. Korf, C. Vosse, H. Hayen, *Rapid Commun. Mass Spectrom.* **2019**, *33*, 86–94.

[177] W. Zhang, B. Shang, Z. Ouyang, Y. Xia, *Anal. Chem.* **2020**, *92*, 6719–26.

[178] P. Esch, S. Heiles, *J. Am. Soc. Mass Spectrom.* **2018**, *29*, 1971–80.

[179] A. Cerrato, A. L. Capriotti, C. Cavaliere, C. M. Montone, S. Piovesana, A. Lagana, *Anal. Chem.* **2022**, *94*, 13117–25.

[180] J. Zhao, X. Xie, Q. Lin, X. Ma, P. Su, Y. Xia, *Anal. Chem.* **2020**, *92*, 13470–7.

[181] F. Wäldchen, S. Becher, P. Esch, M. Kompauer, S. Heiles, *Analyst* **2017**, *142*, 4744–55.

[182] F. Wäldchen, B. Spengler, S. Heiles, *J. Am. Chem. Soc.* **2019**, *141*, 11816–20.

[183] H.-F. Li, J. Zhao, W. Cao, W. Zhang, Y. Xia, Z. Ouyang, *Research* **2022**, *2022*, 1–12.

[184] H. M. Hynds, K. M. Hines, *J. Am. Soc. Mass Spectrom.* **2022**, *33*, 1982–9.

[185] P. Esch, S. Heiles, *Analyst* **2020**, *145*, 2256–66.

[186] T. Xia, M. Yuan, Y. Xu, F. Zhou, K. Yu, Y. Xia, *Anal. Chem.* **2021**, *93*, 8345–53.

[187] Y. Chen, C. Xie, X. Wang, G. Cao, Y. Ru, Y. Song, A. Iyaswamy, M. Li, J. Wang, Z. Cai, *Anal. Chem.* **2022**.

[188] G. Feng, M. Gao, L. Wang, J. Chen, M. Hou, Q. Wan, Y. Lin, G. Xu, X. Qi, S. Chen, *Nat. Commun.* **2022**, *13*, 2652.

[189] X. Xie, Y. Xia, *Anal. Chem.* **2019**, *91*, 7173–80.

[190] Y. Zhao, H. Zhao, X. Zhao, J. Jia, Q. Ma, S. Zhang, X. Zhang, H. Chiba, S. P. Hui, X. Ma, *Anal. Chem.* **2017**, *89*, 10270–8.

[191] W. Cao, X. Ma, Z. Li, X. Zhou, Z. Ouyang, *Anal. Chem.* **2018**, *90*, 10286–92.

[192] Y. Feng, B. Chen, Q. Yu, L. Li, *Anal. Chem.* **2019**, *91*, 1791–5.

[193] T. H. Kuo, H. H. Chung, H. Y. Chang, C. W. Lin, M. Y. Wang, T. L. Shen, C. C. Hsu, *Anal. Chem.* **2019**, *91*, 11905–15.

[194] H. Zhang, M. Xu, X. Shi, Y. Liu, Z. Li, J. C. Jagodinsky, M. Ma, N. V. Welham, Z. S. Morris, L. Li, *Chem. Sci.* **2021**, *12*, 8115–22.

[195] C. Song, D. Gao, S. Li, L. Liu, X. Chen, Y. Jiang, *Anal. Chim. Acta* **2019**, *1086*, 82–9.

[196] Y. Feng, Y. Lv, T. J. Gu, B. Chen, L. Li, *Anal. Chem.* **2022**, *94*, 13036–42.

[197] X. Zhao, Y. Zhao, L. Zhang, X. Ma, S. Zhang, X. Zhang, *Anal. Chem.* **2018**, *90*, 2070–8.

[198] D. J. Swiner, D. S. Kulyk, H. Osae, G. R. Durisek III, A. K. Badu-Tawiah, *Anal. Chem.* **2022**, *94*, 2358–65.

[199] S. Tang, H. Cheng, X. Yan, *Angew. Chem. Int. Ed.* **2020**, *59*, 209–14.

[200] H. Cheng, S. Tang, T. Yang, S. Xu, X. Yan, *Angew. Chem. Int. Ed.* **2020**, *59*, 19862–7.

[201] S. Tang, X. Chen, Y. Ke, F. Wang, X. Yan, *Anal. Chem.* **2022**, *94*, 12750–6.

[202] M. Bouza, Y. Li, A. C. Wang, Z. L. Wang, F. M. Fernandez, *Anal. Chem.* **2021**, *93*, 5468–75.

[203] M. C. Thomas, T. W. Mitchell, D. G. Harman, J. M. Deeley, J. R. Nealon, S. J. Blanksby, *Anal. Chem.* **2008**, *80*, 303–11.

[204] D. L. Marshall, A. Criscuolo, R. S. E. Young, B. L. J. Poad, M. Zeller, G. E. Reid, T. W. Mitchell, S. J. Blanksby, *J. Am. Soc. Mass Spectrom.* **2019**, *30*, 1621–30.

[205] B. L. J. Poad, H. T. Pham, M. C. Thomas, J. R. Nealon, J. L. Campbell, T. W. Mitchell, S. J. Blanksby, *J. Am. Soc. Mass Spectrom.* **2010**, *21*, 1989–99.

[206] R. L. Kozlowski, J. L. Campbell, T. W. Mitchell, S. J. Blanksby, *Anal. Bioanal. Chem.* **2015**, *407*, 5053–64.

[207] B. L. J. Poad, M. R. Green, J. M. Kirk, N. Tomczyk, T. W. Mitchell, S. J. Blanksby, *Anal. Chem.* **2017**, *89*, 4223–9.

[208] F. Berthias, B. L. J. Poad, H. A. Thurman, A. P. Bowman, S. J. Blanksby, A. A. Shvartsburg, *J. Am. Soc. Mass Spectrom.* **2021**, *32*, 2827–36.

[209] B. S. R. Claes, A. P. Bowman, B. L. J. Poad, R. S. E. Young, R. M. A. Heeren, S. J. Blanksby, S. R. Ellis, *Anal. Chem.* **2021**.

[210] B. L. J. Poad, R. S. E. Young, D. L. Marshall, A. J. Trevitt, S. J. Blanksby, *Anal. Chem.* **2022**, *94*, 3897–903.

[211] H. T. Pham, A. T. Maccarone, M. C. Thomas, J. L. Campbell, T. W. Mitchell, S. J. Blanksby, *Analyst* **2014**, *139*, 204–14.

[212] D. L. Marshall, H. T. Pham, M. Bhujel, J. S. Chin, J. Y. Yew, K. Mori, T. W. Mitchell, S. J. Blanksby, *Anal. Chem.* **2016**, *88*, 2685–92.

[213] X. Liu, B. Jiao, W. Cao, X. Ma, Y. Xia, S. J. Blanksby, W. Zhang, Z. Ouyang, *Anal. Chem.* **2022**.

[214] D. J. Foreman, S. A. McLuckey, *Anal. Chem.* **2020**, *92*, 252–66.

[215] P. Li, G. P. Jackson, *J. Mass Spectrom.* **2017**, *52*, 271–82.

[216] C. E. Randolph, S. J. Blanksby, S. A. McLuckey, *Chem. Phys. Lipids* **2020**, *232*, 104970.

[217] C. E. Randolph, D. J. Foreman, S. K. Betancourt, S. J. Blanksby, S. A. McLuckey, *Anal. Chem.* **2018**, *90*, 12861–9.

[218] C. E. Randolph, D. J. Foreman, S. J. Blanksby, S. A. McLuckey, *Anal. Chem.* **2019**, *91*, 9032–40.

[219] C. E. Randolph, S. J. Blanksby, S. A. McLuckey, *Anal. Chem.* **2020**, *92*, 1219–27.

[220] C. E. Randolph, D. M. Shenault, S. J. Blanksby, S. A. McLuckey, *J. Am. Soc. Mass Spectrom.* **2021**, *32*, 455–64.

[221] J. R. Stutzman, S. J. Blanksby, S. A. McLuckey, *Anal. Chem.* **2013**, *85*, 3752–7.

[222] S. Rojas-Betancourt, J. R. Stutzman, F. A. Londry, S. J. Blanksby, S. A. McLuckey, *Anal. Chem.* **2015**, *87*, 11255–62.

[223] S. K. Betancourt, C. R. Canez, S. W. J. Shields, J. M. Manthorpe, J. C. Smith, S. A. McLuckey, *Anal. Chem.* **2017**, *89*, 9452–8.

[224] E. T. Franklin, S. K. Betancourt, C. E. Randolph, S. A. McLuckey, Y. Xia, *Anal. Bioanal. Chem.* **2019**, *411*, 4739–49.

[225] E. T. Franklin, S. W. J. Shields, J. M. Manthorpe, J. C. Smith, Y. Xia, S. A. McLuckey, *J. Am. Soc. Mass Spectrom.* **2020**, *31*, 938–45.

[226] J. T. Specker, S. L. Van Orden, M. E. Ridgeway, B. M. Prentice, *Anal. Chem.* **2020**, *92*, 13192–201.

[227] H. C. Chao, S. A. McLuckey, *Anal. Chem.* **2020**, *92*, 13387–95.

[228] H. C. Chao, S. A. McLuckey, *Anal. Chem.* **2021**, *93*, 7332–40.

[229] H. C. Chao, S. A. McLuckey, *Anal. Chem.* **2021**, *93*, 15752–60.

[230] K. Yang, B. G. Dilthey, R. W. Gross, *Anal. Chem.* **2013**, *85*, 9742–50.

[231] M. Wang, R. H. Han, X. Han, *Anal. Chem.* **2013**, *85*, 9312–20.

[232] R. S. E. Young, C. L. Flakelar, V. R. Narreddula, L. J. Jekimovs, J. P. Menzel, B. L. J. Poad, S. J. Blanksby, *Anal. Chem.* **2022**, *94*, 16180–8.

[233] E. Saparbaev, R. Yamaletdinov, O. V. Boyarkin, *Anal. Chem.* **2021**, *93*, 12822–6.

[234] A. P. Cismesia, L. S. Bailey, M. R. Bell, L. F. Tesler, N. C. Polfer, *J. Am. Soc. Mass Spectrom.* **2016**, *27*, 757–66.

[235] A. P. Cismesia, M. R. Bell, L. F. Tesler, M. Alves, N. C. Polfer, *Analyst* **2018**, *143*, 1615–23.

[236] J. Martens, R. E. van Outersterp, R. J. Vreeken, F. Cuyckens, K. L. M. Coene, U. F. Engelke, L. A. J. Kluijtmans, R. A. Wevers, L. M. C. Buydens, B. Redlich, G. Berden, J. Oomens, *Anal. Chim. Acta* **2020**, *1093*, 1–15.

[237] J. M. Hollas, *Modern Spectroscopy*, 4th Edition, Wiley, New York, **2004**.

[238] P. M. Morse, *Phys. Rev.* **1929**, *34*, 57–64.

[239] N. C. Polfer, P. Dugourd, *Laser Photodissociation and Spectroscopy of Mass-separated Biomolecular Ions*, Springer, Cham, **2013**.

[240] A. Koleżyński in *Molecular Spectroscopy—Experiment and Theory*, (Eds.: A. Koleżyński, M. Król), Challenges and Advances in Computational Chemistry and Physics, Springer, Cham, **2019**, pp. 1–48.

[241] C. A. Krettler, G. G. Thallinger, *Brief. Bioinform.* **2021**, *22*, 1–25.

[242] O. Bąk, P. Borowski in *Molecular Spectroscopy—Experiment and Theory*, (Eds.: A. Koleżyński, M. Król), Challenges and Advances in Computational Chemistry and Physics, Springer, Cham, **2019**, pp. 49–95.

[243] S. Du, M. Su, C. Wang, Z. Ding, Y. Jiang, H. Liu, *Anal. Chem.* **2022**, *94*, 2891–900.

[244] A. M. Rijs, J. Oomens, *Top. Curr. Chem.* **2015**, *364*, 1–42.

[245] J. Oomens, B. G. Sartakov, G. Meijer, G. von Helden, *Int. J. Mass Spectrom.* **2006**, *254*, 1–19.

[246] J. R. Eyler, *Mass Spectrom. Rev.* **2009**, *28*, 448–67.

[247] N. C. Polfer, *Chem. Soc. Rev.* **2011**, *40*, 2211–21.

[248] R. E. van Outersterp, J. Martens, A. Peremans, L. Lamard, F. Cuyckens, J. Oomens, G. Berden, *Analyst* **2021**, *146*, 7218–29.

[249] K. Lehmann, G. Scoles, B. Pate, *Annu. Rev. Phys. Chem.* **1994**, *45*, 241–74.

[250] T. R. Rizzo, J. A. Stearns, O. V. Boyarkin, *Int. Rev. Phys. Chem.* **2009**, *28*, 481–515.

[251] A. B. Wolk, C. M. Leavitt, E. Garand, M. A. Johnson, *Acc. Chem. Res.* **2014**, *47*, 202–10.

[252] D. Verma, R. M. P. Tanyag, S. M. O. O'Connell, A. F. Vilesov, *Adv. Phys.: X* **2019**, *4*, 1553569.

[253] S. Smolarek, N. B. Brauer, W. J. Buma, M. Drabbels, *J. Am. Chem. Soc.* **2010**, *132*, 14086–91.

[254] W. B. Clarke, W. J. Jenkins, Z. Top, *Int. J. Appl. Radiat. Isot.* **1976**, *27*, 515–22.

[255] D. R. Tilley, J. Tilley, *Superfluidity and Superconductivity*, 3rd Edition, IOP Publishing, Bristol, **1990**.

[256] J. P. Toennies, A. F. Vilesov, *Annu. Rev. Phys. Chem.* **1998**, *49*, 1–41.

[257] F. London, *Nature* **1938**, *141*, 643–4.

[258] J. P. Toennies, A. F. Vilesov, *Angew. Chem. Int. Ed.* **2004**, *43*, 2622–48.

[259] R. J. Donnelly, C. F. Barenghi, *J. Phys. Chem. Ref. Data* **1998**, *27*, 1217–74.

[260] R. J. Donnelly, *Phys. Today* **1995**, *48*, 30–8.

[261] H. K. Onnes, *Proc. K. Ned. Akad. Wet.* **1908**, *11*, 1908–9.

[262] J. F. Allen, H. Jones, *Nature* **1938**, *141*, 243–4.

[263] L. Jackson, L. Grimes, *Adv. Phys.* **1958**, *7*, 435–78.

[264] H. E. Hall, *Philos. Trans. R. Soc. London Ser. A* **1957**, *250*, 359–85.

[265] L. F. Gomez, K. R. Ferguson, J. P. Cryan, C. Bacellar, R. M. Tanyag, C. Jones, S. Schorb, D. Anielski, A. Belkacem, C. Bernando, R. Boll, J. Bozek, S. Carron, G. Chen, T. Delmas, L. Englert, S. W. Epp, B. Erk, L. Foucar, R. Hartmann, A. Hexemer, M. Huth, J. Kwok, S. R. Leone, J. H. Ma, F. R. Maia, E. Malmerberg, S. Marchesini, D. M. Neumark, B. Poon, J. Prell, D. Rolles, B. Rudek, A. Rudenko, M. Seifrid, K. R. Siefermann, F. P. Sturm, M. Swiggers, J. Ullrich, F. Weise, P. Zwart, C. Bostedt, O. Gessner, A. F. Vilesov, *Science* **2014**, *345*, 906–9.

[266] L. Tisza, *Nature* **1938**, *141*, 913.

[267] L. Landau, *Phys. Rev.* **1941**, *60*, 356–8.

[268] E. L. Andronikashvili, *J. Phys. USSR* **1946**, *10*, 201.

[269] M. Hartmann, F. Mielke, J. P. Toennies, A. F. Vilesov, G. Benedek, *Phys. Rev. Lett.* **1996**, *76*, 4560–3.

[270] S. Grebenev, J. P. Toennies, A. F. Vilesov, *Science* **1998**, *279*, 2083–6.

[271] J. P. Toennies, A. F. Vilesov, K. B. Whaley, *Phys. Today* **2001**, *54*, 31–7.

[272] A. Scheidemann, J. P. Toennies, J. A. Northby, *Phys. Rev. Lett.* **1990**, *64*, 1899–902.

[273] E. Whittle, D. A. Dows, G. C. Pimentel, *J. Chem. Phys.* **1954**, *22*, 1943.

[274] S. Albertini, E. Gruber, F. Zappa, S. Krasnokutski, F. Laimer, P. Scheier, *Mass Spectrom. Rev.* **2022**, *41*, 529–67.

[275] I. F. Silvera, *Phys. Rev. B* **1984**, *29*, 3899–904.

[276] M. Hartmann, R. E. Miller, J. P. Toennies, A. Vilesov, *Phys. Rev. Lett.* **1995**, *75*, 1566–9.

[277] J. Harms, M. Hartmann, J. P. Toennies, A. F. Vilesov, B. Sartakov, *J. Mol. Spectrosc.* **1997**, *185*, 204–6.

[278] L. G. Mendoza-Luna, N. M. Shiltagh, M. J. Watkins, N. Bonifaci, F. Aitken, K. von Haeften, *J. Phys. Chem. Lett.* **2016**, *7*, 4666–70.

[279] S. Goyal, D. L. Schutt, G. Scoles, *Phys. Rev. Lett.* **1992**, *69*, 933–6.

[280] N. B. Brauer, S. Smolarek, X. Zhang, W. J. Buma, M. Drabbels, *J. Phys. Chem. Lett.* **2011**, *2*, 1563–6.

[281] F. Bierau, P. Kupser, G. Meijer, G. von Helden, *Phys. Rev. Lett.* **2010**, *105*, 133402.

[282] A. I. González Flórez, D. S. Ahn, S. Gewinner, W. Schöllkopf, G. von Helden, *Phys. Chem. Chem. Phys.* **2015**, *17*, 21902–11.

[283] A. I. González Flórez, E. Mucha, D. S. Ahn, S. Gewinner, W. Schöllkopf, K. Pagel, G. von Helden, *Angew. Chem. Int. Ed.* **2016**, *55*, 3295–9.

[284] E. Mucha, A. I. González Flórez, M. Marianski, D. A. Thomas, W. Hoffmann, W. B. Struwe, H. S. Hahm, S. Gewinner, W. Schöllkopf, P. H. Seeberger, G. von Helden, K. Pagel, *Angew. Chem. Int. Ed.* **2017**, *56*, 11248–51.

[285] E. Mucha, M. Marianski, F. F. Xu, D. A. Thomas, G. Meijer, G. von Helden, P. H. Seeberger, K. Pagel, *Nat. Commun.* **2018**, *9*, 4174.

[286] D. A. Thomas, R. Chang, E. Mucha, M. Lettow, K. Greis, S. Gewinner, W. Schöllkopf, G. Meijer, G. von Helden, *Phys. Chem. Chem. Phys.* **2020**, *22*, 18400–13.

[287] A. I. González Flórez, *Biomolecular Ions in Helium Nanodroplets*, PhD Thesis, Freie Universität Berlin, Berlin, **2016**.

[288] E. Mucha, *Vibrational Spectroscopy of Glycans in Helium Nanodroplets*, PhD Thesis, Radboud Universiteit Nijmegen, Nijmegen, **2020**.

[289] D. Pentlehner, R. Riechers, B. Dick, A. Slenczka, U. Even, N. Lavie, R. Brown, K. Luria, *Rev. Sci. Instrum.* **2009**, *80*, 043302.

[290] W. Schöllkopf, S. Gewinner, H. Junkes, A. Paarmann, G. von Helden, H. Bluem, A. M. M. Todd, *Proc. SPIE* **2015**, *9512*, 95121L.

[291] L. Jašíková, J. Roithová, *Chem. Eur. J.* **2018**, *24*, 3374–90.

[292] H. P. Freund, T. M. Antonsen, *Principles of Free Electron Lasers*, 3rd Edition, Springer, Cham, **2018**.

[293] S. Warnke, G. von Helden, K. Pagel, *Proteomics* **2015**, *15*, 2804–12.

[294] M. Lettow, *Fucosylated and Sulfated Glycans Investigated using Cryogenic Infrared Spectroscopy*, PhD Thesis, Radboud Universiteit Nijmegen, Nijmegen, **2022**.

[295] S. J. Allen, K. Giles, T. Gilbert, M. F. Bush, *Analyst* **2016**, *141*, 884–91.

[296] K. Giles, J. P. Williams, I. Campuzano, *Rapid Commun. Mass Spectrom.* **2011**, *25*, 1559–66.

[297] H. E. Revercomb, E. A. Mason, *Anal. Chem.* **2002**, *47*, 970–83.

[298] V. Gabelica, A. A. Shvartsburg, C. Afonso, P. Barran, J. L. P. Benesch, C. Bleiholder, M. T. Bowers, A. Bilbao, M. F. Bush, J. L. Campbell, I. D. G. Campuzano, T. Causon, B. H. Clowers, C. S. Creaser, E. De Pauw, J. Far, F. Fernandez-Lima, J. C. Fjeldsted, K. Giles, M. Groessl, J. Hogan, C. J., S. Hann, H. I. Kim, R. T. Kurulugama, J. C. May, J. A. McLean, K. Pagel, K. Richardson, M. E. Ridgeway, F. Rosu, F. Sobott, K. Thalassinos, S. J. Valentine, T. Wyttenbach, *Mass Spectrom. Rev.* **2019**, *38*, 291–320.

[299] M. Habgood, T. James, A. Heifetz in *Quantum Mechanics in Drug Discovery*, (Ed.: A. Heifetz), Springer, New York, **2020**, pp. 207–29.

[300] P. Pracht, F. Bohle, S. Grimme, *Phys. Chem. Chem. Phys.* **2020**, *22*, 7169–92.

[301] C. Bannwarth, S. Ehlert, S. Grimme, *J. Chem. Theory Comput.* **2019**, *15*, 1652–71.

[302] A. Supady, V. Blum, C. Baldauf, *J. Chem. Inf. Model.* **2015**, *55*, 2338–48.

[303] V. Blum, R. Gehrke, F. Hanke, P. Havu, V. Havu, X. Ren, K. Reuter, M. Scheffler, *Comput. Phys. Commun.* **2009**, *180*, 2175–96.

[304] J. P. Perdew, K. Burke, M. Ernzerhof, *Phys. Rev. Lett.* **1996**, *77*, 3865–8.

[305] A. Tkatchenko, M. Scheffler, *Phys. Rev. Lett.* **2009**, *102*, 073005.

[306] F. Pedregosa, G. Varoquaux, A. Gramfort, V. Michel, B. Thirion, O. Grisel, M. Blondel, P. Prettenhofer, R. Weiss, V. Dubourg, *J. Mach. Learn. Res.* **2011**, *12*, 2825–30.

[307] M. J. Frisch, G. W. Trucks, H. B. Schlegel, G. E. Scuseria, M. A. Robb, J. R. Cheeseman, G. Scalmani, V. Barone, G. A. Petersson, H. Nakatsuji, X. Li, M. Caricato, A. V. Marenich, J. Bloino, B. G. Janesko, R. Gomperts, B. Mennucci, H. P. Hratchian, J. V. Ortiz, A. F. Izmaylov, J. L. Sonnenberg, Williams, F. Ding, F. Lipparini, F. Egidi, J. Goings, B. Peng, A. Petrone, T. Henderson, D. Ranasinghe, V. G. Zakrzewski, J. Gao, N. Rega, G. Zheng, W. Liang, M. Hada, M. Ehara, K. Toyota, R. Fukuda, J. Hasegawa, M. Ishida, T. Nakajima, Y. Honda, O. Kitao, H. Nakai, T. Vreven, K. Throssell, J. A. Montgomery Jr., J. E. Peralta, F. Ogliaro, M. J. Bearpark, J. J. Heyd, E. N. Brothers, K. N. Kudin, V. N. Staroverov, T. A. Keith, R. Kobayashi, J. Normand, K. Raghavachari, A. P. Rendell, J. C. Burant, S. S. Iyengar, J. Tomasi, M. Cossi, J. M. Millam, M. Klene, C. Adamo, R. Cammi, J. W. Ochterski, R. L. Martin, K. Morokuma, O. Farkas, J. B. Foresman, D. J. Fox, Gaussian 16, Rev. A.03, Computer Program, Wallingford, **2016**.

[308] J. P. Perdew, M. Ernzerhof, K. Burke, *J. Chem. Phys.* **1996**, *105*, 9982–5.

[309] C. Adamo, V. Barone, *J. Chem. Phys.* **1999**, *110*, 6158–70.

[310] A. D. Becke, *J. Chem. Phys.* **1993**, *98*, 5648–52.

[311] A. D. Becke, *J. Chem. Phys.* **1993**, *98*, 1372–7.

[312] S. Grimme, J. Antony, S. Ehrlich, H. Krieg, *J. Chem. Phys.* **2010**, *132*, 154104.

[313] K. Greis, C. Kirschbaum, M. I. Taccone, M. Götze, S. Gewinner, W. Schöllkopf, G. Meijer, G. von Helden, K. Pagel, *Angew. Chem. Int. Ed.* **2022**, *61*, e202115481.

[314] L. Zanotto, G. Heerdt, P. C. T. Souza, G. Araujo, M. S. Skaf, *J. Comput. Chem.* **2018**, *39*, 1675–81.

[315] M. F. Mesleh, J. M. Hunter, A. A. Shvartsburg, G. C. Schatz, M. F. Jarrold, *J. Phys. Chem.* **1996**, *100*, 16082–6.

[316] U. C. Singh, P. A. Kollman, *J. Comput. Chem.* **1984**, *5*, 129–45.

[317] S. Grimme, *Angew. Chem. Int. Ed.* **2013**, *52*, 6306–12.

[318] V. Asgeirsson, C. A. Bauer, S. Grimme, *Phys. Chem. Chem. Phys.* **2016**, *18*, 31017–26.

[319] J. Koopman, S. Grimme, *ACS Omega* **2019**, *4*, 15120–33.

[320] J. Koopman, S. Grimme, *J. Am. Soc. Mass Spectrom.* **2021**, *32*, 1735–51.

[321] J. Koopman, S. Grimme, **2022**, ChemRxiv preprint DOI: 10.26434/chemrxiv-2022–w5260.

[322] C. Kirschbaum, K. Greis, E. Mucha, L. Kain, S. Deng, A. Zappe, S. Gewinner, W. Schöllkopf, G. von Helden, G. Meijer, P. B. Savage, M. Marianski, L. Teyton, K. Pagel, *Nat. Commun.* **2021**, *12*, 1201.

[323] T. Yamashita, R. Wada, T. Sasaki, C. Deng, U. Bierfreund, K. Sandhoff, R. L. Proia, *Proc. Natl. Acad. Sci. U. S. A.* **1999**, *96*, 9142–7.

[324] W. Stoffel, A. Bosio, *Curr. Opin. Neurobiol.* **1997**, *7*, 654–61.

[325] L. Kain, B. Webb, B. L. Anderson, S. Deng, M. Holt, A. Costanzo, M. Zhao, K. Self, A. Teyton, C. Everett, M. Kronenberg, D. M. Zajonc, A. Bendelac, P. B. Savage, L. Teyton, *Immunity* **2014**, *41*, 543–54.

[326] T. Kawano, J. Cui, Y. Koezuka, I. Toura, Y. Kaneko, K. Motoki, H. Ueno, R. Nakagawa, H. Sato, E. Kondo, H. Koseki, M. Taniguchi, *Science* **1997**, *278*, 1626–9.

[327] J. Mattner, K. L. Debord, N. Ismail, R. D. Goff, C. Cantu III, D. Zhou, P. Saint-Mezard, V. Wang, Y. Gao, N. Yin, K. Hoebe, O. Schneewind, D. Walker, B. Beutler, L. Teyton, P. B. Savage, A. Bendelac, *Nature* **2005**, *434*, 525–9.

[328] T. Natori, Y. Koezuka, T. Higa, *Tetrahedron Lett.* **1993**, *34*, 5591–2.

[329] V. F. Vartabedian, P. B. Savage, L. Teyton, *Immunol. Rev.* **2016**, *272*, 109–19.

[330] A. K. Stanic, A. D. De Silva, J. J. Park, V. Sriram, S. Ichikawa, Y. Hirabyashi, K. Hayakawa, L. Van Kaer, R. R. Brutkiewicz, S. Joyce, *Proc. Natl. Acad. Sci. U. S. A.* **2003**, *100*, 1849–54.

[331] L. Kain, A. Costanzo, B. Webb, M. Holt, A. Bendelac, P. B. Savage, L. Teyton, *Mol. Immunol.* **2015**, *68*, 94–7.

[332] P. J. Brennan, T. Y. Cheng, D. G. Pellicci, G. F. M. Watts, N. Veerapen, D. C. Young, J. Rossjohn, G. S. Besra, D. I. Godfrey, M. B. Brenner, D. B. Moody, *Proc. Natl. Acad. Sci. U. S. A.* **2017**, *114*, 8348–53.

[333] P. J. Brennan, R. V. V. Tatituri, M. Brigl, E. Y. Kim, A. Tuli, J. P. Sanderson, S. D. Gadola, F.-F. Hsu, G. S. Besra, M. B. Brenner, *Nat. Immunol.* **2011**, *12*, 1202–11.

[334] J. Li, T. Vosegaard, Z. Guo, *Prog. Lipid Res.* **2017**, *68*, 37–56.

[335] N. Yin, X. Long, R. D. Goff, D. Zhou, C. Cantu III, J. Mattner, P. S. Mezard, L. Teyton, A. Bendelac, P. B. Savage, *ACS Chem. Biol.* **2009**, *4*, 199–208.

[336] V. Chaudhary, L. A. Albacker, S. Deng, Y. T. Chuang, Y. Li, D. T. Umetsu, P. B. Savage, *Org. Lett.* **2013**, *15*, 5242–5.

[337] W. Du, S. S. Kulkarni, J. Gervay-Hague, *Chem. Commun.* **2007**, 2336–8.

[338] E. Manzo, M. L. Ciavatta, D. Pagano, A. Fontana, *Tetrahedron Lett.* **2012**, *53*, 879–81.

[339] J. Folch, M. Lees, G. H. Sloane Stanley, *J. Biol. Chem.* **1957**, *226*, 497–509.

[340] E. G. Bligh, W. J. Dyer, *Can. J. Biochem. Physiol.* **1959**, *37*, 911–7.

[341] L. J. Morris, *J. Lipid Res.* **1966**, *7*, 717–32.

[342] G. Dobson, W. W. Christie, B. Nikolova-Damyanova, *J. Chromatogr. B Biomed. Appl.* **1995**, *671*, 197–222.

[343] D. D. Lee, H. S. Seung, *Nature* **1999**, *401*, 788–91.

[344] M. Marianski, A. Supady, T. Ingram, M. Schneider, C. Baldauf, *J. Chem. Theory Comput.* **2016**, *12*, 6157–68.

[345] M. Marianski, E. Mucha, K. Greis, S. Moon, A. Pardo, C. Kirschbaum, D. A. Thomas, G. Meijer, G. von Helden, K. Gilmore, P. H. Seeberger, K. Pagel, *Angew. Chem. Int. Ed.* **2020**, *59*, 6166–71.

[346] K. B. Bec, C. W. Huck, *Front. Chem.* **2019**, *7*, 48.

[347] V. Barone, *J. Chem. Phys.* **2005**, *122*, 14108.

[348] P. T. Panek, C. R. Jacob, *J. Phys. Chem. Lett.* **2016**, *7*, 3084–90.

[349] J. C. Howard, J. D. Enyard, G. S. Tschumper, *J. Chem. Phys.* **2015**, *143*, 214103.

[350] S. Deng, L. Kain, C. S. Pereira, S. Mata, M. F. Macedo, A. Bendelac, L. Teyton, P. B. Savage, *Chem. Sci.* **2017**, *8*, 2204–8.

[351] B. L. Anderson, L. Teyton, A. Bendelac, P. B. Savage, *Molecules* **2013**, *18*, 15662–88.

[352] D. Zhou, J. Mattner, C. Cantu III, N. Schrantz, N. Yin, Y. Gao, Y. Sagiv, K. Hudspeth, Y. P. Wu, T. Yamashita, S. Teneberg, D. Wang, R. L. Proia, S. B. Levery, P. B. Savage, L. Teyton, A. Bendelac, *Science* **2004**, *306*, 1786–9.

[353] Y. Kinjo, E. Tupin, D. Wu, M. Fujio, R. Garcia-Navarro, M. R. Benhnia, D. M. Zajonc, G. Ben-Menachem, G. D. Ainge, G. F. Painter, A. Khurana, K. Hoebe, S. M. Behar, B. Beutler, I. A. Wilson, M. Tsuji, T. J. Sellati, C. H. Wong, M. Kronenberg, *Nat. Immunol.* **2006**, *7*, 978–86.

[354] Y. Kinjo, P. Illarionov, J. L. Vela, B. Pei, E. Girardi, X. Li, Y. Li, M. Imamura, Y. Kaneko, A. Okawara, Y. Miyazaki, A. Gomez-Velasco, P. Rogers, S. Dahesh, S. Uchiyama, A. Khurana, K. Kawahara, H. Yesilkaya, P. W. Andrew, C. H. Wong, K. Kawakami, V. Nizet, G. S. Besra, M. Tsuji, D. M. Zajonc, M. Kronenberg, *Nat. Immunol.* **2011**, *12*, 966–74.

[355] Z. Huang, A. Zhou, G. Zhang in *Computational Intelligence and Intelligent Systems*, (Eds.: Z. Li, X. Li, Y. Liu, Z. Cai), Springer, Heidelberg, **2012**, pp. 331–40.

[356] K. Tang, J. S. Page, R. D. Smith, *J. Am. Soc. Mass Spectrom.* **2004**, *15*, 1416–23.

[357] A. H. Abikhodr, V. Yatsyna, A. Ben Faleh, S. Warnke, T. R. Rizzo, *Anal. Chem.* **2021**, *93*, 14730–6.

[358] Y. Fujiwara, K. Hama, K. Yokoyama, *Carbohydr. Res.* **2020**, *490*, 107959.

[359] J. P. O'Brien, J. S. Brodbelt, *Anal. Chem.* **2013**, *85*, 10399–407.

[360] K. Greis, C. Kirschbaum, G. von Helden, K. Pagel, *Curr. Opin. Struct. Biol.* **2022**, *72*, 194–202.

[361] C. Kirschbaum, E. M. Saied, K. Greis, E. Mucha, S. Gewinner, W. Schöllkopf, G. Meijer, G. von Helden, B. L. J. Poad, S. J. Blanksby, C. Arenz, K. Pagel, *Angew. Chem. Int. Ed.* **2020**, *59*, 13638–42.

[362] C. Kirschbaum, K. Greis, M. Lettow, S. Gewinner, W. Schöllkopf, G. Meijer, G. von Helden, K. Pagel, *Anal. Bioanal. Chem.* **2021**, *413*, 3643–53.

[363] M. A. Lone, T. Santos, I. Alecu, L. C. Silva, T. Hornemann, *Biochim. Biophys. Acta Mol. Cell Biol. Lipids* **2019**, *1864*, 512–21.

[364] A. Penno, M. M. Reilly, H. Houlden, M. Laura, K. Rentsch, V. Niederkofler, E. T. Stoeckli, G. Nicholson, F. Eichler, J. Brown, R. H., A. von Eckardstein, T. Hornemann, *J. Biol. Chem.* **2010**, *285*, 11178–87.

[365] I. Alecu, A. Othman, A. Penno, E. M. Saied, C. Arenz, A. von Eckardstein, T. Hornemann, *J. Lipid Res.* **2017**, *58*, 60–71.

[366] R. Cuadros, E. Montejo de Garcini, F. Wandosell, G. Faircloth, J. M. Fernández-Sousa, J. Avila, *Cancer Lett.* **2000**, *152*, 23–9.

[367] N. C. Zitomer, T. Mitchell, K. A. Voss, G. S. Bondy, S. T. Pruett, E. C. Garnier-Amblard, L. S. Liebeskind, H. Park, E. Wang, M. C. Sullards, A. H. Merrill, R. T. Riley, *J. Biol. Chem.* **2009**, *284*, 4786–95.

[368] J. T. Hannich, A. G. Haribowo, S. Gentina, M. Paillard, L. Gomez, B. Pillot, H. Thibault, D. Abegg, N. Guex, A. Zumbuehl, A. Adibekian, M. Ovize, J.-C. Martinou, H. Riezman, *Nat. Metab.* **2019**, *1*, 996–1008.

[369] M. Bertea, M. F. Rutti, A. Othman, J. Marti-Jaun, M. Hersberger, A. von Eckardstein, T. Hornemann, *Lipids Health Dis.* **2010**, *9*, 84.

[370] J. Mwinyi, A. Bostrom, I. Fehrer, A. Othman, G. Waeber, H. Marti-Soler, P. Vollenweider, P. Marques-Vidal, H. B. Schioth, A. von Eckardstein, T. Hornemann, *PLoS One* **2017**, *12*, e0175776.

[371] R. Steiner, E. M. Saied, A. Othman, C. Arenz, A. T. Maccarone, B. L. J. Poad, S. J. Blanksby, A. von Eckardstein, T. Hornemann, *J. Lipid Res.* **2016**, *57*, 1194–203.

[372] Y. Bai, J. G. McCoy, E. J. Levin, P. Sobrado, K. R. Rajashankar, B. G. Fox, M. Zhou, *Nature* **2015**, *524*, 252–6.

[373] H. Guillou, D. Zadravec, P. G. Martin, A. Jacobsson, *Prog. Lipid Res.* **2010**, *49*, 186–99.

[374] N. Nicolaides, *Science* **1974**, *186*, 19–26.

[375] S. M. Prouty, A. Pappas in *Lipids and Skin Health*, (Ed.: A. Pappas), Springer, New York, **2015**, pp. 139–57.

[376] E. Vongerichten, A. Köhler, *Chem. Ber.* **1909**, *42*, 1638–9.

[377] Y. Poirier, V. D. Antonenkov, T. Glumoff, J. K. Hiltunen, *Biochim. Biophys. Acta* **2006**, *1763*, 1413–26.

[378] W. Yu, X. Liang, R. E. Ensenauer, J. Vockley, L. Sweetman, H. Schulz, *J. Biol. Chem.* **2004**, *279*, 52160–7.

[379] C. Ferreri, C. Chatgilialoglu, *ChemBioChem* **2005**, *6*, 1722–34.

[380] C. Ferreri, A. Sansone, S. Buratta, L. Urbanelli, E. Costanzi, C. Emiliani, C. Chatgilialoglu, *Cancers* **2020**, *12*, 900.

[381] D. J. Harvey, *Biol. Mass Spectrom.* **1982**, *9*, 33–8.

[382] W. W. Christie, K. Stefanov, *J. Chromatogr. A* **1987**, *392*, 259–65.

[383] X. Li, A. A. Franke, *Anal. Chem.* **2011**, *83*, 3192–8.

[384] E. M. Saied, T. L. Le, T. Hornemann, C. Arenz, *Bioorg. Med. Chem.* **2018**, *26*, 4047–57.

[385] J. Ren, E. M. Saied, A. Zhong, J. Snider, C. Ruiz, C. Arenz, L. M. Obeid, G. D. Girnun, Y. A. Hannun, *J. Lipid Res.* **2018**, *59*, 2126–39.

[386] E. M. Saied, C. Arenz, **2020**, ChemRxiv preprint DOI: 10.26434/chemrxiv.12094041.v1.

[387] V. Matyash, G. Liebisch, T. V. Kurzchalia, A. Shevchenko, D. Schwudke, *J. Lipid Res.* **2008**, *49*, 1137–46.

[388] S. M. Stow, T. J. Causon, X. Zheng, R. T. Kurulugama, T. Mairinger, J. C. May, E. E. Rennie, E. S. Baker, R. D. Smith, J. A. McLean, S. Hann, J. C. Fjeldsted, *Anal. Chem.* **2017**, *89*, 9048–55.

[389] B. L. J. Poad, A. T. Maccarone, H. Yu, T. W. Mitchell, E. M. Saied, C. Arenz, T. Hornemann, J. N. Bull, E. J. Bieske, S. J. Blanksby, *Anal. Chem.* **2018**, *90*, 5343–51.

[390] X. Han, K. Yang, R. W. Gross, *Mass Spectrom. Rev.* **2012**, *31*, 134–78.

[391] C. M. Bassett, A. L. Edel, A. F. Patenaude, R. S. McCullough, D. P. Blackwood, P. Y. Chouinard, P. Paquin, B. Lamarche, G. N. Pierce, *J. Nutr.* **2010**, *140*, 18–24.

[392] C. Kirschbaum, K. Greis, L. Polewski, S. Gewinner, W. Schöllkopf, G. Meijer, G. von Helden, K. Pagel, *J. Am. Chem. Soc.* **2021**, *143*, 14827–34.

[393] C. Kirschbaum, K. Greis, S. Gewinner, W. Schöllkopf, G. Meijer, G. von Helden, K. Pagel, *Anal. Bioanal. Chem.* **2022**, *414*, 5275–85.

[394] M. Wuhrer, A. M. Deelder, Y. E. van der Burgt, *Mass Spectrom. Rev.* **2011**, *30*, 664–80.

[395] E. Mucha, M. Lettow, M. Marianski, D. A. Thomas, W. B. Struwe, D. J. Harvey, G. Meijer, P. H. Seeberger, G. von Helden, K. Pagel, *Angew. Chem. Int. Ed.* **2018**, *57*, 7440–3.

[396] R. W. Vachet, B. M. Bishop, B. W. Erickson, G. L. Glish, *J. Am. Chem. Soc.* **1997**, *119*, 5481–8.

[397] M. R. Anari, R. I. Sanchez, R. Bakhtiar, R. B. Franklin, T. A. Baillie, *Anal. Chem.* **2004**, *76*, 823–32.

[398] T. Kind, K. H. Liu, D. Y. Lee, B. DeFelice, J. K. Meissen, O. Fiehn, *Nat. Methods* **2013**, *10*, 755–8.

[399] R. M. Borges, S. M. Colby, S. Das, A. S. Edison, O. Fiehn, T. Kind, J. Lee, A. T. Merrill, J. Merz, K. M., T. O. Metz, J. R. Nunez, D. J. Tantillo, L. P. Wang, S. Wang, R. S. Renslow, *Chem. Rev.* **2021**, *121*, 5633–70.

[400] A. Carrà, R. Spezia, *Chemistry–Methods* **2021**, *1*, 123–30.

[401] U. W. Liebal, A. N. T. Phan, M. Sudhakar, K. Raman, L. M. Blank, *Metabolites* **2020**, *10*.

[402] N. C. Polfer, J. Oomens, S. Suhai, B. Paizs, *J. Am. Chem. Soc.* **2005**, *127*, 17154–5.

[403] N. C. Polfer, J. Oomens, S. Suhai, B. Paizs, *J. Am. Chem. Soc.* **2007**, *129*, 5887–97.

[404] M. Thevis, S. Beuck, S. Hoppner, A. Thomas, J. Held, M. Schafer, J. Oomens, W. Schanzer, *J. Am. Soc. Mass Spectrom.* **2012**, *23*, 537–46.

[405] J. Martens, G. Berden, H. Bentlage, K. L. M. Coene, U. F. Engelke, D. Wishart, M. van Scherpenzeel, L. A. J. Kluijtmans, R. A. Wevers, J. Oomens, *J. Inherit. Metab. Dis.* **2018**, *41*, 367–77.

[406] R. E. van Outersterp, K. J. Houthuijs, G. Berden, U. F. Engelke, L. A. J. Kluijtmans, R. A. Wevers, K. L. M. Coene, J. Oomens, J. Martens, *Int. J. Mass Spectrom.* **2019**, *443*, 77–85.

[407] S. Becher, G. Berden, J. Martens, J. Oomens, S. Heiles, *J. Am. Soc. Mass Spectrom.* **2021**, *32*, 2874–84.

[408] F.-F. Hsu, A. Bohrer, J. Turk, *J. Am. Soc. Mass Spectrom.* **1998**, *9*, 516–26.

[409] P. Domingues, M. R. Domingues, F. M. Amado, A. J. Ferrer-Correia, *Rapid Commun. Mass Spectrom.* **2001**, *15*, 799–804.

[410] F.-F. Hsu, J. Turk, *J. Am. Soc. Mass Spectrom.* **2003**, *14*, 352–63.

[411] N. J. Miller, C. Rice-Evans, M. J. Davies, V. Gopinathan, A. Milner, *Clin. Sci.* **1993**, *84*, 407–12.

[412] E. Perri, F. Mazzotti, A. Raffaelli, G. Sindona, *J. Mass Spectrom.* **2000**, *35*, 1360–1.

[413] M. Takayama, T. Kosaka, T. Kinoshita, *J. Mass Spectrom. Soc. Jpn.* **1996**, *44*, 473–81.

[414] O. Montero, M. Ramirez, A. Sanchez-Guijo, C. Gonzalez, *Biomed. Chromatogr.* **2012**, *26*, 1228–33.

[415] S. Ben-Shabat, N. Baruch, A. C. Sintov, *Drug Dev. Ind. Pharm.* **2007**, *33*, 1169–75.

[416] T. Hayes, Y. Hu, S. A. Sanchez-Vazquez, H. C. Hailes, A. E. Aliev, J. R. G. Evans, *J. Polym. Sci. Part A: Polym. Chem.* **2016**, *54*, 3159–70.

[417] D. R. Kodali, A. Tercyak, D. A. Fahey, D. M. Small, *Chem. Phys. Lipids* **1990**, *52*, 163–70.

[418] J. A. Laszlo, D. L. Compton, K. E. Vermillion, *J. Am. Oil Chem. Soc.* **2008**, *85*, 307–12.

[419] S. Warnke, J. Seo, J. Boschmans, F. Sobott, J. H. Scrivens, C. Bleiholder, M. T. Bowers, S. Gewinner, W. Schöllkopf, K. Pagel, G. von Helden, *J. Am. Chem. Soc.* **2015**, *137*, 4236–42.

[420] K. Jiang, G. Gachumi, A. Poudel, B. Shurmer, Z. Bashi, A. El-Aneed, *J. Am. Soc. Mass Spectrom.* **2019**, *30*, 1700–12.

[421] L. M. Amundson, B. C. Owen, V. A. Gallardo, S. C. Habicht, M. Fu, R. C. Shea, A. B. Mossman, H. I. Kenttamaa, *J. Am. Soc. Mass Spectrom.* **2011**, *22*, 670–82.

[422] R. Yamauchi in *Food Factors for Cancer Prevention*, (Eds.: H. Ohigashi, T. Osawa, J. Terao, S. Watanabe, T. Yoshikawa), Springer, Tokyo, **1997**, pp. 483–7.

[423] R. Velasco, C. Silva López, O. Nieto Faza, R. Sanz, *Chem. Eur. J.* **2016**, *22*, 15058–68.

[424] F. Wang, J. Wang, Y. Zhang, J. Yang, *Tetrahedron* **2020**, *76*, 130857.

[425] S. Warnke, A. Ben Faleh, R. P. Pellegrinelli, N. Yalovenko, T. R. Rizzo, *Faraday Discuss.* **2019**, *217*, 114–25.

[426] S. Warnke, A. Ben Faleh, T. R. Rizzo, *ACS Meas. Sci. Au* **2021**, *1*, 157–64.

[427] C. Kirschbaum, K. Pagel, *Anal. Sens.* **2022**, e202200103.

[428] E. Saparbaev, A. Zviagin, O. V. Boyarkin, *Anal. Chem.* **2022**, *94*, 9514–8.

[429] P. Figueiredo, M. Suttinger, R. Go, E. Tsvid, C. K. N. Patel, A. Lyakh, *Appl. Opt.* **2017**, *56*, H15–H23.

[430] S. B. Mirov, I. S. Moskalev, S. Vasilyev, V. Smolski, V. V. Fedorov, D. Martyshkin, J. Peppers, M. Mirov, A. Dergachev, V. Gapontsev, *IEEE J. Sel. Top. Quantum Electron.* **2018**, *24*, 1–29.

[431] V. Yatsyna, A. H. Abikhodr, A. Ben Faleh, S. Warnke, T. R. Rizzo, *Anal. Chem.* **2022**, *94*, 2912–7.

[432] B. Schindler, G. Laloy-Borgna, L. Barnes, A. R. Allouche, E. Bouju, V. Dugas, C. Demesmay, I. Compagnon, *Anal. Chem.* **2018**, *90*, 11741–5.

[433] O. Yeni, B. Schindler, B. Moge, I. Compagnon, *Analyst* **2022**, *147*, 312–7.

[434] R. F. Kranenburg, F. van Geenen, G. Berden, J. Oomens, J. Martens, A. C. van Asten, *Anal. Chem.* **2020**, *92*, 7282–8.

[435] R. E. van Outersterp, J. Martens, G. Berden, V. Koppen, F. Cuyckens, J. Oomens, *Analyst* **2020**, *145*, 6162–70.

[436] P. Bansal, V. Yatsyna, A. H. Abikhodr, S. Warnke, A. Ben Faleh, N. Yalovenko, V. H. Wysocki, T. R. Rizzo, *Anal. Chem.* **2020**, *92*, 9079–85.

[437] R. Han, R. Ketkaew, S. Luber, *J. Phys. Chem. A* **2022**, *126*, 801–12.

[438] J. Martens, G. Berden, R. E. van Outersterp, L. A. J. Kluijtmans, U. F. Engelke, C. D. M. van Karnebeek, R. A. Wevers, J. Oomens, *Sci. Rep.* **2017**, *7*, 3363.

[439] M. J. Carlo, A. L. Patrick, *J. Mass Spectrom. Adv. Clin. Lab.* **2022**, *23*, 14–25.

[440] V. A. Mikhailov, I. Liko, T. H. Mize, M. F. Bush, J. L. Benesch, C. V. Robinson, *Anal. Chem.* **2016**, *88*, 7060–7.

List of Publications

Peer-Reviewed Journal Publications

1) L. Bechtella, C. Kirschbaum, M. Cosset, G. Clodic, L. Matheron, G. Bolbach, S. Sagan, A. Walrant, E. Sachon, Benzophenone Photoreactivity in a Lipid Bilayer To Probe Peptide/Membrane Interactions: Simple System, Complex Information, *Anal. Chem.* **2019**, *91*, 9102–9110.

2) M. Marianski, E. Mucha, K. Greis, S. Moon, A. Pardo, C. Kirschbaum, D. A. Thomas, G. Meijer, G. von Helden, K. Gilmore, P. H. Seeberger, K. Pagel, Direct Evidence for Remote Participation in Galactose Building Blocks during Glycosylations Revealed by Cryogenic Vibrational Spectroscopy, *Angew. Chem. Int. Ed.* **2020**, *59*, 6166–6171.

3) C. Kirschbaum, E. M. Saied, K. Greis, E. Mucha, S. Gewinner, W. Schöllkopf, G. Meijer, G. von Helden, B. L. J. Poad, S. J. Blanksby, C. Arenz, K. Pagel, Resolving Sphingolipid Isomers using Cryogenic Infrared Spectroscopy, *Angew. Chem. Int. Ed.* **2020**, *59*, 13638–13642.

4) K. Greis, E. Mucha, M. Lettow, D. A. Thomas, C. Kirschbaum, S. Moon, A. Pardo-Vargas, G. von Helden, G. Meijer, K. Gilmore, P. H. Seeberger, K. Pagel, The Impact of Leaving Group Anomericity on the Structure of Glycosyl Cations of Protected Galactosides, *ChemPhysChem* **2020**, *21*, 1905–1907.

5) K. Greis, C. Kirschbaum, S. Leichnitz, S. Gewinner, W. Schöllkopf, G. von Helden, G. Meijer, P. H. Seeberger, K. Pagel, Direct Experimental Characterization of the Ferrier Glycosyl Cation in the Gas Phase, *Org. Lett.* **2020**, *22*, 8916–8919.

6) C. Kirschbaum, K. Greis, E. Mucha, L. Kain, S. Deng, A. Zappe, S. Gewinner, W. Schöllkopf, G. von Helden, G. Meijer, P. B. Savage, M. Marianski, L. Teyton, K. Pagel, Unravelling the Structural Complexity of Glycolipids with Cryogenic Infrared Spectroscopy, *Nat. Commun.* **2021**, *12*, 1201.

7) C. Kirschbaum, K. Greis, M. Lettow, S. Gewinner, W. Schöllkopf, G. Meijer, G. von Helden, K. Pagel, Non-Covalent Double Bond Sensors for Gas-Phase Infrared Spectroscopy of Unsaturated Fatty Acids, *Anal. Bioanal. Chem.* **2021**, *413*, 3643–3653.

8) C. Kirschbaum, K. Greis, L. Polewski, S. Gewinner, W. Schöllkopf, G. Meijer, G. von Helden, K. Pagel, Unveiling Glycerolipid Fragmentation by Cryogenic Infrared Spectroscopy, *J. Am. Chem. Soc.* **2021**, *143*, 14827–14834.

9) M. Grabarics, M. Lettow, C. Kirschbaum, K. Greis, C. Manz, K. Pagel, Mass Spectrometry-Based Techniques to Elucidate the Sugar Code, *Chem. Rev.* **2022**, *122*, 7840–7908.

10) K. Greis[‡], C. Kirschbaum[‡], G. von Helden, K. Pagel, Gas-Phase Infrared Spectroscopy of Glycans and Glycoconjugates, *Curr. Opin. Struct. Biol.* **2022**, *72*, 194–202.

11) C. Kirschbaum[‡], K. Greis[‡], S. Gewinner, W. Schöllkopf, G. Meijer, G. von Helden, K. Pagel, Cryogenic Infrared Spectroscopy Provides Mechanistic Insight into the Fragmentation of Phospholipid Silver Adducts, *Anal. Bioanal. Chem.* **2022**, *414*, 5275–5285.

12) K. Greis[‡], C. Kirschbaum[‡], M. I. Taccone, M. Götze, S. Gewinner, W. Schöllkopf, G. Meijer, G. von Helden, K. Pagel, Studying the Key Intermediate of RNA Autohydrolysis by Cryogenic Gas-Phase Infrared Spectroscopy, *Angew. Chem. Int. Ed.* **2022**, *61*, e202115481.

13) K. Greis, C. Kirschbaum, G. Fittolani, E. Mucha, R. Chang, G. Meijer, G. von Helden, M. Delbianco, P. H. Seeberger, K. Pagel, Neighboring Group Participation of Benzoyl Protecting Groups in C3- and C6-Fluorinated Glucose, *Eur. J. Org. Chem.* **2022**, e202200255.

14) K. Greis[‡], S. Leichnitz[‡], C. Kirschbaum, C. Chang, M. Lin, G. Meijer, G. von Helden, P. H. Seeberger, K. Pagel, The Influence of the Electron Density in Acyl Protecting Groups on the Selectivity of Galactose Formation, *J. Am. Chem. Soc.* **2022**, *144*, 20258–20266.

15) C. Kirschbaum, K. Pagel, Lipid Analysis by Mass Spectrometry coupled with Laser Light, *Anal. Sens.* **2022**, e202200103.

Other Publications

C. Kirschbaum, Emerging Scientists in Analytical Sciences: Carla Kirschbaum, *Anal. Sci. Adv.* **2022**, *3*, 255–257.

[‡] *Equal contribution of the respective authors.*

Cover Features

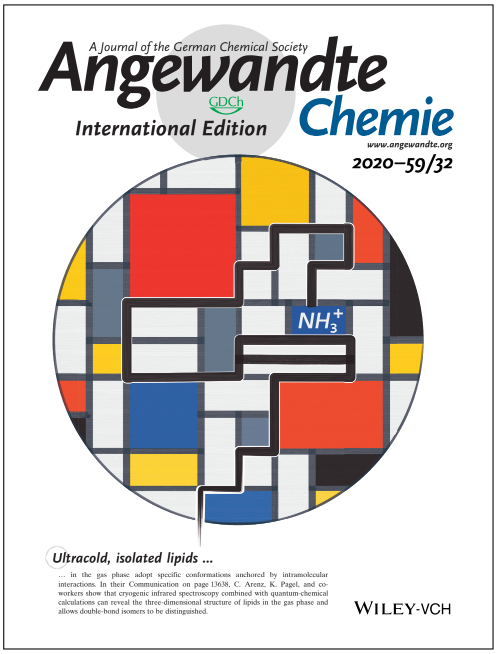
A Journal of the German Chemical Society
Angewandte Chemie
International Edition
www.angewandte.org
2020–59/32

Ultracold, isolated lipids …

… in the gas phase adopt specific conformations anchored by intramolecular interactions. In their Communication on page 13638, C. Arenz, K. Pagel, and co-workers show that cryogenic infrared spectroscopy combined with quantum-chemical calculations can reveal the three-dimensional structure of lipids in the gas phase and allows double-bond isomers to be distinguished.

WILEY-VCH

Inside Cover *Angew. Chem. Int. Ed.* **2020**, *59* (32)

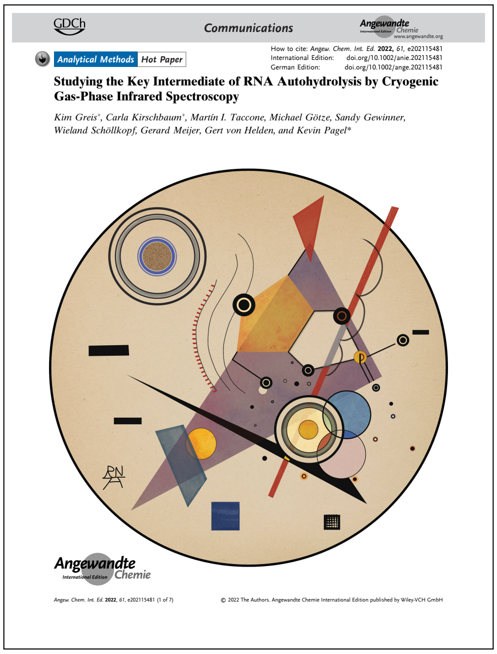
GDCh Communications Angewandte Chemie www.angewandte.org

Analytical Methods Hot Paper

How to cite: *Angew. Chem. Int. Ed.* **2022,** *61,* e202115481
International Edition: doi.org/10.1002/anie.202115481
German Edition: doi.org/10.1002/ange.202115481

Studying the Key Intermediate of RNA Autohydrolysis by Cryogenic Gas-Phase Infrared Spectroscopy

*Kim Greis+, Carla Kirschbaum+, Martín I. Taccone, Michael Götze, Sandy Gewinner, Wieland Schöllkopf, Gerard Meijer, Gert von Helden, and Kevin Pagel**

Angewandte Chemie International Edition

Angew. Chem. Int. Ed. **2022**, *61*, e202115481 (1 of 7)

© 2022 The Authors. Angewandte Chemie International Edition published by Wiley-VCH GmbH

Frontispiece *Angew. Chem. Int. Ed.* **2022**, *61* (19)

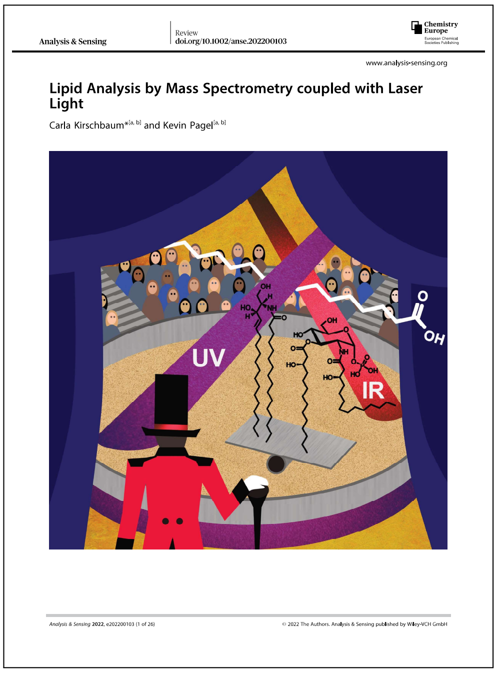
Analysis & Sensing
Review
doi.org/10.1002/anse.202200103
Chemistry Europe
European Chemical Societies Publishing

www.analysis-sensing.org

Lipid Analysis by Mass Spectrometry coupled with Laser Light

Carla Kirschbaum*[a, b] and Kevin Pagel[a, b]

Analysis & Sensing **2022**, e202200103 (1 of 26)

© 2022 The Authors. Analysis & Sensing published by Wiley-VCH GmbH

Frontispiece *Anal. Sens.* **2022**

Acknowledgments

Research often progresses slowly and requires a great deal of perseverance and patience, but eventually every project comes to an end. That's why the quote from Marcel Proust's *A la recherche du temps perdu* reminded me so much of my work when the book accompanied me during the first Corona lockdown. Now my thesis is finally finished, and there are many people I would like to thank at this point for their continued support that has made the sometimes lengthy work worthwhile and enjoyable.

First and foremost, I thank Prof. Kevin Pagel for sparking my interest in biomolecules in his bioorganic chemistry lecture back in 2016, for entrusting me with interesting research projects, and for introducing me to other researchers around the world. Kevin has always been a mentor to me, giving me as much support as I needed and as much responsibility as I could handle. I also thank Prof. Gert von Helden for trustingly letting me work on the HeDrop instrument and for being there when we needed help, for example when the helium bottle had to be replaced late in the evening. Furthermore, I thank Prof. Rainer Haag, who immediately agreed to be the second reviewer of my thesis.

In the four years that I have worked at the Fritz Haber Institute, I have met many supportive and humorous colleagues and friends. The first person I met was Eike, the supervisor of my master thesis, who taught me all the secrets of the HeDrop instrument and other useful things, such as which fonts to use and which to avoid (Comic Sans). Kim the Old Man has accompanied me from the beginning of my master thesis until now, and we have become known as the *Dynamic Duo*, sharing numerous beamtimes, cookies, and oven cheese. I thank him for introducing me to computational chemistry, for his constant support in my research projects, and for sharing my passion for Mario Kart. This passion was also shared by Clemens, whom I thank for being a good office mate making sure we would never get cold or hungry. The M&M duo Maike and Márkó were very good senior PhD students who taught me how the group works. I especially enjoyed the short but always funny time that I shared with Freiherr Márkó von Grabarics in our enclave office. This cohabitation gave me the opportunity to learn the most important words to survive in Hungary, such as *fehér-, tej-*, and *étcsoki* and my all-time favorite *csütörtök*, from the exceptionally qualified teachers Márkó and Gergő.

I thank the entire *HeDrop Crew* including Martín, Katja, and América. In particular, I thank América for supporting my efforts to learn Spanish in our weekly tandem sessions and for always understanding me and being on my side in any discussion, especially when it comes to food. Discussions during lunch were often enriched by the *iMob Peoplez* Jan, Jerome, and Paula, who tend to have their own view on the world and are among the most generous people I know. Furthermore, I thank the *FU Crew* Andreas, Christian, Lukasz, Leïla, Micha, Marc, Emeline, Eunjin, Tom, Chun-Wei, and Anna, who are unfortunately far away, but have always welcomed me very cordially when I came to visit them. My special thanks go to Marc, whose unfailing optimism helped me survive the OC Praktikum, and to Micha, who keeps me up to date on board games and repairs things, while Lukasz is more inclined to disassemble items in my home, but is otherwise a very entertaining fellow.

I thank Prof. Gerard Meijer, Manuela, Karin, Evelyn, Stefan, Sebastian, Martin, and all the other helpful people who provided me with everything I needed for my work at the Fritz Haber Institute. Because a good infrared experiment requires above all a very good light source, special thanks go to the best laser operators, Sandy and Wieland, who should have their own entertainment show. Besides always being up for a joke and being generous with beamtimes for their favorite users, I thank them for their confidence in Kim and me and for training us as FEL operators. This teaching allowed us to extend our beamtimes even when the laser crashed at night, which preferably happened right after Wieland left the institute.

Many projects in this thesis would not have been possible without the numerous collaborations with other research groups around the world. I hereby thank Prof. Christoph Arenz and Essa, Prof. Luc Teyton, Prof. Paul Savage, and coworkers for providing the unique, unpurchasable reference samples for this work. A big thank you goes to Prof. Tim Causon and to my favorite research team in Brisbane, consisting of Prof. Stephen Blanksby, Reuben, Philipp, and Berwyck, who are extremely helpful and kind and with whom I really enjoyed working. Finally, I thank the Dahlem Research School and the Fonds der Chemischen Industrie for funding my work and the Studienstiftung des deutschen Volkes for the great ideational support.

While I was writing this thesis, many people volunteered (or couldn't say no) to proofread my work. I am grateful to my dedicated proofreaders Gergő, Kim, Márkó, Maike, Martín, Jan, Wieland, and especially the *Carla-Correction-Club*, whose members América and Thorren were brave enough to read this thesis from the beginning to the end. I thank Thorren for many more things, most of all for being an understanding and caring husband and a very good home office mate during the first lockdown, reliably replenishing our cookie, carrot, and cheese supplies. Furthermore, a warm thank you goes to my parents, brother, aunt and uncle, as well as my parents-in-law and brother-in-law for their continued support. I thank my family for taking care of me, saving food for me, and always being in a cheerful mood on Friday evenings when they have to watch TV shows with me that no one else wants to watch. I also thank my friends who have been with me since we were 10 or even younger, and who support me in everything I want to do. Overall, I look back with gratitude on my time as a PhD student at the Fritz Haber Institute and am now looking forward to joining Prof. Carol Robinson's group in Oxford.